XVI INTERNATIONAL SCIENTIFIC CONGRESS

WINTER SESSION

13 - 16.03.2019, BOROVETS BULGARIA

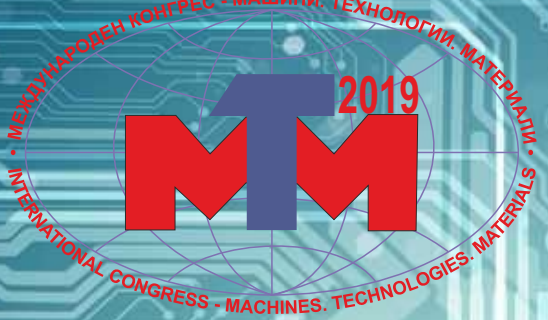

MACHINES. TECHNOLOGIES. MATERIALS 2019

PROCEEDINGS

VOLUME I
MACHINES. TECHNOLOGIES. MATERIALS

ISSN 2535-0021 (PRINT)
ISSN 2535-003X (ONLINE)

SCIENTIFIC-TECHNICAL UNION OF MECHANICAL ENGINEERING - INDUSTRY 4.0
BULGARIA

INTERNATIONAL SCIENTIFIC CONFERENCE

MACHINES. TECHNOLOGIES. MATERIALS

13-16.03.2019, BOROVETS, BULGARIA

PROCEEDINGS

YEAR III, ISSUE 1 (12), BOROVETS, BULGARIA 2019

VOLUME I

MACHINES. TECHNOLOGIES. MATERIALS

ISSN 2535-0021 (PRINT)
ISSN 2535-003X (ONLINE)

PUBLISHER:

SCIENTIFIC TECHNICAL UNION OF MECHANICAL ENGINEERING INDUSTRY-4.0

108, Rakovski Str., 1000 Sofia, Bulgaria
tel. (+359 2) 987 72 90,
tel./fax (+359 2) 986 22 40**,**
office@mtmcongress.com
www.mtmcongress.com

INTERNATIONAL EDITORIAL BOARD

Chairman: Prof. DHC Georgi Popov

Vice Chairman: Prof. Dr. Eng. Tsanka Dikova

Members:

Acad. Ivan Vedyakov	RU	Prof. Mihail Aurel Titu	RO
Acad. Yurij Kuznetsov	UA	Prof. Mladen Velev	BG
Prof. Aleksander Mihaylov	UA	Prof. Mohamed El Mansori	FR
Prof. Anatoliy Kostin	RU	Prof. Movlazade Vagif Zahid	AZ
Prof. Adel Mahmud	IQ	Prof. Nikolay Dyulgerov	BG
Prof. Ahmet Ertas	TR	Prof. Oana Dodun	RO
Prof. Andrzej Golabczak	PL	Prof. Olga Krivtsova	KZ
Prof. Boncho Bonev	BG	Prof. Peter Kostal	SK
Prof. Gennady Bagluk	UA	Prof. Raul Turmanidze	GE
Prof. Detlef Redlich	DE	Prof. Renato Goulart	BR
Prof. Dipten Misra	IN	Prof. Roumen Petrov	BE
Prof. Dmitry Kaputkin	RU	Prof. Sasho Guergov	BG
Prof. Dmitry Dmitriev	UA	Prof. Seiji Katayama	JP
Prof. Eugene Eremin	RU	Prof. Sergej Dobatkin	RU
Prof. Ernest Nazarian	AM	Prof. Sergej Nikulin	RU
Prof. Juan Alberto Montano	MX	Prof. Stefan Dimov	UK
Prof. Esam Husein	KW	Prof. Svetan Ratchev	UK
Prof. Ilir Doci	KO	Prof. Svetlana Gubenko	UA
Prof. Ivo Malakov	BG	Prof. Sveto Cvetkovski	MK
Prof. Katia Vutova	BG	Prof. Tale Geramitchioski	MK
Prof. Krasimir Marchev	USA	Prof. Vadim Kovtun	BY
Prof. Leon Kukielka	PL	Prof. Viktor Vaganov	RU
Prof. Lyudmila Ryabicheva	UA	Prof. William Singhose	USA
Prof. Milan Vukcevic	ME	Prof. Wu Kaiming	CN
		Prof. Yasar Pancar	TR

C O N T E N T S

SECTION "MACHINES"

SPATIAL GEARING: KINEMATIC CHARACTERISTICS OF THE INSTANTANEOUS CONTACT
Assoc. Prof. Abadjieva E. PhD., Prof. Sc. D. Abadjiev V. PhD. 5

OPTIMISATION OF GEAR GEOMETRICAL PARAMETERS USING KISSSOFT
Emre Can, Mehmet Bozca 10

FINITE ELEMENTS METHOD MODELLING OF ROLLING BEARINGS
Mustafa Koç, Mehmet Bozca 14

SUBSTITUTION OF GEAR-BAR MECHANISM WITH BAR MECHANISM ON THE INFEED MECHANISM OD BOTTLE WASHER
Spec. Sci. Vidak Šabanović , Prof. Dr. Goran Ćulafić 18

NUMERICAL ANALYSIS OF TURBO-GENERATOR STEAM TURBINE ENERGY EFFICIENCY AND ENERGY POWER LOSSES CHANGE DURING THE VARIATION IN DEVELOPED POWER
PhD. Mrzljak Vedran, PhD. Poljak Igor, Prof. PhD. Prpić-Oršić Jasna 22

INFLUENCE OF THE AMBIENT TEMPERATURE CHANGE ON STEAM PRESSURE REDUCTION VALVE EXERGY DESTRUCTION AND EXERGY EFFICIENCY
PhD. Mrzljak Vedran, PhD. Poljak Igor, PhD. Orović Josip, Prof. PhD. Prpić-Oršić Jasna 26

COMPARISON OF NUMERICAL METHODS FOR MODELING THE EFFECT OF EXPLOSION ON PROTECTIVE STRUCTURES
PhD.Bisyk S., PhD.Davydovskyi L., PhD.Hutov I., Ass. Prof. PhD. Slyvinskyi O., M.Sc. Aristarkhov O., Prof. PhD. Lilov 30

SECTION "TECHNOLOGIES"

МОДЕЛИРОВАНИЕ РАДИАЛЬНО-СДВИГОВОЙ ПРОКАТКИ АУСТЕНИТНОЙ НЕРЖАВЕЮЩЕЙ СТАЛИ AISI-321 С ЦЕЛЬЮ ОПРЕДЕЛЕНИЯ ОПТИМАЛЬНЫХ ТЕХНОЛОГИЧЕСКИХ ПАРАМЕТРОВ ДЛЯ ПОЛУЧЕНИЯ УМЗ-СТРУКТУРЫ
Д.т.н., проф. Найзабеков А.Б., к.т.н., доцент Лежнев С.Н., PhD Арбуз А.С., PhD Панин Е.А. 34

A-TIG WELDING AS A SOLUTION FOR NICKEL AND MANGANESE SAVINGS IN DUPLEX STAINLESS STEEL WELDED JOINTS
Ph.D. Bušić M., Ph.D. Jurica M., Prof. Ph.D. Garašić I., Prof. Ph.D. Kožuh Z. 38

CALCULATING CONTOURING TOOL BY FINITE DIFFERENCE METHOD
Prof. Dr. Kikvidze O., Assoc.Prof. Dr.Sakhanberidze N.., senior teacher Kordzadze L 42

AN EXPERIMENTAL STUDY FOR THERMAL AND HYDRAULIC PERFORMANCE OF A MINI CHANNEL SHELL AND TUBE HEAT EXCHANGER USING LOW CONCENTRATION NANOFLUIDS PREPARED WITH AL2O3 NANOMATERIALS
M.Sc. Mehmet Senan Yilmaz, Assist. Prof. PhD. Hasan Kucuk, Res. Assist. PhD. Murat Unverdi 47

DETERMINATION OF GEOMETRIC PARAMETERS OF GRADIENT STRUCTURES FORMED IN OPTICAL GLASS BY THE ELECTRON BEAM METHOD
Grechana O., Skoryna E., PhD Bondarenko I. 54

UNIVERSAL THERMAL MICROSYSTEMS BASED ON SILICON CARBIDE
Phd Student Eng Daniil Evstigneev, Prof. Grand PhD in Engeneers Science Eng . Vladimir Karachinov, Master's degree courses Eng. AntonVarshavsiy, PhD Applicant Eng. Petrov Dmitriy 59

DIAGNOSTICS OF THERMAL PIPES WITH SYMMETRIC STRUCTURE THERMAL IMPACT METHOD
Grand PhD in Engeneers Science Eng . Vladimir Karachinov,Phd Student Eng Daniil Evstigneev, Prof.,PhD in Engeneering sciences Eng. Alexander Abramov, , PhD Applicant Eng. Petrov Dmitriy 62

AN EFFICIENT COMBINATION OF WATER TREATMENT AND ELECTRICITY GENERATION BY DIFFERENT MICROORGANISMS
Assoc. Prof. PhD M. Nicolova, Assoc. Prof. PhD I.Spasova, Assoc. Prof. PhD P. Georgiev, Prof. PhD V. Groudeva, Prof. DSc S. Groudev 65

AN EXPERIMENTAL STUDY ON CUTTING FORCES AND SURFACE ROUGHNESS IN MQL MILLING OF ALUMINUM 6061
B.Sc. Conger D.B., M.Sc. Emiroglu U., Assoc. Prof. M.Sc. Uysal A. PhD., Prof. M.Sc. Altan E. PhD. 67

FLANK WEAR OF SURFACE TEXTURED TOOL IN DRY TURNING OF AISI 4140 STEEL
Mech. Eng. Eskizara H. B., R. Assist. Emiroglu U., Prof. Dr. Altan E. 71

EFFECTS OF PROCESS PARAMETERS IN PLASMA ARC CUTTING ON STAINLESS STEELS AND STRUCTURAL STEEL
Erbilen M., Çakır O. 75

ГЛОБАЛЕН МАКСИМУМ – ПРАКТИЧЕСКИ ОЦЕНКИ В ОБЛАСТТА НА МЕТАЛУРГИЧНИЯ ДИЗАЙН
Йордан Калев, Николай Тончев 78

TECHNOGENIC RAW MATERIALS FOR THE PRODUCTION OF MAGNESIUM AND SILICON-CONTAINING COMPOUNDS
Candidate of technical sciences Shayakhmetova R.A., PhD student Mukhametzhanova A.A. , Candidate of geological and mineralogical sciences Samatov I.B.1, doctor of chemical sciences, assoc. prof. Akbayeva D.N. 85

GEOMETRIC METHOD FOR DETERMINIG RADIANT HEAT EXCHANGE IN VACUUME FURNACE
PhD Eng. Angelova E, Assoc.Prof. PhD Eng. Ronkova V., Assoc.Prof. PhD Eng. 88

HOME PAGES, DEFINITION AND CLASSIFICATION OF THEIR ELEMENTS AND THEIR DISPLAY ON THE USERS' COMPUTERS
Asst. Prof. Bidjovski Goran PhD. 91

DAMAGE FUNCTIONS EVALUATION COHERENT TO WEAPON TARGET INTERACTION
Assistant M.Sc. Ing. Katsev I., Prof. PhD. Evlogiev S. 96

СТЕГАНАЛИЗ НА ИЗОБРАЖЕНИЯ ЧРЕЗ ИЗПОЛЗВАНЕ НА МУЛТИ-КЛАСИФИКАТОР
Диан Велев, Ст. Павлова, полк. проф. д-р инж. И.Лилов, И. Кичуков 99

SECTION "MATERIALS"

INCREASE IN STRENGTH PROPERTIES OF LOW-CARBON STEELS DUE TO STRUCTURAL TRANSFORMATIONS AT DEFORMATION BY ROTARY SWAGING
Prof., Dr.Sci. Dobatkin S.V., Dr. Rybalchenko O.V., Tokar A.A., Prof., Dr.Sci. Odessky P.D., Lunev V.A., Morozov M.M., Dr.Sci. Yusupov V.S. 102

FEATURES OF STRUCTURE FORMATION AND MECHANICAL BEHAVIOR OF METALLIC MATERIALS UNDER CONDITIONS OF APPLICATION OF GRADIENT DEFORMATIONS
A.G. Raab - Ph.D., A.P. Zhilyaev– Dr. Sci, I.S.Kodirov, G.N. Aleshin - Ph.D. 105

TRIBOLOGICAL PROPERTIES OF COMMERCIALLY PURE COPPER AND A LOWALLOYED CHROMIUM BRONZE
Lead. Res., Dr. Semenov V.I., PhD Stud. Alemayehu D.B., Prof., Dr. Lin H.-C., Lead. Res., Prof. Raab G.I.1, Prof., Dr. Huang S.-J., Prof., Dr. Chun Chiu 107

COMPARATIVE TRIBOLOGICAL PROPERTIES OF AZ91D MAGNESIUM ALLOY AFTER STRENGTHENING BY SiC POWDER AND AFTER SEVERE PLASTIC DEFORMATION
Lead. Res., Dr. Semenov V. I., Prof., Dr. Lin H.-C., Prof. Shuster L.Sh., Prof. N. Tontchev, Prof., Dr. Chun Chiu, Prof., Dr. Huang S.-J. 111

PREPARATION AND PROPERTIES OF CARBON ADSORBENTS BASED ON PLANT RAW MARERIALS AND POLYMERIC WASTE
Доц. к.т.н. Нистратов А.В., проф. д.т.н. Клушин В.Н. 115

GEOPOLYMERS BASED ON BULGARIAN RAW MATERIALS – PRELIMINARY STUDIES
Ass. Prof. Dr. Eng. Nikolov A. 120

CRACK RESISTANCE EVALUATION FOR Al+3.5% Mg ALLOYS BY MEASURMENTS OF ULTRASONIC VELOCITIES AND HARDNESS
Assoc. Prof. PhD Alexander Popov, PhD. Eng. Georgy Dobrev 124

DETERMINATION OF GEYSER EVENTS IN A THERMOSYPHON WORKING WITH GRAPHENE OXIDE NANOFLUID
Kujawska A., Zajaczkowski B., Woluntarski M., Buschmann M.H. 128

GRADIENT STRUCTURE AND METHODS FOR THEIR PREPARATION
G.I. Raab – Dr.Sci, A.G. Raab - Ph.D., A.P. Zhilyaev – Dr.Sci 132

SURFACE HARDENING OF METALLIC MATERIALS BY USE OF COMBINED MAT-FORMING TREATMENT AND ELECTROSPARK DOPING
Prof. Bagliuk G., Dr. Sc., Makovey V., PhD. Borodiy Yu., PhD. 134

INFLUENCE OF THE SYNTHESIS METHOD ON THE CRYSTALLINE STRUCTURE, PHASE COMPOSITION AND PROPERTIES OF TiCrFeNiCuC EQUIATOMIC ALLOYS
M.Sc. Marych M., Mamonova A., PhD., Prof. Bagliuk G., Dr. Sc. 138

FATIGUE ANALYSIS APPROACHES FOR VEHICLE COMPONENTS MADE OF RUBBER
M.Sc. Tomposne Szüle V. 141

RECYCLED TIRE RUBBER MODIFIED BITUMENS FOR IMPROVING THE QUALITY OF THE ROAD CONSTRUCTIONS IN ALBANIA
Dhoska K. PhD., Markja I. PhD. 145

SURFACE TREATMENTS AND COATINGS APPLICATION ON THE ALUMINUM PRODUCTS
PhD. Markja I, PhD. Dhoska K., Prof. As. Elezi D. 147

IDENTIFICATION OF TEKRONE POLYMER MATERIAL
д. н. гос. упр., к.т.н., проф. Кобец А., к.т.н. доц. Деркач А., к.т.н., доц. Кабат О., асп. Муранов Е., инж. Шаповал А. 149

SPATIAL GEARING: KINEMATIC CHARACTERISTICS OF THE INSTANTANEOUS CONTACT

Assoc. Prof. Abadjieva E. PhD.[1,2], Prof. Sc. D. Abadjiev V. PhD.[2]
Graduate School of Engineering Science, Akita University, Japan[1]
Institute of Mechanics, Bulgarian Academy of Sciences, Bulgaria [2]

abadjieva@gipc.akita-u.ac.jp

Abstract: *In this work, case of rotations transformation between arbitrary crossed shafts (axes of rotations) by means of high kinematic joints, which elements configure active tooth surfaces of hyperboloid gear mechanisms is treated. |Analytical dependencies, defining the law of rotations transformation are illustrated. This law of transformation in this concrete case is a constant function of the relations of the angular velocities of the movable links of the spatial three-link gear mechanism. The shown functions are applicable both to the synthesis of the studied transmissions, and for the determining and control of the kinematic errors of these transmissions, caused by manufacturing and assembly errors.*

Keywords: SPATIAL GEARING, HYPERBOLOID GEAR DRIVES, INSTANTANEOUS TANGENTIAL CONTACT, INSTANTANEOUS ANGULAR VELOCITY RATIO

1. Introduction

The *Science of Spatial Gearing*, that studies the processes of rotations transformation upon a preliminary defined law between non-coplanar (in the most common case) axes by means of three-links mechanisms, having high kinematic joints, essentially can be considered as an independent direction of the science *Applied Mechanics*. It studies kinematic and dynamic behavior of these body systems, in relation to the geometric characteristics of the elements of the constituting high kinematic joints.

Three-links mechanisms, for which the transformation of rotations between non-coplanar axes is accomplished through a system of high kinematic joints, which elements come into and go out of *tangent contact* (*instantaneous contact*), by observing a definite law of order, are named *hyperboloid0 gear mechanisms*. This name is derived from the fact that their axoids are two revolution hyperboloids, which geometric axes coincide with the axes of rotations of the movable links of the three-links gear mechanism. For them the rotations transformation is realized as a result of the action of normal forces in the places of tangent contact of the elements of the kinematic joints. The process of sequential occurrence and disintegration of kinematic joints is a permanent and regular one, and during its realization over time there should be more than one configured kinematic joint. The state in which kinematic joints exist is called *gearing*. For gear sets, when their axes of rotations do not lie in one plane, is talked about *spatial gearing*.

The main focus of the current research is put on defining of specific characteristics of the instantaneous contact of the elements of high kinematic joints, when the processes of the rotations transformation by means of hyperboloid gear mechanisms are realized.

2. Instantaneous Velocity Ratio in the Pitch Contact Point

The exactness of the realization of a preliminary given law of rotations transformation between shafts with crossed axes by means of three-links gear mechanism, is in a direct dependency on geometric and kinematic conjugation of the active tooth surfaces, which come in and go out of contact. In this process, every occurred *instantaneous contact point* (for gear mechanisms with a point contact) or *instantaneous contact line* (for gear transmissions with linear contact) is characterized by an *instantaneous velocity ratio.* The main requirement to the synthesis and design of gear mechanisms are that their instantaneous velocity ratio should correspond to a preliminary given design value, by observing an adequate exactness. Hence, the defining of the instantaneous velocity ratio, as a function of the geometric parameters of spatial gear sets, is of a great importance, especially for the kinematic types of gear mechanisms, when it is necessary to study their sensitivity, while these parameters are changing.

Main interest, from view point of the synthesis of spatial gear drives upon a pitch contact point, is to be defined the instantaneous velocity ratio when the instantaneous conjugated contact point, respectively the instantaneous conjugated line, passes through the pitch contact point. For this case it is necessary to define the instantaneous velocity ratio by means of the geometric parameters of the pitch contact point [1, 2].

Considering the symbols given in Fig. 1, for the instantaneous velocity ratio at one arbitrary contact point it can be written [3, 4]:

$$i_{12} = \frac{\omega_1}{\omega_2} = \frac{d_2}{d_1} = \frac{e_2 \sin\varepsilon_2}{e_1 \sin\varepsilon_1}. \qquad (1)$$

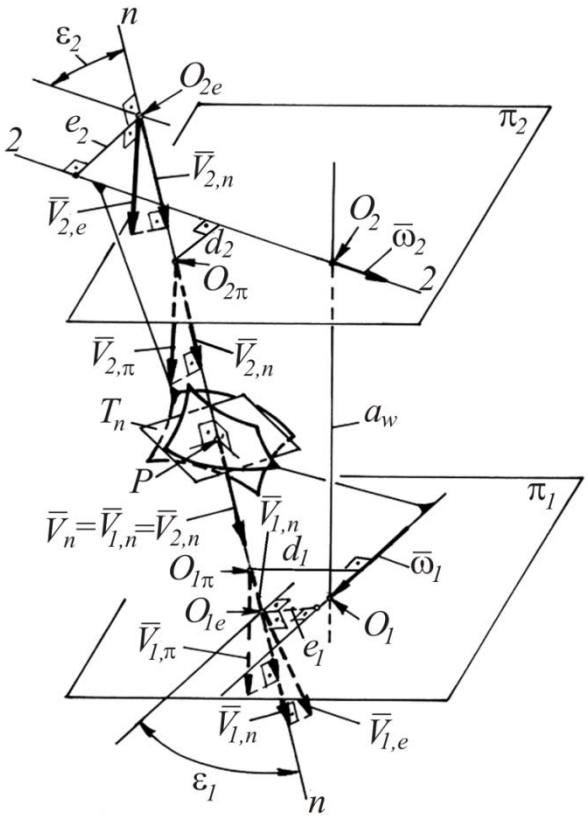

Fig. 1. *Kinematic scheme for determining the instantaneous velocity ratio of a hyperboloid gear mechanism*

Here ω_i $(i=1,\ 2)$ are the magnitudes of the instantaneous angular velocities $\overline{\omega}_1$ and $\overline{\omega}_2$; d_i $(i=1,\ 2)$ - minimal distance between the points of piercing $O_{i\pi}$ $(i=1,\ 2)$ of the normal $n-n$ with planes Π_i $(i=1,\ 2)$ and the rotations axes $i-i$ $(i=1,\ 2)$. $n-n$ is a normal line to the tooth surfaces Σ_1 and Σ_2 passing through the conjugated contact point P. The planes Π_i $(i=1,\ 2)$ are perpendicular to the axis O_1O_2 of the crossed axes of rotations $1-1$ and $2-2$ and contain as well the corresponding crossed axes $i-i$ $(i=1,\ 2)$; e_i $(i=1,\ 2)$ - minimal distances between $n-n$ and the crossed axes $i-i$; ε_i $(i=1,\ 2)$ - angles between the normal $n-n$ and the axes of rotation $i-i$ $(i=1,\ 2)$.

Here, it will be reminded that in general case, in order to realize rotations transformation between fixed crossed axes $i-i$ $(i=1,\ 2)$ by means of the conjugated contact point P it is appropriate the instantaneous contact in it to be considered by means of two infinitely small regions from the surfaces Σ_1 and Σ_2, respectively. Actually, these regions have a relative motion, determined by the vector of the relative velocity $\overline{V}_{12}$, which is a result of the rotation of Σ_i $(i=1,\ 2)$ around axes $i-i$ $(i=1,\ 2)$ (see Fig. 1). The fact, that one of the surfaces Σ_i $(i=1,\ 2)$ transmits motion to the other one, means that the $\overline{V}_{12}$ lies in their common tangent plane T_n. If this condition is fulfilled, from it follows the equality of the normal components of the absolute velocities of P, considered as a point from Σ_i $(i=1,\ 2)$ and vice versa. Both conditions are equivalent ones for the kinematically conjugated action in the point P, namely:

$$\overline{V}_{1,n}=\overline{V}_{2,n}, \tag{2}$$

where $\overline{V}_{i,n}$ is a normal component of the absolute velocity $\dot{\overline{\rho}}_i$ and of the circumferential velocity $\overline{V}_i$.

Let's first show how equality (1) is obtained, from the condition (2), and taking into account Fig. 1:

- From $\overline{V}_{1,n}=\overline{V}_{2,n} \Rightarrow \overline{V}_{1,\pi}=\overline{V}_{2,\pi} \Rightarrow \omega_1.d_1=\omega_2.d_2$ and $i_{12}=\dfrac{\omega_1}{\omega_2}=\dfrac{d_2}{d_1}$;

-From $\overline{V}_{1,n}=\overline{V}_{2,n} \Rightarrow V_{1,e}.\sin\varepsilon_1=V_{2,e}.\sin\varepsilon_2 \Rightarrow$

$\omega_1.e_1.\sin\varepsilon_1=\omega_2.e_2.\sin\varepsilon_2$ and $i_{12}=\dfrac{\omega_1}{\omega_2}=\dfrac{e_2.\sin\varepsilon_2}{e_1.\sin\varepsilon_1}$.

When taking into account the symbols, given in Fig. 1 and Fig. 2 (assuming that the conjugated contact point is a pitch contact point) then from (2) it can be written:

$$V_{i,n}=V_i\cos\beta_i\cos\alpha_n=\omega_i r_i\cos\beta_i\cos\alpha_n, \tag{3}$$

where V_i is the magnitude of the circumferential velocity $\overline{V}_i$; r_i - radius of the pitch circle H_i; β_i - angle of inclination of the longitudinal line of the tooth in the pitch contact point P; α_n - normal profile angle of Σ_i in the pitch contact point P (a pitch normal angle); $V_{i,n}$ - magnitude of the projection of the circumferential velocity vector $\overline{V}_i$ on the common normal $n-n$.

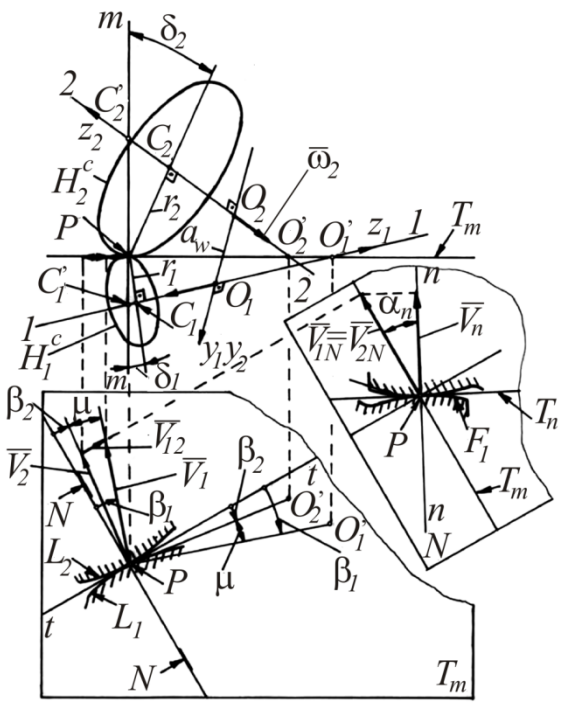

Fig. 2. *Geometric-kinematic scheme of a spatial gear pair with an opposite orientation of the longitudinal line of the teeth*

Then from (2) and (3), the well-known dependency is obtained [5, 6, 7, 8]:

$$i_{12}=\frac{\omega_1}{\omega_2}=\frac{r_2\cos\beta_2}{r_1\cos\beta_1}. \tag{4}$$

When the rotations transformation between crossed axes $1-1$ and $2-2$ by means of contacting in pitch contact point P tooth surfaces Σ_1 and Σ_2 with an opposite orientation of the longitudinal lines L_1 and L_2 (see Fig. 2) is realized, then the equation (4) can be presented in the type [1, 2]:

$$i_{i,i\pm1}=\frac{\omega_i}{\omega_{i\pm1}}=\frac{r_{i\pm1}}{r_i}(\cos\mu\pm\tan\beta_i\sin\mu), \tag{5}$$

where $i=1,\ 2$ is the number of the gear, and μ - hypoid angle.

For the case of spatial rotations transformation between crossed axes, by means of contacting in the pitch contact point P tooth surfaces Σ_1 and Σ_2 with one-way orientation of their longitudinal lines L_1 and L_2 (see Fig. 3), then the equality (4) is of the type [2]:

$$i_{i,i\pm1}=\frac{\omega_i}{\omega_{i\pm1}}=\frac{r_{i\pm1}}{r_i}(\cos\mu+\tan\beta_i\sin\mu). \tag{6}$$

In equations (5) and (6) the above signs refer to $i=1$, and bellow ones – $i=2$.

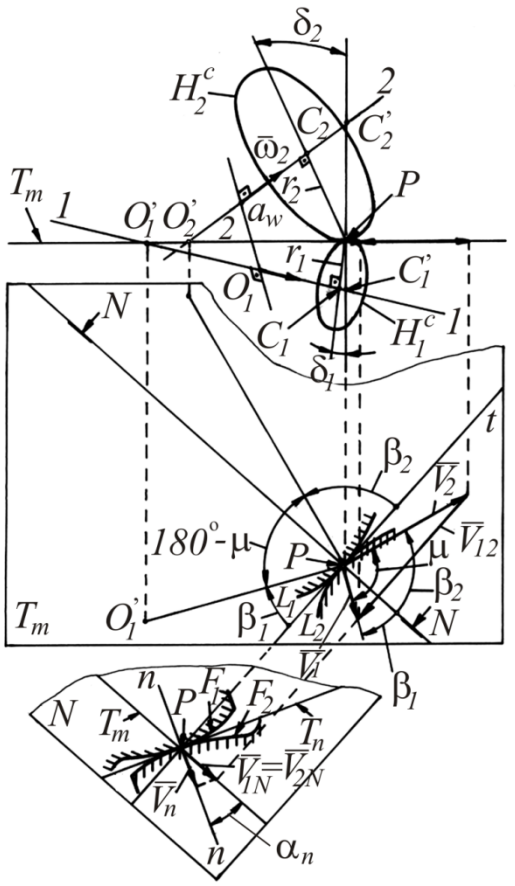

Fig. 3. *Geometric –kinematic scheme of spatial gear pair with one-way orientation of the longitudinal line of the teeth*

If from a formal view point it is assumed that i represents the number of the movable link of the three-links spatial gear mechanism, then the cases $i=1$ define the instantaneous velocity ratio in the pitch contact point, when a rotation from axis $1-1$ is transmitted towards axis $2-2$, and $i=2$ covers the cases of rotations transformation form $2-2$ towards $1-1$.

In order, the rotations transformation between crossed axes $i-i$ $(i=1,\ 2)$ are realized, when the active tooth surfaces Σ_1 and Σ_2 have a contact in the pitch contact point P, (for a nominal velocity ratio, which is equal to the instantaneous velocity ratio), the longitudinal lines L_1 and L_2 of the mentioned above tooth surfaces, should have an inclination angles, defined by the expressions [2]:

- When the longitudinal lines L_i $(i=1,\ 2)$ have opposite orientations

$$tan\,\beta_i = \pm\frac{r_i.i_{i,i\pm1} - r_{i\pm i}.cos\,\mu}{r_{i\pm i}.sin\,\mu}, \tag{7}$$

- When the longitudinal lines L_i $(i=1,\ 2)$ have one-way orientation

$$tan\,\beta_i = \frac{r_i.i_{i,i\pm1} - r_{i\pm i}.cos\,\mu}{r_{i\pm i}.sin\,\mu}. \tag{8}$$

For the case when the analysis of the instantaneous velocity ratio requires estimations to be made on the basis of the analytical dependence (1), it is necessary the defined distances e_i and d_i to be expressed, by means of the geometric parameters of the tooth surfaces Σ_1 and Σ_2 in the pitch contact point.

Then from (1), taking into account the symbols shown in Fig. 1, Fig. 2 and Fig. 3, it can be written

$$\begin{aligned} &\frac{V_{i,n}}{V_{i,\pi}} = cos\,\Delta, \\ &V_{i,n} = \omega_i.r_i\,cos\,\beta_i\,cos\,\alpha_n, \\ &V_{i,\pi} = \omega_i.d_i. \end{aligned} \tag{9}$$

From (9) it is obtained

$$d_i = \frac{r_i\,cos\,\beta_i\,cos\,\alpha_n}{cos\,\Delta}, \tag{10}$$

where Δ is an acute angle between the normal $n-n$ and the direction of the line O_1O_2 of the crossed axes of rotations $i-i$ $(i=1,\ 2)$.

Analogically, for the distance e_i, the following expression can be received:

$$\begin{aligned} &\frac{V_{i,n}}{V_{i,e}} = sin\,\varepsilon_i, \\ &V_{i,n} = \omega_i.r_i\,cos\,\beta_i\,cos\,\alpha_n, \\ &V_{i,e} = \omega_i.e_i, \end{aligned} \tag{11}$$

whence

$$e_i = \frac{r_i\,cos\,\beta_i\,cos\,\alpha_n}{sin\,\varepsilon_i}. \tag{12}$$

When (10) and (12) are solved together, then the following relation between the distances d_i and e_i, (for the case when the instantaneous contact is realized in the pitch contact point P) is obtained:

$$\frac{d_i}{e_i} = \frac{sin\,\varepsilon_i}{cos\,\Delta}. \tag{13}$$

3. Geometric-Kinematic Model of the Object of the Research

As it has already been mentioned, the transformation of rotations according to a preliminary defined law is a basic process, to the realization of which are oriented to the predominant part of the *three-links hyperboloid gear mechanisms*. From a theoretical view point, the most common process is the process of spatial rotations transformation with the crossed placement of the axes of the movable links of the three-links transmission mechanism, which determines the predominant interest of the researchers. For this reason, for the current study, a mechano-mathematical model will be illustrated, that treats this most common case, but in an aspect determined by its practical application. In other words, the study will consider a hyperboloid gear mechanism, transforming rotations with constant angular velocities between crossed shafts (axes). The model presented below illustrates geometric-kinematic characteristics - an object of the current work.

On Fig. 4 a geometric-kinematic scheme of three-links gear mechanism, transforming by means of movable links (gears) 1 and 2 rotations with angular velocities $\overline{\omega}_1$ and $\overline{\omega}_2$ between fixed crossed axes $1-1$ and $2-2$ (placed in the static space) of the links 1 and 2 is illustrated. The studied case of the process of rotations transformation is characterized by the following conditions:

$$\begin{aligned} &\omega_i = constant,\ \ i = (1,\ 2),\\ &\delta = \angle(\overline{\omega}_1, \overline{\omega}_2) = constant,\\ &a_w = constant,\\ &i_{12} = \frac{\omega_1}{\omega_2} = \frac{1}{i_{21}} = constant, \end{aligned} \tag{14}$$

where ω_i is a magnitude of the angular velocity vector $\overline{\omega}_i$ of rotations of the movable link i; δ - crossed angle of the axes $1-1$ and $2-2$; a_w - minimal distance between the crossed axes $1-1$ and $2-2$ (offset); i_{12} (i_{21}) - velocity ratio.

The rotations transformation is realized by means of high kinematic joint ($\Sigma_1 : \Sigma_2$), which elements are the surfaces Σ_1 and Σ_2, that in a given moment have a conjugate contact point P (the tangent point of contact P can belong to the conjugated instantaneous contact line D_{12}). Here, it should be mentioned, that in the case of a real gear mechanism, in every moment more than one pair of tooth surfaces Σ_1 and Σ_2 exists, forming kinematic joints ($\Sigma_1 : \Sigma_2$). When one of the movable links, for example $i = 1$, is put into rotation with an angular velocity $\overline{\omega}_1$, then the other movable link $i = 2$ starts to rotate. And if the obtained rotation of the second movable link is determined by the angular velocity $\overline{\omega}_2$, (for which the condition $\omega_2 = \omega_1 i_{21} = constant$ is fulfilled, that is equivalent to the last equality of conditions (14)), then it can be affirmed, that the kinematic joints ($\Sigma_1 : \Sigma_2$) (illustrated on Fig. 4), and the studied gear mechanism respectively, are kinematically conjugated.

The research is realized with introducing the right-handed coordinate systems $S(O, x, y, z)$ and $S_i(O_i, x_i, y_i, z_i)$ $(i = 1,\ 2)$, from which S is a static coordinate system (connected with the non-movable link (posture) of the three-links gear mechanism), and S_i $(i = 1,\ 2)$ are the coordinate systems, firmly connected with the movable links $i = 1,\ 2$. The mentioned above coordinate systems are not shown in Fig. 4. The current position of S_1 and S_2 towards S is given by the parameters of rotations (meshing) φ_i $(i = 1,\ 2)$.

Let's the elements Σ_1 and Σ_2 of the high kinematic joint are described parametrically in the static coordinate system S [2, 5-8].

$$\begin{aligned} &\overline{\rho}_{i,s} = \overline{\rho}_{i,s}(u_i, \vartheta_i, \varphi_i),\\ &\overline{n}_{i,s} = \overline{n}_{i,s}(u_i, \vartheta_i, \varphi_i), \end{aligned} \tag{15}$$

where $\overline{\rho}_{i,s}$ is a radius-vector of the contact point P, considered as a point from Σ_i; $\overline{n}_{i,s}$ - normal vector to Σ_i at the same point; u_i, ϑ_i - independent parameters, determining the location of point P on Σ_i.

As it has already been mentioned, at the point of geometric conjugation of the surfaces Σ_1 and Σ_2, the following conditions are fulfilled:

$$\begin{aligned} &\overline{\rho}_{1,s}(u_1, \vartheta_1, \varphi_1 = constant) =\\ &= \overline{\rho}_{2,s}(u_2, \vartheta_2, \varphi_2 = constant),\\ &\overline{n}_{1,s}(u_1, \vartheta_1, \varphi_1 = constant) =\\ &= \overline{n}_{2,s}(u_2, \vartheta_2, \varphi_2 = constant). \end{aligned} \tag{16}$$

For concrete values of the parameters of rotation φ_1 and $\varphi_2 = \varphi_1 i_{21}$, u_1 and ϑ_1 are pair of independent parameters, defining point P as a point from Σ_1, which has a tangent contact with the corresponding point P from Σ_2, defined by the parameters u_2 and ϑ_2.

In the process of motion of the kinematic conjugated joints for the current points P, the conditions (16) are constantly fulfilled for the $\varphi_i = varia,\ \ i = 1,\ 2$. Then [5 - 8]

$$\begin{aligned} &\dot{\overline{\rho}}_{1,s}(u_1, \vartheta_1, \varphi_1) = \dot{\overline{\rho}}_{2,s}(u_2, \vartheta_2, \varphi_2),\\ &\dot{\overline{n}}_{1,s}(u_1, \vartheta_1, \varphi_1) = \dot{\overline{n}}_{2,s}(u_2, \vartheta_2, \varphi_2), \end{aligned} \tag{17}$$

$$\begin{aligned} &\ddot{\overline{\rho}}_{1,s}(u_1, \vartheta_1, \varphi_1) = \ddot{\overline{\rho}}_{2,s}(u_2, \vartheta_2, \varphi_2),\\ &\ddot{\overline{n}}_{1,s}(u_1, \vartheta_1, \varphi_1) = \ddot{\overline{n}}_{2,s}(u_2, \vartheta_2, \varphi_2), \end{aligned} \tag{18}$$

where $\dot{\overline{\rho}}_{i,s}$ is an absolute velocity of the contact point P, joined to the Σ_i; $\dot{\overline{n}}_{i,s}$ - an absolute velocity of the tip of the normal vector $\overline{n}_i$ in the contact point P, joined to the Σ_i; $\ddot{\overline{\rho}}_{i,s}$ - an absolute acceleration of the contact point P, considered as a point from Σ_i; $\ddot{\overline{n}}_{i,s}$ - an absolute acceleration of the tip of the $\overline{n}_i$, in point P, joined to the Σ_i.

Here and further under conjugation of the kinematic joints, and functioning through them transmission mechanisms, it will be understood their theoretically kinematic conjugation. The systems (17) and (18) are the vector conditions for conjugation of the studied hyperboloid gear mechanism. The first equality from (7) can be presented easily in the form [5 - 8]:

$$\overline{V}_{r,2} = \overline{V}_{r,1} + (\overline{V}_1 - \overline{V}_2) = \overline{V}_{r,1} + \overline{V}_{12}, \tag{19}$$

As it can be seen, these vector equations are determining for both the circumferential and the relative motion of the conjugated contact points. Moreover, (19) shows, that vectors $\overline{V}_{12}$ $\overline{V}_{r,1}$ and $\overline{V}_{r,2}$, as well as the vectors $\overline{V}_{12}$, $\overline{V}_1$ and $\overline{V}_2$ are two triplets of coplanar vectors.

The first triplet determines the tangent plane T_n in the conjugated contact point P of Σ_1 and Σ_2. The second triplet of vectors, determines plane T_m, which under concrete conditions contains the *pole of meshing/pitch contact point* of the synthesized gear set. The above comment is illustrated on Fig. 4.

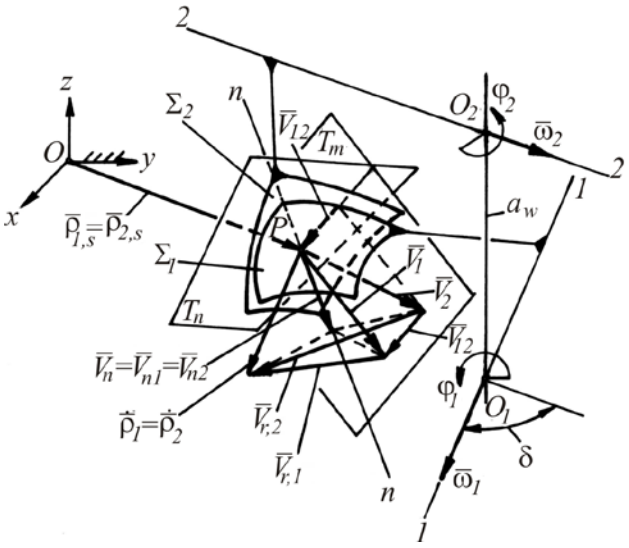

Fig. 4. *Kinematic scheme of the conjugated action of the active tooth surfaces* Σ_1 *and* Σ_2 *of the three-links hyperboloid gear transmission in the contact point* P*:* $i-i$ $(i=1,\ 2)$ *- rotation axes of the movable links;* a_w *- offset;* δ *- crossed angle of the axes* $1-1$ *and* $2-2$*;* T_n *- common tangent plane of* Σ_1 *and* Σ_2 *at point* P*;* $n-n$ *- common normal of* Σ_i $(i=1,\ 2)$ *at point* P*;* $\bar{\rho}_{i,s}$ *- radius-vector of point* P*, joined to the* Σ_i *in the static space* $S(O,x,y,z)$*;* $\dot{\bar{\rho}}_i$ *is an absolute velocity of the contact point* P*;* $\bar{V}_{12}$ *- relative velocity of point* P*;* $\bar{V}_{r,i}$ *- relative velocity of the motion of point* P *on the tooth surface* Σ_i*;* $\bar{V}_{n,i}$ *- normal components of* $\dot{\bar{\rho}}_i$

The model of the process of spatial transformation of rotations, described briefly in this paragraph, by means of a hyperboloid gear drive with arbitrary crossed axes of rotation, is in the basis of the current work.

4. Conclusion

For the synthesis of hyperboloid gear transmissions, it is necessary to be defined an analytical approach for determining the kinematic error in the spatial gearing, which as a rule occurs as a result of manufacturing and assembly inaccuracies during the realization of these transmissions. In the present work it is illustrated sequentially:

- A generalized mathematical model of the hyperboloid transmissions (based on their geometric and kinematic features) is defined.
- The analytical relations, for the instantaneous velocity ratio in an arbitrary contact point of the instantaneous tangent contact of the gear drives with an arbitrary crossed axes are illustrated in the current reserach.
- Generalized dependencies for determination of the instantaneous velocity ratio in the pitch contact point are written. Dependencies by which kinematic and geometric estimations of the synthesized spatial gear mechanisms (upon a pitch contact point) by introducing geometric-kinematic parameters of the pitch contact point, are also written.
- Generalized expressions for the angles, defining the inclination of the longitudinal lines of the teeth (when their synthesis is realized upon a pitch contact point) are expressed by the obtained analytical dependencies for the instantaneous velocity ratio in the pitch contact point.

The received analytical dependencies are applicable for the realization of the process of synthesis of spatial gear mechanisms, as in the case of application of the mathematical model for synthesis upon a *pitch contact point*, and when in the process of synthesis, the change of the velocity ratio at instantaneous tangent contact points (different than the pitch one) is also taken into account.

References

1. Abadjiev, V. Spatial Transformation of Rotation When the Conjugate Tooth Surfaces Contact in the Pitch Contact Point. Engineering Mechanics, Vol. 10, No 4, Brno, 2003, pp. 277-284.

2. Abadjiev, V. Gearing Theory and Technical Applications of Hyperboloid Mechanisms, Sc. D. Thesis, Institute of Mechanics, Bulgarian Academy of Sciences, Sofia, 2007, 309 p. (In Bulgarian).

3. Korostelev, L. The Instantaneous Velocity Ratio in Spatial Gearings. Theory of Gears in Machines, Collected papers, edited by Sc. Dr. Prof. F. L. Litvin, Publisher “Mashinostroyeniye”, Moscow, 1970, pp. 39-40.

4. Yasko, V. Definition of the Instantaneous Velocity Ratio in Relation with Spatial Gear Mechanisms. “Mashinovedenie”, № 5, Moscow, 1973, pp. 48-50.

5. Litvin, F. Theory of Gearing. Publishing house "Nauka," Moscow, 1968, 584 p. (in Russian).

6. Litvin, F. Theory of Gearing. NASA Reference Publication 1212, AVSCOM Technical Report 88-C-035, US Government Printing Office, Washington, 1989, 470 p.

7. Litvin, F. Gearing Geometry and Applied Theory. PTR Prentice Hall, A Paramount Communication Company, Englewood Eliffs, New Jersey 07632, 1994, 724 p.

8. Litvin, F., Fuentes, A. Gearing Geometry and Applied Theory. Second Edition. Cambridge University Press, Cambridge, New York, Melbourne, Cape Town, Singapure, Sao Paulo, Delhi, Tokyo, Mexico City, 2004, 800 p

OPTIMISATION OF GEAR GEOMETRICAL PARAMETERS USING KISSSOFT

Emre Can[1], Mehmet Bozca[2]

Yildiz Technical University, Science Institute, Yildiz, Istanbul, Turkey[1]

Yildiz Technical University, Mechanical Engineering Faculty, Yildiz, İstanbul, Turkey[2]

E-mail: canemrecan@hotmail.com, mbozca@yildiz.edu.tr

Abstract:

In this study, optimisation of speed gears for a tractor transmission was performed with KISSsoft software. Optimisation was carried out under three constraints. These constraints are input power-torque, volume for system in transmission and gear ratio for each speed. The purpose of this study was to optimize the module, face width, gear quality, centre distance, number of teeth, helix angle, addendum modification coefficient and pressure angle for each speed considering the constraints. Tooth bending stress, tooth contact stress, contact ratio and specific sliding were considered for evaluation during optimisation. Strength calculation of gear pairs which were optimized and defined all geometrical parameters with KISSsoft were also calculated with mathematical model indicated in ISO 6336. Then, the results were compared.

KEYWORDS: GEARS, GEOMETRICAL PARAMETERS, OPTIMISATION, KISSSOFT

1. Introduction

Gears are used for many mechanical system in particular to automotive at the present time. Gears can be designed more reliable, lighter, quieter with optimisation studies. Also, gears can be more competitive in terms of cost during optimisation. In this study, optimisation of speed gears for a tractor transmission was performed with KISSsoft software. Input power-torque, volume for system in transmission and gear ratios for each speed were considered during optimisation. Module, facewidth, gear quality, centre distance, number of teeth, helix angle, addendum modification coefficient and pressure angle of eight quantity of gears for four speed were defined considering tooth bending stress, tooth contact stress, contact ratio and specific sliding during optimisation. Strength calculation of gear pairs which were optimized and defined all geometrical parameters with KISSsoft were also calculated with mathematical model indicated in ISO 6336. Then, the results were compared.

2. Calculating the load capacity of helical gears

Gears face the tooth bending stress and the tooth contact stress during power-torque transfers. Therefore, some damages can occur on gears. The damages which can arise from stress on gears should be considered during design phase.

2.1. Tooth bending stress

Distribution of forces on gears are shown in Fig.1. The tooth bending stress according to ISO 6336 standard is calculated as the following

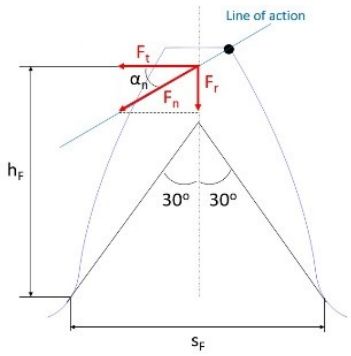

Fig.1 Tooth bending stress

The real tooth-root stress, σ_F is calculated as the following[1-6]:

$$\sigma_F = \frac{F_t}{bm_n} Y_F Y_S Y_\varepsilon Y_\beta K_A K_v K_{F\beta} K_{F\alpha} \quad (1)$$

where F_t is the nominal tangential load [N], b is the facewidth [mm], m_n is the normal module [mm], Y_F is the form factor [-], Y_S is the stress correction factor [-], Y_ε is the contact ratio factor [-], Y_β is the helix angle factor [-], K_A is the application factor [-], K_V is the dynamic factor [-], $K_{F\beta}$ is the face load factor [-], $K_{F\alpha}$ is the transverse load factor [-].

The permissible bending stress, σ_{FP} is calculated as the following:

$$\sigma_{FP} = \sigma_{Flim} Y_{ST} Y_N Y_\delta Y_R Y_X \quad (2)$$

where σ_{Flim} is the nominal stress [N/mm^2], Y_{ST} is the stress correction factor [-], Y_N is the life factor [-], Y_δ is the relative notch sensitivity factor [-], Y_R is the relative surface factor [-], Y_X is the size factor [-].

The safety factor for bending stress, S_F is calculated as the following:

$$S_F = \frac{\sigma_{FP}}{\sigma_F} \quad (3)$$

2.2. Tooth contact stress

Surface pressure which occurs on gears is calculated according to ISO 6336 standard as the following [1-6]:

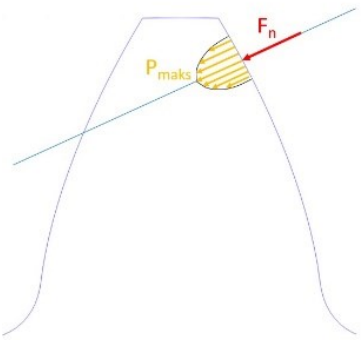

Fig.2 Tooth contact stress

The real contact stress, σ_H is calculated as the following:

$$\sigma_H = \sqrt{\frac{F_t}{bm_n}\frac{u+1}{u}} Z_H Z_E Z_\varepsilon Z_\beta \sqrt{K_A K_V K_{H\beta} K_{H\alpha}} \quad (4)$$

where u is gear ratio [-], Z_H is the zone factor [-], Z_E is the elasticity factor [$\sqrt{N/mm^2}$], Z_ε is the contact ratio factor [-], Z_β is the helix angle factor [-], $K_{H\beta}$ is the face load factor, $K_{H\alpha}$ is the transverse load factor [-].

The permissible contact stress, σ_{HP} is calculated as the following:

$$\sigma_{Hp} = \sigma_{Hlim} Z_N Z_L Z_V Z_R Z_W Z_X \quad (5)$$

where σ_{Hlim} is the allowable stress [N/mm^2], Z_N is the life factor [-], Z_L is the lubrication factor [-], Z_V is the velocity factor [-], Z_R is the roughness factor [-], Z_W is the work hardening factor [-], Z_X is the size factor [-].

The safety factor for contact stress, S_H is calculated as the following:

$$S_H = \frac{\sigma_{Hp}}{\sigma_H} \quad (6)$$

3. Optimisation with KISSsoft

In this scope of work, four speed gears of a tractor transmission were optimized via KISSsoft software. Input power is 50 kW and torque is 238 Nm for speed gears which is optimized in this study. These four speed gears have ratios like in Table 1 with tolerances of %4.

Table 1 Ratios

Speed	Ratio
1	3,1
2	1,9
3	1,1
4	0,7

Maximum volume which can be used in transmission for these speed gear group as Fig.3.

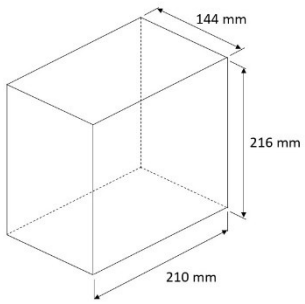

Fig.3 Volume

Firstly face width, quality and module range were defined so that optimum gear pairs can be determined for volume constraint. In beginning, other gear geometrical parameters were accepted as constant. Then, other gear parameters were optimized. Material of gears was preferred as 16MnCr5. Distance for synchroniser (s_1 and s_3), assembly distance (s_2) and volume constraint were considered for determining of gear face width.

$$b_1 + s_1 + b_2 + s_2 + b_3 + s_3 + b_4 = 210\ mm \quad (7)$$

Then, all possible gear pairs according to ratios were calculated with KISSsoft considering input values and constraints.

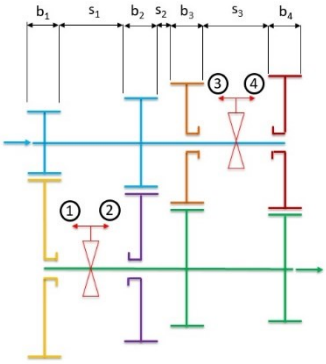

Fig.4 Speed Gears

Optimal face width, quality and module range for gear pairs were determined via graphics like Fig.5 which contain the results of all gear pairs calculated by KISSsoft according to module, minimum root safety and minimum flank safety .

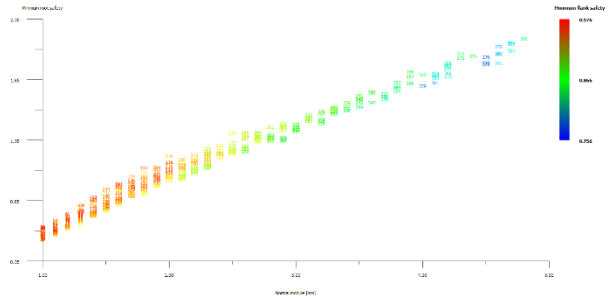

Fig.5 Module, S_F, S_H

Then, proper centre distance was specified for speed gears group. After determining of face width, quality and module range of gears, all results of gear pairs which were calculated by KISSsoft for different centre distance values were placed in graphics like Fig.6 according to tip diameters of gear pairs and centre distance in order to specify the optimal centre distance.

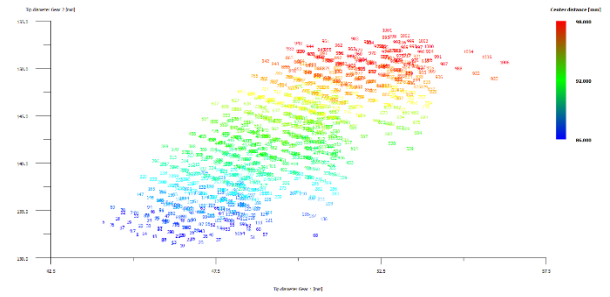

Fig.6 Tip diameter of gear pairs, centre distance values

After determining of centre distance from in graphics like Fig.6 and module from module range which was defined in graphics like Fig.5, then optimisation of number of teeth of gear pairs was applied. Proper number of teeth of gear pairs were determined considering maximum specific sliding and contact ratio of gear pairs.

After determining of face width, quality, module, centre distance and number of teeth, optimisation of helix angle was applied. Helix gears create additional axial forces in system according to spur gears. Therefore, contact ratio and axial forces were considered during determining of helix angle.

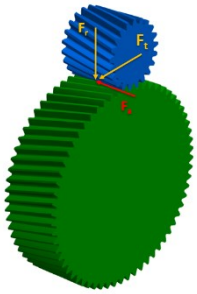

Fig.7 Forces on gear

Finally, addendum modification coefficient and pressure angle of gears were specified via KISSsoft. Addendum modification coefficient and pressure angle have effect on gear profile so contact ratio, specific sliding and safety factors were considered during optimisation.

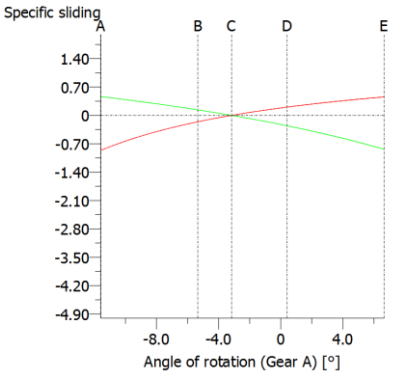

Fig.8 Specific sliding

Optimisation results of face width, quality, module, centre distance, number of teeth, helix angle, addendum modification coefficient and pressure angle for four speed gears groups are like Table 2 below.

Table 2 Optimisation results

	1.Speed	2.Speed	3.Speed	4.Speed
Number of teeth z_1	20	30	40	57
Number of teeth z_2	64	55	45	41
Module [mm]	2	2	2	1,75
Pressure angle [°]	20°	20°	20°	20°
Helix angle [°]	13°	15°	17°	15°
Addendum modification coefficient x_1	0,6	0,3	0,1	0
Addendum modification coefficient x_2	0,9419	0,2201	-0,0416	0,1297
Facewidth [mm]	40	25	20	20
Quality	6	7	8	8

Optimal four speed gears group which were defined all geometrical parameters like Table 2 was placed in volume as Fig.9. According to Fig.9, ıt seems that there is no any problem about volume constraint. All gears can be assembled properly in volume.

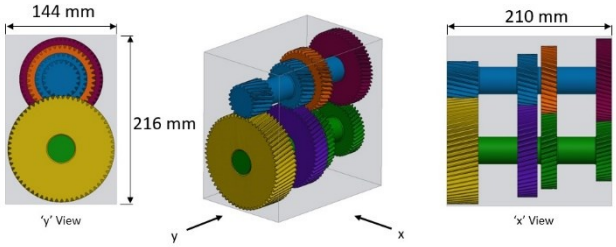

Fig.9 Speed gears in volume

4. Results and discussion

Tooth bending stress, tooth contact stress and safety factor of pinion gears for each speed which were optimized via KISSsoft were also calculated according to mathematical model in ISO 6336. The results of pinion gears for both KISSsoft and mathematical model are like Table 3 below.

Table 3 Results

	1.Pinion	2.Pinion	3.Pinion	4.Pinion
Tooth-root stress σ_F from KISSsoft [N/mm^2]	543,96	569,46	576,47	570,03
Tooth-root stress σ_F from mat. Model [N/mm^2]	546,97	607,52	625,93	561,37
Safety factor for bending stress S_F from KISSsoft	1,41	1,34	1,32	1,34
Safety factor for bending stress S_F from mat. Model	1,46	1,32	1,28	1,43
Contact stress σ_H from KISSsoft [N/mm^2]	1363,60	1286,05	1292,8	1197,23
Contact stress σ_H from mat. Model [N/mm^2]	1345,09	1264,66	1239,2	1226,15
Safety factor for contact stress S_H from KISSsoft	1,10	1,13	1,13	1,22
Safety factor for contact stress S_H from mat. model	1,12	1,19	1,21	1,22

Regarding to results in Table 3, tooth root stress of pinion 1 (546,97 N/mm^2) according to mathematical model is bigger (%0,5) than KISSsoft result (543,96 N/mm^2). For root safety factor, results of mathematical model (1,46) is bigger (%3,5) than the results of KISSsoft (1,41). Tooth contact stress of pinion 1(1345,09 N/mm^2) according to mathematical model is smaller (%1,4) than the results of KISSsoft (1363,60 N/mm^2). For flank safety factor, mathematical model result(1,12) is bigger (%1,8) than KISSsoft result (1,1).

Regarding to results for pinion 2, mathematical model result is bigger (%6,7) than KISSsoft result for tooth root stress. Tooth contact stress according to mathematical model is smaller (%1,7) than KISSsoft result. For root safety factor, mathematical model result is smaller (%1,5) than KISSsoft result and flank safety factor of mathematical model is bigger (%5,3) than KISSsoft result.

Regarding to results for pinion 3, tooth root stress according to mathematical model is bigger (%8,5) and tooth contact stress according to mathematical model is smaller (%4,1). For root safety factor, result of mathematical model is smaller (%3) and flank safety factor of KISSsoft result is smaller (%7) than mathematical model.

Regarding to results for pinion 4, tooth root stress according to mathematical model is smaller (%1,5) and tooth contact stress is bigger (%2,4) than KISSsoft result. The root safety factor of mathematical model is bigger (%6,7) than KISSsoft result. For flank safety factor, results are same.

According to results, ıt seems that there are maximum %8 differences between KISSsoft and mathematical results. There are some reasons for these differences. KISSsoft considers the tolerances and deformation of gears during calculation. Besides, KISSsoft specifies some correction coefficients according to own experiences. Although there are some differences between results, ıt seems that safety factors for both method are suitable according to target values. Therefore, KISSsoft can be used reliably for strength calculation of gears.

5. Conclusion

Four speed gears of a tractor transmission were optimized by KISSsoft software. During optimisation, input power-torque, ratios and maximum volume were considered as constraint. Facewidth, centre distance, module, quality, number of teeth, helix angle, addendum modification coefficient and pressure angle of gear pairs were specified with optimisation. Then, tooth root stress, tooth contact stress and safety factors were also calculated according to mathematical model in ISO 6336. After calculations, the results were compared. Regarding to tooth root stresses, maximum differences is %8,5 for pinion 3. Regarding to tooth contact stresses, maximum differences is %4,1 for pinion 3. Regarding to root safety factors, maximum differences is %6,7 for pinion 4. Regarding to flank safety factors, maximum differences is %7 for pinion 3. According to this study, both KISSsoft results and mathematical model results are within the range of target value.

Also, the results below were determined during optimisation:

i. Increasing the module has a positive effectiveness on root safety factor and negative effectiveness on flank safety factor.
ii. Increasing the face width of gears has a positive effectiveness on flank safety factor.
iii. Increasing the centre distance results decreased tooth contact stress.
iv. Increasing the number of teeth results increased contact ratio.
v. Increasing the helix angle results increased both contact ratio and axial forces.
vi. Increasing the addendum modification coefficient has a positive effectiveness on root safety factor.

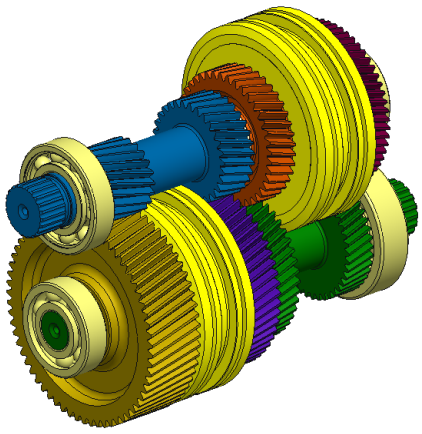

Fig.10 Concept design

Acknowledgements

This work was supported by Research Fund of the Yildiz Technical Üniversity (BAP) Project Number: FYL-2018-3506.

6. Literature

[1] ISO 6336-1: calculation of load capacity os spur and helical gears, part: basic principle, introduction and general influence factors.

[2] ISO 6336-2: calculation of load capacity of spur and helical gears, part2: calculation of surface durability (pitting).

[3] ISO 6336-3: calculation of load capacity of spur and helical gears, part 3: calculation of tooth bending strength.

[4] ISO 6336-5: calculation of load capacity of spur and helical gears, part 5: strength and quality of materials.

[5] Mehmet Bozca, Optimisation of the geometrical design parameters of a five speed gearbox for an automotive transmission, The Latest Methods of Construction Design, Springer International Publishing, Switzerland, 2016, pp. 313-318.

[6] Mehmet Bozca, Optimisation of effective design parameters for an automotive transmission gearbox to reduce tooth bending stress, Modern Mechanical Engineering, 2017, vol. 7, pp. 35-36.

FINITE ELEMENTS METHOD MODELLING OF ROLLING BEARINGS

Mustafa Koç[1], Mehmet Bozca[2]

Yildiz Technical University, Science Institute, Yildiz, Istanbul, Turkey [1]

Yildiz Technical University, Mechanical Engineering Faculty, Yildiz, Istanbul, Turkey[2]

E-Mail: f5215001@std.yildiz.edu.tr, mbozca@yildiz.edu.tr

Abstract: *This study presents to determine the contact stress in rolling bearings by using analytical and numerical method. Analytical solution is obtained by using Hertizan contact theory. Obtained analytical solution by this theory require comparison with the numerical calculations to obtain more accurate results for contact problems. Because of that the same problems are also examined by using finite element method. The geometry of the model being studied gives different type of contact configurations such as a point or line of contact. In cylindrical roller bearing the contact form is line contact and for the ball bearing the contact characteristic is point contact. High stress occurs on both of these two contact areas. Contact stress causes elastic or plastic deformation and the contact area will change depending on the magnitude of the contact stress. Therefore, it is really important to calculate more accurate stress at the contact area.*

KEYWORDS*: HERTZ CONTACT, NON-LINEAR CONTACT, ROLLER BEARING, FINITE ELEMENT METHOD, ANSYS.*

1. Introduction

Bearings, having a crucial role in the machine design, are the components to provide smooth rotation by reducing friction between the rotating machine parts.

The general structure of bearing are shown in Fig 1, consists of inner and outer rings and the roller elements which vary depending on the application. The cage prevents the roller elements rubbing against each other.

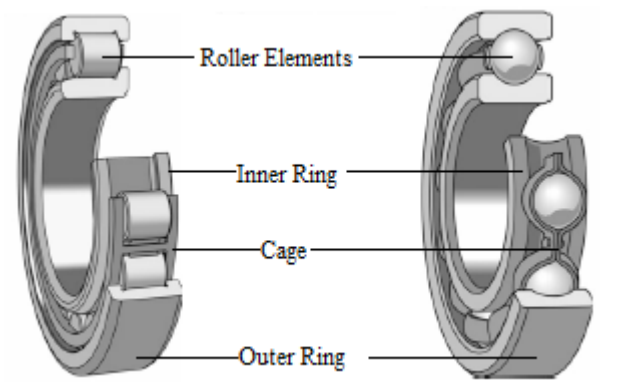

Fig. 1 *Roller bearing structure. a)Cylindrical roller bearing b)Ball bearing*

There are two main functions of roller bearings: First is to reduce frictional forces between moving parts by giving a surface to roll on instead of sliding. The secondary function of bearings is to transmit the force. The roller bearings are classified according to the direction in which the load is applied. Generally bearings carry two kinds of force: radial and axial and some bearings can also carry both radial and axial load at the same time.

In this study a ball bearing and a cylindrical roller bearing are examined.

2. Theoretical Aspects

The force and motion are transferred between machine parts by means of contact phenomena. A contact problem occurs when at least two bodies not mechanically joined touch each other without becoming rigidly attached.

When there are non-conforming surfaces come into mate the contact form can be point or line. The localized stress value on this area is very high. Since the stress is the force over the area, any load on a point contact would be infinite stress as mathematical view. The original analysis of elastic contact stresses was published in1881 by H. Hertz. In his honour, the stresses at the mating surfaces of curvature bodies in compression are called *Hertz contact stresses*.

Hertzian contact stress is one of the major reasons of surface failures especially for bearings, cams, gear teeth, locomotive wheels, valve tappets and pin joints linkages [1].

Hertz calculations are limited to case of contact of elastic bodies with simple quadratic shapes and when he was developing his theory Hertz made some important assumptions which are written below [1]:

i. Contacting bodies are isotropic, homogeneous and elastic.

ii. The contact areas are essentially flat and small relative to the radii of curvature of the undeflected bodies in the vincinity of the interface.

iii. The strains are small and within the elastic limits.

iv. The contacting bodies are perfectly smooth; therefore, friction forces between mated parts need not to be taken into account.

Boussinesq developed Hertz's theory by using theory of elasticity. Boussinesq improved the equations for the state of stress within an isotropic, homogeneous and linearly elastic space, under a concentrated load, which will act perpendicular to the surface. He studied the deformation of semi-infinite solid due to pressure exerted on a small area of its plane surface [2].

Ludenberg in 1939 developed a general theory of elastic contact between two semi-in finite bodies, in which the effect on the stress of the presence of tangential load is taken into consideration.

Midlin investigated the distribution of the tangential forced across the area of contact when one elastic body slides over another.

Lure presented a general three-dimensional punch contact problems

The stress examined in two contacting bodies at a rolling interface is highly dependent on the geometry of the mate surfaces as well as on the loading material properties.

In this study ball and cylindrical roller bearings are examined. In a ball roller bearing, a ball passes over the raceway surface, the theoretical contact form is assumed as a point in this application. A cylindrical roller bearing, cylinders passes over the raceway, the theoretical contact shape is assumed as line contact for this application.

In order to examine contact stresses for cylindrical and ball bearing, traditional Hertzian contact theory is used. According to the theory

sphere to sphere contact presents ball bearing and cylinder to cylinder contact presents cylindrical roller bearing

Hertz contact theory equations for point and line contact types, used in analytical solutions, are shown below:

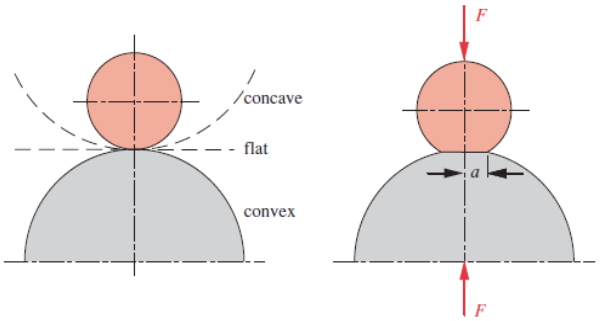

Fig. 2 *Two spheres or cylinders contact zone [3]*

2.1. Point contact:

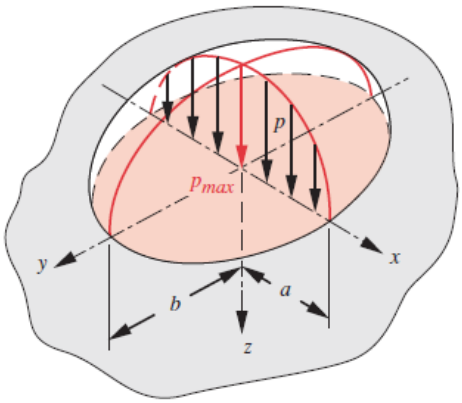

Fig.3 *Spherical contact, pressure distribution.(a=b) [3].*

Two spheres in contact are shown in Fig2. The theoretical contact form is assumed as hemisphere with circular contact shape is shown in Fig3.

Total applied load F on the contact patch is written as follows [4]:

$$F = \frac{2}{3} p a^2 p_{\max} \tag{1}$$

Where a is radius of contact patch. Maximum pressure is written as follows:

$$P_{\max} = \frac{3}{2} \frac{F}{p a^2} \tag{2}$$

Average pressure is written as follows:

$$P_{avg} = \frac{F}{p a^2} \tag{3}$$

Maximum pressure is written depending on average pressure

$$P_{\max} = \frac{3}{2} P_{avg} \tag{4}$$

Material constant can be written as follows:

E_1, E_2 are elasticity modulus and ν_1, ν_2 are Poisson's ratios of mated materials.

$$m_1 = \frac{1-\nu_1^2}{E_1} \quad , \quad m_2 = \frac{1-\nu_2^2}{E_2} \tag{5}$$

Geometry constant can be written as follows:

$$B = \frac{1}{2}\left(\frac{1}{R_1} + \frac{1}{R_2} \right) \tag{6}$$

The contact-patch radius a is written as follows:

$$a = \frac{p}{4} p_{\max} \frac{m_1 + m_2}{B} \tag{7}$$

$$a = \sqrt[3]{0.375 \frac{m_1 + m_2}{B} F} \tag{8}$$

The pressure distribution within the hemisphere is written as follows:

$$P = P_{\max} = \sqrt{1 - \frac{x^2}{a^2} - \frac{y^2}{a^2}} \tag{9}$$

Static stress distributions in spherical contact:

$$\sigma_z = -p_{\max} \tag{10}$$

$$\sigma_{x\max} = \sigma_{y\max} = -\left(\frac{1+2\nu}{2} \right) p_{\max} \tag{11}$$

$$\tau_{xy} = \left(\frac{1-2\upsilon}{3} \right) p_{\max} \tag{12}$$

Von Misses equivalent stress is written as follows:

$$\sigma_{vM} = \frac{1}{\sqrt{2}} \sqrt{(\sigma_x - \sigma_y)^2 + (\sigma_y - \sigma_z)^2 + (\sigma_z - \sigma_x)^2 + 6(\tau_{xy}^2 + \tau_{yz}^2 + \tau_{zx}^2)} \tag{13}$$

2.2. Line contact:

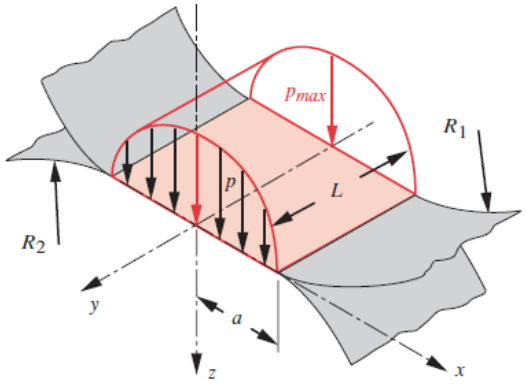

Fig. 4 *Cylindrical contact, pressure distribution.[3].*

When two cylinders roll together, their contact patch will be rectangular as shown in Fig4.

Total applied load F on the contact patch is written as follows [5]:

$$F = \frac{1}{2} p a L p_{\max} \tag{14}$$

where L is the length of contact along the cylinder axis.

$$P_{\max} = \frac{2F}{paL} \tag{15}$$

$$P_{avg} = \frac{F}{2aL} \quad (16)$$

$$P_{\max} @1.273P_{avg} \quad (17)$$

Geometry constant can be written as follows:

$$B = \frac{1}{2}\left(\frac{1}{R_1} + \frac{1}{R_2}\right) \quad (18)$$

Radius of contact patch a is written as follows:

$$a = \sqrt{\frac{2}{p}\frac{m_1 + m_2}{B}\frac{F}{L}} \quad (19)$$

The pressure distribution within the semi-elliptical prism:

$$P = P_{\max} = \sqrt{1 - \frac{x^2}{a^2}} \quad (20)$$

Static stress distributions in cylindrical contact:

$$\sigma_{xn} = -p_{\max}\sqrt{1 - \frac{x^2}{a^2}} \quad (21)$$

$$\sigma_{zn} = -p_{\max}\sqrt{1 - \frac{x^2}{a^2}} \quad (22)$$

$$\tau_{xzn} = 0 \quad (23)$$

Von Misses equivalent stress is written as follows:

$$\sigma_{vM} = \sqrt{\sigma_x^2 + \sigma_y^2 + \sigma_x\sigma_y + 3\tau_{xz}^2} \quad (23)$$

3. Finite Element Model

All of these theories discuss the contact problem with in the analytical methods and use highly idealised model. Unfortunately these approaches have limited application in engineering.

The more accurate results are examined for rolling bearing such as ball and cylindrical roller bearings contact problem with numerical method .Therefore same problem is also modelled in ANSYS-18.1 workbench environment.

4. Numerical example

4.1. 6208 Ball Bearing Analytical Solution

Firstly 6208 ball bearing shown in Fig5 is analyzed according to Hertizan contact theory. Applied load is F=5000N.

According to Hertzian theory, the analytical results for 6208 ball bearings are shown in Table 1.

Table.1 *6208 Ball bearing analytical solution results*

$\tau_{\max}$ [MPa]	$P_{\max}$ [MPa]	σ_{vM} [MPa]
2570	5474	2744

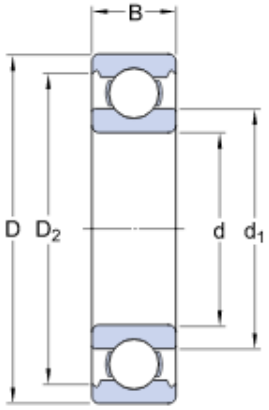

d:40	[mm]
D:80	[mm]
B:18	[mm]
d_1:52,6	[mm]
D_2:69,8	[mm]

Fig.5 *6208 Ball bearing dimensions.*

4.2. 6208 Ball Bearing FEA Analysis

Modelling and the analysis of the problem are completed in ANSYS 19-1 Workbench software.

In terms of accuracy and simplicity the problem is modeled for one ball by using cyclic symmetry.

In order to obtain more accurate results, the mesh density over the contact area is increased as shown in Fig6.

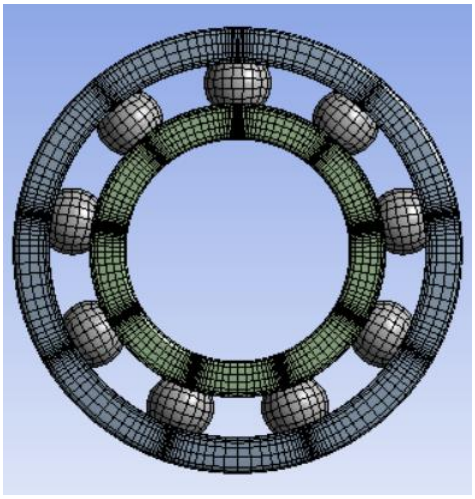

Fig.6 *6208 Ball bearing Solid-FEM model.*

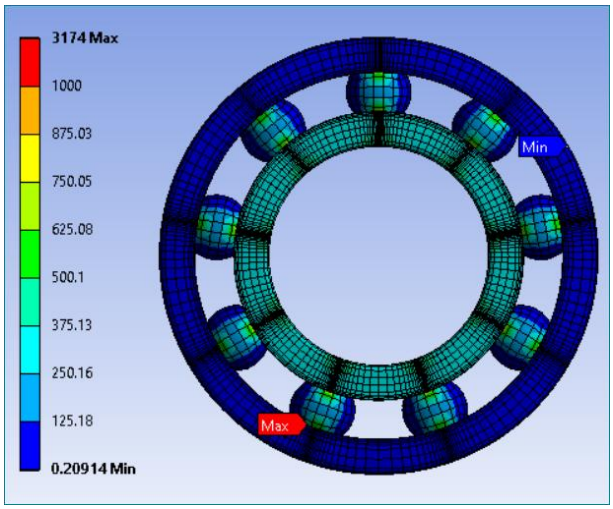

Fig.7 *6208 Ball bearing FEA solution.*

The obtained maximum Von Misses stress is 3174 [MPa].

4.3. NU210 Cylindrical roller bearing analytical Solution

Firstly NU210 cylindrical roller bearing as shown in Fig8 is analyzed according to Hertizan contact theory. Applied load is F=5000N.

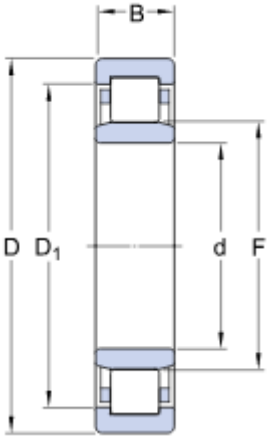

d:50	[mm]
D:90	[mm]
B:20	[mm]
F:59,5	[mm]
D_1:77,4	[mm]

Fig.8 *NU210 Cylindrical roller bearing dimensions*

According to Hertzian theory, the analytical results for NU210 cylindrical roller bearings are shown in Table.2

Table.2 NU210 cylindrical bearing analytical solution results.

τ_{max} [MPa]	P_{max} [MPa]	σ_{vM} [MPa]
480	1464	3000

4.4. NU210 Cylindrical roller bearing FEA Solution

In order to obtain more accurate results, the mesh density over the contact area is increased shown in Fig9.

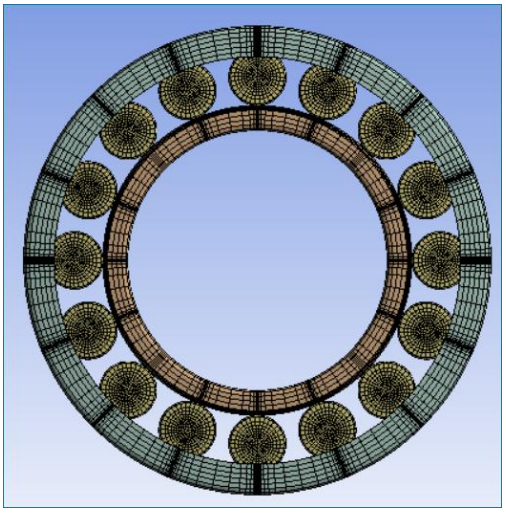

Fig.9 *NU210 Cylindrical roller bearing Solid-FEM model.*

The obtained maximum Von Misses stress is 3781 [MPa].

5. Results and discussion

Comparison of obtained Von Mises stress results for ball and cylindrical roller bearings are presented in Table 3.

Table 3 Comparison of Von Mises stress

Bearing type	Analytical σ_{vM}	FEM σ_{vM}	% Deviation
Ball	2744 [Mpa]	3174 [Mpa]	13,5
Roller	3000 [Mpa]	3781 [Mpa]	20,6

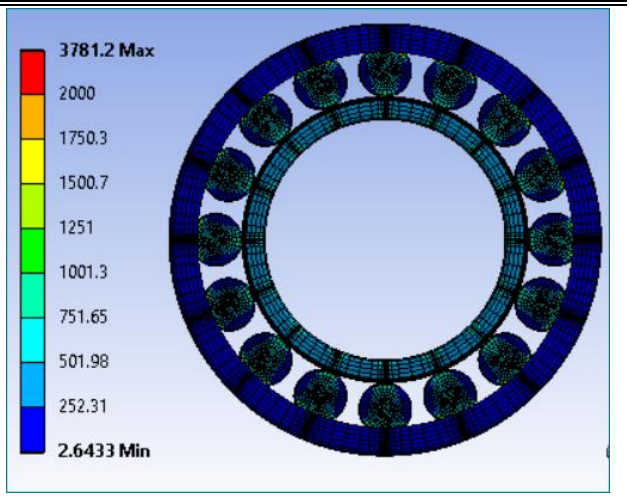

Fig.10 *NU210 cyindrical roller bearing FEA solution.*

All obtained results are acceptable for required Von Mises stress calculation for ball and cylindrical roller bearings.

6. Conclusion

Numerical analysis of rolling bearing contact problem is simulated by using ANSYS workbench environment. Thus the contact stresses are analysed for point and line contact types with 3D model.
For ball bearing applications the contact area is actually an elliptical geometry and the contact form depends on the applied force which means, both of these problems are non-linear and analytical theory has lots of assumptions.
Bearings load capacity and reliability are so important. Therefore the rolling bearings play such a prominent machine elements. Calculation the life of a bearing with considerable accuracy become even more important. Thus making it possible to match the bearing life with the service life of the machine involved.
In this study FEM is used to examine the contact analysis of rolling bearing. Specifically, the normal and tangential forces as well as the rolling friction between mated parts are analysed in order to more accurate results. Numerical analysis of contact problems by computer programs gives more accurate results.

Acknowledgements

This work was supported by Research Fund of the Yildiz Technical Üniversity (BAP) Project Number: FYL-2018-3491.

7. Literature

[1] FISCHER, Anthony C., Introduction to Contact Mechanics, 2nd ed. Springer,2007. ISBN: 978-0387-68187-0

[2] UGURAL, Ansel C., Mechanical Design of Machine Components, 2nd ed. CRC Press, 2015. ISBN: 978-1-4987-3536-0.

[3] NORTON, Robert C., Machine Design, an integrated approach,4th ed. Pearson,2011. ISBN: 978-0-471-74285-2.

[4] BOZCA M., "Theoretical Investigation of Point Contact for Ball Bearings Application".
ICMD'2006, 57thInternational Conference of Machine Design Departments, pp. 195-200. 6-9 September 2016, Zelezna Ruda, Plzen, CZECH REPUBLIC.

[5] BOZCA M., "Theoretical Investigation of Line Contact for Roller Bearings Application".
ICMD'2006, 57thInternational Conference of Machine Design Departments, pp. 201-206. 6-9 September 2016, Zelezna Ruda, Plzen, CZECH REPUBLIC.

SUBSTITUTION OF GEAR-BAR MECHANISM WITH BAR MECHANISM ON THE INFEED MECHANISM OD BOTTLE WASHER

Spec. Sci. Vidak Šabanović [1], Prof. Dr. Goran Ćulafić [2]
Brewery Trebjesa - MolsonCoors Europe, Montenegro[1]
Faculty of Mechanical engineering – University of Montenegro, Montenegro[2]

vidak.sabanovic@molsoncoors.com

Abstract: *In this paper we will consider substitution of special mechanism, part of bottle washer, which caries bottles to special „baskets“. These mechanism are mostly gear- bar mechanism and their construction is very expensive and overhauls last too long because of complexity of mechanisms..*
Mechanisms synthesis based on highly developed analytical / numerical procedures will be considered in this thesis. This means that we will develop procedure for constructing bar mechanism which will be able to fulfill our task to transfer bottles into „ baskets”, and to return into start position. The mechanism should also meet requirements in terms of main dimensions, which should be the same as for the old mechanism so the substitution can be performed. Special attention will be paid to analyze the singular positions of the mechanism when it loses mobility. These positions it is necessary to solve in a way so that mechanism continues to move and perform its function.

Key words: BAR MECHANISM, PLANETARY MECHANISM, MECHANISM SYNTESIS, ANALYTICAL MECHANISM SYNTESIS, MECHANISM ANALYSIS.

1. Introduction

In every beverage filling line there are many mechanisms which in combination with high automation level, provides efficient work of beverage filling lines with almost no hand manipulation. All glass bottle filling lines must include bottle washer that is, because of washing standards, large and in it there is many bottles located in special baskets. These baskets are fixed on chain mechanism which transports them trough baths with cleaning fluids, and above spray nozzles. Because of this it is necessary to insert many bottles into baskets at the same time. Bottle should be transferred from vertical into horizontal position and transported in baskets. This type of movement should be also synchronized with movement of baskets. . Special gear-bar mechanism does this task. Production of these mechanisms is very expensive, also maintenance is very difficult and it requires very long time. Breakdowns are not often but when it happens it is very difficult to repair the mechanism. Because of these problems, possibility of replacement of gear-bar mechanism with bar mechanism, whose connection link makes full rotation, will be shown in this paper.

Mechanisms synthesis based on highly developed analytical / numerical procedures will be considered in this paper. This means that the geometric parameters should be defined, on the basis of set tasks, which mechanism should complete. The main task to be achieved is the positioning of the element for transferring the bottle into the basket from the initial (catching the bottle) into the final position (delivery of the bottle to the "basket") and after realization of this task, mechanism should return to the starting position so the operation can be repeated. The mechanism should also meet requirements in terms of main dimensions, which should be the same as for the bevel-lever mechanism so the substitution can be performed.

2. Short analysis of gear-bar mechanism and main task short introduction

Bottle washer infeed mechanism main task is to transfer bottles from nearly vertical position ($\approx 10^o$ between bottle and vertical axis) into baskets in horizontal position across special made guides (Fig 1).

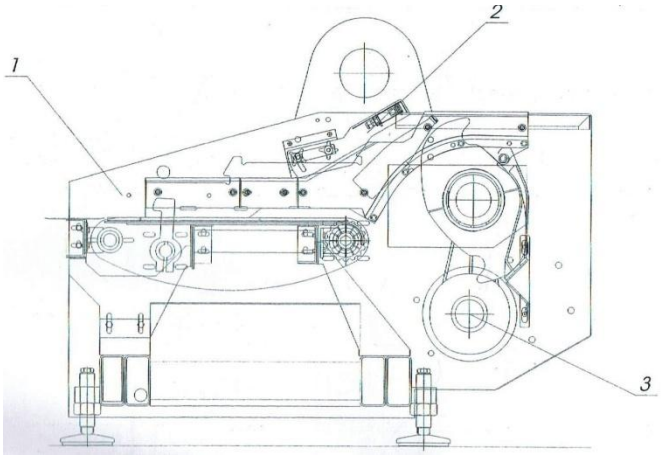

Fig. 1

This task fulfills special gear-bar mechanism which is expensive for production and complicated for maintenance and adjustment. Draft of this mechanism is shown on figure 2.

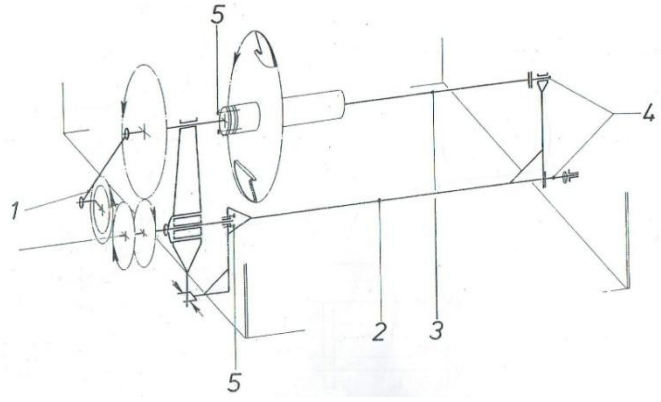

Fig. 2

Mechanism on figure 2 generates special cam movement necessary to fulfill the task transferring bottle from vertical into horizontal position. This mechanism also returns into start position, and it is ready to repeat this action.

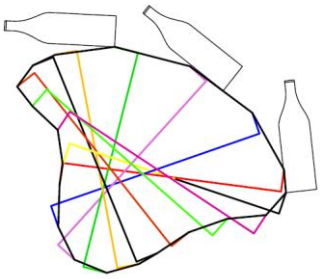

Fig 3

Special cam path through multiple positions is shown on figure 3. We can clearly see the path of cam peak and specially the part of this path that matches with task demanded movement. Also we see that during comeback movement cam peak makes longer path, and this fact made us to consider optimization of this movement. Attention should be paid on static strength of this mechanism because during task fulfill there are many blockages and high torsion loads. Also we should mention that mechanism should follow movements of other machine parts and mechanism, and it should have possibilities for adjustment, that is not case with mechanism shown on figure 2. Because of deficiencies of gear-bar mechanism, mentioned before, and due to set tasks in further paper paragraphs we will consider possibility of replacing this mechanism with bar mechanism, whose connection link performs full rotation and replaces a gear with a special cam.

3.Procedure for forming of bar-planetary mechanism

Because of task that bar mechanism needs to fulfill (five specific positions), it is necessary that the connection link makes full rotation. This means that this connection link is the shortest bar in mechanism.

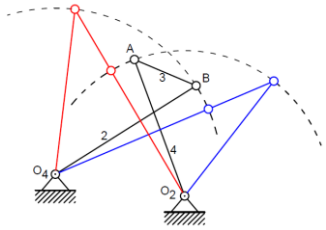

Fig. 4

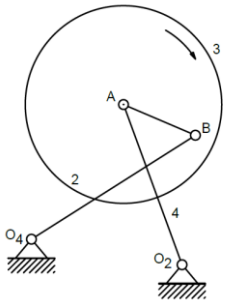

Fig. 5

On figure 4 we can see four bar mechanism that does the demanded tasks. Connection link AB does planar movement and full 360 degrees angular rotation.

Bar AB makes planar movement and we can see that it rotates around point A so we can substitute bar 3 with a gear (figure 5).

Because gear 3 makes planar movement during point A rotates on circular arc which center is in point O_2, this mechanism can be planetary mechanism shown on figure 6.

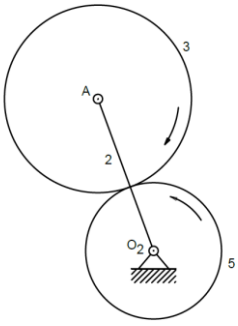

Fig 6

Rotation courses of gears 3 and 5 are opposite

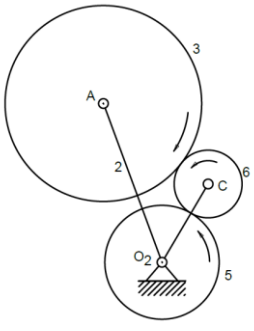

Fig 7

Rotation courses of gears 3 and 5 are the same

Planetary mechanism shown on figure 6 has two degrees of freedom if the gear 5 is movable. Gear 3 is called satellite (planate), gear 5 is central gear (the sun) and the bar 2 is called satellite carrier. If we want that the rotation courses of gear 3 and 5 is the same than we can enter gear 4 between them. Satellite carrier 2 now has triangle form O_2CA (figure 7). This bar can change its form and be even more complex depending on mechanism purpose.

If we install gears 7 and 8 on shafts A and C in parallel plain (gear 7 is located on shaft C and gear 8 is located on shaft A) and rotation velocity of gears 4 and 7 are the same (fix connection), rotation velocity of gears 3 and 8 are different. This planetary mechanism is shown on figure 8.

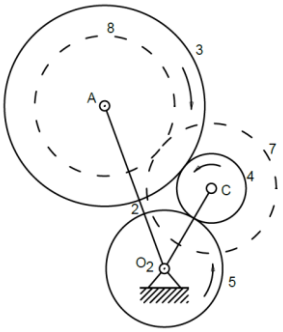

Fig. 8

If the teeth number of individual gears of mechanism are: z_5, z_4, z_3, z_7, z_8 than the transmission ratio relative to bar 2 is:

$$i_{5-3} = \frac{\dot{\theta}_5 - \dot{\theta}_2}{\dot{\theta}_3 - \dot{\theta}_2} = \left(-\frac{z_4}{z_5}\right)\left(-\frac{z_3}{z_4}\right) = \frac{z_3}{z_5} > 0$$

$\dot{\theta}_5 - \dot{\theta}_2$ – relative rotation velocity of gear 5 relative to bar 2;

$\dot{\theta}_3 - \dot{\theta}_2$ – relative rotation velocity of gear 3 relative to bar 2;

$\dot{\theta}_3$ – absolute rotation velocity of gear 3 relative to stationary point;

$\dot{\theta}_5$ – absolute rotation velocity of gear 5 relative to stationary point.

When we bring together bar mechanism shown on figure 5 and planetary mechanism shown on figure 8 we get bar-planetary mechanism-figure 9.

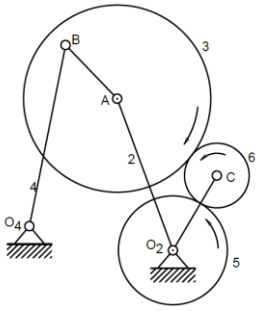

Fig. 9

This bar-planetary mechanism has further characteristics:

- it has one degree of freedom;
- connection link AB i.e. gear 3 makes full rotation during planar movement;
- rotation courses of gears 3 and 5 are the same
- drive electric motor can be connected with gear 5 and connected on shaft O_2
- if necessary on satellite carrier (on triangle bar 2) can be installed other gear pairs on parallel plains (figure 7).

So now we see that we can get movement on the shortest bar in mechanism that we got using mechanism synthesis. Analysis of bar-planetary mechanism is giving mathematical procedure for determination positions and velocities of all mechanism members. This will give us many qualitative and quantitative mechanism characteristics.

4. Bar mechanism synthesis

Using bar mechanism synthesis procedure we should create mechanism whose connection link would make full rotation and during that movement it would take five specified positions. Applying procedures from [1], [2] and [3] this task is coming down to determine zeros of a fourth degree polynomial.

5. Bar-planetary mechanism analysis

5.1 Bar mechanism position analysis

On figure 10 we can see bar mechanism which bar 3 is the shortest bar and it makes complete rotation. Due to that fact mechanism can be transformed into mechanism shown with dashed lines. Its shortest part is connected to ground pivot and rotates 360 degrees.

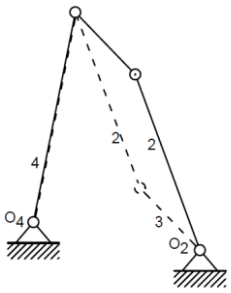

Fig. 10

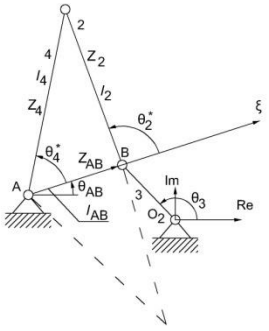

Fig. 11

If we apply position presentation using complex numbers [5] figure 11 can be presented like this:

$$Z_{AB} = Z_B - Z_A; \quad Z_B = l_3 e^{i\theta_3}; \quad Z_A = x_A + iy_A; \quad A(x_A, y_A);$$
$$l_{AB} = |Z_{AB}|; \quad \theta_{AB} = img Z_{AB}$$
$$l_4 e^{i\theta_4^*} = l_{AB} + l_2 e^{i\theta_2^*}$$
$$l_4 e^{-i\theta_4^*} = l_{AB} + l_2 e^{-i\theta_2^*}$$

Eliminating θ_4^* we get:

$$\theta_{2_{1,2}}^* = \pm 2 \arctan\sqrt{(1-c)/(1+c)} = \theta_2(\theta_3) \quad (1)$$
$$c = \cos\theta_2^* = (l_4^2 - l_{AB}^2 - l_2^2)/2 l_{AB} l_2 = (1-x^2)/(1-x^2);$$
$$x = \tan\frac{\theta_2^*}{2}$$

Now:

$$\theta_{4_{1,2}}^* = 2\arctan\frac{l_2 \sin\theta_2^*}{l_{AB} + l_2 \cdot \cos\theta_2^*}$$
$$\theta_{2_{1,2}} = \theta_{2_{1,2}}^* + \theta_{AB}; \quad \theta_{4_{1,2}} = \theta_{4_{1,2}}^* + \theta_{AB}$$

Solutions with prefix "+" in equation (1) determines closed loop presented with continuous line on figure 11 (left from ξ-axis), and solutions with prefix "–" in equation (1) determines closed loop presented with dashed line on figure 11 (right from ξ-axis).

Equation (1) presents relation between angles θ_2 i θ_3. So if we know geometrical characteristics of mechanism: (x_A, y_A), l_2, l_3, l_4 and if θ_3 is known we can calculate θ_2 and after that θ_4. When we determine these parameters mechanism is completely determined.

5.2 Planetary mechanism position mechanism

On figure 12 we can see planetary mechanism that is part of bar-planetary mechanism.

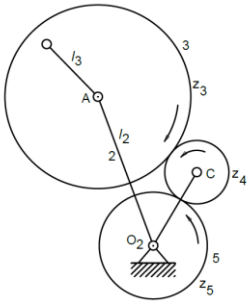

Fig. 12

For planetary mechanism we can determine position like this:

$$i_{5-3} = \frac{\dot\theta_5 - \dot\theta_2}{\dot\theta_3 - \dot\theta_2} = \left(-\frac{z_4}{z_5}\right)\left(-\frac{z_3}{z_4}\right) = \frac{z_3}{z_5}$$
$$\dot\theta_5 - \dot\theta_2 = \frac{z_3}{z_5}\left(\dot\theta_3 - \dot\theta_2\right)$$

From this equation we get:

$$\theta_2\left(\frac{z_3}{z_5} - 1\right) + \theta_5 = \theta_3\frac{z_3}{z_5} + C \quad (2)$$

C- integral constant

5.3 Bar-planetary mechanism position analysis

If we consider equations (1) and (2) and due to the fact that mechanism has one degree of freedom, determination positions of bar-planetary mechanism should be done just by solving equations (1) and (2). So if θ_3 is given, than equations (1) and (2) are not related. First from equation (1) θ_2 should be calculated (than θ_4), and after that from (2) θ_5 should be calculated. If θ_5 is given than calculating θ_3 (and after that from equation (1) θ_2 and θ_4 are calculated) should be done by solving nonlinear equation:

$$\theta_2(\theta_3)\left(\frac{z_3}{z_5} - 1\right) - \theta_3\frac{z_3}{z_5} + \theta_5 + C = 0 \quad (3)$$

Specially if $z_3 = z_5$ than $\theta_3 = \theta_5 + C$

5.4 Bar mechanism velocity analysis

By derivation of equation $l_4 e^{i\theta_4} = Z_{AB} + l_2 e^{i\theta_2}$ in respect to time we get $l_4 e^{i\theta_4}\cdot i\dot\theta_4 = \dot{Z_{AB}} + l_2 e^{i\theta_2}\cdot i\dot\theta_2$, than multiplication this equation with $e^{i\theta_4}$ we get $l_4 \cdot i\dot\theta_4 = \dot{Z_{AB}} e^{-i\theta_4} + l_2 e^{i(\theta_2-\theta_4)}\cdot i\dot\theta_2$. By separation of real part of equation we get:

$$\dot\theta_2 = \frac{Re\left(\dot{Z_{AB}}\, e^{-i\theta_4}\right)}{l_2 \cdot \sin(\theta_2 - \theta_4)} = \frac{l_3 \cdot \sin(\theta_3 - \theta_4)\cdot\dot\theta_3}{l_2 \cdot \sin(\theta_2 - \theta_4)} \quad (4)$$

On same way we get:

$$\dot\theta_4 = \frac{Re\left(\dot{Z_{AB}}\, e^{-i\theta_2}\right)}{l_4 \cdot \sin(\theta_2 - \theta_4)} = \frac{l_3 \cdot \sin(\theta_3 - \theta_2)\cdot\dot\theta_3}{l_2 \cdot \sin(\theta_2 - \theta_4)} \quad (5)$$

where:

$$\dot{Z_{AB}} = \dot{Z_A} - \dot{Z_B} = l_3 e^{i\theta_3}\cdot i\dot\theta_3 - (\dot{x_A} - i\dot{y_A})$$

5.5 Planetary mechanism velocity analysis

$$\frac{\dot\theta_5 - \dot\theta_2}{\dot\theta_3 - \dot\theta_2} = \frac{z_3}{z_5}$$

$$\dot\theta_5 - \dot\theta_2 = \frac{z_3}{z_5}\left(\dot\theta_3 - \dot\theta_2\right) \quad (6)$$

5.6 Bar-planetary mechanism velocity analysis

Considering equations (4), (5) and (6) and fact that mechanism has one degree of freedom it can be concluded that velocity analysis equation is linear. It is a system of three equations with three variables when one of four rotation velocities $\dot{\theta}_2$, $\dot{\theta}_3$, $\dot{\theta}_4$, $\dot{\theta}_5$ is given.

From equations (4) and (5) we can see that there are special mechanism positions when $\theta_3 = \theta_4 \pm \pi$ and when $\theta_2 \neq \theta_4$. These are trivial positions when $\dot{\theta}_2 = 0$ and $\dot{\theta}_4 = 0$, while $\dot{\theta}_3 \neq 0$. Singular positions appear when $\theta_2 = \theta_4 \pm \pi$;$\theta_3 = \theta_2 \pm \pi$. In this case two bars are placed on one straight line (figure 13).

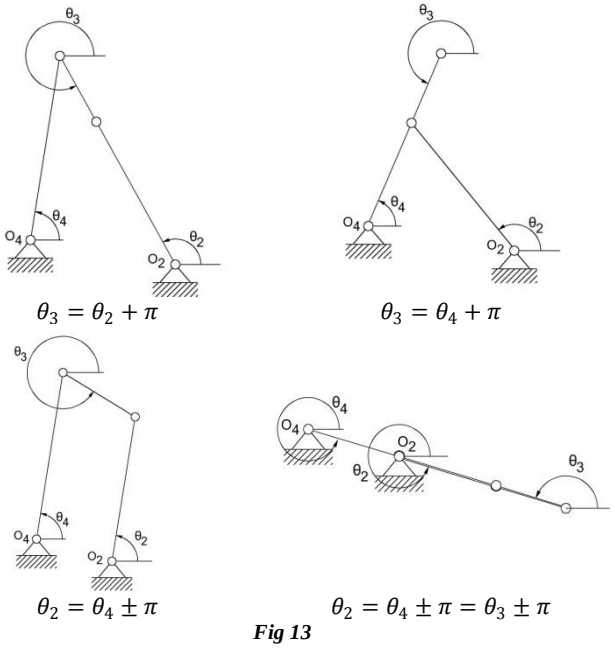

Fig 13

6. Mechanism synthesis-example with specific parameters for bottle washer

Mechanism synthesis should give us positions of special cam while making work path and during return path (figure 3).

For five positions from table 1 we applied mechanism synthesis mentioned earlier.

Table 1: *Five positions of special cam that mechanism should generate*

	X (mm)	Y (mm)	θ
1	665	-287	0
2	95	-245	-109°
3	-78	-293	-176°
4	95	-245	-241°
5	383	-228	-289°

For these 5 specific positions we get two solutions and one of them is acceptable (figure 14). On figure 14 also we can see path comparison of old special cam peak path (green line) and new mechanism (purple line) point of connection link paths.

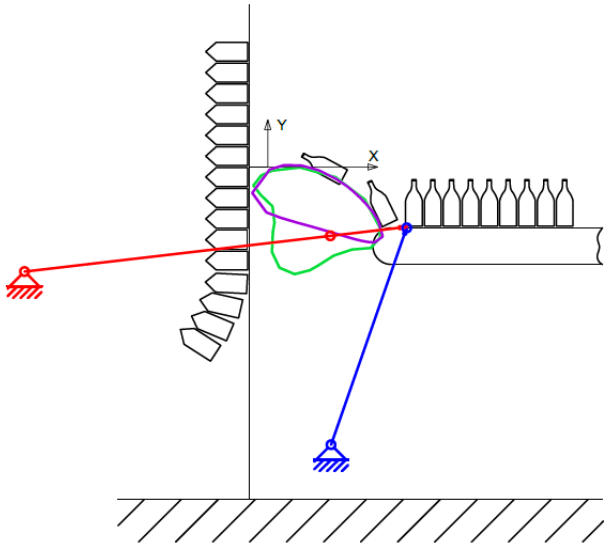

Fig 14

We can conclude that the point of connection link of a four-bar mechanism, which represents also a peak of a new special cam, matches with path of the old mechanism.

Connection link of this mechanism makes full rotation and we can say that this is a good solution for the task that was set on the beginning of this paper.

7. Conclusion

On machines that do bottle washing gear-bar mechanism should be replaced with bar mechanism because they are cheaper, easier to maintenance and adjustment. To get mechanism with this type of movement it is necessary to connection link makes planar movement and full rotation. Planetary mechanism is added to four-bar mechanism to perform this movement. This mechanism has one degree of freedom.

In this paper is shown that using analytical mechanism synthesis (5 specific positions given) we can define mechanism which has connection link that makes full rotation. Planetary mechanism can be different due to the movement that we want to achieve.

Position and velocity analysis gives us possibility to determine mechanism movement during whole movement cycle. Determination of mechanism position is solving nonlinear equation (3) which can be solved numerically. In this analysis possibility of determination of specific positions is given. Also in this analysis influence of geometrical parameters on output parameters (especially on rotation velocity) is shown.

7. References

[1] Todor Pantelić, Goran Ćulafić MEHANIZMI SINTEZA MEHANIZAMA – Mašinski fakultet Beograd 1986.

[2] KHS Technical documentation for Inoclean – Bottle washer Revision 2014.

[3] Lipovina Zoran DIPLOMSKI RAD - PRIMJENA POSTUPAKA ANALITIČKE SINTEZE POLUŽNIH MEHANIZAMA NA KONKRETNIM PROBLEMIMA – Podgorica 1999.

[4] Popović Vanja DIPLOMSKI RAD – SINTEZA MEHANIZMA ZA PODIZANJE TOČKOVA AVIONA SA ASPEKTA VEZIVANJA ZA TRUP AVIONA – Podgorica 2005.

[5] Goran D. Ćulafić MODELIRANJE MEHANIZAMA-ANALIZA I OPTIMALNA SINTEZA – Podgorica 1997

NUMERICAL ANALYSIS OF TURBO-GENERATOR STEAM TURBINE ENERGY EFFICIENCY AND ENERGY POWER LOSSES CHANGE DURING THE VARIATION IN DEVELOPED POWER

PhD. Mrzljak Vedran[1], PhD. Poljak Igor[2], Prof. PhD. Prpić-Oršić Jasna[1]
[1]Faculty of Engineering, University of Rijeka, Vukovarska 58, 51000 Rijeka, Croatia
[2]University of Zadar, Maritime Department, M. Pavlinovića 1, 23000 Zadar, Croatia
E-mail: vedran.mrzljak@riteh.hr, ipoljak1@unizd.hr, jasna.prpic-orsic@riteh.hr

Abstract: *Developed power variation of turbo-generator (TG) steam turbine allows insight into the change of turbine energy efficiency and energy power losses. Measurements were performed in five different TG steam turbine operating points and analysis is presented in three randomly selected operating points. Turbine developed power was varied from 500 kW until the maximum power of 3850 kW in steps of 100 kW. Turbine energy efficiency increases from 500 kW to 2700 kW and maximum energy efficiency was obtained at 70.13 % of maximum turbine power (at 2700 kW) in each operating point. From 2700 kW until the maximum of 3850 kW, TG turbine energy efficiency decreases. Change in TG turbine energy efficiency is caused by an uneven intensity of increase in turbine power and steam mass flow. For all observed operating points, energy efficiency during turbine exploitation is approximately 10 % or more lower than the maximum obtained one. A continuous increase in turbine energy power losses during the developed turbine power increase are the most influenced by the continuous increase in steam mass flow through the turbine.*

KEYWORDS: STEAM TURBINE, ENERGY EFFICIENCY, ENERGY POWER LOSSES, POWER VARIATION

1. Introduction

Steam turbine propulsion plants are not a rarity for a number of LNG carriers [1]. Such steam propulsion plants have many essential components, not only for ship propulsion, but also for electricity and heat production. Each component from the steam propulsion plant can and should be investigated and optimized to achieve the optimal operating parameters. One of the constituent components of such marine steam propulsion plant is turbo-generator (TG) which steam turbine is analyzed in this paper from the energy aspect [2].

Measurements of required TG steam turbine operating parameters were performed on conventional LNG carrier. Every LNG carrier with steam propulsion system has at disposals at least two or more turbo-generator sets which are designed to cover all ship requirements for electrical power.

On the analyzed LNG carrier is mounted two identical TG operating sets. Each TG turbine has identical operating parameters (inlet and outlet temperatures, pressures and mass flows). For the analysis in this paper is selected one TG steam turbine. Steam turbine, which drives an electric generator on the analyzed LNG carrier comprises of nine Rateau stages. Steam turbines with Rateau stages, analysis of their operation and its characteristics is presented in [3]. Usual and specific designs of marine steam turbines along with their auxiliary systems are presented in [4].

The main goal of the TG steam turbine analysis in this paper was to present change in steam turbine energy efficiency and energy power losses during the change in turbine developed power. Measurements of necessary operating parameters were provided in five different turbine operating points, at five different loads. In each turbine operating point was varied turbine developed power from the lowest to the highest one. During the power variation was calculated turbine energy efficiency and energy power losses. The results of the analysis were presented for three selected turbine operating points, but presented conclusions are valid also for all the other operating points. Steam turbine developed power variation allows detecting optimal turbine loads with the highest energy efficiency, for each operating point. It was compared turbine energy efficiency and energy power losses from the real exploitation (measured operating parameters) with achieved optimal operating conditions when the turbine has the highest energy efficiency. TG steam turbine load depends on ship electrical consumers and their current needs for the electrical power. From the aspect of energy efficiency, for the analyzed TG steam turbine will be better to be more loaded to achieve maximal energy efficiency in each operating point.

Main characteristics and specifications of the LNG carrier in which steam propulsion system is mounted analyzed TG steam turbine are presented in Table 1.

Table 1. *Main characteristics of the analyzed LNG carrier*

Dead weight tonnage	84,812 DWT
Overall length	288 m
Max breadth	44 m
Design draft	9.3 m
Propulsion turbine	Mitsubishi MS40-2 (max. power 29.420 kW)
Turbo-generators	2 x Shinko RGA 92-2 (max. power 3.850 kW each)

2. Low power steam turbine energy analysis

2.1. Steam turbine energy analysis equations

The first law of thermodynamics defined energy analysis of any steam system component [5]. Mass and energy balance equations for a standard volume in steady state disregarding potential and kinetic energy can be expressed according to [6]:

$$\sum \dot{m}_{\mathrm{IN}} = \sum \dot{m}_{\mathrm{OUT}} \tag{1}$$

$$\dot{Q} - P = \sum \dot{m}_{\mathrm{OUT}} \cdot h_{\mathrm{OUT}} - \sum \dot{m}_{\mathrm{IN}} \cdot h_{\mathrm{IN}} \tag{2}$$

Energy power of a flow for any fluid stream can be calculated according to the [7] by using the equation:

$$\dot{E}_{\mathrm{en}} = \dot{m} \cdot h \tag{3}$$

Energy efficiency may take different forms and types. Usually, energy efficiency can be written as [8]:

$$\eta_{\mathrm{en}} = \frac{\text{Energy output}}{\text{Energy input}} \tag{4}$$

2.2. Energy efficiency and energy power losses for the TG steam turbine

Steam turbine for a turbo-generator drive is a condensing type [9]. Schematic view of steam turbine connected to an electric generator (the whole set of steam turbine and electric generator is usually called turbo-generator) is presented in Fig. 1. Superheated steam mass flow, specific steam enthalpies and specific steam entropies at the TG steam turbine can also be seen in Fig. 1. All variables important for TG turbine numerical analysis were marked with 1 for inlet variables and with 2 for outlet variables.

According to producer specifications [9], TG turbine power can be expressed with the following third degree polynomial:

$$P_{\mathrm{TG}} = -4.354 \cdot 10^{-10} \cdot \dot{m}_{\mathrm{TG}}^3 + 6.7683 \cdot 10^{-6} \cdot \dot{m}_{\mathrm{TG}}^2 + \\ + 0.251318 \cdot \dot{m}_{\mathrm{TG}} - 256.863 \tag{5}$$

where P_{TG} was obtained in (kW) when $\dot{m}_{TG}$ in (kg/h) was placed in the equation (5). Steam mass flow through the TG turbine ($\dot{m}_{TG}$) was measured component, while the developed TG turbine power was calculated according to equation (5).

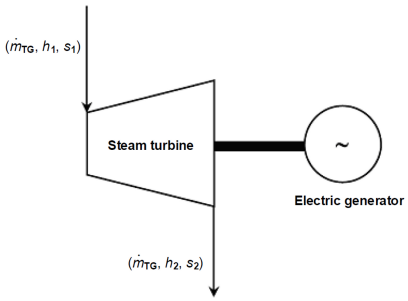

Fig. 1. *Inlet and outlet variables for the TG steam turbine*

During measurements, no steam leakage on the analyzed TG turbine was observed, so the mass balance for the TG steam turbine inlet and outlet is:

$$\dot{m}_{TG,1} = \dot{m}_{TG,2} = \dot{m}_{TG} \tag{6}$$

According to Fig. 1 and Fig. 2, h_1 is steam specific enthalpy at the turbine inlet, and h_2 is steam specific enthalpy at the turbine outlet after real (polytropic) expansion. Steam specific enthalpy at the turbine inlet was calculated from the measured pressure and temperature at each operating point. Steam specific entropy at the turbine inlet s_1 was also calculated from measured steam pressure and temperature at the turbine inlet. Steam real specific enthalpy at the turbine outlet was calculated from the turbine power P_{TG} in (kW) and measured steam mass flow $\dot{m}_{TG}$ in (kg/s) according to [10] by using an equation:

$$h_2 = h_1 - \frac{P_{TG}}{\dot{m}_{TG}} \tag{7}$$

Steam specific enthalpy after isentropic expansion h_{2S} was calculated from the measured steam pressure at the turbine outlet p_2 and from known steam specific entropy at the turbine inlet s_1. Ideal isentropic expansion assumes no change in steam specific entropy ($s_1 = s_{2S}$), Fig. 2.

Steam specific enthalpy at the turbine inlet, steam specific enthalpy at the end of isentropic expansion and steam specific entropy at the turbine inlet were calculated by using NIST REFPROP 8.0 software [11].

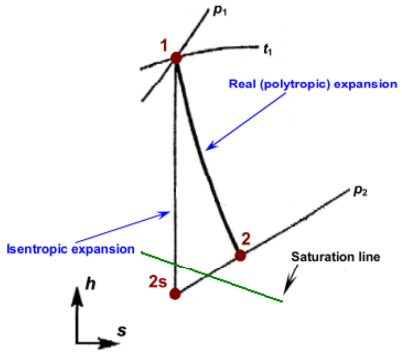

Fig. 2. *TG real (polytropic) and ideal (isentropic) expansion*

TG steam turbine energy power losses in each operating point can be calculated according to Fig. 2 as:

$$\dot{E}_{TG,en,PL} = \dot{m}_{TG} \cdot h_2 - \dot{m}_{TG} \cdot h_{2S} = \dot{m}_{TG} \cdot (h_2 - h_{2S}) \tag{8}$$

Energy efficiency of TG steam turbine can be calculated according to [12] by using the following equation:

$$\eta_{TG,en} = \frac{(h_1 - h_2)}{(h_1 - h_{2S})} \tag{9}$$

2.3. The principle of the TG developed power variation

TG steam turbine real developed power can be calculated according to Fig. 2 by an equation:

$$P_{TG} = \dot{m}_{TG} \cdot (h_1 - h_2) \tag{10}$$

Three different methods can be used for the power change of TG turbine (if it is assumed always the same inlet pressure and temperature and the same outlet pressure):

1) Change in steam mass flow through the TG steam turbine
2) Change in the value of steam specific enthalpy at the steam turbine outlet (h_2)
3) Combination of method 1 and 2

To present the change of TG steam turbine energy efficiency and energy power losses in this paper is selected combined method (method 3) for each operating point.

Turbine developed power was varied from 500 kW up to a maximum of 3850 kW in steps of 100 kW. Power change requires a change in steam mass flow through the turbine, so the adequate steam mass flow for any turbine power was calculated by using the reversed equation (5). In each operating point, steam pressure and temperature at the turbine inlet and steam pressure at the turbine outlet remain identical to the measured data. Steam enthalpy at the turbine outlet (h_2) was calculated for each turbine power and mass flow by using equation (7). Change in steam enthalpy at the turbine outlet (h_2) along with the change of steam mass flow causes the change of TG steam turbine energy efficiency and energy power losses, equations (8) and (9).

3. Measurement results of the analyzed TG

Measurement results for TG steam turbine at different loads are presented in Table 2. Measured operating parameters were: steam pressure at the TG turbine inlet and outlet, steam temperature at the TG turbine inlet and the steam mass flow through TG turbine.

Table 2. *Measurement results for TG steam turbine at several loads*

Operating point	Steam pressure at the TG turbine inlet (MPa)	Steam temperature at the TG turbine inlet (°C)	Steam pressure at the TG turbine outlet (MPa)	Steam mass flow through TG turbine (kg/h)
1	5.97	490.5	0.00425	4000.58
2	6.07	491.0	0.00392	3838.78
3	6.07	502.5	0.00397	3778.91
4	6.02	504.0	0.00412	3951.37
5	5.80	493.0	0.00557	4428.43

4. Used measuring equipment

All the measurement results were obtained from the existing measuring equipment mounted on the TG steam turbine inlet and outlet. All measuring equipment is calibrated by producers. List of all used measuring equipment was presented in Table 3.

Table 3. *Used measuring equipment for the TG turbine analysis*

Steam temperature (TG inlet)	Greisinger GTF 601-Pt100 - Immersion probe [13]
Steam pressure (TG inlet)	Yamatake JTG980A - Pressure Transmitter [14]
Steam pressure (TG outlet)	Yamatake JTD910A - Differential Pressure Transmitter [15]
Steam mass flow (TG inlet)	Yamatake JTD960A - Differential Pressure Transmitter [15]

5. Energy efficiency and energy power losses during TG turbine developed power variation

Change in TG steam turbine energy efficiency and energy power losses during the turbine developed power variation was presented in three operating points from Table 2 – operating points 1, 3 and 5. Obtained conclusions and trends are also valid for the other TG steam turbine operating points.

5.1. Developed power variation for operating point 1

Change in energy efficiency for TG turbine in operating point 1 (Table 2), during the developed power variation is shown in Fig. 3. Increase in turbine developed power causes an increase in energy efficiency until the maximum value, after which follows a decrease in turbine energy efficiency. Maximum turbine energy efficiency is obtained at power of 2700 kW (70.13 % of maximum turbine power) and amounts 67.82 %. At the highest turbine load of 3850 kW, energy efficiency amounts 65.72 % in this operating point.

Turbine energy efficiency in each operating point, as well as in operating point 1, is calculated by using equation (9). For each operating point, energy efficiency change is affected only with the change in steam specific enthalpy after real polytropic expansion (h_2) which is calculated according to equation (7). Steam mass flow through the TG turbine in equation (7) is calculated by using the reversed equation (5) where the turbine power is known, and steam mass flow is an unknown variable. Values of steam specific enthalpy after real polytropic expansion (h_2) decreases in the turbine power range from 500 kW until the 2700 kW, because the intensity of increase in turbine power is higher in comparison with an increase in steam mass flow through the turbine. In the turbine power range from 2700 kW until the highest turbine load of 3850 kW, steam specific enthalpy after real polytropic expansion (h_2) increases because the intensity of increase in turbine power is lower in comparison to an increase in steam mass flow through a turbine in that operating area.

TG steam turbine load depends on ship electrical consumers and their current needs for the electrical power. In operating point 1, TG steam turbine energy efficiency during LNG carrier exploitation amounts only 56.13 % what is much lower energy efficiency than possible maximum one for this operating point. To obtain better energy efficiencies of TG steam turbine in exploitation, it can be recommended that TG turbine should be more loaded, but not more than 2700 kW.

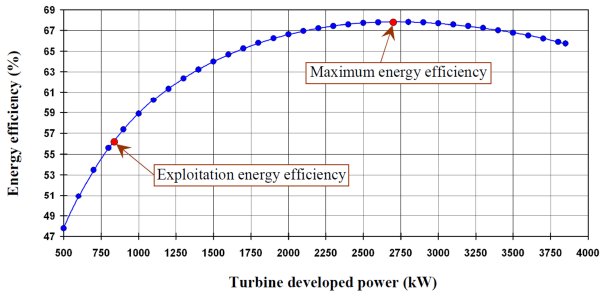

Fig. 3. *Steam turbine energy efficiency change during the developed power variation for operating point 1*

TG steam turbine energy power loss is calculated by using equation (8) for each observed operating point. Turbine energy power loss is the most influenced by steam mass flow through the turbine. Continuous increase in steam mass flow during the TG turbine power increase from 500 kW to 3850 kW causes a continuous increase in turbine energy power loss, Fig. 4.

During LNG carrier exploitation in operating point 1, TG steam turbine energy power loss amounts 648 kW, while at TG turbine maximum energy efficiency in this operating point (at turbine developed power of 2700 kW) turbine energy power loss amounts 1281.16 kW. At maximum turbine power of 3850 kW, energy power loss is the highest and amounts 2008 kW.

For TG steam turbine is not valid a conclusion that the lowest energy power losses are obtained at the highest energy efficiency. TG steam turbine developed power variation showed that energy power losses are proportional to turbine load - higher load results with the higher energy power losses and vice versa. Energy power losses are not proportional to the energy efficiency of the TG steam turbine.

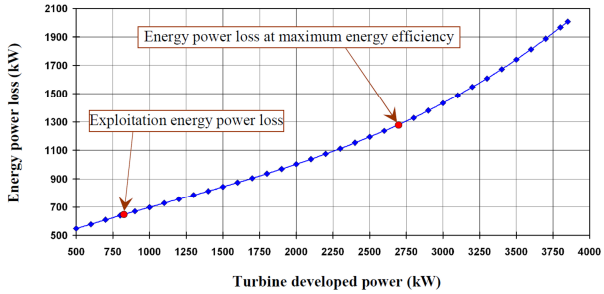

Fig. 4. *Steam turbine energy power loss change during the developed power variation for operating point 1*

5.2. Developed power variation for operating point 3

Change in energy efficiency for TG turbine in operating point 3 (Table 2), during the developed power variation is shown in Fig. 5. As in observed operating point 1, an increase in turbine developed power causes an increase in energy efficiency until the maximum value, after which follows decrease in turbine energy efficiency.

In operating point 3, maximum energy efficiency is obtained also at turbine developed power of 2700 kW and amounts 66.50 %. For this operating point, at the highest turbine load of 3850 kW, energy efficiency amounts 64.44 %, while during LNG carrier exploitation turbine energy efficiency amounts only 53.84 %. The reasons for such TG turbine energy efficiency change are identical as in operating point 1 described earlier.

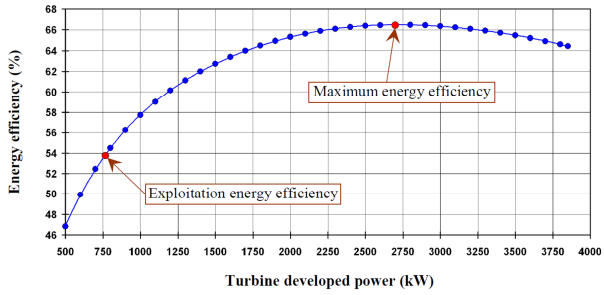

Fig. 5. *Steam turbine energy efficiency change during the developed power variation for operating point 3*

Continuous increase in steam mass flow during the TG turbine power increase from 500 kW to 3850 kW causes a continuous increase in turbine energy power loss, as presented in Fig. 6, also in TG turbine operating point 3.

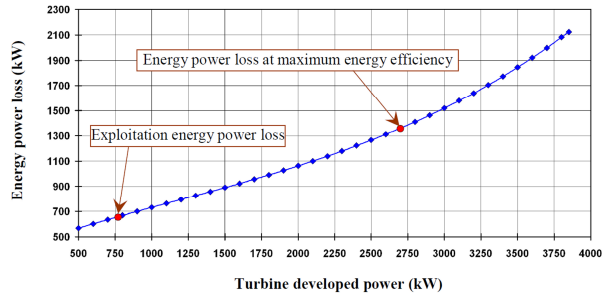

Fig. 6. *Steam turbine energy power loss change during the developed power variation for operating point 3*

TG steam turbine energy power loss during LNG carrier exploitation in operating point 3 amounts 656.86 kW. At maximum energy efficiency (2700 kW) turbine energy power loss amounts 1360.24 kW, while at maximum turbine power of 3850 kW, energy power loss is the highest and amounts 2124.40 kW in this turbine

operating point. As in TG turbine operating point 1, energy power losses are proportional to turbine load - higher load results with the higher energy power losses and vice versa.

5.3. Developed power variation for operating point 5

The same trends and conclusions obtained from TG steam turbine operating points 1 and 3 are also valid for operating point 5 (Table 2). In operating point 5 maximum turbine energy efficiency amounts 69.37 % and as before, is obtained at turbine developed power of 2700 kW. At the highest turbine load (3850 kW) in this operating point energy efficiency is 67.22 %, while during LNG carrier exploitation TG turbine energy efficiency is 59.50 %, Fig. 7. TG turbine operating point 5 also confirmed conclusion that energy power losses are proportional to turbine load - higher load results with the higher energy power losses and vice versa, Fig. 8.

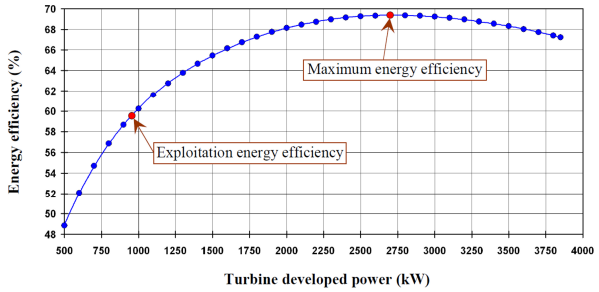

Fig. 7. *Steam turbine energy efficiency change during the developed power variation for operating point 5*

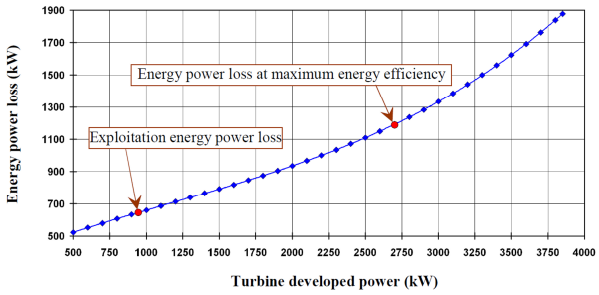

Fig. 8. *Steam turbine energy power loss change during the developed power variation for operating point 5*

6. Conclusions

The paper presents numerical analysis of TG steam turbine energy efficiency and energy power losses change during the variation in turbine developed power. Measurements were performed in five different TG steam turbine operating points and analysis is presented in three randomly selected operating points, but major conclusions are valid in each of them.

Analyzed TG steam turbine energy efficiency increases from 500 kW to 2700 kW of developed power and maximum energy efficiency was obtained at 70.13 % of maximum turbine power (at 2700 kW) in each operating point. From 2700 kW until the maximum of 3850 kW, TG turbine energy efficiency decreases. Increase and decrease in TG turbine energy efficiency is caused by an uneven intensity of increase in turbine power and steam mass flow. For all observed operating points, turbine energy efficiency in LNG carrier exploitation is approximately 10 % or more lower than the maximum obtained ones.

TG steam turbine energy power losses are proportional to turbine load - higher load results with the higher energy power losses and vice versa. The main reason for continuous increase in turbine energy power losses during the developed power increase are found in continuous increase in steam mass flow through the turbine.

7. Acknowledgment

The authors would like to extend their appreciations to the main ship-owner office. This work has been fully supported by the Croatian Science Foundation under the project IP-2018-01-3739.

NOMENCLATURE

Abbreviations:

LNG	Liquefied Natural Gas
TG	Turbo-generator

Latin Symbols:

$\dot{E}$	stream flow power, kJ/s
h	specific enthalpy, kJ/kg
$\dot{m}$	mass flow rate, kg/s
p	pressure, MPa
P	power, kJ/s
$\dot{Q}$	heat transfer, kJ/s
s	specific entropy, kJ/kg·K

Greek symbols:

η	efficiency, -

Subscripts:

en	energy
IN	inlet
OUT	outlet
PL	power loss

8. References

[1] Schinas, O., Butler, M.: *Feasibility and commercial considerations of LNG-fueled ships*, Ocean Engineering 122, p. 84–96, 2016. (doi:10.1016/j.oceaneng.2016.04.031)

[2] Mrzljak, V.: *Low power steam turbine energy efficiency and losses during the developed power variation*, Technical Journal 12 (3), p. 174-180, 2018. (doi:10.31803/tg-20180201002943)

[3] Bloch, H. P., Singh, M. P.: *Steam turbines-Design, Applications and Re-rating,* 2nd edition, The McGraw-Hill Companies, Inc., 2009.

[4] Baldi, F., Ahlgren, F., Melino, F., Gabrielii, C., Andersson, K.: *Optimal load allocation of complex ship power plants*, Energy Conversion and Management 124, p. 344–356, 2016. (doi:10.1016/j.enconman.2016.07.009)

[5] Orović, J., Mrzljak, V., Poljak, I.: *Efficiency and Losses Analysis of Steam Air Heater from Marine Steam Propulsion Plant*, Energies 2018, 11 (11), 3019; (doi:10.3390/en11113019)

[6] Hafdhi, F., Khir, T., Ben Yahyia, A., Ben Brahim, A.: *Energetic and exergetic analysis of a steam turbine power plant in an existing phosphoric acid factory*, Energy Conversion and Management 106, p. 1230-1241, 2015. (doi:10.1016/j.enconman.2015.10.044)

[7] Mrzljak, V., Prpić-Oršić, J., Senčić, T.: *Change in Steam Generators Main and Auxiliary Energy Flow Streams During the Load Increase of LNG Carrier Steam Propulsion System*, Scientific Journal of Maritime Research 32, p. 121-131, 2018. (doi:10.31217/p.32.1.15)

[8] Mrzljak, V., Poljak, I., Medica-Viola, V.: *Dual fuel consumption and efficiency of marine steam generators for the propulsion of LNG carrier*, Applied Thermal Engineering 119, p. 331–346, 2017. (doi:10.1016/j.applthermaleng.2017.03.078)

[9] *Final drawing for generator turbine*, Shinko Ind. Ltd., Hiroshima, Japan, 2006., internal ship documentation

[10] Mrzljak, V., Senčić, T., Žarković, B.: *Turbogenerator Steam Turbine Variation in Developed Power: Analysis of Exergy Efficiency and Exergy Destruction Change*, Modelling and Simulation in Engineering 2018. (doi:10.1155/2018/2945325)

[11] Lemmon, E.W., Huber, M.L., McLinden, M.O.: *NIST reference fluid thermodynamic and transport properties-REFPROP*, version 8.0, User's guide, Colorado, 2007.

[12] Mrzljak, V., Poljak, I., Mrakovčić, T.: *Energy and exergy analysis of the turbo-generators and steam turbine for the main feed water pump drive on LNG carrier*, Energy Conversion and Management 140, p. 307–323, 2017. (doi:10.1016/j.enconman.2017.03.007)

[13] https://www.greisinger.de, (accessed 15.10.18.)

[14] http://www.industriascontrolpro.com, (accessed 15.10.18.)

[15] http://www.krtproduct.com, (accessed 12.10.18.)

INFLUENCE OF THE AMBIENT TEMPERATURE CHANGE ON STEAM PRESSURE REDUCTION VALVE EXERGY DESTRUCTION AND EXERGY EFFICIENCY

PhD. Mrzljak Vedran[1], PhD. Poljak Igor[2], PhD. Orović Josip[2], Prof. PhD. Prpić-Oršić Jasna[1]
[1]Faculty of Engineering, University of Rijeka, Vukovarska 58, 51000 Rijeka, Croatia
[2]University of Zadar, Maritime Department, M. Pavlinovića 1, 23000 Zadar, Croatia
E-mail: vedran.mrzljak@riteh.hr, ipoljak1@unizd.hr, jorovic@unizd.hr, jasna.prpic-orsic@riteh.hr

Abstract: *The paper presents an exergy analysis of pressure reduction valve mounted in the steam propulsion system on conventional LNG carrier. From exploitation are obtained that the valve pressure and temperature decrease become as higher as steam system load increases. Valve exergy power input and output decreases during the increase in steam system load, mostly because of the steam mass flow decrease. Steam system load increase in exploitation also causes a decrease in valve exergy destruction with a simultaneous decrease in valve exergy efficiency (from 68.42 % to 68.09 %). The ambient temperature variation showed that the valve exergy destruction is the lowest for the lowest observed ambient temperature, in any steam system load. The exergy efficiency of the pressure reduction valve is reverse proportional to valve exergy destruction. An increase in the ambient temperature for 10 °C causes a decrease in analyzed valve exergy efficiency for between 2.5 % and 3 %.*

KEYWORDS: AMBIENT TEMPERATURE, STEAM PRESSURE REDUCTION VALVE, EXERGY DESTRUCTION, EXERGY EFFICIENCY

1. Introduction

The main function of pressure reduction valves is reducing pressure of operating medium (in steam plants that operating medium is usually superheated steam). If the operating medium is superheated steam, along with the pressure reduction through the pressure reduction valve was also reduced steam temperature while steam specific entropy increases [1]. In such way the steam system maintained desired operating parameters [2] in all of its parts.

The basic rule for pressure reduction valve operation is that before and after valve specific enthalpy of operating medium remains constant [3]. It is irrelevant to investigate steam pressure reduction valves from the viewpoint of energy, because without any mass flow leakage, steam pressure reduction valves have energy efficiency of 100 % and energy power losses equal to zero, in any observed operating point.

In the land-based steam power plants pressure reduction valves are very rare [4], because in that kind of steam power plants is not necessary to reduce the masses of plant components. In order to remain the walls of every component from the marine steam plant as thick as possible and thus reduce their mass, pressure reduction valves are necessary on ship steam systems [5].

A detailed analysis of any valve type can be rarely found in the scientific literature. If some were found, mostly it is investigations of control valves for steam turbines [6], in some cases along with its actuation systems [7]. Investigations of steam pressure reduction valves are rare, especially for several steam system loads [8].

In this paper was analyzed steam pressure reduction valve, mounted on the main condenser "dump" line, through a several steam system loads. For each load is presented a decrease in steam temperature and pressure on the analyzed valve from the ship exploitation. Based on the measurements of valve operation parameters are presented valve exergy power inputs and outputs, as well as exergy destruction and exergy efficiency in each observed system load. Exergy power inputs and outputs, as well as exergy efficiency and exergy destruction of any steam system component are changeable when the ambient temperature increases or decreases. Engine room temperature variation is performed from 10 °C to 50 °C in steps of 10 °C what is usually expected change of engine room temperature. For observed ambient temperature variation is calculated and presented pressure reduction valve exergy destruction and exergy efficiency in each observed steam system load.

2. Analyzed pressure reduction valve elements and operation characteristics

Analyzed pressure reduction valve is mounted in LNG carrier steam propulsion plant near steam generators. Main characteristics of the LNG carrier which steam propulsion system includes the analyzed pressure reduction valve are presented in Table 1:

Table 1. *LNG carrier characteristics*

Dead weight tonnage	84.812 DWT
Overall length	288 m
Max breadth	44 m
Design draft	9.3 m
Propulsion turbine	Mitsubishi MS40-2 (29420 kW)
Steam generators	2 x Mitsubishi MB-4E-KS

The position of the analyzed pressure reduction valve in the LNG carrier steam system is near the steam generators. The pressure reduction valve is mounted on steam generators "dump" pipeline. This pressure reduction valve is involved in steam system operation during the system startup. During system startup, steam generators produce much more superheated steam than is necessary for system operation. These facts occur because from the ecological point of view, it is more appropriate to burn LNG surplus in steam generators, than release it into the atmosphere. The superheated steam amount which is not used in steam system was directed to the main condenser. Before entering the main condenser, it is necessary to reduce superheated steam pressure after which follows steam cooling by water spray injection. For pressure reduction of superheated steam before its entrance into the main condenser is responsible analyzed valve. So, the measurements of necessary steam operating parameters before and after pressure reduction valve are and can be performed only during the steam system startup period. General pressure reduction operating range of the analyzed valve is reduction from 6.13 MPa to 0.4 MPa.

Analyzed steam pressure reduction valve intersection, along with all main components can be seen in Fig. 1. This type of pressure reduction valve has two valves (main and auxiliary) for pressure pulsation compensation and for ensuring accurate outlet pressure.

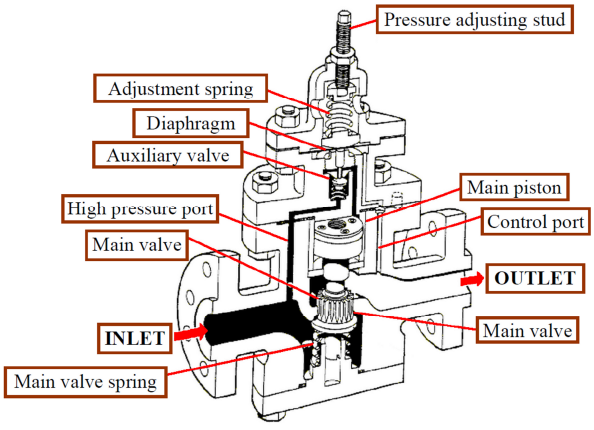

Fig. 1. *Analyzed steam pressure reduction valve intersection [9]*

3. Exergy analysis equations

3.1. Governing exergy analysis equations

Mass balance equation for a volume in steady state disregarding potential and kinetic energy can be expressed as [10]:

$$\sum \dot{m}_{IN} = \sum \dot{m}_{OUT} \quad (1)$$

Exergy analysis is based on the second law of thermodynamics [11]. The main exergy balance equation for a volume in steady state is [12]:

$$\dot{X}_{heat} - P = \sum \dot{m}_{OUT} \cdot \varepsilon_{OUT} - \sum \dot{m}_{IN} \cdot \varepsilon_{IN} + \dot{E}_{ex,D} \quad (2)$$

where the net exergy transfer by heat ($\dot{X}_{heat}$) at the temperature T is equal to [13]:

$$\dot{X}_{heat} = \sum (1 - \frac{T_0}{T}) \cdot \dot{Q} \quad (3)$$

Specific exergy can be defined according to [14] by an equation:

$$\varepsilon = (h - h_0) - T_0 \cdot (s - s_0) \quad (4)$$

The exergy power of a flow can be calculated according to [15]:

$$\dot{E}_{ex} = \dot{m} \cdot \varepsilon = \dot{m} \cdot \left[(h - h_0) - T_0 \cdot (s - s_0) \right] \quad (5)$$

Exergy efficiency [16] is usually defined as:

$$\eta_{ex} = \frac{\text{Exergy output}}{\text{Exergy input}} \quad (6)$$

3.2. Steam pressure reduction valve exergy analysis

For the analyzed pressure reduction valve, all necessary operating points were presented in Fig. 2. The required specific enthalpies and specific entropies were calculated from measured steam pressures and temperatures by using NIST REFPROP software [17].

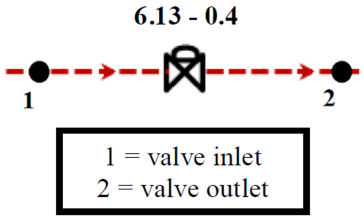

Fig. 2. *Steam pressure reduction valve scheme with a general operating range*

Mass and exergy balances for the analyzed steam pressure reduction valve are:

Mass balance:

$$\dot{m}_1 = \dot{m}_2 \quad (7)$$

Exergy balance:

- Exergy power input:

$$\dot{E}_{ex,IN} = \dot{m}_1 \cdot \varepsilon_1 \quad (8)$$

- Exergy power output:

$$\dot{E}_{ex,OUT} = \dot{m}_2 \cdot \varepsilon_2 \quad (9)$$

- Exergy destruction:

$$\dot{E}_{ex,D} = \dot{E}_{ex,IN} - \dot{E}_{ex,OUT} = \dot{m}_1 \cdot \varepsilon_1 - \dot{m}_2 \cdot \varepsilon_2 \quad (10)$$

- Exergy efficiency:

$$\eta_{ex} = \frac{\dot{E}_{ex,OUT}}{\dot{E}_{ex,IN}} = \frac{\dot{m}_2 \cdot \varepsilon_2}{\dot{m}_1 \cdot \varepsilon_1} \quad (11)$$

The ambient state in the LNG carrier engine room during the provided measurements was:

- pressure: $p_0 = 0.1$ MPa = 1 bar,
- temperature: $T_0 = 25$ °C = 298.15 K.

4. Measuring equipment and measurement results of pressure reduction valve

Measurements were performed in three different LNG carrier steam system operation points during the system startup. After system startup, all produced superheated steam is used in steam system and "dump" line is not in operation from that moment on. Required operating parameters (pressures, temperatures and mass flows) for each steam pressure reduction valve operating point are presented in Table 2 in relation to the main propulsion propeller speed. Main propulsion propeller speed is directly proportional to steam system load.

In Table 2 can be seen that as propulsion propeller speed increases, the steam mass flow, which is sent directly to the main condenser decreases. This fact presents that steam system uses more and more produced superheated steam as propulsion propeller speed (steam system load) increases. After 41.78 rpm, steam system uses all of produced superheated steam and steam "dump" line is closed.

Table 2. *Steam pressure reduction valve inlet and outlet - measurement results*

Propulsion propeller speed (rpm)	Pressure reduction valve - steam inlet (1*)			Pressure reduction valve - steam outlet (2*)		
	Temperature (°C)	Pressure (MPa)	Mass flow (kg/h)	Temperature (°C)	Pressure (MPa)	Mass flow (kg/h)
25.58	312.5	6.010	15767	232.6	0.4	15767
34.33	309.0	6.080	13175	225.6	0.4	13175
41.78	304.0	6.110	3695	216.5	0.4	3695

* Streams numeration refers to Fig. 2.

Measurement results presented in Table 2 were obtained by using the existing measuring equipment mounted before and after analyzed pressure reduction valve. List of used measuring equipment is presented in Table 3. From Table 3 only the Shaft Power Meter used for propulsion propeller speed measuring is not mounted at the analyzed pressure reduction valve inlet or outlet, it is mounted directly on propulsion propeller shaft.

Table 3*. List of used measurement equipment*

Steam temperature (valve inlet and outlet)	Greisinger GTF 401-Pt100 - Immersion probe [18]
Steam pressure (valve inlet)	Yamatake JTG960A - Pressure Transmitter [19]
Steam pressure (valve outlet)	Yamatake JTG940A - Pressure Transmitter [19]
Steam mass flow (valve inlet and outlet)	Yamatake JTD960A - Differential Pressure Transmitter [20]
Propulsion propeller speed	Kyma Shaft Power Meter (KPM-PFS) [21]

5. Pressure reduction valve exergy analysis results with the discussion

5.1. Pressure reduction valve exergy analysis - exploitation

Decrease in pressure and temperature on the analyzed pressure reduction valve is presented on Fig. 3. During the increase in steam system load, steam pressure at the analyzed pressure reduction valve inlet increases, Table 2, and this occurrence causes a simultaneous increase in pressure reduction. At the propulsion propeller speed of 25.58 rpm, analyzed valve reduces steam pressure for 5.61 MPa, at 34.33 rpm steam pressure reduction amounts 5.68 MPa, while at the highest observed propulsion propeller speed of 41.78 rpm, right before the closing of "dump" line, pressure reduction amounts 5.71 MPa.

Increase in steam pressure reduction resulted also with the increase in steam temperature reduction. During the increase in steam system load, the steam temperature reduction increases from 79.9 °C (at 25.58 rpm) to 87.5 °C (at 41.78 rpm).

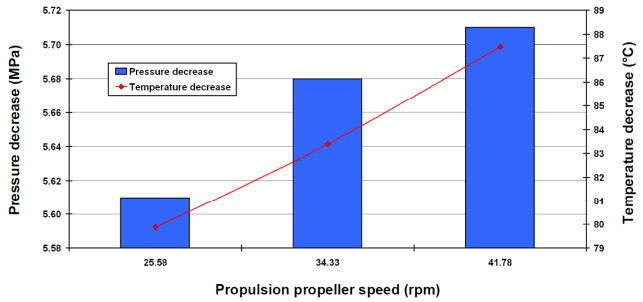

Fig. 3. *The steam pressure and temperature decrease on the pressure reduction valve - exploitation*

Exergy power input and output of the analyzed pressure reduction valve continuously decreases during the increase in steam system load, Fig. 4. According to the equations (8) and (9) the main reason for such decrease in the exergy power input and output can be found in the decrease in steam mass flow, Table 2. After 41.78 rpm, steam system uses all of the produced steam, so amount of steam, which passes directly from steam generators to main condenser is equal to zero.

Increase in steam system load causes decrease in valve exergy power input from 4823.8 kW (at 25.58 rpm) to 1115.7 kW (at 41.78 rpm) while exergy power output simultaneously decreases from 3300.3 kW to 759.7 kW between the same propulsion propeller speeds.

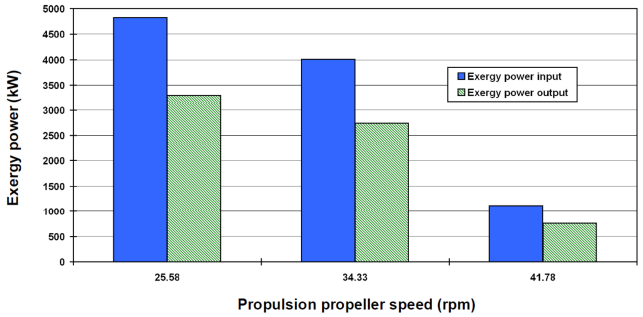

Fig. 4. *Change in exergy power input and output of analyzed valve - exploitation*

Increase in steam system load causes decrease in pressure reduction valve exergy destruction (exergy power losses), Fig. 5, which is caused mostly because of a decrease in steam mass flow. Pressure reduction valve exergy destruction decreases from 1523.5 kW at 25.58 rpm to 356 kW at 41.78 rpm.

The same decrease trend during the increase in propulsion propeller speed can also be seen in pressure reduction valve exergy efficiency, Fig. 5, which decreases from 68.42 % at 25.58 rpm to 68.09 % at 41.78 rpm.

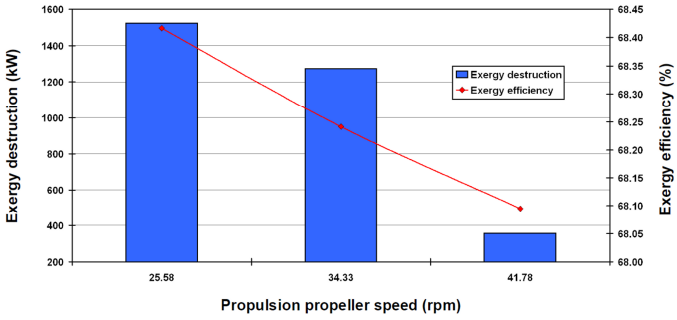

Fig. 5. *Exergy destruction and exergy efficiency of the pressure reduction valve - exploitation*

5.2. Pressure reduction valve exergy analysis during the ambient temperature variation

Exergy analysis of any steam plant component is dependable on the ambient pressure and temperature. In realistic conditions, ambient pressure can not be changed for a significant value, so the influence of the ambient pressure on exergy analysis is almost negligible. Change in the ambient temperature is significant for land-based steam plants during the season change (summer/winter). For the marine steam plants change in the ambient temperature significantly influenced exergy destruction and exergy efficiency of any plant component because it depends on the geographical area in which ship operates. It is realistic to expect that the ambient temperature in the analyzed LNG carrier engine room can be changed from 10 °C (when ship operates in Nordic areas) to 50 °C when ship operates in warm areas (for example Persian Gulf).

At any observed pressure reduction valve operating point, exergy destruction (exergy power loss) is the lowest for the lowest observed ambient temperature. An increase in the ambient temperature causes an increase in valve exergy destruction, Fig. 6.

Valve exergy destruction is also related to steam mass flow through the valve; higher steam mass flow resulted in the higher exergy destruction at any steam system load and at any temperature.

Increase in the ambient temperature causes an increase in valve exergy destruction. Between propulsion propeller speeds of 25.58 rpm and 41.78 rpm, valve exergy destruction amounts from 1446.62 kW to 338.05 kW for the ambient temperature of 10 °C, while for the ambient temperature of 50 °C valve exergy destruction amounts from 1651.16 kW to 385.86 kW in the same operation range.

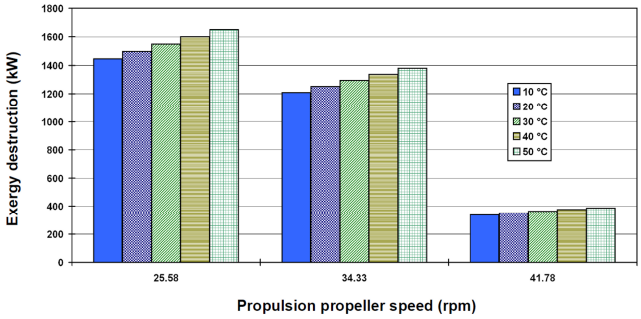

Fig. 6. *Change in the exergy destruction of analyzed valve during the ambient temperature change*

During the ambient temperature variation, exergy efficiency of the analyzed pressure reduction valve is reverse proportional to valve exergy destruction. The highest valve exergy efficiency is obtained for the lowest ambient temperature of 10 °C (and for the lowest exergy destruction), while the lowest valve exergy efficiency is obtained for the highest ambient temperature of 50 °C (and for the highest exergy destruction), Fig. 7.

At each observed ambient temperature, pressure reduction valve exergy efficiency slowly decreases during the increase in steam system load. Increase in the ambient temperature for a 10 °C causes decrease in valve exergy efficiency for between 2.5 % and 3 %.

When compared analyzed pressure reduction valve exergy efficiency with steam turbines, it can be concluded that valve exergy efficiency are much more affected by the change in the ambient temperature than steam turbines in general, because an increase in the ambient temperature for 10 °C causes decrease in steam turbine exergy efficiency for 1 % or less [5].

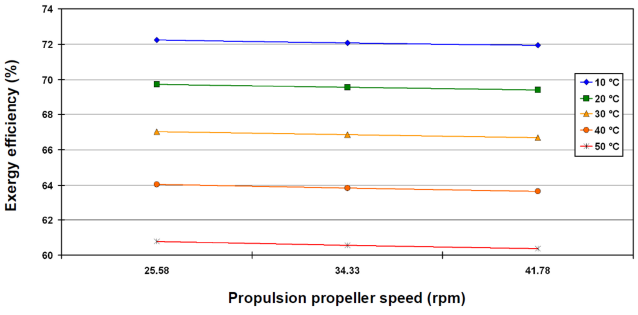

Fig. 7. *Change in exergy efficiency of analyzed valve during the ambient temperature change*

6. Conclusion

This paper presented an exergy analysis of pressure reduction valve mounted in the steam propulsion system on conventional LNG carrier. The pressure reduction valve is analyzed in two different ways: based on measurement data from exploitation and based on the ambient temperature variation. Analyzed valve is mounted on the steam generators "dump" line, which led superheated steam surplus direct to the main condenser.

From LNG carrier exploitation data are obtained that the valve pressure and temperature decrease become as higher as steam system load increases. Valve exergy power input and output decreases during the increase in steam system load, mostly because of the steam mass flow decrease (superheated steam surplus is as lower as the system load increases). Steam system load increase in exploitation also causes a decrease in valve exergy destruction (from 1523.5 kW at 25.58 rpm to 356 kW at 41.78 rpm) with a simultaneous decrease in valve exergy efficiency (from 68.42 % at 25.58 rpm to 68.09 % at 41.78 rpm).

Pressure reduction valve exergy destruction is the lowest for the lowest observed ambient temperature, in any steam system load. An increase in the ambient temperature causes an increase in valve exergy destruction. Valve exergy destruction is related to steam mass flow through the valve; higher steam mass flow resulted in the higher exergy destruction at any steam system load and at any temperature.

The exergy efficiency of the pressure reduction valve is reverse proportional to valve exergy destruction - the highest exergy efficiency is obtained for the lowest observed ambient temperature (and for the lowest exergy destruction), while the lowest valve exergy efficiency is obtained for the highest observed ambient temperature (and for the highest exergy destruction). An increase in the ambient temperature for 10 °C causes a decrease in analyzed valve exergy efficiency for between 2.5 % and 3 %.

7. Acknowledgment

The authors would like to extend their appreciations to the main ship-owner office for conceding measuring equipment and for all help during the exploitation measurements. This work has been fully supported by the Croatian Science Foundation under the project IP-2018-01-3739.

NOMENCLATURE

Abbreviations:

LNG	Liquefied Natural Gas

Latin Symbols:

$\dot{E}$	stream flow power, kJ/s
h	specific enthalpy, kJ/kg
$\dot{m}$	mass flow rate, kg/s or kg/h
p	pressure, MPa
P	work done, kJ/s
$\dot{Q}$	heat transfer, kJ/s
s	specific entropy, kJ/kg·K
T	temperature, °C or K
$\dot{X}_{heat}$	heat exergy transfer, kJ/s

Greek symbols:

ε	specific exergy, kJ/kg
η	efficiency, -

Subscripts:

0	ambient conditions
D	destruction
ex	exergy
IN	inlet (input)
OUT	outlet (output)

8. References

[1] Bloch, H. P.: *Petrochemical Machinery Insights*, Elsevier Inc., 2017.

[2] Sutton, I.: *Plant Design and Operations*, Elsevier Inc., 2015.

[3] Mrzljak, V., Poljak, I., Žarković, B.: *Exergy Analysis of Steam Pressure Reduction Valve in Marine Propulsion Plant on Conventional LNG Carrier*, International Journal of Maritime Science & Technology "Our Sea" 65(1), p. 24-31, 2018. (doi:10.17818/NM/2018/1.4)

[4] Adibhatla, S., Kaushik, S. C.: *Energy and exergy analysis of a super critical thermal power plant at various load conditions under constant and pure sliding pressure operation*, Applied Thermal Engineering, 73, p. 51-65, 2014. (doi:10.1016/j.applthermaleng.2014.07.030)

[5] Mrzljak, V., Poljak, I., Mrakovčić, T.: *Energy and exergy analysis of the turbo-generators and steam turbine for the main feed water pump drive on LNG carrier*, Energy Conversion and Management, 140, p. 307–323, 2017. (doi:10.1016/j.enconman.2017.03.007)

[6] Wang, P., Liu, Y.: *Influence of a circular strainer on unsteady flow behavior in steam turbine control valves*, Applied Thermal Engineering, 115, p. 463–476, 2017. (doi:10.1016/j.applthermaleng.2016.12.073)

[7] Pondini, M., Colla, V., Signorini, A.: *Models of control valve and actuation system for dynamics analysis of steam turbines*, Applied Energy, In Press, Corrected Proof, (doi:10.1016/j.apenergy.2017.05.117)

[8] Qian, J. Y., Wei, L., Zhang, M., Chen, F. Q., Chen, L. L., Jiang, W. K., Jin, Z. J.: *Flow rate analysis of compressible superheated steam through pressure reducing valves*, Energy, 135, p. 650-658, 2017. (doi:10.1016/j.energy.2017.06.170)

[9] http://hawsepipe.net (accessed: 24.10.2018.)

[10] Mrzljak, V., Prpić-Oršić, J., Senčić, T.: *Change in Steam Generators Main and Auxiliary Energy Flow Streams During the Load Increase of LNG Carrier Steam Propulsion System*, Scientific Journal of Maritime Research 32, p. 121-131, 2018. (doi:10.31217/p.32.1.15)

[11] Kanoğlu, M., Çengel, Y.A., Dincer, I.: *Efficiency Evaluation of Energy Systems*, Springer Briefs in Energy, Springer, 2012. (doi:10.1007/978-1-4614-2242-6)

[12] Mrzljak, V., Senčić, T., Žarković, B.: *Turbogenerator Steam Turbine Variation in Developed Power: Analysis of Exergy Efficiency and Exergy Destruction Change*, Modelling and Simulation in Engineering 2018. (doi:10.1155/2018/2945325)

[13] Ahmadi, G., Toghraie, D., Azimian, A., Ali Akbari, O.: *Evaluation of synchronous execution of full repowering and solar assisting in a 200 MW steam power plant, a case study*, Applied Thermal Engineering, 112, p. 111–123, 2017. (doi:10.1016/j.applthermaleng.2016.10.083)

[14] Orović, J., Mrzljak, V., Poljak, I.: *Efficiency and Losses Analysis of Steam Air Heater from Marine Steam Propulsion Plant*, Energies 2018, 11 (11), 3019; (doi:10.3390/en11113019)

[15] Mrzljak, V., Poljak, I., Medica-Viola, V.: *Dual fuel consumption and efficiency of marine steam generators for the propulsion of LNG carrier*, Applied Thermal Engineering, 119, p. 331–346, 2017. (doi:10.1016/j.applthermaleng.2017.03.078)

[16] Mrzljak, V., Poljak, I., Medica-Viola, V.: *Thermodynamical analysis of high-pressure fed water heater in steam propulsion system during exploitation*, Shipbuilding: Theory and Practice of Naval Architecture, Marine Engineering and Ocean Engineering 68 (2), p. 45-61, 2017. (doi:10.21278/brod68204)

[17] Lemmon, E. W., Huber, M. L., McLinden, M. O.: *NIST Reference Fluid Thermodynamic and Transport Properties REFPROP*, Version 8.0, User's Guide, Colorado, 2007.

[18] https://www.greisinger.de, (accessed: 25.10.18.)

[19] http://www.industriascontrolpro.com, (accessed: 25.10.18.)

[20] http://www.krtproduct.com, (accessed: 28.10.18.)

[21] https://www.kyma.no, (accessed: 29.10.18.)

COMPARISON OF NUMERICAL METHODS FOR MODELING THE EFFECT OF EXPLOSION ON PROTECTIVE STRUCTURES

PhD.Bisyk S.[1], PhD.Davydovskyi L.[1], PhD.Hutov I.[2], Ass. Prof. PhD. Slyvinskyi O.[3], M.Sc. Aristarkhov O.[4], Prof. PhD. Lilov I.[5]
Central Research Institute of Weapons and Military Equipment of the Armed Forces of Ukraine, Kyiv [1], Ukraine
Institute of defence - Sofia1[2], Bulgaria, National Military University – Veliko Turnovo[5], Bulgaira,
NationalTechnicalUniversity of Ukraine "Igor Sikorsky Kyiv Polytechnic Institute", Kyiv [3], Ukraine
IvanChernyakhovskyNationalDefenseUniversity of Ukraine, Kyiv [4], Ukraine
sergey-new@ukr.net, davidovskiy14@ukr.net

Abstract: *Comparison of numerical methods for modeling the impact of an explosion on a metal plate such as LOAD_BLAST; LOAD_BLAST_ENHANCED; Arbitrary Lagrangian-Eulerian; Particle Blast Method; Smooth Particle Hydrodynamics which are implemented in the program LS-DYNA. The adequacy and accuracy of these methods are evaluated depending on the distance ratio to the explosive charge. The advantages and disadvantages of each method and recommendations for their use based on the results of this modeling and the experience of the authors of thisarticleare presented..*

Keywords: EXPLOSION, MINE RESISTANCE, MODELING, LS-DYNA

1. Introduction

The results of the combat losses analysis in armed conflicts over the past decades have shown that a large number of damages to armored combat vehicles (ACV) and their crews are caused by mines and improvised explosive devices[1]. Therefore, a topical solution to the problem of determining the effectiveness of protective structures during explosive loading is to improve of the anti-mine protection of ACV. Nowadays, numerical methods are used for solving physic problems on high-speed processes . This is quite effective tool for modeling processes occurring in conditions of explosive load of the protective structure. Modern software with integrated numerical methods allows us to estimate the influence of design parameters and physical and mechanical characteristics of the material and its elements on the operation of the structure as a whole during impulse influence. Numerical modeling can't replace traditional experimental research methods, but can significantly reduce their number and make the whole process more efficient and improve the anti-mine protection of ACV.

Currently, one of the most popular programs that allows to model the impact of explosion on protective structures is LS-DYNA [2]. Usually researchers choose one of the methods of numerical modeling that is implemented in this software package without substantiation of their choice. Each of these methods has errors for specific modeling conditions, so we must compare its accuracy and adequacy for determining the explosive loads and deflections of armored shell of ACV.

2. Preconditions and means for resolving the problem

2.1. Theoretical Model

The main criterion for assessing the impact of explosion on protective structures is the coefficient of distance Z (Table 1) to the explosive charge, which is determined in such a manner [3]:

$$Z = \frac{R}{\sqrt[3]{W}} \tag{1}$$

where: Z – coefficient of distance to the explosive charge; R – distance from center of charge: W– charge weight in TNT.

Table 1:*Conditional classification of the explosion depending on the value of Z*

Classification	Z, kg/m$^{1/3}$
Far field	>4 - ≈40
Average field	0,4-4
Near field	≈0,053-0,4
Contact explosion	≈0,053

The application of the coefficient of distance Z to the explosive charge avoids the attachment to the actual mass of charge, the distance to it, and conducts an assessment taking into account similarity laws.

The following calculation methods are implemented in the form of commands in LS-DYNA [2]:

LOAD_BLAST;
LOAD_BLAST_ENHANCED;
Arbitrary Lagrangian-Eulerian (ALE);
Particle Blast Method (PBM);
Smooth Particle Hydrodynamics (SPH).

Application of these calculation methods is possible depending on the value of Z (Table 2).

Correspondence of theoretical results with experimental data allows to control the legality of the main references laid down in the calculation scheme, as well as the certainty of the resulting numerical results. As experimental data, these works are selected[4,5].

Table 2: *Possibility of application of calculation methods depending on [6].*Note: in conjunction with the LOAD_BLAST_ENHANCED method*

Classification	Z, kg/m$^{1/3}$	LOAD_ BLAST	LOAD_BLAST _ENHANCED	ALE	PBM	SPH
Far field	>4 - ≈40	Yes	Yes	Yes*	No	No
Average field	0,4-4	Yes	Yes	Yes/Yes*	possibly	No
Near field	0,053-0,4	Yes	Yes	Yes	Yes	Yes?
Contact explosion	≈0,053	No	No	Yes	Yes	Yes

The general view of the experimental setup for the explosive load of the armor plate is shown in Fig. 1.[4, 5].When performing research, the armor plate was clamped between two plates (Fig. 1).The explosive charge of trinitrotoluene (TNT) in the form of a sphere was placed at different distances (R) from the target plate. The value of the charge weight also varied. The scheme of conducting an experiment is shown in Fig. 1b.

Cowper-Symonds model (2) for the material of plate was used in the course of numerical modeling [2].

$$\begin{aligned} \sigma_T &= \left[1+\left(\frac{\dot{\varepsilon}}{C}\right)^{1/p}\right]\left(\sigma_0 + \beta E_p \varepsilon_{eff}^p\right), \\ E_p &= E_{tg} E /\left(E - E_{tg}\right), \\ \varepsilon_{eff}^p &= \int_0^t \left(\frac{2}{3}\dot{\varepsilon}_{ij}^p\right)^{1/2} dt, \end{aligned} \tag{2}$$

where: C– parameters of strain rate; $\dot{\varepsilon}$ – equivalent strain rate;
σ_0, σ_T – Static and dynamic yield stress; E – Young's modulus;
E_{tg} - hardening modulus.

The equation of the state of explosive detonation products[2]:

$$p = A(1-\frac{\omega}{R_1V})\exp\{-R_1V\} + B(1-\frac{\omega}{R_2V})\exp\{-R_2V\} + \frac{\omega}{V}\bar{E}, \quad (3)$$

where: $V = \rho_0/\rho = \upsilon/\upsilon_0$ – relative specific volume; A, B, C, R_1, R_2, ω – empirical constants; $\bar{E}$ – internal energy.

The equation of state of air [2]:

$$p = e\cdot(\gamma-1)\rho/\rho_0 \quad (4)$$

where: $\gamma = 1{,}4$ – indicator of air adiabatic.

The mechanical characteristics of the armor plate are summarized in Table 3. Characteristics for the equation of the state of explosive detonation products are given in Table 4.

Table 3:*Characteristics of the plate material [4, 5]*

Characteristic	Value
Young's modulus, GPa	210
Poisson's ratio	0,28
Static yield stress, MPa	950
Dynamic yield stress, MPa	1250
Relative elongation, %	9
Density, kg/m3	7838

Table4:*Characteristics of the equation of state of detonation products [7]*

explosive index	Chapman-Jouget Parameters, *MAT_HIGH_EXPLOSIVE_BURN				
	ρ_0	P	D	E_0	G
	kg/m³	*GPa*	*м/с*	*GJ/m³*	
TNT	1630	21,0	6930	7,00	2,727

The coefficients of the state equation of detonation products in the form Jones-Wilkens-Lee, *EOS_JWL					
A	B	C	R_1	R_2	ω
GPa	*GPa*	*m³/kg*			
371,2	3,231	1,045	4,15	0,95	0,30

2.2. Experimental stand

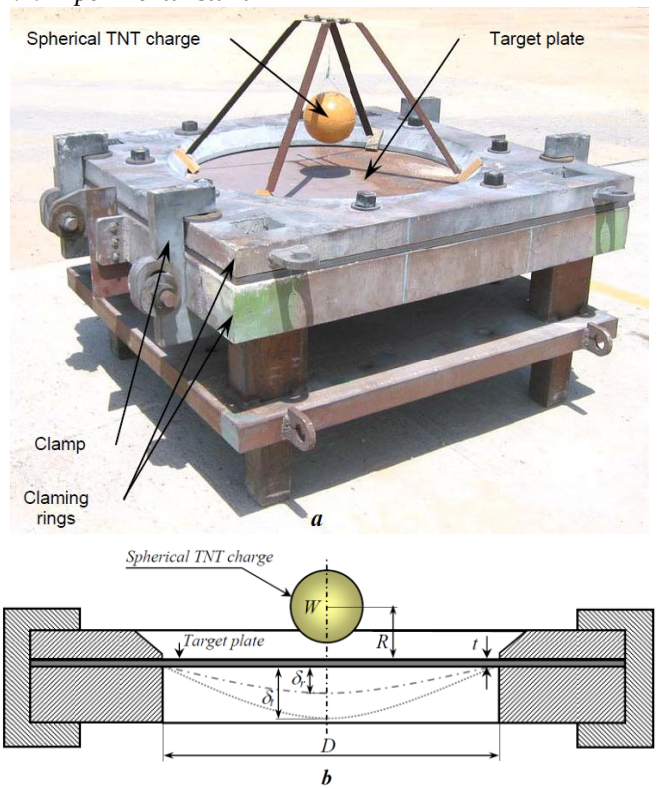

Fig. 1*The general view of the experimental setup (a) and the scheme of conducting an experiment (b) [4,5]: R – distance from center of charge, t – plate thickness; D – plate diameter; δ_r – maximal mid-point transient deflection; δ_r – residual mid-point deflection.*

2.3. Numericalmodeling

Theplateonwhichtheexplosionacts, ismodeledas three-dimensional, four-node, shellfiniteelements (Shell) and three-dimensional, eight-node, solidelements (Solid)inallvariants.Accordingly, in each calculation scheme, the weight of the explosive varied and the distance to it varied.

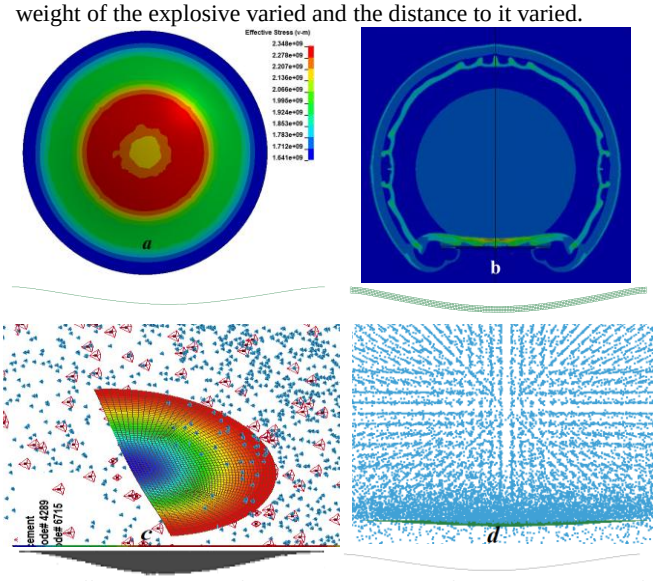

Fig. 2*Different methods of numerical modeling of explosive loading of a plate: a – LOAD_BLAST ma LOAD_BLAST_ENHANCED; b – ALE 2D; c – PBM; d – SPH; under each of the figures - maximum deflections of the plate with the application of the appropriate method*

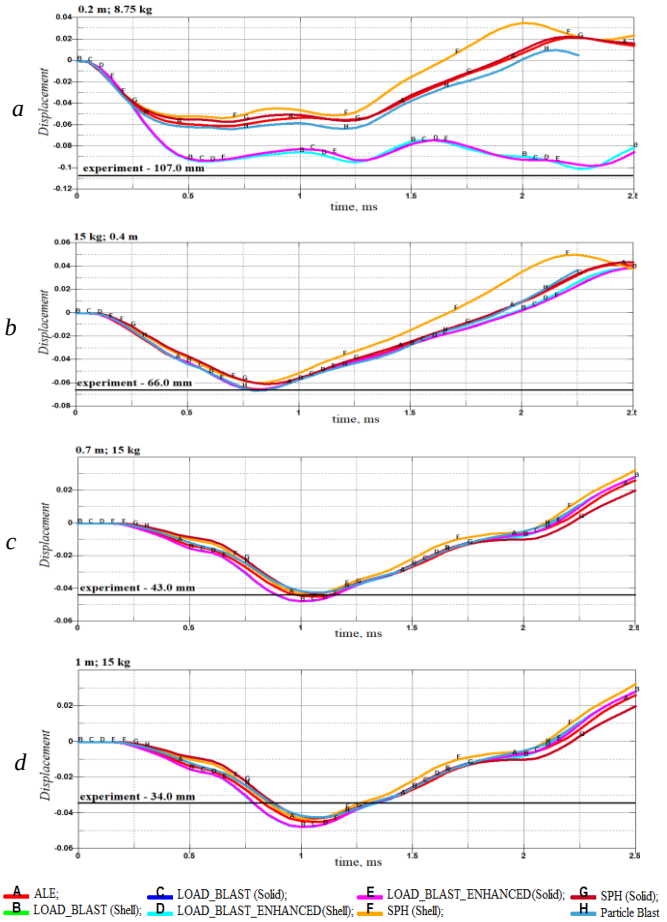

Fig. 3*Graphs of the displacement of the central node of a plate during the simulation of the explosion of charge with the use of various calculation methods: a – W=8,75 kg,R=0,2 m; b – W=15 kg,R=0,4 m; c – W=15 kg,R=0,7 m; d – W=15 kg,R=1 m.*

Table 5: Results of numerical modeling of the impact of explosion on a plate using various calculation methods

Calculation method	W, kg	R, m	δ_r, mm experiment	δ_r, mm calculation	Δ, %	Time of calculation, s	Data volume, MB	Dimensions of a finite element, mm	Number of finite elements, units.	Z, kg/m$^{1/3}$
LOAD_BLAST (Shell)	8,75	0,13	165,0	109,7	33,5	81	41,8	12x12	4380	0,063
		0,2	107,0	100,9	5,7	78				0,097
	15	0,4	66,0	66,2	0,3	79				0,162
		0,7	43,0	47,7	10,9	80				0,284
		1	34	34,6	1,8	83				0,405
LOAD_BLAST (Solid)	8,75	0,13	165,0	105,2	36,2	377	128	14x14	18150	0,063
		0,2	107,0	98,1	8,3	374				0,097
	15	0,4	66,0	66	0,0	371				0,162
		0,7	43,0	47,6	10,7	367				0,284
		1	34	34,6	1,8	371				0,405
LOAD_BLAST (ENHANCED) (Shell)	8,75	0,13	165,0	109,8	33,5	98	55,8	12x12	4380	0,063
		0,2	107,0	100,9	5,7	96				0,097
	15	0,4	66,0	66,3	0,5	88				0,162
		0,7	43,0	47,7	10,9	86				0,284
		1	34	34,6	1,8	85				0,405
LOAD_BLAST (ENHANCED) (Solid)	8,75	0,13	165,0	105,2	36,2	376	151	14x14	18150	0,063
		0,2	107,0	98,1	8,3	374				0,097
	15	0,4	66,0	66	0,0	366				0,162
		0,7	43,0	47,6	10,7	361				0,284
		1	34	34,5	1,5	367				0,405
SPH (Shell)	8,75	0,13	165,0	84,1	49,0	608	498	12x12	65752 (SPH)	0,063
		0,2	107,0	54,5	49,1	596				0,097
	15	0,4	66,0	59,6	9,7	585				0,162
		0,7	43,0	43,2	0,5	505			4380 (Shell)	0,284
		1	34	27,2	20,0	498				0,405
SPH (Solid)	8,75	0,13	165,0	97,8	40,7	2630	583	14x14	65752 (SPH)	0,063
		0,2	107,0	56,5	47,2	2421				0,097
	15	0,4	66,0	60,8	7,9	2305				0,162
		0,7	43,0	42,6	0,9	2032			18150(Solid)	0,284
		1	34	25,9	23,8	1918				0,405
ALE 2D (Solid)	8,75	0,13	165,0	70,8	57,1	37850	2100	5x5	196400	0,063
		0,2	107,0	61	43,0	37630				0,097
	15	0,4	66,0	65,1	1,4	21030				0,162
		0,7	43,0	44,8	4,2	8951				0,284
		1	34	32,1	5,6	9748				0,405
Particle Blast (with air) (Shell)	8,75	0,13	165,0	100,9	38,8	136			4380 (Shell)	0,063
		0,2	107,0	63,8	40,4	133				0,097
	15	0,4	66,0	66,4	0,6	130			100 000 (PBM)	0,162
		0,7	43,0	42,2	1,9	122				0,284
		1	34	42,1	23,8	65				0,405

3.Result and Discussion.

The obtained simulation results using the considered calculation methods showed high accuracy in comparison with the experimental data, which were selected as reference ones. An additional point is that obtained results correlate with results of other works. [8-10].

The use of Solid or Shell elements in the numerical model has approximately the same level of precision while solving tasks. However, the amount of data needed to store the solution of the same task for Solid elements will be on average three times more than Shell. It is clear that the time of solving the problem with the use of Solid elements will be significantly higher compared with the use of shell elements. Such conclusions aren't new and completely logically proceed from the mathematical content of both elements. For the majority of tasks regarding the assessment of the impact of explosions on protective structures, it is quite sufficient to use Shell elements except for the presence of significant plastic deformations and the destruction of structural elements. In this case, the use of Solid elements will be expedient.

Application of the LOAD_BLAST and LOAD_BLAST_ENHANCED method has significant advantages over other methods because of their ease of use, relative simplicity of the preparation of the finite element model, the smallest volumes of data compared with other methods, the smallest hardware requirements for computers. The disadvantages of such calculation methods are the impossibility of taking into account "shading" by one design of another, the absence of reflection and overlay of shock waves, which leads to an increase of measure of inaccuracy in the evaluation of the protective properties of complex structures. By the way, there is a fairly small choice of charge explosive form. The effect of a spherical charge in the air or on the surface of the soil is integrated in this calculation method. This requires a recalculation of the charge value of the charge, taking into account the soil and coefficients taking into account the shape of the charge. LOAD_BLAST_ENHANCED further allows us to estimate the pressure acting on the protective structure on its surface and the effect of the negative phase of the shock wave (this isn't counted in LOAD_BLAST).

Using the SPH method allows us to take into account processes of reflection and overlaying of shock waves, but requires considerable hardware resources. In addition, this method is very sensitive to grid density, the number of SPH elements, and the correct choice of contact between the elements of the SPH and the elements of the Lagrange.

The ALE method requires a lot of hardware resources, requires the greatest amount of time in order to calculate the task and consumes the highest volume of data to note.

The Particle Blast method has the advantage because of the lack of a mesh, needs a relatively small amount of data to note, has a fairly high accuracy and high speed of problem solution. The application of this method is quite promising at the present time.

4. Conclusion

The obtained results show that for the conditions of charge demolition under the bottom or chassis of the ACV, all the methods of modeling the impact of the explosion described in this article have high adequacy and accuracy. The use of each method is expedient in view of their disadvantages and advantages at the discretion of the researcher. Taking into account the authors' experience, it is expedient to carry out the research of the protective structure in the initial stages using the methods LOAD_BLAST and LOAD_BLAST_ENHANCED. We should use one of the methods such as Arbitrary Lagrangian-Eulerian, Corpuscular Particle Method, Smooth Particle Hydrodynamics in order to receive more detailed information about the protective structure.

5. Literature

1. Summaryofglobalarmouredvehiclemarketreport 2013URL: https://http://rfventures.co/wp-content/uploads/2018/01/iq2018.pdf
2. LS-DYNA keyword user's manual Version 970. Livermore: LSTC, 1998. 498 c
3. *Beiker U., Koks P., Uestain P.* [et al].Vzryivnyieyavleniya.Otsenkaiposledstviya [Explosive phenomena.Assessment and implications]. Moscow, Myr, 1986. 319 p.
4. *Neuberger A., Peles S., Rittel D.* Scaling the response of circular plates subjected to large and close-range spherical explosions. Part I: Air-blast loading, International Journal of Impact Engineering 34, 2007, pp. 859-873.
5. *Neuberger A., Peles S., RittelD.*Springback of circular clamped armor steel plates subjected to spherical air-blast loading, International Journal of Impact Engineering 36, 2009, pp. 53–60.
6. *Hilding D.* Methods for modelling Air blast on structures in LS-DYNA // Nordic LS-DYNA Users Conference, Gothenburg, Sweden, 2016
7. *OrlenkoL.P.*Fizikavzryiva[Physics of the explosion]. Moscow, FYZMATLYT, 2004. 656 p.
8. *Olovsson, L., Hanssen, A.G., Børvik, T., Langseth, M.* A particle-based approach to close-range blast loading, European Journal of Mechanics / A Solids (2009), DOI: 10.1016/j.euromechsol.2009.06.003
9. *Schwer L., Teng H., Souli M.* LS-Dyna Air Blast Techniques: Comparios with Experiments for Close-in Charges // 10-th European LS-Dyna Conference, Wurzburg, Germany, 2015.
10. *Teng H., Wang J.* Particle Blast Method (PBM) for the Simulation of the Simulation of Blast Loading // 13-th International LS-Dyna Users Conference, Dearborn, USA, 2014.

МОДЕЛИРОВАНИЕ РАДИАЛЬНО-СДВИГОВОЙ ПРОКАТКИ АУСТЕНИТНОЙ НЕРЖАВЕЮЩЕЙ СТАЛИ AISI-321 С ЦЕЛЬЮ ОПРЕДЕЛЕНИЯ ОПТИМАЛЬНЫХ ТЕХНОЛОГИЧЕСКИХ ПАРАМЕТРОВ ДЛЯ ПОЛУЧЕНИЯ УМЗ-СТРУКТУРЫ

Д.т.н., проф. Найзабеков А.Б.[1], к.т.н., доцент Лежнев С.Н.[1], PhD Арбуз А.С.[2], PhD Панин Е.А.[3]
[1] Рудненский индустриальный институт, Рудный, Казахстан; [2] Nazarbayev University, Астана, Казахстан
[3] Карагандинский государственный индустриальный университет, Темиртау, Казахстан;
E-mail: naizabekov57@mail.ru

Аннотация: *В статье рассматриваются результаты компьютерного моделирования процесса радиально-сдвиговой прокатки аустенитной нержавеющей стали AISI-321, в ходе которого было проведено варьирование основными технологическими параметрами - температурой нагрева заготовки и скоростью вращения валков. Установлено, что с понижением начальной температуры нагрева заготовки измельчение начального размера зерна происходит более интенсивно, причем наибольшее измельчение зерна наблюдается в поверхностной зоне. В то же время, снижение скорости вращения валков является малоэффективным способом для интенсификации процесса измельчения зерна.*

Ключевые слова: РАДИАЛЬНО-СДВИГОВАЯ ПРОКАТКА, МОДЕЛИРОВАНИЕ, РАЗМЕР ЗЕРНА, АУСТЕНИТНАЯ НЕРЖАВЕЮЩАЯ СТАЛЬ

1. Введение

Несмотря на современный уровень развития технологий виртуальных вычислений, основным методом исследования какого-либо технологического процесса остается физический эксперимент. Поскольку только в натурном опыте, имеется возможность учесть все параметры, оказывающие влияние на исследуемый процесс. В то же время, проведение только физических экспериментов – задача весьма нерациональная, требующая больших затрат сил, времени и материальных средств.

Идеальным компромиссом является использование программных комплексов виртуального моделирования, которые позволяют провести симуляцию изучаемого процесса, учесть практически все параметры, влияющие на него, а также провести оптимизацию исследуемого процесса, т.е. определить значения всех зависимых параметров, при которых исследуемый процесс будет протекать наиболее стабильно. После этого, при проведении физического эксперимента с оптимальными значениями, результат будет наиболее успешным, без отбраковки заготовки или поломки оборудования.

Для проведения компьютерного моделирования была выбрана программа Simufact Forming, которая наравне с традиционно используемой программой Deform позволяет моделировать процессы обработки давлением любой сложности. Однако Simufact Forming имеет определенные преимущества перед Deform: в ней имеются более гибкие возможности для построения сетки конечных элементов, в том числе и разные построители сеток; также в ней имеется дополнительная база материалов Matilda, с помощью которой имеется возможность моделирования эволюции микроструктуры.

Ранее уже была рассмотрена модель процесса радиально-сдвиговой прокатки (РСП) заготовки из стали AISI-321 [1]. В ходе тех исследований были рассмотрены такие параметры напряженно-деформированного состояния, как эквивалентные напряжения и деформации, усилие деформирования, среднее гидростатическое давление, а также изменение размера зерна. Помимо этого, данные параметры были рассмотрены в контексте многопроходного деформирования (7 проходов). Было установлено, что после семи проходов в заготовке развивается уровень деформации, достаточный для формирования УМЗ-структуры. Настоящая работа посвящена исследованию влияния на процесс РСП основных технологических параметров, таких как температура нагрева заготовки и скорость вращения валков.

2. Параметры моделирования

В качестве модели для исследования использовалась модель, описанная в работе [1]. Исходная заготовка диаметром 30 мм и длиной 150 мм прокатывалась на стане с обжатием 3 мм (рис. 1).

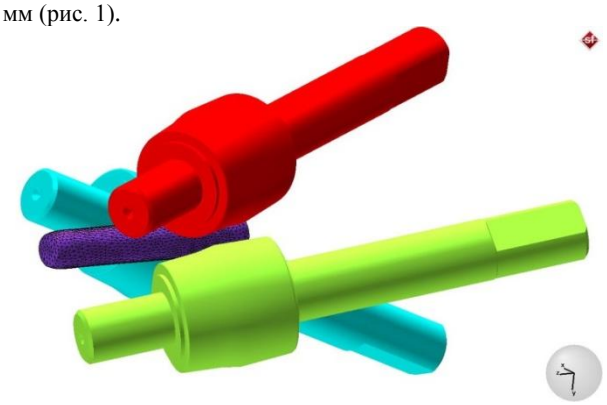

Рис 1 *Модель радиально-сдвиговой прокатки*

Материал заготовки – нержавеющая аустенитная сталь AISI-321 (0,08% C, 17-19% Cr; 9-11% Ni; 2% Mn; 0,8% Si; 0,5-0,7% Ti). Поскольку для выбранной марки стали начальная температура рекристаллизации или диффузионного отжига равна 1020 °C [2], то температура нагрева стали была равна 1000 °C, как максимально возможная для исключения процесса рекристаллизации; скорость прокатки была равна 50 об/мин, как номинальное значение на стане СВП-08. Коэффициент трения на контакте заготовки и валков был принят равным 0,3, как рекомендуемое значение для горячей прокатки [3].

При создании многопроходной модели были использованы следующие параметры (таблица 1).

Таблица 1 – Режим обжатий по проходам

	1 проход	2 проход	3 проход	4 проход	5 проход	6 проход	7 проход
Начальный диаметр, мм	30	27	24	21	18	15	12
Конечный диаметр, мм	27	24	21	18	15	12	9

Помимо изменения уровня обжатия, также было проведено варьирование двумя технологическими параметрами - температурой нагрева и скоростью вращения валков. Дополнительные значения начальной температуры нагрева были заданы равными 900 и 800 °C, поскольку повышение температуры является нерациональным решением - нагрев стали AISI-321 выше 1000 °C приведет к началу процесса рекристаллизации в ходе деформирования.

Учитывая тот факт, что во многих работах [4], которые посвящены многократной интенсивной пластической

деформации, было установлено незначительное влияние скорости деформации на параметры деформирования, было решено проанализировать лишь одно дополнительное значение скорости – 40 об/мин. Также данное решение связано с тем, что базовое значение скорости 50 об/мин является максимально возможным для стана СВП-08, расположенного в Рудненском индустриальном институте. И понижение скорости в любом случае приведет к более интенсивному охлаждению заготовки, что приведет к повышению силовых нагрузок на стан.

Для определения значений напряжения необходимо находить значения компонентов соответствующих тензоров, что для трехмерного течения металла является очень сложной задачей. Поэтому обычно используют простой показатель интенсивности напряжения, или так называемое эквивалентное напряжение. Также необходимо исследовать не только эквивалентное напряжение, но и параметры, которые позволяют оценить долю растягивающих и сжимающих напряжений в очаге деформации. Таковыми являются главные напряжения σ_1, σ_2 и σ_3. Все три главных напряжения в совокупности представляют собой среднее гидростатическое давление.

3. Изучение моделей с пониженными температурами нагрева

При анализе моделей с температурами нагрева 900 и 800 °С проводилось изучение энергосиловых параметров (напряжения и усилие), а также эволюции микроструктуры. Исследование деформированного состояния не проводилось, т.к. от данного параметра эквивалентная деформация не зависит.

При понижении начальной температуры нагрева заготовка имеет меньший уровень пластичности. Это вызывает повышение энергосиловых параметров, что является негативным фактором с точки зрения стойкости инструмента. В то же время, повышение уровня сжимающих напряжений и преобладание их значений над растягивающими напряжениями является наиболее благоприятной картиной НДС. В этом случае происходит залечивание возможных внутренних дефектов (пустот, пор, несплошностей) в обрабатываемом металле. Результаты анализа энергосиловых параметров в моделях с пониженными температурами нагрева приведены в таблицах 2-4.

Таблица 2 – Значения напряжений по проходам в модели с температурой нагрева 900 °С

	1 проход	2 проход	3 проход	4 проход	5 проход	6 проход	7 проход
Эквивалентное напряжение, МПа							
Поверхность	155	163	176	193	209	226	243
Периферия	103	114	127	144	162	181	197
Центр	78	84	92	106	122	148	160
Среднее гидростатическое давление, МПа							
Поверхность	-312	-323	-338	-357	-374	-392	-410
Периферия	-127	-135	-149	-167	-182	-205	-227
Центр	-62	-74	-82	-102	-121	-138	-156

Таблица 3 – Значения напряжений по проходам в модели с температурой нагрева 800 °С

	1 проход	2 проход	3 проход	4 проход	5 проход	6 проход	7 проход
Эквивалентное напряжение, МПа							
Поверхность	164	176	188	205	219	244	278
Периферия	108	123	147	164	182	208	237
Центр	83	94	105	129	142	167	184
Среднее гидростатическое давление, МПа							
Поверхность	-320	-334	-348	-363	-384	-412	-437
Периферия	-134	-152	-169	-184	-202	-228	-255
Центр	-73	-84	-97	-118	-133	-154	-172

Таблица 4 – Значения усилий прокатки по проходам в моделях с пониженными температурами нагрева заготовки

	1 проход	2 проход	3 проход	4 проход	5 проход	6 проход	7 проход
900 °С							
Среднее усилие, кН	23	26	29	35	38	42	48
Пиковое усилие, кН	37	40	46	50	54	58	69
800 °С							
Среднее усилие, кН	27	30	34	39	44	51	62
Пиковое усилие, кН	41	43	48	55	61	70	78

Анализ таблиц 2-4 показал, что понижение начальной температуры нагрева является эффективным способом повышения уровня как сжимающих, так и эквивалентных напряжений. Так, по сравнению с базовой моделью, при снижении нагрева на 100 °С уровень эквивалентных напряжений после 7 прохода повышается на 23% в осевой зоне, на 34% в периферийной зоне и на 9% в поверхностной зоне. При снижении нагрева на 200 °С уровень эквивалентных напряжений после 7 прохода повышается на 42% в осевой зоне, на 62% в периферийной зоне и на 24% в поверхностной зоне. Резкое снижение процентной разницы эквивалентных напряжений в поверхностной зоне связано с тем, что после 7 прохода поверхность заготовки имеет более низкую температуру, чем внутренние слои. Это, в свою очередь вызывает значительный рост сжимающих напряжений в этой зоне.

Отчетливо видно, что после каждого прохода значения сжимающих напряжений на поверхности превышают значения в центре в несколько раз – в 5,5 раз после 1 прохода и в 2,7 раз после 7 прохода. Снижение разницы значений напрямую связано с двумя факторами – с понижением температуры заготовки в ходе деформирования, за счет чего идет общий рост сжимающих напряжений; и с уменьшением диаметра заготовки, за счет чего осевая зона подвергается сжимающему действию со стороны валков более интенсивно.

При изучении усилия деформирования было отмечено, что данный параметр, как и напряжения, находится в обратной зависимости от температуры нагрева, т.е. при понижении температуры заготовки усилие прокатки увеличивается.

Анализ значений усилий показал, что снижение начальной температуры нагрева заготовки вплоть до 800 °С позволит осуществлять все 7 циклов деформирования на стане СВП-08 без перегрузок электродвигателей. В обоих случаях ни средние, ни пиковые значения не превышают допустимой величины (100 кН).

Анализ эволюции микроструктуры показал, что снижение температуры нагрева заготовки является весьма эффективным методом для интенсификации процесса измельчения зерна. Несмотря на то, что во всех трех рассмотренных моделях уровень динамической рекристаллизации остается постоянным (за счет неизменности уровня обжатия), доля статической рекристаллизации при снижении температуры нагрева также снижается. Это приводит к большему повышению степени измельчения исходного зерна в металле, особенно в поверхностной зоне. Также, для наглядности были построены диаграммы, отражающие значения среднего размера зерна для трех температур (рисунок 2).

При анализе данных диаграмм было установлено, что с понижением начальной температуры измельчение начального размера зерна происходит более интенсивно во всех трех зонах, но наибольшее измельчение зерна наблюдается в поверхностной зоне, где после 7 прохода при температуре нагрева заготовки 900°С был зафиксирован размер зерна 5 мкм, что в 1,4 раза меньше значения в базовой модели. А в случае нагрева заготовки до 800°С в поверхностной зоне был зафиксирован размер зерна 2 мкм, что в 3,5 раза меньше значения в базовой модели.

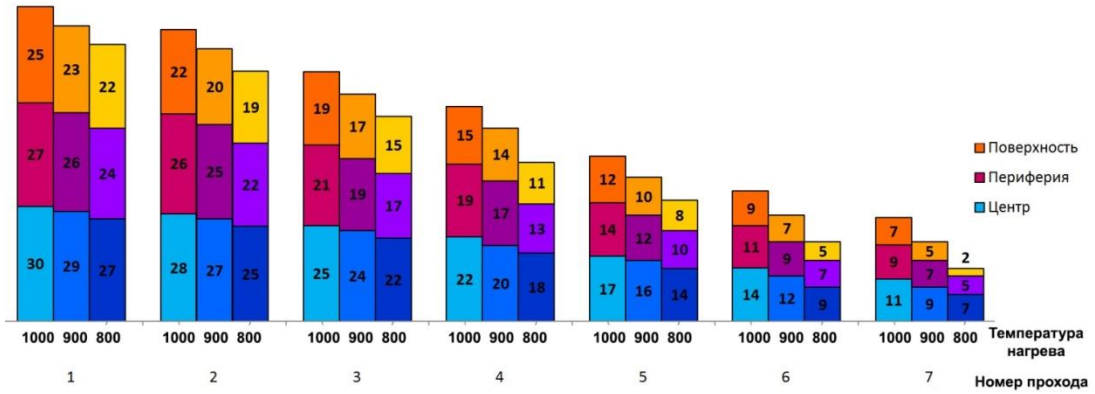

Рис 2 *Распределение среднего размера зерна по проходам при варьировании температурой нагрева, мкм*

4. Изучение модели с пониженной скоростью деформации

При рассмотрении модели со скоростью вращения валков 40 об/мин было отмечено значительно меньшее влияние (по сравнению с температурой нагрева) данного фактора на энергосиловые параметры радиально-сдвиговой прокатки и эволюцию микроструктуры. Это напрямую связано с природой влияния основных параметров деформации на уровень пластичности – скорость деформации имеет наименьшее влияние, что подтверждается многочисленными данными, в частности, значениями термомеханических коэффициентов

Для наглядности, вместо таблиц, были построены диаграммы (рисунки 3-5), отражающие значения напряжений во всех зонах для обеих скоростей: 40 об/мин и для базового значения скорости 50 об/мин.

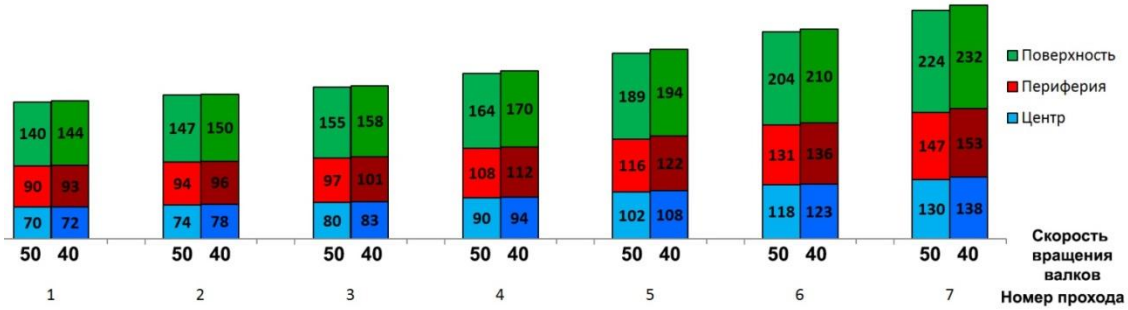

Рис 3 *Распределение эквивалентного напряжения по проходам при варьировании скоростью вращения валков, МПа*

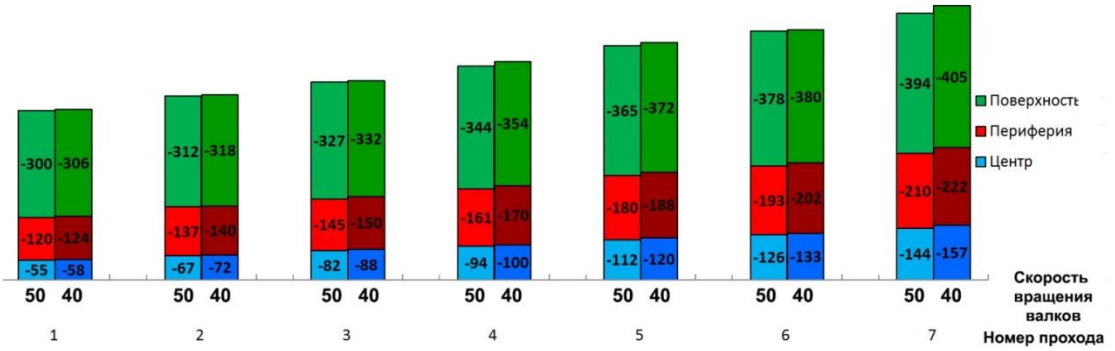

Рис 4 *Распределение среднего гидростатического давления по проходам при варьировании скоростью вращения валков, МПа*

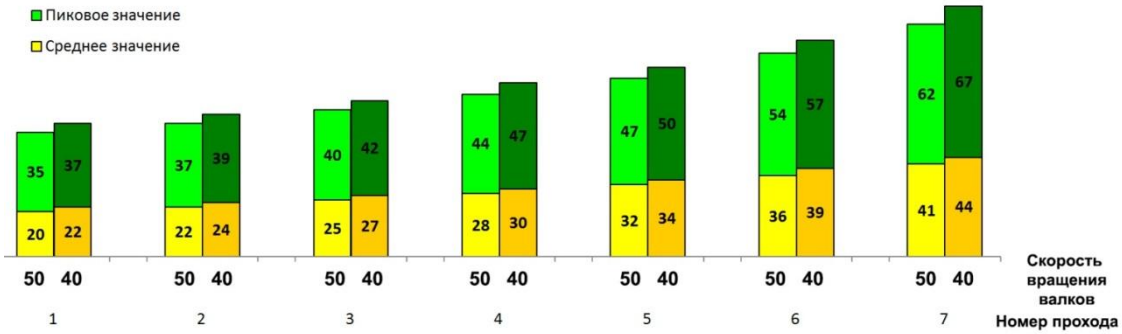

Рис 5 *Распределение усилия прокатки по проходам при варьировании скоростью вращения валков, кН*

Анализ диаграмм на рисунках 2-4 показал, что понижение скорости вращения валков при радиально-сдвиговой прокатке имеет весьма незначительное влияние на формирование напряженного состояния. При этом отмечена обратная зависимость этих параметров, т.е. при снижении скорости вращения валков, значения эквивалентного напряжения и среднего гидростатического давления возрастают.

Так, по сравнению с базовой моделью, при снижении скорости вращения валков на 10 об/мин уровень эквивалентных напряжений после 7 прохода повышается на 6% в осевой зоне, на 4% в периферийной зоне и на 3,5% в поверхностной зоне. Уровень сжимающих напряжений при

снижении скорости вращения валков на 10 об/мин после 7 прохода повышается на 9% в осевой зоне, на 5% в периферийной зоне и на 3% в поверхностной зоне.

Анализ возникающих усилий показал, что пониженная скорость вращения валков позволяет осуществлять все 7 циклов деформирования на стане СВП-08 без превышения нагрузок на электродвигатели, т.к. в этом случае ни средние, ни пиковые значения не превышают допустимой величины (100 кН). Так, после 7 прохода среднее значение усилия составило 67 кН. Это больше базового значения на 7%. Пиковое значение усилия составило 78 кН, что больше базового значения на 8%.

Анализ эволюции микроструктуры показал, что снижение скорости вращения валков является неэффективным методом для процесса измельчения зерна. Несмотря на то, что с увеличением числа проходов размер зерна в рассматриваемой модели меньше, чем в базовой – это объясняется несколько большей степенью остывания заготовки за счет увеличения времени деформирования.

Анализ диаграмм на рисунке 6 показал, что снижение скорости вращения валков, как единственного варьируемого параметра, является малоэффективным способом для усиления процесса измельчения зерна. После 7 прохода наибольшее измельчение зерна наблюдается в поверхностной зоне, где был зафиксирован размер зерна 6 мкм, что в 1,2 раза меньше значения в базовой модели. В остальных двух зонах размеры зерна в 1,1 раза меньше базовых значений.

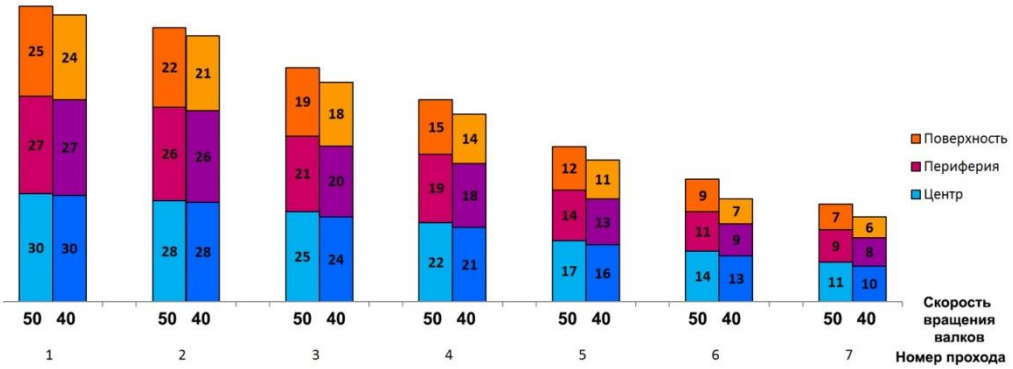

Рис 6 *Распределение среднего размера зерна по проходам при варьировании скоростью вращения валков, мкм*

5. Определение оптимальных параметров обжатия, температуры нагрева и скорости вращения валков

При установлении оптимальных параметров любого технологического процесса необходимо сначала определиться с параметрами оптимизации. В случае процессов обработки металлов давлением это, в первую очередь, возможность осуществления деформирования, т.е. возможно ли провести деформирование на существующем оборудовании или нет. Здесь анализируется возникающее усилие деформирования и сравнивается с допускаемыми значениями. В результате были определены следующие оптимальные параметры деформирования нержавеющей аустенитной стали AISI-321 на стане СВП-08:

- уровень обжатия: 21 мм (7 проходов);
- температура нагрева заготовки: 900 °С или 800 °С;
- скорость вращения валков: 50 об/мин или 40 об/мин.

Здесь необходимо пояснить наличие двух значений температуры и скорости. При варьировании каким-то одним из этих параметров все модели получались удачными в плане отсутствия перегрузки электродвигателей. Однако, при выборе температуры нагрева заготовки 800 °С и скорости вращения валков 40 об/мин в дополнительно построенной модели уже в 5 проходе было зафиксировано превышение допустимого уровня усилия (108,5 кН). Поэтому, для удобства использования результатов моделирования была составлена итоговая таблица варьируемых параметров (таблица 5).

Таблица 5 – Варианты использования варьируемых параметров

	1 проход	2 проход	3 проход	4 проход	5 проход	6 проход	7 проход
50 об/мин							
1000°С	да	да	да	да	да	да	да
900 °С	да	да	да	да	да	да	да
800 °С	да	да	да	да	да	да	да
40 об/мин							
1000 °С	да	да	да	да	да	да	да
900 °С	да	да	да	да	да	да	да
800 °С	да	да	да	да	нет	нет	нет

Значение температуры равное 1000 °С не рекомендуется как оптимальное, поскольку при нагреве до 900 °С имеется возможность провести 7 циклов данного процесса и получить более высокий уровень проработки металла.

6. Заключение

Представлены результаты моделирования процесса радиально-сдвиговой прокатки аустенитной нержавеющей стали AISI-321, в ходе которого было проведено варьирование основными технологическими параметрами - температурой нагрева заготовки и скоростью вращения валков. Установлено, что с понижением начальной температуры нагрева заготовки измельчение начального размера зерна происходит более интенсивно, причем наибольшее измельчение зерна наблюдается в поверхностной зоне. В то же время, снижение скорости вращения валков является малоэффективным способом для интенсификации процесса измельчения зерна.

7. Сведения о грантовой программе

Данная работа выполнена в рамках выполнения темы №AP05131382 «Разработка и исследование технологии получения ультрамелкозернистых материалов с улучшенными механическими свойствами и повышенной радиационной стойкостью для использования их в качестве материалов первой стенки термоядерных реакторов и в ядерной энергетике» по программе грантового финансирования по научным и (или) научно-техническим проектам на 2018-2020 годы в Республики Казахстан..

8. Литература

1. Naizabekov A., Lezhnev S., Panin E.A.,Arbuz A.,Koinov T.A. Computer modelling of radial-shear rolling of austenitic stainless steel AISI-321. II International Scientific Conference “Mathematical Modeling”, Year II, Volume 1, 12 – 15 December, 2018, Borovets, Bulgaria, p. 48-51

2. Сорокин В.Г. Стали и сплавы. Марочник. М.:Интермет Инжиниринг, 2001, 608 с.

3. www.Simufact.com - Simufact Forming manual

4. ASM Metals HandBook Vol. 19 - Fatigue and Fracture. ASM International, 2002.

A-TIG WELDING AS A SOLUTION FOR NICKEL AND MANGANESE SAVINGS IN DUPLEX STAINLESS STEEL WELDED JOINTS

Ph.D. Bušić M.[1], Ph.D. Jurica M.[1], Prof. Ph.D. Garašić I.[1], Prof. Ph.D. Kožuh Z.[1],
University of Zagreb, Faculty of Mechanical Engineering and Naval Architecture, Ivana Lučića 5, 10002 Zagreb, Republic of Croatia [1]
matija.busic@fsb.hr

Abstract: *The paper presents the influence of the activation flux and shielding gas on tungsten inert gas welding of the duplex stainless steel. In introduction part the productivity and the cost-effectiveness of A-TIG welding for duplex stainless steels was explained. In the experimental part X2CrNiMoN22-5-3 7 mm thick stainless steel has been welded in butt joint. The welding process was performed by a robot with TIG equipment. With selected A-TIG welding technology preparation of plates and consumption of filler material (containing Cr, Ni and Mn) have been avoided. Specimens from the produced welds have been subjected to tensile strength test, macrostructure analysis and corrosion resistance analysis. The results have confirmed that this type of stainless steel can be welded without edge preparation and addition of filler material containing critical raw materials as Cr, Ni and Mn when the following welding parameters are set: current 200 A, welding speed 9,1 cm/min, heat input 1,2 kJ/mm and specific activation flux is used.*

Keywords: TUNGSTEN INERT GAS, DUPLEX STAINLESS STEEL, ACTIVATION FLUX, EDGE PREPARATION

1. Introduction

Stainless steels are most important for their corrosion resistance. Stainless steels have a chromium content of at least 10,5 % [1,2]. The high degree of chromium activity is the principal basis for utilizing it as an alloying element in corrosion resisting alloys. As a result of reactions of chromium with the oxygen from the air, a protective oxide film forms and prevents further rapid oxidation. Additions of Mo increase corrosion resistance in reducing acids and against pitting attack in chloride solutions. Varying additions of Ni, N, Cu, Mn, W, Ti, Ni and other elements may also be present. [1-7]. Thus, there are numerous grades of stainless steel alloys with varying contents of chemical elements to suit the environment the alloy must endure. Stainless steels are classified on the basis of their matrices as ferritic, martensitic and austenitic stainless steels. The soft austenitic steels have exceptional ductility, elongation exceeding 50 %. The ferritic stainless steels offer good strength and ductility, but without the outstanding formability of the austenitic varieties. Duplex stainless steel (DSS) with austenitic and ferritic grains possess beneficial combinations of these two phases. The ferrite/austenite ratio in DSS must be close to 50:50. According to the standard HRN EN 10088-1:2015 different DSS can have 22 – 28 % of Cr, 6 – 22 % of Ni, less than 2,00 % of Mn and less than 2,5 % of Mo. DSS exhibit greater toughness and better weldability than ferritic stainless steel [6]. Compared with austenitic grades, DSS have higher resistance to pitting and stress corrosion cracking. Accordingly, they are widely used in various chemical, petrochemical, food, power, transportation, paper and oil industries. Most of these applications require welding as a joining method. DSSs undergo microstructural changes during heat treatment or welding process [6]. During welding of DSS, it is essential to maintain a ferrite–austenite ratio close to 50:50. This phase balance, may however, be upset due to rapid cooling involved in most weld thermal cycles resulting in weld metal ferrite contents in excess of 50 %. The resultant phase ratio is dependent on the energy input during welding, as this determines the cooling rate and the extent of the phase transformation which is diffusion based. If high heat inputs are used, coarse grains are produced in the weld region, wide heat-affected zones and possibly, precipitation of brittle intermetallic phases may develop [7].

Tungsten inert gas (TIG) welding is a widely used technology for joining stainless steels. When conventional TIG welding process is applied for thick sections it has some disadvantages as low penetration and small deposit, and consequently reduced productivity compared to the other welding processes. Material thickness greater than 3 mm is necessary to weld in multiple passes and this greatly reduces productivity of the process. One variety of TIG is welding with activation flux coating (A-TIG) on the upper surface of the plates that should be joined. The application of flux in TIG was proposed for the first time in the 1960s by Paton Welding Institute of National Academy of Sciences, Ukraine, by Gurevich et al. [8]. Activating flux is a mixture of inorganic material suspended in an evaporative medium. A thin layer of flux is applied with a brush or sprayed over the prepared surface to be welded [9]. Fluxes are fabricated by mixing, usually metallic oxide powders with solvents, most frequently acetone or ethanol. In A-TIG process, penetration is increased and a lower electric energy consumption is achieved. The increase in weld penetration can be attributed to the reversal of Marangoni convection. Marangoni convection is a surface-tension-driven convection depending on surface tension gradient in the fluid: fluids flow from areas where surface tension is lower towards areas where it is higher, which is the case with conventional TIG. The reversed Marangoni convection in A-TIG influences the molten metal to flow towards the center of the weld and to the bottom of the weld, causing a narrow and deep penetration.

ISO 9692-1:2013 [10] gives a recommendation for edge preparation according to the thicknesses of steel parts to be welded (Fig. 1). According to this standard for TIG welding of steels in thicknesses $3 < t \leq 8$ mm edge preparation should be square groove with gap between plates $b \approx t$, where t is the thickness of the plate (figure 1.a). Edge preparation for thicknesses $3 < t \leq 10$ should be single V groove with root gap $b \leq 4$ and a V groove angle $40° \leq \alpha \leq 60°$ (figure 1.b). It is notable that edge preparation requires material loss prior the welding and additional filler material during the welding. A-TIG technology makes it possible to intensify the conventional TIG practices for joining the thickness of 8 - 10 mm by single pass full penetration welds, with no edge preparation. With A-TIG technology the edge preparation is simplified, loss of the material and additional filler material are avoided.

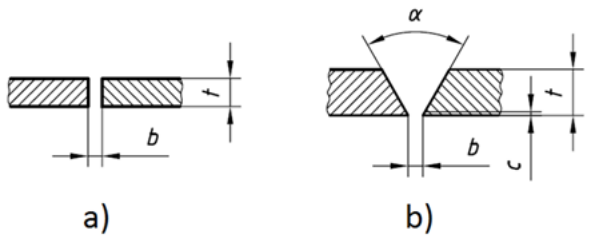

Fig. 1 *Joint preparation for TIG welding of steels according to the ISO 9692-1:2013 [10].*

In this research the intention was to clarify the improvements in productivity when TIG welding is applied with activation flux on X2CrNiMoN22-5-3 7 mm thick stainless steel. This material is austenitic-ferritic stainless steel with high resistance to general corrosion, pitting and crevice corrosion and high resistance to stress corrosion cracking (SCC) in chloride-bearing environments and environments containing hydrogen sulphide. It has also high resistance to erosion corrosion and corrosion fatigue. The tensile strength and weldability of this material are suitable for various applications.

General objective was to produce a sound weld without consumption of nickel and manganese by omitting the edge preparation and additional filler material. Direct substitution of expensive alloying elements, as it is nickel and manganese in the filler materials for welding is not easy to achieve. However, development of welding technology without filler materials can generate welds that can be acceptable for some specific applications.

2. Experimental

2.1. Material

Standard duplex stainless steel with designation X2CrNiMoN22-5-3 has been used in this experiment. Mechanical properties of this material according to the standard HRN EN 10088-2:2015 [11] are presented in table 1. Chemical composition has been analysed with Energy-dispersive X-ray spectroscopy (EDS) on scanning electron microscope Tescan Vega TS5136 [12]. The chemical composition is 0,014 % C, 1,903 % Mn, 0,026 % P, 0,002 % S, 0,278 % Si, 5,005 % Ni, 22,421 % Cr, 2,559 % Mo and 0,169 % N.

Activation flux has been prepared from powders SiO_2 and Cr_2O_3 in proportion 1:1. In order to prepare highly concentrated powder suspensions 96 % ethyl alcohol has been added in proportion 1:2 to this mixture.

Table 1: *Mechanical properties of duplex stainless steel X2CrNiMoN22-5-3 [11]*

Thickness [mm]	Yield stress min. $R_{p0,2}$ [MPa]	Tensile strength R_m [MPa]	Elongation min. A [%]
7	460	640 to 840	25

2.2. Penetration of the electric arc

Penetration of the electric arc has been tested on the test coupons in dimensions 200 × 200 × 7 mm. Plates were cleaned with acetone prior deposition of the activation flux. One thin layer of activation flux was laid on the surface of the work-piece using a paintbrush prior each A-TIG bead on plate welding. Welding was performed with FRONIUS MagicWave 2200 Job G/F TIG welding machine. Tungsten electrode with diameter 2,4 mm and designation WT20 has been used for welding. In order to have a linear motion of the electric arc with accurate speed of moving a TIG welding torch has been installed on the „BUG-O Systems“ Modular Drive Systems automatic machine used for guidance in welding. Two types of shielding gas have been used with the same flow of 9 l/min. Table 2 presents welding parameters for all weld runs in the first part of the experiment. Four samples 1A, 2A, 3A and 4A have been welded with 100 % Ar shielding gas. Other samples 1B, 2B, 3B and 4B have been welded with shielding gas composed of 97,5 % Ar and 2,5 % N_2. Nitrogen has been added to stimulate occurrence of austenitic phase and prevent ferritization.

Table 2: *Welding parameters in bead on plate welding*

Sample	Activation flux	Welding speed [cm/min]	Current [A]	Heat input [kJ/mm]
1A	NO	10,2	160	0,666
2A	NO	7,8	200	1,209
3A	YES	10,2	160	0,762
4A	YES	7,8	200	1,310
1B	NO	10,2	160	0,768
2B	NO	7,8	200	1,320
3B	YES	10,2	160	0,774
4B	YES	7,8	200	1,366

2.3 A-TIG welding parameters

After welding and examination of bead on plate welds, parameters for welded joint have been determined. The constant parameters were:

- welding speed 9,1 cm/min;
- shielding gas flow 9 l/min;
- electrode tip workpiece distance 3 mm;
- tungsten electrode diameter 2,4 mm;
- welding torch inclination 90°.

Two welded joints have been produced without any filler material, first one with 100 % Ar shielding gas (marked as Z1) and the other one with Ar + 2,5 % N_2 shielding gas (marked as Z2). Plates in dimensions 200 × 100 × 7 mm were placed on a 10 mm thick cooper backing plate. Plates had single square edge preparation without any spacing between. Samples have been welded with application of the same activation flux in width of 20 mm on the upper surface. Table 3. Presents welding parameters used for producing welded joints.

Table 3: *Welding parameters used for producing welded joints [12]*

Sample	Welding speed [cm/min]	Current [A]	Voltage [V]	Heat input [kJ/mm]
Z1	9,1	200	14,7	1,163
Z2	9,1	200	15,4	1,218

2.3. Preparation of samples for analysis

From the produced welds specimens for tensile strength testing, and macrostructure analysis have been sectioned perpendicular to the welding direction using a circular band saw. Specimens for tensile strength test have been machined to required dimensions using a universal milling machine according to the requirements of the standard HRN EN ISO 4136:2013.

Specimens for analysis of macrostructure have been grinded and polished using sandpapers: 1) P320, 2) P500, 3) P1000, 4) P2000 and 5) P4000. After polishing the specimens were etched for 40 s in reagent composed of NaOH and H_2O in proportion 2:3 and using DC current with voltage 2 V.

Specimens for corrosion resistance analysis according to standard ASTM G48-03 (method – A) have been plasma cut in dimensions 100 × 45 mm and washed with hot water to eliminate grease and impurities from the surface.

3. Results

3.1. Visual control

During welding with active flux, the weld pool was calm as it is characteristic for the TIG welding process. There were no spatters on the surface of the material around the produced welds. Sample 1A has a wider bead on the plate weld in comparison with sample 3A. Heat affected zone and the root of the weld are wider on the sample 3A in comparison with sample 1A. Welds produced with higher current (samples 2A and 4A) have the same influence of the A-TIG welding on the width of the bead on the plate weld. Sample 4A has sufficient penetration on the root side and narrower bead on plate width in comparison with sample 2A that is without root penetration. The difference between samples made with the second shielding gas (Ar + 2,5 % N_2) is the same as with 100 % Ar.

Figure 2 presents weld face and weld root on Z1 specimen. Figure 3 presents weld face and weld root on Z2 specimen. Appearance of the weld on the face side on both samples is very similar and depends only on the guidance of the electric arc. At the root side of the specimen Z1 lack of fusion can be observed after a few centimetres of a correct joint. The reason can be in the incorrect guidance of the electric arc after half of the path. At the root side of the specimen Z2 full penetration can be observed.

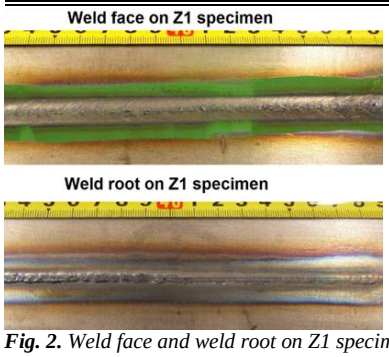

Fig. 2. *Weld face and weld root on Z1 specimen [12]*

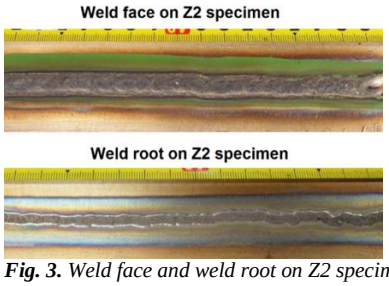

Fig. 3. *Weld face and weld root on Z2 specimen [12]*

3.2 Macrostructure analysis

Macrostructure has been examined on a LEICA MZ6 stereomicroscope. Figure 4 presents a comparison of geometrical features in the produced bead on plate welds in the first part of the experiment. Samples made with 100 % Ar shielding gas are located on the left and samples made with Ar + 2,5 % N_2 are located on the right side of the figure 4. The difference of the geometrical features in dependence on the shielding gas type is clearly seen.

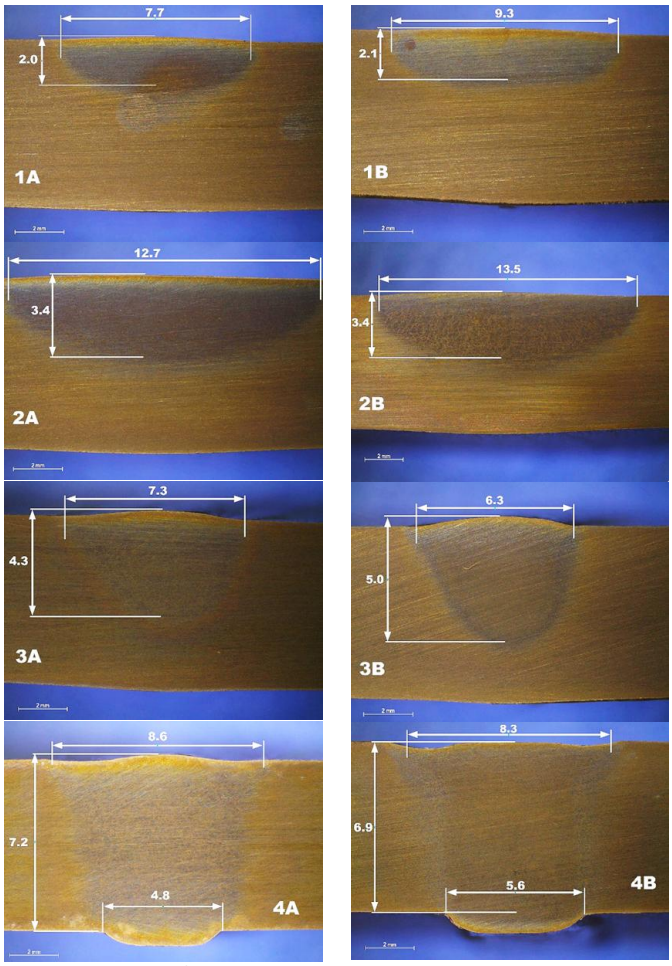

Fig. 4. *Geometrical features in the produced bead on plate welds*

When Ar + 2,5 % N_2 has been used, the produced bead on plate welds have wider and shallower penetration in comparison with 100 % Ar shielding gas. Sufficient penetration through the whole thickness has only been achieved when welding current was 200 A and welding speed was 7,8 cm/min.

Figure 5 presents geometrical features of the produced welds Z1 and Z2. Both welds have a minimal face and root reinforcement but have proper shape. Specimen Z1 has a face width 8,1 mm and root reinforcement 0,3 mm. Specimen Z2 made with Ar + 2,5 % N_2 has a smaller face width, 7,6 mm and the root reinforcement 0,4 mm. Transition from an elongated base metal microstructure (obtained with forming of the sheets) to the weld metal microstructure is clearly seen on both welds. It is also possible to see molten metal flow contours from the outside to the inside. This feature is a clear footprint of the Marangoni's effect.

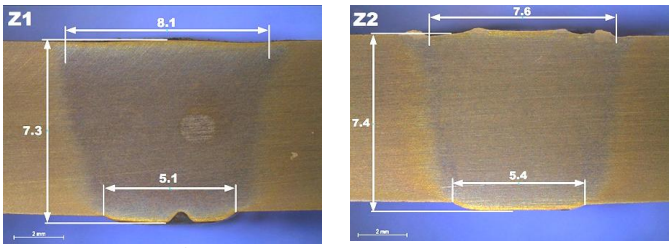

Fig. 5. *Geometrical features in the produced welds Z1 and Z2*

3.3. Tensile strength testing

The uniaxial tensile testing of the specimens has been conducted according to HRN EN ISO 4136:2013 standard [13]. Sample Z1 welded with 100 % Ar shielding gas has a fracture in the heat affected zone. Sample Z2 welded with mixture shielding gas 2,5 % N_2 and 97,5 % Ar has a fracture in the base material approx. 40 mm far from the weld centre. Table 3 presents results of the transversal tensile strength testing of the produced welds. Both welds have similar mechanical properties. Measured mechanical properties of the produced weld Z2 also fulfil requirements of the HRN EN 10088-2:2015 standard for the base material.

Table 5. *Results of the transversal tensile strength testing of produced welds*

Sample	R_m [N/mm^2]	$R_{p0,2}$[N/mm^2]	S_0[mm^2]
Z1	773,23	679,12	176,70
Z2	776,45	683,21	178,57

3.4. Corrosion resistance analysis

Corrosion resistance analysis of the produced welds has been conducted according to the standard ASTM G48 - 03 - method A - Ferric chloride pitting test) [14]. Samples were immersed in 10% solution of $FeCl_3$ in H_2O with a temperature of 50°C for a period of 48 h. Figure 6 presents samples after corrosion analysis. It can be observed that most of the pits have been developed in the weld metal on samples 1A, 3A and 4A. Weld metal on sample 2A is free of any pits. Samples welded with mixture shielding gas 2,5% N_2 and 97,5% Ar (1B, 2B, 3B and 4B) are free of pits in the weld metal and the heat affected zone. However, some pits occurred in the base material a few millimeters away from the heat affected zone. A-TIG welding resulted with less pits (3B and 4B) in comparison with conventional TIG welding (1B and 2B).

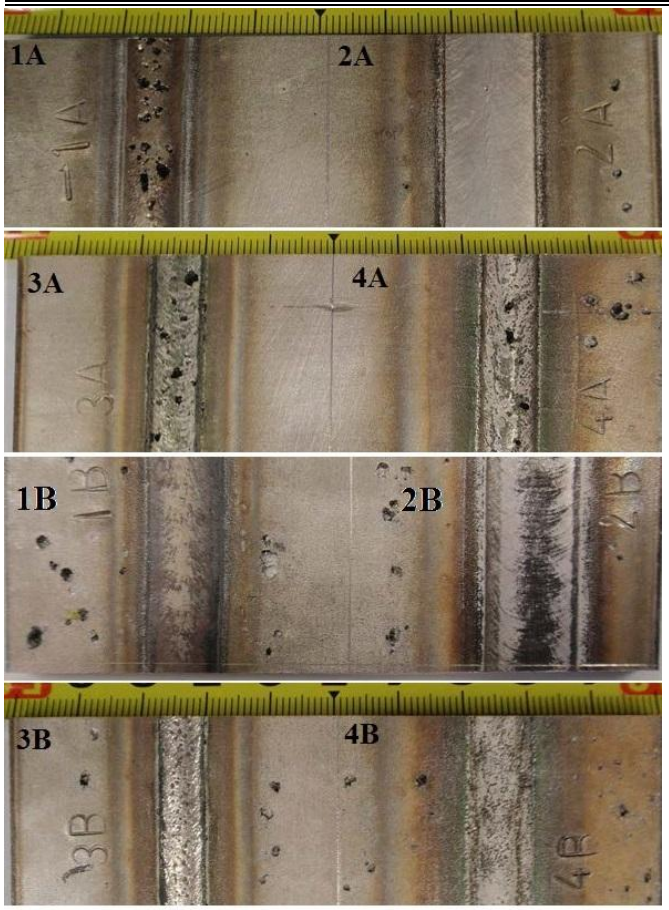

Figure 6. *The appearance of bead on plate welds after 48 hours exposure in aggressive solution*

4. Conclusions

From the obtained results in this investigation the following conclusions can be summarized:

a) When comparing bead on plate width A-TIG welding produces narrower welds in comparison with conventional TIG. The same influence is observed when welding with current 160 A and with 200 A.
b) Appearance of the weld on the face side of samples welded with A-TIG and conventional TIG welding is almost the same and depends only on the guidance of the electric arc.
c) Macrostructure analysis of geometrical features of the produced bead on plate welds has confirmed that A-TIG welding intensifies the penetration and produces narrower and deeper welds. Shielding gasses used in this experiment have small influence on the geometrical features of the produced welded joints. Full penetration has been achieved only in A-TIG welding with 200 A and with welding speed 7,8 cm/min.
d) Transversal tensile testing of the produced welds has confirmed that both shielding gases influence similar on the tensile strength. Measured mechanical properties of the produced welds fulfill requirements of the standard EN 10088-2:2015 for the base material.
e) Corrosion resistance analysis of the produced welds has confirmed a positive effect of mixture shielding gas 2,5 % N_2 and 97,5 % Ar (1B, 2B, 3B and 4B) on increasing resistance to pitting and crevice corrosion. Bead on plate welds made with mixture shielding gas were free of any pits in weld metal and heat affected zone. A-TIG bead on plate welding resulted with less pits (samples 3B and 4B) in comparison with conventional TIG welding (samples 1B and 2B).
f) A-TIG welding is fully applicable technology for welding butt joint of duplex stainless steel in thickness 7 mm, with mixture shielding gas 2,5 % N_2 and 97,5 % Ar, welding speed and current and other constant parameters according to this experiment.

References

[1] Umoru L E, Afonja A A and Ademodi B Corrosion study of AISI 304, AISI 321 and AISI 430 stainless steels in a tar sand digester, Journal of Minerals & Materials Characterization & Engineering, vol. 7, no.4, pp 291-299, 2008.

[2] HRN EN 10088-1:2015, Stainless steels -- Part 1: List of stainless steels

[3] Otokumpu Stainless AB Handbook of Stainless Steel, Avesta Resarch Centre, Avesta, Sweden, 2013.

[4] Davis J R Stainless steels; ASM International, USA, 1994.

[5] Gun R N Duplex stainless steels: microstructure, properties and applications; Woodhead Publishing: Cambridge, UK, 1997.

[6] Chan K W and Tjong S C Effect of secondary phase precipitation on the corrosion behavior of duplex stainless steels, Materials, no. 7, pp. 5268-5304, 2014.

[7] Gideon B, Ward L and Biddle G Duplex stainless steel welds and their susceptibility to intergranular corrosion, Journal of Minerals & Materials Characterization & Engineering, vol. 7, no.3, pp 247-263, 2008.

[8] Gurevich S. M., Zamkov V. N., Kushnirenko N. A., Increase in the efficiency of penetration of titanium alloys in argon arc welding, Avtomatich Svarka, 9, pp 1-5, 1965.

[9] Shyu S W, Huang H Y, Tseng K H and Chou C P Study of the performance of stainless steel A-TIG welds, Journal of Materials Engineering and Performance, vol. 17, no. 2, pp 193-201, 2008.

[10] ISO 9692-1:2013 "Welding and allied processes - Types of joint preparation - Part 1: Manual metal-arc welding, gas-shielded metal-arc welding, gas welding, TIG welding and beam welding of steels

[11] HRN EN 10088-2:2015, Stainless steels -- Part 2: Technical delivery conditions for sheet/plate and strip of corrosion resisting steels for general purposes

[12] Babić N A-TIG welding of duplex steels, Diploma thesis, University of Zagreb, Faculty of Mechanical Engineering and Naval Architecture, 2016.

[13] HRN EN ISO 4136:2013, Destructive tests on welds in metallic materials – Transverse tensile test

[14] ASTM G48 – 03 - Standard test methods for pitting and crevice corrosion resistance of stainless steels and related alloys by use of ferric chloride solution

CALCULATING CONTOURING TOOL BY FINITE DIFFERENCE METHOD

РАСЧЕТ КОНТУРНОГО ИНСТРУМЕНТА МЕТОДОМ КОНЕЧНЫХ РАЗНОСТЕЙ

Prof. Dr. Kikvidze O., Assoc.Prof. Dr.Sakhanberidze N.., Senior teacher Kordzadze L.
Akaki Tsereteli State University, Kutaisi, Georgia
E-mail: kikvidze61@mail.ru , nugzari2555@mail.ru , liakordzadze64@gmail.com

Abstract: During the radial deformation of contouring tool, its active diameter is getting smaller than the initial one, and the cutting depth is becoming lower than planned. Thus, the diametrical size of the machined hole is always smaller than contouring tool, by value of the elastic radial deformation. In this regard, in the manufacture of contouring tool, it is necessary to make appropriate adjustments in the diametrical size of its cutting edge, depending on its elastic radial deformation.

The paper dwells on the thermo-elastic problem of calculating contouring tool for the purpose of determining the actuating diametrical size of its cutting edge, and for determining the area of the application of tool material. Solving of non-dimensional non-stationary problem is carried out by method of finite differences. At each time step, the system of algebraic equations is solved by iterative method.

There have been obtained the results for the temperature field and displacement components.

KEYWORDS: *CONTOUR TOOL, DIAMETRIC CORRECTION, CUTTING FORCES, ELASTIC-RADIAL STRAIN, STRESSES, THERMO-ELASTIC PROBLEM.*

1 . Introduction

In the production process of manufacturing of tubing stocks, the most time-consuming operation is scalping of openings from surface defects. When choosing effective ways of scalping, there are taken into account the defect depth and the nature of technological defects, as well as techno-economic study of the costs of production and waste convertibility. The methods of edge cutting scalping increasingly meet the above requirements [1]. Increase in performance when scalping the openings of tubing stocks from surface defects can be achieved by increasing the width of the cutaway layer, which is restricted only by the rigidity of technological system and does not have a significant impact on durability of the cutting tools [2].

The essence of the method of scalping the openings by a contour tool is that the work-piece 4 (Fig. 1) is fixed immovably on a special machine by means of the specific device and the contour tool 1 with a pusher 2 is moving along the axis of a processing opening. For centering the pusher with a contour tool on a processed surface of opening, the pusher design has the guiding bars 3. A significant feature of this method is that with appropriate selection of processing parameters (section thickness, cutting speed, cutting tool geometry), there are formed the pipe-like chips (flow chips) 5, which are supplied 5to the front of the cutting tool and can be easily removed from the cutting zone. When doing so, the stress state of the contour tool on nature is approaching the scheme of all-round compression, which is a positive factor in terms of increasing its durability.

Testing of this method on various processing materials (a work-piece with a length up to 1000 mm and diameters 60≈70 mm) showed that it is most effective use in the processing of tubing stocksfrom titanium alloys BT 0-0, BT 1-0, PT7M, by a high speed steel tool, at a cutting speed v = 10 m/min,t = 1 mm. Besides, compared with a serial boring technology, the scalping performance increases by 3-5 times.

Removal of the defective surface layer to the desired depth is directly related to the processing accuracy of diametrical dimensions of a contouring tool.

Considering that machining accuracy is influenced by such complex interrelated factors as temperature and cutting force, wear bit, accuracy of machine and so on, then even the slightest increase in machining accuracy poses major difficulties. Therefore, in the manufacture of parts, in technological process there are sought to foresee such operations and cutting modes, in which the negative impact of the above factors on machining accuracy is minimal. And when for technical reasons, it is not possible to eliminate the negative influence of one or another factor on machining accuracy, then the correction enters accounting its influence. Hence, it is impossible to reduce the considerable power loads and the resulting elastic deformations in a technological system when processing the openings of tubing stocks by the contour tool (Fig. 1). It has been established that in this technological operation the contour tool is elastically deformed both in axial and radial directions, while machining accuracy of diametrical dimensions of the openings is affected by radial deformation.

Under radial deformation of the contour tool, its active diameter is getting smaller than the original one, and the cutting depth becomes less than the planned one. Therefore, the diametrical size of the machined opening is always smaller than the size of the contour tool by the magnitude of. In this regard, in the manufacture of the contouring tool, it is necessary to make the appropriate correction on the diametrical size of its cutting edge depending on its elastic radial deformation.

Wear bit has a marked impact on machining accuracy of diametrical sizes. An essential factor influencing on tool wear is a cutting temperature, which should not exceed the red-hardness of tooling material. Therefore, to predict the effective application of the contour tool material by a cutting temperature when processing the tubing stocks from various materials, it is necessary to know the pattern of temperature distribution on the cutting part of the contour tool.

On the basis of the foregoing, there is a need for a methodology of calculation of the stress-strain state of the contour tool during the process of cutting.

Determination of the executing size of the contour tool's cutting edge and the areas of application of tooling material by a cutting temperature with a view to achieving machining accuracy of diametrical sizes, is a practical value of the proposed methodology.

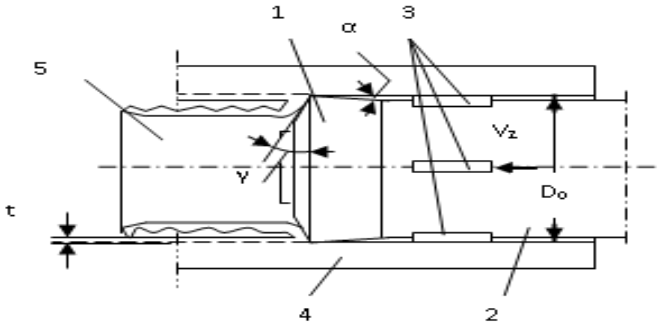

Fig.1. Machining of the opening of the tubing stock by the countour tool:
1-Contour tool; 2- Pusher; 3-Guiding blocks; 4- Work material; 5- Cutting waste

2. Basic Part

2.1 Problem Statement

Consider processing of the inner surface of the tubing stock by the contour tool, which moves at a constant speed using the pusher, and cuts a thin layer (Fig. 1). We assume that, when cutting, the shear stresses reach the limit value, which is specific to the process material, and the pressure is set in the radial and axial directions at the point of contact.

The article [3] describes the basic differential equations of two-dimensional nonstationary thermoelasticity problem for calculating the contour tool:

$$\frac{\partial T}{\partial t}+V_z\frac{\partial T}{\partial z}=a\left(\frac{\partial^2 T}{\partial r^2}+\frac{\partial^2 T}{\partial z^2}+\frac{1}{r}\frac{\partial T}{\partial r}\right)+\frac{\sigma_{ij}\dot{\varepsilon}_{ij}}{c\rho};$$

$$\frac{\partial^2 U}{\partial r^2}+\frac{1}{r}\frac{\partial U}{\partial r}+\frac{1-2\mu}{2(1-\mu)}\frac{\partial^2 U}{\partial Z^2}-\frac{U}{r_2}+\frac{1}{2(1-\mu)}\frac{\partial^2 W}{\partial r\partial Z}-\frac{1+\mu}{1-\mu}\alpha\frac{\partial T}{\partial r}=0;$$

(1)

$$\frac{\partial^2 W}{\partial Z^2}+\frac{1-2\mu}{1-\mu}\frac{\partial^2 W}{\partial r^2}+\frac{1-2\mu}{2r(1-\mu)}\frac{\partial W}{\partial r}+\frac{\partial^2 U}{\partial r\partial Z}+\frac{1}{2r}\frac{\partial U}{\partial Z}-\frac{1+\mu}{1-\mu}\alpha\frac{\partial T}{\partial Z}=0.$$

Initial and boundary conditions:

(2) $\quad T(r,Z,O)=T_0\ ,\quad \frac{\partial T}{\partial r}=-\alpha_0\left(T_*^b-T_0\right)/\lambda$

where $r=d/2, r=D/2$;

$$\frac{\partial T}{\partial Z}=-\alpha_0\left(T_*^T-T_0\right)/\lambda \qquad \text{where } Z=0,l\ ,$$

$r=D/2,\ \sigma_r=P_{a1},\ r=d/2, \sigma_r=P_{a2}$

where: V_z – tool path speed; $a=\lambda/c\rho$; T and T_0 – the tool and ambient temperatures; T_*^T, T_*^b – the temperature on the ends and the side surface of the cutting tool; λ – coefficient of thermal conductivity; c – coefficient of heat capacity; ρ – material density; α_0 – heat-transfer coefficient; U, W – displacements along the axes r and Z, respectively; μ – Poisson ratio; σ_{ij} – stress tensor component; $\varepsilon_{ij}, \dot{\varepsilon}_{ij}$ - strain and strain-rate tensor components; $P_{a1}, P_{a2}, P_{b1}, P_{b2}$ – tool surface pressures; τ_a – shear stress on the external surface; d, D - internal and external diameters of the tool, respectively; l – the width of the tool.

The stress and strain tensor components are determined by the thermoelasticity dependences [4]:

$$\sigma_r=\frac{E}{(1+\mu)(1-2\mu)}\left[(1-\mu)\frac{\partial U}{\partial r}+\mu\left(\frac{\partial W}{\partial Z}+\frac{U}{r}\right)-(1+\mu)\alpha T\right];$$

(4)

$$\sigma_Z=\frac{E}{(1+\mu)(1-2\mu)}\left[(1-\mu)\frac{\partial W}{\partial Z}+\mu\left(\frac{\partial U}{\partial r}+\frac{U}{r}\right)-(1+\mu)\alpha T\right];$$

$$\sigma_\Theta=\frac{E}{(1+\mu)(1-2\mu)}\left[(1-\mu)\frac{U}{r}+\mu\left(\frac{\partial U}{\partial r}+\frac{\partial W}{\partial Z}\right)-(1+\mu)\alpha T\right];$$

$$\tau=\frac{E}{2(1+\mu)}\left(\frac{\partial U}{\partial Z}+\frac{\partial W}{\partial r}\right).$$

(5) $\quad \varepsilon_r=\frac{\partial U}{\partial r};\quad \varepsilon_z=\frac{\partial W}{\partial Z};\quad \varepsilon_\Theta=\frac{U}{r};\quad \gamma=\frac{\partial U}{\partial Z}+\frac{\partial W}{\partial r}.$

$$\frac{\partial U}{\partial r}=\frac{\sigma_r(1+\mu)(1-2\mu)}{E(1-\mu)}-\frac{\mu}{1-\mu}\left(\frac{\partial W}{\partial Z}+\frac{U}{r}\right)+\frac{1+\mu}{1-\mu}\alpha T\ ;$$

where $z=l, \sigma_z=P_{b1}, z=0, \sigma_z=P_{b2}$

(3)

$$\frac{\partial U}{\partial z}=\frac{\sigma_z(1+\mu)(1-2\mu)}{E(1-\mu)}-\frac{\mu}{1-\mu}\left(\frac{\partial W}{\partial r}+\frac{U}{r}\right)+\frac{1+\mu}{1-\mu}\alpha T$$

at the point of contact

$$r=\frac{D}{2};\quad Z=l;$$

$$\frac{\partial U}{\partial r}=\frac{1-\mu^2}{E}\left(P_{a1}-\frac{\mu}{1-\mu}P_{b1}\right)-\mu\frac{U}{r}+(1+\mu)\alpha T;$$

$$\frac{\partial U}{\partial Z}=\frac{2(1+\mu)\tau_a}{E}-\frac{\partial W}{\partial r}\qquad(\tau=\tau_a),$$

With a continuous contour tool on the axis symmetry:

$$r=0;\quad \frac{\partial U}{\partial r}=0;\quad \frac{\partial W}{\partial r}=0;\frac{\partial T}{\partial r}=0,$$

2.2 Solution to the Problem

Integration of a systems of differential equations (1) with initial and boundary conditions (2) and (3) is carried out by finite difference method. The finite difference mesh is shown in Fig. 2.

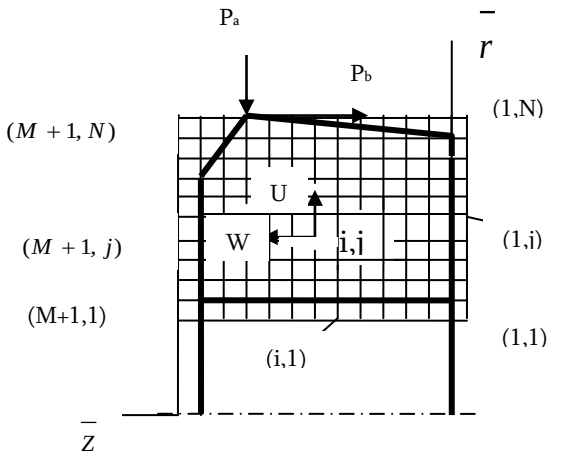

Fig.2 Finite-difference mesh

$$\frac{\partial \bar{T}}{\partial \bar{t}}+\frac{\partial \bar{T}}{\partial \bar{Z}}=\frac{4al}{V_z D^2}\left[\frac{\partial^2 \bar{T}}{\partial \bar{r}^2}+\left(\frac{D}{2l}\right)^2\frac{\partial^2 \bar{T}}{\partial \bar{Z}^2}+\frac{1}{\bar{r}}\frac{\partial \bar{T}}{\partial \bar{r}}\right]+\frac{lE}{V_z T_0}\frac{\bar{\sigma}_{ij}\dot{\bar{\varepsilon}}_{ij}}{c\rho};$$

(6)

$$\frac{\partial^2 \bar{U}}{\partial \bar{r}^2}+\frac{\partial \bar{U}}{\partial \bar{r}}+\frac{(1-2\mu)}{2(1-\mu)}\left(\frac{D}{2l}\right)^2\frac{\partial^2 \bar{U}}{\partial \bar{Z}^2}-\frac{\bar{U}}{\bar{r}^2}+\frac{1}{2(1-\mu)}\frac{D}{2l}\frac{\partial^2 \bar{W}}{\partial \bar{r}\partial \bar{Z}}-\frac{1+\mu}{1-\mu}\frac{\alpha T_0}{2}\frac{\partial \bar{T}}{\partial \bar{r}}=0;$$

$$\frac{\partial^2 \bar{W}}{\partial \bar{Z}^2}+\frac{(1-2\mu)}{1-\mu}\left(\frac{2l}{D}\right)^2\frac{\partial^2 \bar{W}}{\partial \bar{r}^2}+\frac{1-2\mu}{2(1-\mu)}\left(\frac{2l}{D}\right)^2\frac{1}{\bar{r}}\frac{\partial \bar{W}}{\partial \bar{r}}+\frac{2l}{D}\frac{\partial^2 \bar{U}}{\partial \bar{r}\partial \bar{Z}}+\frac{l}{D}\frac{\partial \bar{U}}{\partial \bar{Z}}-\frac{1+\mu}{1-\mu}\alpha T_0\frac{l}{D}\frac{\partial \bar{T}}{\partial \bar{Z}}=0$$

.

(7)

$$\bar{T}\left(\bar{r},\bar{z},0\right)=1;$$

$$\frac{\partial \bar{T}}{\partial \bar{r}}=-\frac{\alpha_0 D}{2\lambda}\left(\bar{T}_*^{\,b}-1\right);\quad \bar{r}=d/D,1;$$

$$\frac{\partial \bar{T}}{\partial \bar{Z}}=-\frac{\alpha_0 l}{\lambda}\left(\bar{T}_*^{\,T}-1\right);\quad \bar{Z}=0;1;$$

(8)

$$\frac{\partial \bar{U}}{\partial \bar{r}}=\frac{(1+\mu)(1-2\mu)}{2(1-\mu)}\bar{P}_a-\frac{\mu}{2(1-\mu)}\left(\frac{D}{l}\frac{\partial \bar{W}}{\partial \bar{Z}}+2\frac{\bar{U}}{\bar{r}}\right)+\frac{1+\mu}{2(1-\mu)}\alpha T_0\bar{T}$$

;

$$\frac{\partial \bar{U}}{\partial \bar{Z}}=\frac{(1+\mu)(1-2\mu)}{2(1-\mu)}\frac{l}{D}\bar{P}_b-\frac{2\mu}{1-\mu}\frac{l}{D}\left(\frac{\partial \bar{U}}{\partial \bar{r}}+\frac{\bar{U}}{\bar{r}}\right)+\frac{1+\mu}{1-\mu}\frac{l}{D}\alpha T_0\bar{T}$$

;

$$\frac{\partial \bar{U}}{\partial \bar{r}}=\frac{1-\mu^2}{2}\left(\bar{P}_a-\frac{\mu}{1-\mu}\bar{P}_b\right)-\mu\frac{\bar{U}}{\bar{r}}+\frac{1+\mu}{2}\alpha T_0\bar{T};$$

$$\bar{r}=1;\quad \bar{Z}=1.$$

$$\bar{r}=0;\ \frac{\partial \bar{U}}{\partial \bar{r}}=0;\quad \frac{\partial \bar{W}}{\partial \bar{r}}=0;\quad \frac{\partial \bar{T}}{\partial \bar{Z}}=0;$$

$$\frac{\partial \bar{U}}{\partial \bar{Z}}=2(1+\mu)\frac{l}{D}\bar{\tau}_a-2\frac{l}{D}\frac{\partial \bar{W}}{\partial \bar{r}}.$$

For the numerical solution, we shall introduce the dimensionless quantities:

$$\bar{T}=T/T_0;\ \ \bar{Z}=Z/l;\ \ \bar{r}=r/\left(D/2\right);\ \ \bar{t}=t/t_0;$$

$$t_0=l_0/V_z;\ \ \bar{U}=U/D;\ \ \bar{W}=W/D;$$

$$\bar{P}_a=P_a/E;\ \ \bar{P}_b=P_b/E;\ \ \bar{\tau}_a=\tau_a/E;\ \ 0\le\bar{Z}\le 1;$$

$$d/D\le\bar{r}\le 1;\quad 0\le\bar{t}\le l_0/l,$$

where l_0 — the length of work material; E — modulus of material elasticity.

In terms of the dimensionless quantities, the above stated equations will take the following form:

For the numerical solution, we use the finite difference schemes [5]:

$$\frac{\partial \bar{U}}{\partial \bar{r}}=\frac{\bar{U}_{i,j+1}-\bar{U}_{i,j-1}}{2\Delta\bar{r}};$$

$$\frac{\partial \bar{U}}{\partial \bar{Z}}=\frac{\bar{U}_{i+1,j}-\bar{U}_{i-1,j}}{2\Delta\bar{Z}};$$

$$\frac{\partial^2 \bar{U}}{\partial \bar{r}^2}=\frac{\bar{U}_{i,j+1}-2\bar{U}_{i,j}+\bar{U}_{i,j-1}}{\Delta\bar{r}^2};$$

$$\frac{\partial^2 \bar{U}}{\partial \bar{Z}^2}=\frac{\bar{U}_{i+1,j}-2\bar{U}_{i,j}+\bar{U}_{i-1,j}}{\Delta\bar{Z}^2};$$

$$\frac{\partial^2 \bar{U}}{\partial \bar{r}\partial \bar{Z}}=\frac{1}{\Delta\bar{r}\Delta\bar{Z}}\left(\bar{U}_{i+1,j+1}+\bar{U}_{i,j}-\bar{U}_{i+1,j}-\bar{U}_{i,j+1}\right).$$

Similar schemes are also used for the functions $\bar{T}$ and $\bar{W}$.

In the finite differences, the differential equations (6) will be written down as follows:

(9)

$$\bar{T}_{i,j}=-\frac{\bar{T}_{i+1,j}-\bar{T}_{i-1,j}}{2\Delta\bar{Z}}+\frac{4al}{V_z D^2}\left[\begin{array}{l}\dfrac{\bar{T}_{i,j+1}-2\bar{T}_{i,j}+\bar{T}_{i,j-1}}{\Delta\bar{r}^2}+\\ +\left(\dfrac{D}{2l}\right)^2\dfrac{\bar{T}_{i+1,j}-2\bar{T}_{i,j}+\bar{T}_{i-1,j}}{\Delta\bar{Z}^2}+\\ +\dfrac{1}{\bar{r}_i}\dfrac{\bar{T}_{i,j+1}-\bar{T}_{i,j-1}}{2\Delta\bar{r}}\end{array}\right]+$$

$$+\frac{lE}{V_z T_0}\frac{\bar{\sigma}_{ij}\dot{\bar{\varepsilon}}_{ij}}{c\rho};$$

$$\overline{U}_{i,j} = \{ \frac{\overline{U}_{i,j+1} + \overline{U}_{i,j-1}}{\Delta\bar{r}^2} + \frac{\overline{U}_{i,j+1} - \overline{U}_{i,j-1}}{2\Delta\bar{r}} +$$

$$\frac{1-2\mu}{2(1-\mu)}\left(\frac{D}{2l}\right)^2 \frac{\overline{U}_{i+1,j} + \overline{U}_{i-1,j}}{\Delta\bar{Z}^2} + \frac{1}{2(1-\mu)}\frac{D}{2l}\frac{1}{\Delta\bar{Z}\Delta\bar{r}} \times$$

$$\times\left(\overline{W}_{i+1,j+1} + \overline{W}i,j - \overline{W}_{i+1,j} - \overline{W}_{i,j+1}\right) - \frac{1+\mu}{1-\mu}\frac{\alpha T_0}{2}\frac{\overline{T}_{i,j+1} - \overline{T}_{i,j-1}}{2\Delta\bar{r}} \}/$$

$$[\frac{2}{\Delta\bar{r}^2} + \frac{1}{\bar{r}_i^2} + \frac{1}{\Delta\bar{Z}^2}\frac{1-2\mu}{1-\mu} \times \left(\frac{D}{2l}\right)^2];$$

$$\overline{W}_{i,j} = \{\frac{\overline{W}_{i+1,j} + \overline{W}_{i-1,j}}{\Delta\bar{Z}^2} + \frac{1-2\mu}{2(1-\mu)}\left(\frac{2l}{D}\right)^2 \frac{1}{\bar{r}_i}\frac{\overline{W}_{i,j+1} - \overline{W}_{i,j-1}}{2\Delta\bar{r}} + \frac{1-2\mu}{1-\mu}\left(\frac{2l}{D}\right)^2 \frac{\overline{W}_{i,j+1} + \overline{W}_{i,j-1}}{\Delta\bar{r}^2} +$$

$$+\frac{2l}{D}\frac{1}{\Delta\bar{Z}\Delta\bar{r}}\left(\overline{U}_{i+1,j+1} + \overline{U}_{i,j} - \overline{U}_{i+1,j} - \overline{U}_{i,j+1}\right) + \frac{l}{D}\frac{\overline{U}_{i+1,j} - \overline{U}_{i-1,j}}{2\Delta\bar{Z}} - \frac{1+\mu}{1-\mu}\alpha T_0\frac{l}{D}$$

$$\text{x}\ \frac{\overline{T}_{i+1,j} - \overline{T}_{i-1,j}}{2\Delta\bar{Z}}\} /$$

$$/[\frac{2}{\Delta\bar{Z}^2} + \frac{2(1-2\mu)}{(1-\mu)\Delta\bar{r}^2}\left(\frac{2l}{D}\right)^2].$$

Initial and boundary conditions in the finite differences:

$$\overline{T}_{i,j}(0) = 1;$$

$$\bar{r} = 0; \quad \overline{T}_{i,j-1} = \overline{T}_{i,j+1}; \quad \overline{U}_{i,j-1} = \overline{U}_{i,j+1};$$

$$\overline{W}_{i,j-1} = \overline{W}_{i,j+1};$$

$$\bar{r} = 1; \quad \overline{T}_{i,j+1} = \overline{T}_{i,j} - \frac{\alpha_0 D\Delta\bar{t}}{2\lambda}\left(\overline{T}_{i,j} - 1\right);$$

$$\bar{Z} = 0; \quad \overline{T}_{i-1,j} = \overline{T}_{i+1,j} - \frac{\alpha_0 l}{\lambda}2\Delta\bar{Z}\left(\overline{T}_{i,j} - 1\right);$$

$$\bar{Z} = 1; \quad \overline{T}_{i+1,j} = \overline{T}_{i-1,j} - \frac{\alpha_0 l}{\lambda}2\Delta\bar{Z}\left(\overline{T}_{i,j} - 1\right);$$

$$\bar{r} = 1; \quad \overline{U}_{i,j+1} = \overline{U}_{i,j-1} + 2\Delta\bar{r}$$

$$[\frac{(1+\mu)(1-2\mu)}{2(1-\mu)}\overline{P}_a - \frac{\mu}{2(1-\mu)}\left(\frac{l}{D}\frac{\overline{W}_{i+1,j} - \overline{W}_{i-1,j}}{2\Delta\bar{Z}} + 2\frac{\overline{U}_{i,j}}{\bar{r}_i}\right) +$$

At the beginning of time integration, as a zero approximation by the coordinates of the functions $\overline{U}$ and $\overline{W}$, we shall will take the linear dependences, and for the temperature, we shall take adopt a uniform distribution. At each time step, the system of algebraic equations is solved by an iterative method, the strain rates deformation on the right side of the first equation (9) is determined as $\dot{\varepsilon}_{ij} = \left(\varepsilon^{k}_{i,j} - \varepsilon^{k-1}_{i,j}\right)/\Delta\bar{t}$, where the values $\varepsilon^{k-1}_{i,j}$ are taken from previous time step.

The stress-strain state and the temperture field of the contour tool were calculated during maching the openings of the tubing stocks from titanium alloy BT1-0, by means of the contour tool made of high-speed steel P6M5, for which the values are as follows:

$$+\frac{1+\mu}{2(1-\mu)}\alpha T_0\overline{T}_{i,j}]; \tag{10}$$

$$\bar{Z} = 0; \quad \overline{U}_{i-1,j} = \overline{U}_{i+1,j} - 2\Delta\bar{Z}\left[2(1+\eta)\frac{l}{D}\bar{\tau}_a - 2\frac{l}{D}\frac{\overline{W}_{i,j+1} - \overline{W}_{i,j-1}}{2\Delta\bar{r}}\right];$$

$$\overline{W}_{i-1,j} = \overline{W}_{i+1,j} - 2\Delta\bar{Z}[\frac{(1+\mu)(1-2\eta)}{1-\mu}\frac{l}{D}\overline{P}_b - \frac{2\mu}{1-\mu}\frac{l}{D}\left(\frac{\overline{U}_{i,j+1} - \overline{U}_{i,j-1}}{2\Delta\bar{r}} + \frac{\overline{U}_{i,j}}{r_i}\right) +$$

$$+\frac{1+\mu}{1-\mu}\frac{l}{D}\alpha T_0\overline{T}_{i,j}];$$

$$\bar{Z} = 1; \quad \overline{U}_{i+1,j} = \overline{U}_{i-1,j} + 2\Delta\bar{Z}\left[2(1+\eta)\frac{l}{D}\bar{\tau}_a - 2\frac{l}{D}\frac{\overline{W}_{i,j+1} - \overline{W}_{i,j-1}}{2\Delta\bar{r}}\right];$$

$$\overline{W}_{i+1,j} = \overline{W}_{i-1,j} + 2\Delta\bar{Z}[\frac{(1+\mu)(1-2\eta)}{1-\mu}\frac{l}{D}\overline{P}_b - \frac{2\mu}{1-\mu}\frac{l}{D}\left(\frac{\overline{U}_{i,j+1} - \overline{U}_{i,j-1}}{2\Delta\bar{r}} + \frac{\overline{U}_{i,j}}{r_i}\right) +$$

$$+\frac{1+\mu}{1-\mu}\frac{l}{D}\alpha T_0\overline{T}_{i,j}];$$

$$\bar{r} = 1;$$

$$\frac{\overline{U}_{i+1,j} - \overline{U}_{i-1,j}}{2\Delta\bar{Z}} = 2(1+\mu)\frac{l}{D}\bar{\tau}_a - 2\frac{l}{D}\frac{\overline{W}_{i,j+1} - \overline{W}_{i,j-1}}{2\Delta\bar{r}};$$

$$\overline{W}_{i,j+1} = \overline{W}_{i,j-1} + \frac{D\Delta\bar{r}}{l}\left[2(1+\mu)\frac{l}{D}\bar{\tau}_a - \frac{\overline{U}_{i+1,j} - \overline{U}_{i-1,j}}{2\Delta\bar{r}}\right];$$

$$\bar{r} = 1; \quad \bar{Z} = 1; \quad \overline{U}_{i,j+1} = \overline{U}_{i,j-1} + 2\Delta\bar{r}$$

$$[\frac{1-\mu^2}{2}\left(\overline{P}_a - \frac{\mu}{1-\mu}\overline{P}_b\right) - \mu\frac{\overline{U}_{i,j}}{\bar{r}_i} + \frac{1+\mu}{2}\alpha T_0\overline{T}_{i,j}],$$

where $\Delta\bar{r} = 1/(n-1)$; $\Delta\bar{Z} = 1/(m-1)$; n, m – number of points of dividing along the axes r and Z, respectively.

$c = 0.14$ J/kg/K; $\rho = 8.0\times10^3$ kg/m^3; $\lambda = 0.065$ J/m.sec.K; $\mu = 0.32$; $E = 224200$ n/mm^2.; $\alpha_0 = 17$ W/(m^2 k).; cutting speed $V_z = 3.5$ m/min; machining diameter $D = 50$ mm.; cutting depth $t = 1$ mm.; the width of the tool $l = 20$ mm.; the length of work material $l_0 = 400$ mm.; radial component of cutting force $P_a = 900$ n/mm.; axial component of cutting force $P_b = 1500$ н/мм.; front clearance angle of the tool $\gamma = -15^0$, back clearance angle $\alpha = 2^0$.

3 . Analysis of the Results

Calculation results (Fig. 3) demonstrate that the temperature of the cutting tool near the contact surface reaches a maximum value of about 300^0C, i.e. is below the red-hardness of tooling material under consideration ($620\ ^0$C) and decreases slowly until $\bar{r} = 0.85$.

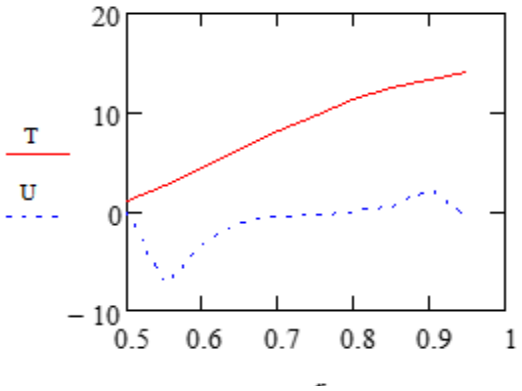

Fig.3. The results of the calculated temperature fiueld ($\overline{T}$) and radial displacement ($\overline{U}10^3$)

Within $\bar{r} = 0.5 - 0.85$, temperature delivers more intensively by the linear principle. The above stated circumstance allows using effectively this tooling material for the given technological operation. The reliability of the obtained results of the temperature study the machinning process with the contour tool, is proved by identical values of theoretical calculations ($300^0 C$) and experimental data ($285^0 C$). The radial displacements are mostly negative and accordingly, the point are moved toward the center of the tool. However, near the contact surface, there are also produced the slightly positive displacements.

In this example (Fig. 3), the value of a diametric correction $\Delta K = 2U$, the radial diplacements of the cutting edge of the contour tool U = 0.001mm. Therefore, with a machining diameter D = 50 mm, the executing size of the contour tool's cutting edge is $D_K = D + \Delta K = 50 + 0.002 = 50.002$ mm.

4. Conclusion

1. When machining the openings of the tubing stocks by the contouring tool, to study the stress-strain state of the tool, it is advisable to consider the associated thermoelasticity problem, which is solved by a finite difference method.
2. The application of the proposed methodology in practice, the known variables (the geometry of the cutting tool (γ, α), components of cutting forces ($P_a . P_b$), cutting mode elements (V, t), as well as physical-mechanical properties of tooling material), will provide an opportunity for determining the executing size of the contour tool for a a specific size machining and the area of applicatuon of tooling material, by the above mentioned algorithm.

5. Literature

1Sozinov A.I., Strazhkov A.N.. Improving the efficiency of roughing machining of work-pieces from titanium alloys. M.: MEATALLURGIA publishers, 1990, 206 p.
2. Loladze T.N.. Strength and durability of the cutting tools. M.: MASHINOSTROYENIE publishers, 1982, 320 p.
3. Kikvidze O., Sakhanberidze N.: The stress-strain state of the annular cutting tool in machining the openings. Science and Technology. Monthly scientific peer-riviewed journal of the national Academy of Sciences of Georgia, No 10-12, 2009. p. 60-64.
4. Nowacki W. Theory of elasticity. - M.: MIR. 1975.-872 p.
5. Turchak L.I.. Fundamentals of numerical methods. M.: NAUKA publishers, 1987.-317 p.

AN EXPERIMENTAL STUDY FOR THERMAL AND HYDRAULIC PERFORMANCE OF A MINI CHANNEL SHELL AND TUBE HEAT EXCHANGER USING LOW CONCENTRATION NANOFLUIDS PREPARED WITH AL_2O_3 NANOMATERIALS

M.Sc. Mehmet Senan Yilmaz [1,2], Assist. Prof. PhD. Hasan Kucuk [2], Res. Assist. PhD. Murat Unverdi [2,*]
Vocational School of Gerede, Abant I.B. University, 14900 Gerede, Bolu, Turkey [1]
Faculty of Engineering, Department of Mechanical Engineering, Sakarya University 54050 Serdivan, Sakarya, Turkey [2]

yilmaz_m1@ibu.edu.tr, kucuk@sakarya.edu.tr, [*]muratunverdi@gmail.com (Corresponding author)

Abstract: *In this study, tube side thermal and hydraulic performance of a mini channel shell and tube heat exchanger (MC-STHE) designed using Kern method was investigated experimentally for water and α-Al_2O_3/water nanofluids prepared in two different low volume fractions (0.02% and 0.2%). The average particle diameter of Al_2O_3 nanomaterial used in the preparation of nanofluids is 50 nm. The copper tubes (L/D=120) with inner diameter of 2 mm and outer diameter of 3 mm and a length of 240 mm were used in the MC-STHE. During the experiments, shell side water flow rate was kept constant at 180 L/h, while the water and nanofluids flow rates on the tube side were changed between 60-600 L/h. The use of nanofluids in the MC-STHE deteriorates tube side convective heat transfer coefficient in the flow rates below 125 L/h, while enhancing convective heat transfer coefficient in the flow rates above 125 L/h, compared to water. The enhancement ratios for convective heat transfer coefficient compared to water were found to be 0.82-1.66 for 0.02% Al_2O_3/water and 0.9-1.74 for 0.2% Al_2O_3/water in the range of 60-600 L/h volume flow rates. However, in the applications in which enhancement of the heat transfer is desired, it was obtained that the increase in pumping power should be taken into consideration depending on the selected nanofluids volume fraction. According to efficiency index in which increase in heat transfer and pressure drop compared to water are evaluated together, it was found that the use of nanofluids was significant in the flow rates above 375 L/h for 0.02% Al_2O_3/water and in the flow rates above 300 L/h for 0.2% Al_2O_3/water. The use of mini-channel increased the compactness by decreasing the weight and volume of the heat exchanger, and in addition to this, higher heat transfer coefficients were obtained by using nanofluids instead of water.*

Keywords: MINI CHANNEL SHELL AND TUBE HEAT EXCHANGER, LOW CONCENTRATION AL_2O_3/WATER NANOFLUIDS, CONVECTIVE HEAT TRANSFER COEFFICIENT, HEAT TRANSFER, PUMPING POWER, KERN METHOD

1. Introduction

Due to the limited energy resources and ever-increasing energy demand, systems with high energy efficiency are gaining importance. It is also known that miniaturized manufacturing, which show a tendency of continuous decrease in the dimensions of devices (such as shell and tube heat exchanger and plate heat exchanger) that exchange thermal energy have been popular in recent years. In other words, interest in small sized and high efficiency heat exchangers is increasing day by day. The importance of heat transfer enhancement techniques can be better understood by considering the coercive conditions for satisfying energy demands at the same thermal powers using thermal energy sources of the same and/or lower temperature by heat exchangers produced with less material and operating with less working fluid. Some of these heat transfer enhancement techniques are passive methods not require external power such as increasing the heat transfer area (corrugated and finned surfaces), roughening of surfaces, solid additives for liquids (e.g. addition of nano-material), while others are active methods require external power such as producing turbulence and/or promoting turbulence intensity, vibrating the surface, and vibrating the fluid **[1,2]**.

The heat transfer area per unit volume in heat exchangers is referred to compactness. In other words, when smaller hydraulic diameter channels are used in a heat exchanger, the surface area that can be used for heat transfer is also increased. The main goal in terms of thermally and hydraulically in compact heat exchangers is to minimize the total cost by reducing physical dimensions of the heat exchanger for a given thermal power under defined temperature limitations, and to make the heat exchange between the two fluids more efficient. If the hydraulic diameter of tube used in shell and tube heat exchangers is below 5 mm, such heat exchangers are considered as compact. Depending on the application, the total heat transfer coefficient is increased, while the required surface area can be reduced by using flat or augmented heat transfer surfaces in heat exchangers. Thus, higher thermal power transmissions are obtained without changing the defined thermal conditions. Heat exchangers have been used in many industrial plants and applications such as oil refineries, thermal and geothermal power plants, and chemical industry etc. Although there are variously designed heat exchangers, the shell and tube heat exchangers are the most preferred type because they are cheap, easy to manufacture and to maintain **[3-7]**.

One of the passive heat transfer enhancement techniques is the addition of solid materials (micro- and nano-sized particles) in a certain proportions to commonly used working fluids (such as water, oil, ethylene glycol). Thus, the working fluids commonly used in heat exchangers are converted into suspensions with improved thermophysical properties. These suspensions, referred to nanofluids, find new applications every day. High thermal conductivity, which is important in terms of heat transfer from the changing thermophysical properties (specific heat, density, heat conduction coefficient and viscosity) of the fluid and the other mechanisms specific to nanofluids that facilitate the diffusion of heat in the fluid, increase the convective heat transfer coefficient. With the developing technology, production of solid materials (particles) with small dimensions in the nanometer range is becoming widespread and their costs are constantly decreasing.

Micro materials have disadvantages when compared to nano materials, such as faster sedimentation, 1000 times smaller surface/volume ratios, lower thermal conductivity when added to liquids at the same concentration, clogging of very small diameter (micro) channels, more mechanical wear on contact surfaces and more increase in pumping power. When using with very small solid material sizes and small volume fractions, the importance of problems such as clogging and increased pumping power are less for nanofluids prepared from nano-materials. Furthermore, the large surface area of nanoparticles increases their stability in the fluids and slows down the sedimentation. Colloid mixtures formed by the addition of nano-sized solid materials into the fluid are referred to nanofluids. The higher heat transfer rates are obtained with nanofluids compared to commonly used working fluids. These fluids are becoming increasingly popular in many applications, such as nuclear reactors, engines of vehicles, air conditioning systems, processors of mobile phones and computers (smart liquids) and even to the cooling of equipment with high thermal density such as medical devices. The enhancement effects of nanofluids on heat transfer coefficients can be summarized as follows **[8-11]**.

- The high surface area/volume ratio of suspended nano-materials in the fluid increases the thermal capacity and the effective thermal conductivity of the fluid.
- The collisions of nano-materials with each other and with the contact surfaces also increases the intensity of interactions for the working fluid molecules with each other and with the contact surfaces.
- The turbulence intensity and irregular fluctuations in the flow are increasing.
- Random scattering of nano-materials in the fluid contributes to the flattening of the temperature gradient in the direction perpendicular to the flow.

Large hydraulic diameter tubes commonly used in the shell and tube heat exchangers also increase the amount of fluid needed for operation. The use of working fluid can be reduced by decreasing the hydraulic diameters of the tubes. However, nanofluids increase the risk of clogging by clumping and/or agglomerating in micro and nano channels and this makes mini channels the most suitable alternative for nanofluids applications. In addition, the use of mini channels in the shell and tube heat exchangers has additional advantages, such as reduction of the dimensions, minimizing space and reduction in weight, as well as increasing thermal efficiency and compactness. The thermal efficiency of the heat exchanger can be further increased if these factors are supported by the use of nanofluids as a working fluid. Mini channels, both reduce dimensions of heat exchangers and the amount of working fluid used and so energy, material and cost savings can be achieved. Depending on the hydraulic diameter used in the flow channels, the mini channel definition range is 3 mm ≥D> 200 μm according to Kandlikar and Grande, whereas it is 6 mm ≥D> 1 mm according to Mehendale et al **[12-14]**. Some of studies used nanofluids in the shell and tube heat exchangers were summarized below.

Arunachala et al. investigated experimentally heat transfer on the shell and tube sides by using water and 4 different concentrations (0.5%, 1%, 1.5%, 2%) of Al_2O_3/water nanofluids (average material diameter of 40 nm) in the shell and tube heat exchanger. The tube length of the heat exchanger is 1000 mm, the outer diameter of tube is 13 mm, the wall thickness is 1 mm and the tube arrangement (tube pitch ratio 1.5) is square. The shell of the heat exchanger made of PVC has a length of 1100 mm, an outer diameter of 63 mm and a wall thickness of 5 mm and the baffle cut ratio is 25%. In the experiments where nanofluids for 2% volumetric concentration and tube-shell side flow rates were kept constant at 1-2, 2-3 and 3-4 L/m, heat transfer enhancement compared to water was reported to be 34%, 44.8% and 57.6% respectively, in the laminar flow (695<Re<1936) conditions **[15]**.

Ramesh and Vivekananthan experimentally studied the heat transfer in a shell and tube heat exchanger using γ-Al_2O_3/water (average material diameter of 20 nm) nanofluids and ethylene glycol. In the experiments performed at 6 different volumetric concentrations (0.2%, 0.5%, 1%, 1.5%, 2% and 2.5%), it was stated that there was an enhancement in the convective heat transfer coefficient as the nanofluids concentration increases. But a decrease in the convective heat transfer coefficient was reported after 2.5% volumetric concentration, compared to ethylene glycol and water **[16]**.

Farajollahi et. al. investigated experimentally tube side thermal performance of γ-Al_2O_3/water (average material diameter of 25 nm and 0.3%, 0.5%, 0.75%, 1%, 2% volume concentrations) and Ti_2O/water (average material diameter of 10 nm and 0.15%, 0.3%, 0.5%, 0.75% volume concentrations) nanofluids in a shell and tube heat exchanger made of stainless steel under turbulent flow (20,000<Pe<70,000) conditions. They used a single tube-pass heat exchanger with 16-tubes and a tube pitch of 8 mm. The wall thickness of stainless steel tubes was 1 mm with an outer diameter of 6.1 mm and a length of 815 mm. The shell inner diameter is 55.6 mm, the distance between the baffles is 50.8 mm and cut of baffles is 25%. The researchers found that the overall heat transfer coefficients in the water to water experiments were consistent with Gnielinski correlation. Besides, the use of 0.5% Al_2O_3/water and 0.3% Ti_2O/water nanofluids on the tube side have been reported that there were enhanced convective heat transfer coefficient more than 50% compared to water **[17]**.

Godson et al. studied experimentally tube side heat transfer from 3 different volumetric fractions (0.01%, 0.03% and 0.04%) of hot silver/water (average material diameter of 54 nm) nanofluids to cold water in a single pass shell and tube heat exchanger with counter flow, in the range of Reynolds 5000-25,000. In the heat exchanger where 25 copper tubes are used, inner diameter of the tubes is 4 mm, while the outer diameter is 6 mm and the length (L/D≅175) is 700 mm. The shell made of stainless steel had an inner diameter of 150 mm and an outer diameter of 200 mm. The researchers found that Nusselt numbers obtained from water to water experiments were consistent with the Dittus-Boelter correlation with a ±9.2% difference. In addition when used nanofluids instead of water, convective heat transfer coefficient was augmented 9.2%, 10.87% and 12.4% for 0.01%, 0.03% and 0.04% volume fractions respectively and also they stated that pumping power increased with increase in the volume fraction and viscosity of the nanofluids **[18]**.

Mapa and Mazhar experimentally investigated tube side heat transfer of a MC-STHE with an inner diameter of 2.4 mm, wall thickness of 0.25 mm, and length of 248 mm (L/D≅103) and manufactured from 37 stainless steel tubes. They studied heat transfer from the hot water and hot copper-oxide/water nanofluid at two different volume fractions of 0.01% and 0.02% (average material diameter of 29 nm) passing through the tube (50<Re<450) to the cold water on the shell side. Researchers stated that the nanofluids enhanced heat transfer and the presence of nano-materials in the fluid thinned the thermal boundary layer, but the thermal power did not increase after Reynolds 200 **[19]**.

In this study, the tube side thermal and hydraulic performances of water and two different low volume fractions Al_2O_3/water (0.02% and 0.2%) nanofluids were investigated experimentally in a MC-STHE designed based on Kern method and Kandlikar and Grande mini channel approach. The experiments were carried out with hot water on the shell side and cold water and cold nanofluids on the tube side in the MC-STHE. The average particle diameter of the Al_2O_3 nanomaterial used in the preparation of the nanofluids is 50 nm. During the experiments, shell side flow rate was kept constant at 180 L/h, while the tube side flow rate was changed between 60-600 L/h. The enhancement and deterioration effects in convective heat transfer and hydraulic performance for the use of nanofluids instead of water on the tube side of MC-STHE were experimentally investigated and discussed.

2. Experimental setup

The inner and the outer diameters of the tubes used in MC-STHE which thermal and hydraulic performance investigated experimentally were 2 mm and 3 mm respectively. The rotated equilateral triangular tube arrangement ($p_t = 1.5\ D_o$) having a higher heat transfer coefficient on the shell side was preferred in the design of tube bundle. A total of 13 tubes were used in the tube bundle and L/D ratio was selected as 120 in determining the tube lengths. 4 baffles with 25% baffle cut were used on the shell side. The material of the shell and baffle plates is cast cestamide, while the material of tubes is copper. The experiments have been carried out under steady state and at the room temperature. A schematic drawing of the experimental setup and photo of the test section were presented in Fig. 1. In the experimental setup, there are two cycles that heat removed (hot fluid) and heat absorbed (nanofluids). The flow rates of hot and cold fluids were measured by float type flow meters (rotameters) and measurement accuracy of the flow meters was controlled by weighted vessel method.

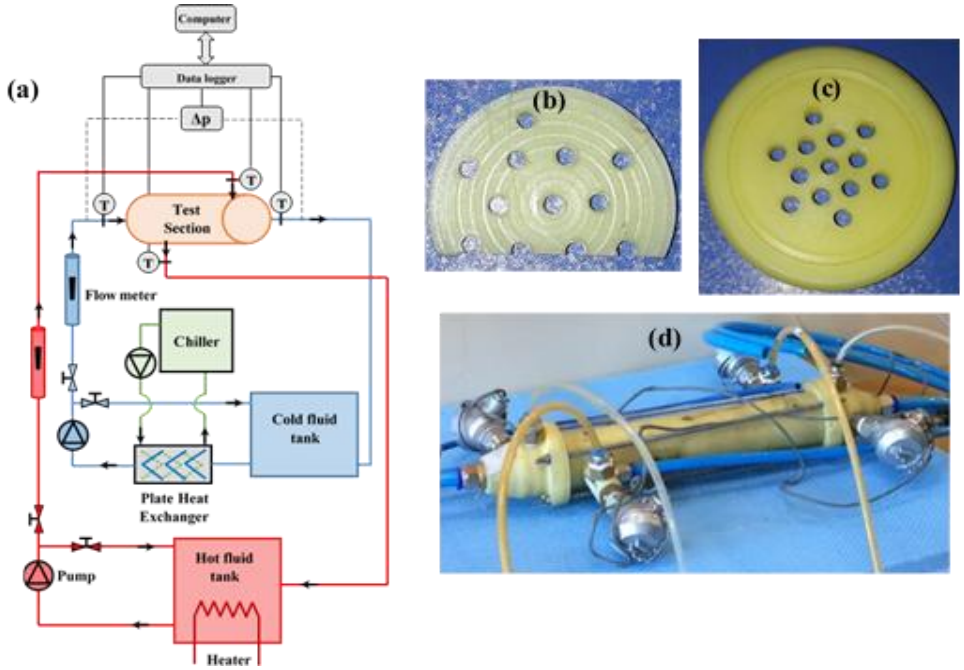

Fig. 1 *(a) Schematic of experimental setup (b) Baffle (25% baffle cut) (c) Tube sheet (d) Test section.*

The fluid inlet and outlet temperatures at the test section was measured by K-type thermocouples, which were checked the measurement accuracy in an ice-water bath. The pressure drop on the tube side, in which the thermal and hydraulic performance was investigated, was measured by a digital differential pressure gauge and the measurement accuracy checked with a mercury U-manometer. The shell side (hot fluid) flow rate and the inlet temperature were kept constant at 180 L/h and 40°C, respectively. While the tube side (water and nanofluids) flow rate was changed between 60-600 L/h and the inlet temperature was kept constant at 20°C. During the experiments, flow rate, differential pressure and temperature measurements were saved on computer. Detailed information about the experimental setup, Kern method and the design of MC-STHE is given in Ref. **[20]**.

3. Preparation and thermophysical properties of nanofluids

It is known from literature that the researchers prefer two step method which is a more stable and more reliable method in the preparation of nanofluids. In this method, previously prepared or supplied nano material powders can be added to working fluid in the desired proportions (volume or mass fractions) **[2, 21]**. In this study, α-Al_2O_3 nano materials with a purity rate of 99% and an average particle size of 50 nm were used. In order to prevent agglomeration of the nano materials according to two-step method and to obtain a stable structure in the nanofluids, the nano materials added to pure water were mixed in an ultrasonic mixer for 3 hours at room temperature. In addition, the nanofluids were transferred into a continuously operated mechanical stirrer during the experiments and the sedimentation of nano materials was prevented. In this study, Al_2O_3/water nanofluids were prepared at two different low volume fractions of 0.02% and 0.2%.

The preferred expressions for the calculation of Al_2O_3/water nanofluids thermophysical properties used in the experimental study are as follows.

Analytically obtained density expression which was confirmed with experimental studies carried out at room temperature for Al_2O_3 nanofluids by Pak and Cho **[22]** and Ho et al **[23]**:

$$\rho_{nf} = (1-\theta)\rho_w + \theta\rho_{nm} \tag{1}$$

Nanofluids specific heat which was analytically obtained and confirmed by experimental studies performed by Zhou and Ni **[24]** for Al_2O_3/water nanofluid at room temperature:

$$c_{p,nf} = \frac{(1-\theta)\rho_w c_{p,w} + \theta\rho_{np} c_{p,nm}}{\rho_{nf}} \tag{2}$$

There are many different expressions for thermal conductivity and viscosity of nanofluids in the literature. In this study, the simplest and most commonly used expressions suitable for Al_2O_3/water nanofluids and low volume fractions (<0.5%) were preferred.

Thermal conductivity expression for Al_2O_3/water nanofluids by Timofieeva et al **[25]**:

$$k_{nf} = (1+3\theta)k_w \tag{3}$$

Nanofluid viscosity, referred Einstein equation **[26]**, used for nanofluids with volume fractions of less than 2%.

$$\mu_{nf} = (1+2.5\theta)\mu_w \tag{4}$$

In the above expressions, the subscripts nf, nm, w and θ refer to nanofluid, nano material and base fluid water, and a volume fraction of nanofluids, respectively. The thermophysical properties of water are calculated from the expressions given for the temperature range 0-100°C in Ref. **[27]**.

4. Thermal and hydraulic performance calculations

The equations used in the calculation of experimental thermal and hydraulic performance in the MC-STHE prototype designed using Kern method are as follows.

Thermal powers for hot fluid and cold fluid (nanofluid):

$$Q_h = \dot{m}_h c_{p,h}(T_{h,i} - T_{h,o}) \tag{5}$$

$$Q_{nf} = \dot{m}_{nf} c_{p,nf}(T_{nf,o} - T_{nf,i}) \tag{6}$$

Here, the subscripts nf and h refer to cold nanofluids on the tube side and hot water on the shell side, respectively, $\dot{m}_h$ and $\dot{m}_{nf}$ to mass flow rates, $c_{p,h}$ and $c_{p,nf}$ to specific heats, $T_{h,o}$, $T_{nf,o}$ to outlet temperatures, $T_{h,i}$, $T_{nf,i}$ to inlet temperatures. Average thermal power in the MC-STHE:

$$Q_{ave.} = (Q_h + Q_{nf})/2 \tag{7}$$

$$Q_{ave.} = UAF\Delta T_{lm} \tag{8}$$

Here, U refers to overall heat transfer coefficient, A to heat transfer surface area, F to non-dimensional correction factor for logarithmic mean temperature difference and ΔT_{lm} to a logarithmic mean temperature difference. When TEMA (Tubular Exchanger Manufacturers Association) E-type single shell and single tube pass and more than three or four baffles are used, heat exchangers are regarded as counter flow, hence F=1 **[28]**.

Logarithmic mean temperature difference for counter flow:

$$\Delta T_{lm} = \frac{\left(T_{h,i} - T_{c,o}\right)\left(T_{h,o} - T_{c,i}\right)}{In\left[\left(T_{h,i} - T_{c,o}\right)/\left(T_{h,o} - T_{c,i}\right)\right]} \quad (9)$$

Convective heat transfer coefficient for shell side (hot water) according to Kern method **[29]**:

$$h_h = k\, j_h\ \mathrm{Re}\ \mathrm{Pr}^{1/3}/D_e \quad (10)$$

Here, j_h is obtained from graphs proposed by Kern, depending on the baffle cut used on the shell side, tube arrangement and the Reynolds number. Overall heat transfer coefficient (U_i) according to inner surface of tubes with circular cross section:

$$\frac{1}{U_i} = \frac{1}{h_h} + \frac{D_i}{2k_t}\ln\frac{D_o}{D_i} + \frac{D_i}{D_o h_{nf}} \quad (11)$$

The tube side convective heat transfer coefficient for nanofluid h_{nf} is calculated by the above equation. The pumping power selected as hydraulic performance criterion **[30]**:

$$W_p = \dot{\forall}\Delta p \quad (12)$$

Here, $\dot{\forall}$ is the volume flow rate, and Δp is the pressure drop between the inlet and outlet of the tubes. Efficiency index, in which increase in heat transfer and pressure drop compared to water is calculated together, defined in order to evaluate enhancement in heat transfer by using nanofluids at similar Reynolds numbers **[1]**:

$$\eta_e \equiv \left(j_{nf}/j_w\right)/\left(f_{nf}/f_w\right) \quad (13)$$

5. Uncertainty analysis

Measurement uncertainties may occur due to sensitivities of measurement equipment used in the experimental study, the accuracy of measurement, reading error of the experimenter, ambient conditions (such as heat, light, humidity and electronic oscillations) and error ratios of the equipment. The uncertainties in the experimental results were calculated using the method proposed by Kline and McClintock **[31]**. Relative errors of the measuring equipment used in the experimental setup are 4% for the flow meter and 1% for the thermocouples. The results of the average uncertainty calculated were given in Tab. 1.

6. Result and discussion

The prototype of a MC-STHE designed for an average thermal power of 1-1.5 kW using Kern method was manufactured in Gerede Vocational School workshop. Water to water test experiments were carried out to check the accuracy of measurements with experimental setup, before the thermal and hydraulic performance measurements for water and nanofluids in the MC-STHE. While the heat exchanger was very well insulated against the surroundings during the experiments, it was observed that there were heat losses and thermal power differences between the shell side and tube side. In the final experiments with prepared nanofluids and water, the average thermal power differences between the shell and tube sides were approximately 7%. The overall heat transfer coefficient (U) for water and nanofluids was obtained from Eq. (8), and the shell side convective heat transfer coefficient was obtained from Eq. (10) and, experimental convective heat transfer coefficients for water and nanofluids on the tube side from Eq. 11 were obtained.

In case of the shell side flow rate is kept constant at 180 L/h, the change of experimental convective heat transfer coefficients, heat transfer enhancement ratios, efficiency indexes and pumping powers obtained in the range of 60-600 L/h flow rates for water and nanofluids on the tube side has been shown in Fig. 2-5 depending on the volume flow rates.

Table 1: *Uncertainty result.*

	Average uncertainty (%)		
	Water	0.02% Al_2O_3/water	0.2% Al_2O_3/water
Reynolds number	1.38	1.37	1.26
Tube side thermal power	3.73	3.53	3.28
Shell side thermal power	11.79	12.61	12.22
Overall heat transfer coefficient	6.72	6.47	6.16
Logarithmic mean temperature	1.93	2.03	2.02

As seen in Fig. 2, the experimental convective heat transfer coefficients, which are the thermal performance indicators, showed a similar trend for water and nanofluids in the range of volume flow rates 60 to 125 L/h (in the region where the flow is considered as laminar). However, it was found that convective heat transfer coefficients obtained with nanofluids gave results under the convective heat transfer coefficients for water. Therefore, low volume fraction nanofluids have an effect on decreasing the convective heat transfer coefficient compared to water. In other words, the use of nanofluids in the laminar region has been found to have adverse effects on the convective heat transfer coefficient. The average decrease in the convective heat transfer coefficient compared to water was −14% for 0.02% volume fraction while was −5% for 0.2% volume fraction.

Both water and nanofluids showed a similar trends as in the laminar region in the volume flow rate range of 150-350 L/h (where the flow is considered in the transition region). However, it has been observed that the results for nanofluids were above the convective heat transfer coefficient of water in the range of volume flow rates 150-350 L/h and therefore, the use of nanofluids had a positive effect. The use of nanofluids in the transition region was provided an average enhancement of 3.7% for 0.02% volume fraction compared to water in the convective heat transfer coefficient, while providing an average 13% enhancement for 0.2% volume fraction. These results indicate that the random motion of nanoparticles added to water and their interactions with each other slightly increased the fluctuations in the channel through which the flow passes. In addition, the changing thermophysical properties of the fluid were also effective in the increase of the convective heat transfer coefficient.

The similar trend between water and nanofluids was impaired in the range of volume flow rates 350-600 L/h (turbulent region), but the similar trend for different volume fractions of nanofluids has been continued. In other words, the use of nanofluids in this range of volume flow rates delayed the transition to the fully developed turbulent regime and extended the transition region. The average enhancement in convective heat transfer coefficient compared to water was obtained 25% for the 0.02% volume fraction, and 34% for the 0.2% volume fraction. The intensity of fluctuations of the nano materials and their effects on the convective heat transfer have been increased much more with increasing volume flow rate as in the range of 150-350 L/h. Therefore, the use of nanofluids instead of water even in very small volume fractions such as 0.02% significantly augmented the convective heat transfer in the range of 350-600 L/h.

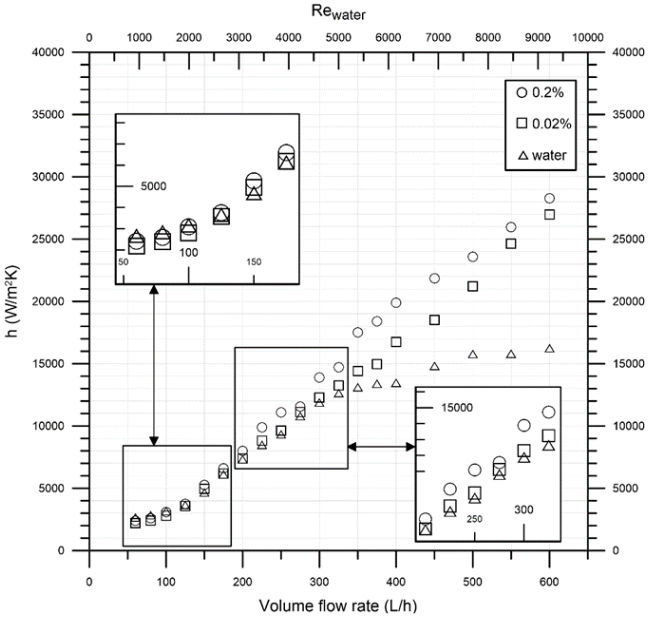

Fig. 2 *Experimental convective heat transfer coefficients versus volume flow rate.*

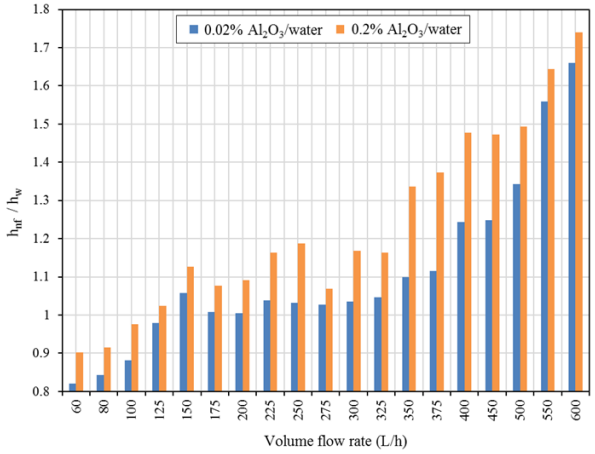

Fig. 3 *Convective heat transfer enhancement ratios versus volume flow rate.*

The convective heat transfer enhancement ratios of nanofluids compared to water were given in Fig. 3. The enhancement ratios in the range of volume flow rates 60-125 L/h were lower than one, while the enhancement ratios in the range of 150-600 L/h were higher than one. The lowest and highest enhancement ratios in the flow range of 60-600 L/h were between 0.82 and 1.66 for 0.02% volume fraction, while for 0.2% volume fraction between 0.9 and 1.74%. The results of convective heat transfer coefficient and enhancement ratio were evaluated together, while the use of nanofluid on the tube side of MC-STHE has a negative effect at the volume flow rates up to 125 L/h. It has been found that the negative effects were disappeared and the positive affects of the nanofluids has been become apparent gradually after 125 L/h.

In Fig. 4, the change in pumping power, selected for the hydraulic performance variable of water and nanofluids, was given by volume flow rate. The pumping power of nanofluids at constant volume flow rate is higher than water. The pumping power of the nanofluids is higher than that of water, because the flow induced pressure drop depends on density and viscosity of the fluid. The nano materials added to the water were increased the density and viscosity of the fluid. The average pumping power is 4% higher for 0.02% and 42% higher for 0.2% compared to water in the range of volume flow rate 60-600 L/h. In high volume flow rates, the volume fraction of nanofluids had less effect on pumping power than water, whereas in low volume flow rates, it had a greater effect on pumping power than water. When the heat transfer in a MC-STHE was desired to improve with nano fluids, pumping power and heat transfer results should be evaluated together and the increase in pumping power, depending on the selected volume ratio must be considered.

It is understood that a significant improvement was made when the value of the efficiency index, used to evaluate the effect of the nanofluids on improving the heat transfer, is greater than one. According to this definition and to Fig. 5, upwards 350 L/h for a 0.02% volume fraction and upwards 300 L/h for a 0.2% volume fraction, the use of nanofluids was meaningful in terms of the heat transfer enhancement.

Efficiency indexes were obtained as 1.67 and 1.4 for 0.02% and 0.2% respectively at the highest volume flow rate (600 L/h) in the study. According to Fig. 2, the highest convective heat transfer coefficients in the range of volume flow rates 60-600 L/h were obtained for 0.2% volume fraction. In this volume flow rate range, the Prandtl numbers for the volume fractions of 0.02% and 0.2% are very close to each other.

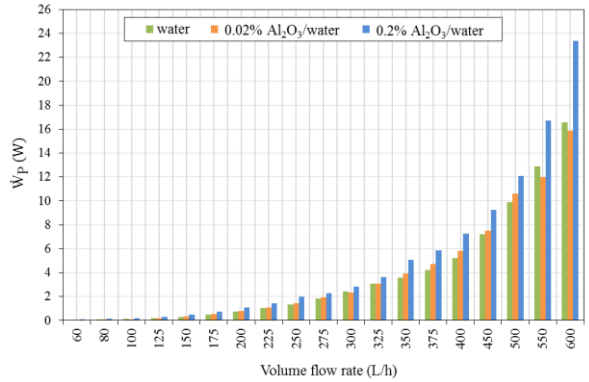

Fig. 4 *Pumping powers versus volume flow rate.*

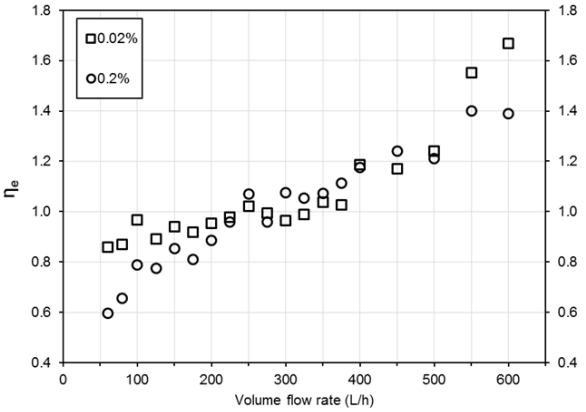

Fig. 5 *Efficiency index versus volume flow rate for nanofluids.*

Due to the changing thermophysical properties of nanofluids, higher Reynolds numbers were obtained for 0.2%. As can be seen from the definition of Colburn factor, increase in the Reynolds number with the use of nanofluids was less than increase in the convective heat transfer coefficient and so the increase in average Colburn factor at 0.2% volume fraction was greater than 0.02% volume fraction. According to the results of j_{nf}/j_w ratio in the numerator of efficiency index, the increase in Colburn factor was obtained higher for 0.2% volume fraction. Also, the f_{nf}/f_w ratio in the denominator of the efficiency index has been found higher at 0.2% volume fraction. Because of the effectiveness index is inversely proportional to f_{nf}/f_w ratio (Eq. 13), better enhancement with 0.02% volume fraction nanofluid has been determined in terms of the efficiency index in the flow rate range of 60-600 L/h. Empirical correlations in the 95% confidence interval have been proposed to correlate the convective heat transfer coefficient results obtained from experimental studies with the Reynolds number, Prandtl number and the volume fraction of nanomaterial. Proposed correlations are given in Tab. 2.

Table 2: *Empirical correlations for water and nanofluids.*

Correlation	Comments and Limitations
$Nu = 0.00093\ \mathrm{Re}^{1.183}\ \mathrm{Pr}^{1/3}$	Water, 1900 ≤Re≤ 5100, Pr=6.7, R^2= 0.995
$Nu = 0.43\ \mathrm{Re}^{1.183}\ \mathrm{Pr}^{1/3}$	Water, 5100 < Re≤ 10,000, Pr=6.7, R^2= 0.941
$Nu_{0.02\%} = 0.000876\ \mathrm{Re}^{1.193}\ \mathrm{Pr}^{1/3}$	Al_2O_3/water (θ=0.02%), 1000 <Re< 10,000, Pr=6.67, R^2= 0.994
$Nu_{0.2\%} = 0.000734\ \mathrm{Re}^{1.219}\ \mathrm{Pr}^{1/3}$	Al_2O_3/water (θ=0.2%), 1000 <Re< 10,000, Pr=6.64, R^2= 0.983
Alternative correlation for Al_2O_3/water nanofluids	
$Nu_{\theta} = 0.0009\ \mathrm{Re}^{1.201}\ \mathrm{Pr}^{1/3}\ \theta^{0.0249}$	Al_2O_3/water (0% <θ≤ 0.2%), 1000 <Re< 10,000, Pr=6.65, R^2= 0.988

7. Conclusions

In this study, a MC-STHE is designed using the proposed relations for macro pipes by Kern. According to the design conditions, average thermal power of 1-1.5 kW, single shell, single tube pass and counter flow heat exchanger is manufactured. The volume flow rate of the shell side was kept constant at 180 L/h during the experiments. The volume flow rate of the tube side was changed from 60 to 600 L/h. In the experimental studies, hot water on the shell side and cold water and Al_2O_3/water nanofluids, prepared in two different low volume fractions, on the tube side were used. The selected thermal and hydraulic performance criterions, convective heat transfer coefficient and pumping power were obtained depending on the volume flow rate by using the tube side experimental results. In addition, the efficiency index selected for the evaluation of thermal and hydraulic affects together was also calculated for experimental results. The results obtained in this study are as follows:

- It was observed that experimental convection heat transfer coefficients and pumping power increased with increasing Reynolds number and nano material's volume fraction.
- The use of nanofluids, in the range of volume flow rates 60-125 L/h, adversely affected the convective heat transfer coefficient and deteriorated the convective heat transfer coefficient compared to water.
- In the volume flow rate of 150-350 L/h, the nanofluids positively affected the convective heat transfer coefficient, whereas even in very small volume fractions, the use of nanofluids in the MC-STHE significantly increased the heat transfer compared to water. Average enhancements in the convective heat transfer coefficient for 0.02% and 0.2% volume fractions in the range of volume flow rates 150-350 L/h are 3.7% and 13% respectively.
- While the rate of increase in the convective heat transfer coefficient of water decreased in the 350-600 L/h volume flow rates, the convective heat transfer coefficient of nanofluids has been continued to increase at the same rate by volume flow rate. The nanofluids were delayed the flow to be turbulent and extended the transition region. The obtained average enhancements in the convective heat transfer coefficient for nanofluids with the volume fractions of 0.02% and 0.2% are 25% and 34% respectively in these volume flow rates.
- The pumping power has been higher 66% to 8% and 68% to 24% for 0.02% and 0.2% nanofluids volume fraction compared to water respectively, in the investigated volume flow rate range (60-600 L/h). Therefore, the increase in pumping power should also be taken into account depending on the selected nanofluids volume fraction.
- A better enhancement was obtained for 0.02% volume fraction in terms of the efficiency index where the thermal and hydraulic performances were evaluated together, in the volume flow range 60-600 L/h.
- The use of nanofluids instead of water in MC-STHEs has a positive effect on the tube side convective heat transfer coefficient, especially after the volume flow rate of 125 L/h. While the use of mini channels instead of macro tube reducing the weight and volume of the heat exchanger and increasing the compactness, higher convective heat transfer coefficients can be obtained in the MC-STHE by using nanofluids instead of water.

8. Acknowledgments

This work was supported by Research Fund of the Bolu Abant İzzet Baysal. Project Number: BAP 2011.19.19.415.

This paper was prepared with the contributions of the third author from the continuing PhD study of the first author under the supervision of the second author.

9. Nomenclature

A	- area (m^2)
c_p	- specific heat (J kg^{-1} K^{-1})
D_h	- hydraulic diameter (m)
D_e	- shell equivalent diameter (m)
D_i	- inner diameter (m)
D_o	- outer diameter (m)
F	- non-dimensional correction factor
f	- Fanning friction factor [=Δp/(4 (L/D) (ρ u^2))]
h	- convective heat transfer coefficient (W m^{-2} K^{-1})
j	- Colburn factor [=Nu/ Re $Pr^{1/3}$]
k	- thermal conductivity (W m^{-1} K^{-1})
L	- length (m)
MC-STHE	- mini-channel shell and tube heat exchanger
$\dot{m}$	- mass flow rate (kg s^{-1})
Nu	- Nusselt number [=h D/ k]
Pr	- Prandtl number [=μ c_p/ k]
p_t	- tube pitch (m)
Δp	- pressure drop (Pa)
Q	- heat transfer rate (W)
Re	- Reynolds number [=ρ u D/ μ]
T	- temperature (K)

U	- overall heat transfer coefficient (W m^{-2} K^{-1})
$\dot{\forall}$	- volume flow rate (L h^{-1})
$\dot{W}$	- power (W)
ΔT_{lm}	- logarithmic mean temperature difference (K)

Greek Letters

η	- efficiency index [≡ $(j_{nf}/j_w)/(f_{nf}/f_w)$]
θ	- volume fraction (%)
μ	- dynamic viscosity (kg m^{-1} s^{-1})
ρ	- density (kg m^{-3})

Subscripts

ave.	- average	o	- outlet
h	- hot fluid	p	- pump
i	- inlet, inner	s	- shell
nf	- nanofluid	t	- tube
nm	- nanomaterial	w	- water

10. References

1. Webb, R.L., Kim, N., Principles of Enhanced Heat Transfer, 2nd edn. Taylors & Francis Group, New York, 2005.

2. Unverdi, M., Islamoglu, Y., Characteristics of heat transfer and pressure drop in a chevron-type plate heat exchanger with Al_2O_3/water nanofluids, Thermal Science 21-6A:2379–2391, 2017.

3. Kakac, S., Liu, H., Pramuanjaroenkij, A., Heat Exchangers Selection, Rating, and Thermal Design, 3nd edn. CRC Press, New York, 2012.

4. Shah, R.K., Sekulic´, D.P., Fundamentals of Heat Exchanger Design, John Wiley & Sons, Inc., Hoboken, New Jersey, 2003.

5. Hesselgreaves, J.E., Law, R., Reay, D.A., Compact Heat Exchangers Selection, Design and Operation, 2nd edn. Butterworth Heinemann, Oxford, 2017.

6. Unverdi, M., Cerci, Y., Thermodynamic Analysis and Performance Improvement of Irem Geothermal Power Plant in Turkey: A Case Study of Organic Rankine Cycle, Environmental Progress & Sustainability Energy 37(4):1523–1539, 2018.

7. Unverdi, M., Investigation of waste heat recovery of binary geothermal plants using single component refrigerants, IOP Conf. Series: Earth and Environmental Science 83:012007, 2017.

8. Vajpai, A., Rajvanshi, A.K., Prajapati, O.S., Thermal Conductivity of Nanofluids, LAP LAMBERT Academic Publishing, USA, 2012.

9. Prajapati, O.S., Rajvanshi, A.K., Heat Transfer with Nanofluid, LAP LAMBERT Academic Publishing, USA, 2011.

10. Saidur, R., Leong, K.Y., Mohammad, H.A., A Review on Applications and Challenges of Nanofluids, Renewable and Sustainable Energy Reviews (15):1646-1668, 2011.

11. Wong, K.V., Leon, O.D., Applications of Nanofluids: Current and Future, Advances in Mechanical Engineering, Volume 2010, Article ID 519659, 11 pages, 2010.

12. Kandlikar, S.G., Grande, W.J., Evolution of Microchannel Flow Passages Thermohydraulic Performance and Fabrication Technology, Heat Transfer Engineering 24(1):3–17, 2003.

13. Mehendale, S.S., Jacobi, A.M., Shah, R.K., Fluid flow and heat transfer at micro-and meso-scales with applications to heat exchanger design, Appl Mech Rev 53(7):175–193, 2000.

14. Kandlikar, S.G., Garimella, S., Li, D., Colin, S., King, M.R., Heat Transfer and Fluid Flow in Minichannels and Microchannels (First Edt.) USA, Elsevier, 2014.

15. Arunachala, U.C., Ambuj, B., Eklavya, S., Vinay, J.R., Performance Investigation of a Shell and Tube Heat Exchanger Using Water Based Al_2O_3 as a Nanofluid, 4th World Conference on Applied Sciences, Engineering & Technology 24-26 October, Kumamoto University, Japan, 2015.

16. Ramesh, R., Vivekananthan, R., Application of Al_2O_3 Nanofluid for Enhance Heat Transfer Rate in Shell and Tube Heat Exchanger, IOSR Journal of Mechanical and Civil Engineering (IOSR-JMCE) e-ISSN: 2278-1684, p-ISSN: 2320-334X, Volume 11, Issue 2 Ver. I (Mar- April), PP 29-33, 2014.

17. Farajollahi, B., Etemad, S. Gh., Hojjat, M., Heat transfer of nanofluid in a shell and tube heat exchanger, J. Heat and Mass Transfer (53), 12-17, 2010.

18. Godson, L., Deepak, K., Enoch, C., Jefferson, B., Raja, B., Heat transfer characteristics silver/water nanofluids in a shell and tube heat exchanger, Archives of Civil and Mechanical Engineering, 14, 489-496, 2014.

19. Mapa, L.B., Mazhar, S., Heat Transfer in mini heat exchanger using nanofluids, American Society for Engineering Education, 2005 IL/IN Sectional Conference, April 1-2, 2005.

20. Ünverdi, M., Kücük, H., Yılmaz, M.S., Heat and Mass Transfer, https://doi.org/10.1007/s00231-018-2514-0, 2018.

21. Das, S.K., Choi, S.U.S., Yu, W.H., Pradeep, T., Nanofluid: Science and Technology, John Wiley & Sons Inc., 2007.

22. Pak, B.C., Cho, Y.I., Hydrodynamic and heat transfer study of dispersed fluids with submicron metallic oxide particles, Experimental Heat Transfer 11, 151–170, 1999.

23. Ho, C.J., Liu, W.K., Chang, Y.S., Lin, C.C., Natural convection heat transfer of alumina-water nanofluid in vertical square enclosures: An experimental study, International Journal of Thermal Sciences 49, 1345–1353, 2010.

24. Zhou, S.Q., Ni, R., Measurement of the specific heat capacity of water-based Al_2O_3 nanofluid, Applied Physics Letters 92, 093123, 2008.

25. Timofeeva, E.V., Gavrilov, A.N., McCloskey, J.M., Tolmachev Y.V., Thermal conductivity and particle agglomeration in alümina nanofluids: experiment and theory, Physical Review, 76.061203, 2007.

26. Einstein, A., Eine neue bestimmung der molekuldimensionen, Annalen der Physik, Leipzig, 19, 289–306, 1906.

27. Unverdi, M., Islamoglu, Y., Effect of Al_2O_3 nanomaterials on convection heat transfer enhancement in a plate heat exchanger channel, Scientific Technical Journal Material Science, Vol. 2, Issue 1, 41-45, 2016.

28. Kreith, F., Mechanical Engineering Handbook, CRC Press LLC, Boca Raton, 1999.

29. Kern, D.Q., Process heat transfer, International student edn. McGraw-Hill, New York, 1950.

30. Çengel, Y.A., Cimbala, J.M., Fluid Mechanics, Fundamentals and Applications, Third Edition, USA, McGraw-Hill, 2014.

31. Kline, S.J., McClintock, F.A., Describing Uncertainties in Single-Sample Experiments, Mechanical Engineering 75(1):3–8, 1953.

DETERMINATION OF GEOMETRIC PARAMETERS OF GRADIENT STRUCTURES FORMED IN OPTICAL GLASS BY THE ELECTRON BEAM METHOD

ВИЗНАЧЕННЯ ГЕОМЕТРИЧНИХ ПАРАМЕТРІВ ГРАДІЄНТНИХ СТРУКТУР, СФОРМОВАНИХ В ОПТИЧНОМУ СКЛІ ЕЛЕКТРОННО-ПРОМЕНЕВИМ МЕТОДОМ

Grechana O.[1], Skoryna E.[2], PhD Bondarenko I.[2]
Faculty of computer engineering technology and design[1], Faculty of Electronically Technologies and Robotics[2]
Cherkassy State Technological University, Ukraine

Abstract: *The results of experimental studies of the geometry of gradient structures formed in optical glass by the method of electron-beam modification of its surface are presented. The expediency of using the atomic force microscopy method for determining the geometrical parameters of microlayers formed in the surfaces of optical materials by the method of their electron-beam modification is substantiated. A new method for determining the basic geometric parameters (thickness of the gradient layer, topology of the interface "gradient layer - the basis of the material", surface microrelief, etc.) gradient structures, based on the method of atomic force microscopy is proposed. The proposed method is based on the principle of the complex application of various operating modes of an atomic-force microscope (the results of the instrument operation are considered, both in contact and in non-contact modes) in one measurement cycle. According to the proposed method, the dependencies between the change in the refractive index and the modes of electron-beam modification of the optical glass surface, as well as the dependence between the electron-beam effect modes and the geometric parameters of the gradient structure on the glass (thickness of the gradient structure, surface microrelief and interface between the layers and the base material). The possibility of predicting the development of hidden microdefects at the interface "gradient layer - the basis of the material" is shown. Proved high reliability and adequacy of the proposed method by comparing the results obtained with the results of determining the geometric parameters obtained by other alternative methods.*

KEYWORDS: *ELECTRON-BEAM METHOD, GRADIENT STRUCTURE, OPTICAL GLASS, GEOMETRIC PARAMETER, ATOMIC-FORCE MICROSCOPY*

1. Introduction

In modern instrumentation technology, gradient structures formed in optical glass are widely used. Such coatings have unique properties (high strength, reflective and refractive power, etc.) that can be used as functional elements in various areas of precision instrument making, micro-optics, integrated optics, etc. [1, 2].

As shown in the work [3], the microgeometry of the gradient structures formed in the surface of optical glass determines their performance characteristics depending on the method of preparation. Various methods for obtaining such structures are presented in the work [4, 5], the most popular among them is the electron-beam method [6], which allows forming various layers of the chemical composition and physical properties in the surface layer of the optical glass, which possess, among other things, the property of the gradient change of the refractive index in the thickness of the optical material.

The method of obtaining and the features of the surface microrelief determine the operational characteristics of optical elements (reflection and refraction coefficients, diffusion of the light flux) associated with the instability of their properties through the thickness of the optical material. As it was shown in the work [7], the reasons for such instability are size effects (uneven distribution of material density across the thickness of an optical product, surface structure) and the operating conditions of these elements (aggressiveness of the environment, time and temperature of operation, thermal and mechanical effects in contact with other elements of the product).

The issues of obtaining and studying gradient structures in optical materials were studied by domestic and foreign scientists, including: Dubrovskaya G.N., Kanashevich G.V., Kotelnikov D.I., Lisochenko N.I., Marjan N.I., Yurkovich N.V. and etc. [8-10].

At the same time, among the methods for studying gradient structures, the most promising are analytical methods of scanning probe microscopy. The atomic force microscopy method [11] has significant advantages in studying the microrelief of gradient surfaces modified by electron flow, namely: high accuracy of fixed surface asperities (up to units of angstroms) and sensitivity of the measuring console ($\approx 10^{-8}$ N), and the method itself refers to non-destructive research methods that do not require preliminary preparation of the research material and pretend on the expressivity of the research.

The aim of the work is to study the gradient structures formed by the electron beam effect on the surface of optical glass by atomic force microscopy, which allows determining with sufficient accuracy and reliability the geometric parameters of such structures.

2. Experiment methodology

The objects under study were plane-parallel plates of circular shape (diameter 20 mm and thickness 2; 4; 6 mm) made of K8 optical glass (analog Schott Glass BK7) and a rectangular photographic plate (25×20×1 mm).

Electron-beam modification was carried out on a special laboratory setup (ISTC «Micronanotechnologies and equipment», ChSTU, Cherkasy), containing the Pierce Electron Gun.

A plate made of optical glass (base), preheated to a temperature of 840 K (K8, photographic plate), was rotated in a vacuum chamber above an electron gun with the help of a rotational movement mechanism. The substrate moved nonstop above the electron gun. At the same time, the surface was affected by the low-energy ribbon-shaped electron flow (width 3.0 mm, length 60.0 mm). Electron beam exposure was carried out in the following modes: accelerating voltage 3,5…4,0 kV; electron flow current 175…200 mA; cathode heating current 14,5 A; electron flow rate 4,5…5,0 sm/s; the distance from the anode of the electron gun to the surface being processed is 40 mm; single pass treatment.

Surface microgeometry was studied by atomic force microscopy on an instrument «NT-206» (manufacturer: «Microtestmashines Co.», Belarus) with silicon probes «Ultrasharp

CSC12», by the system of micro-positioning and a Logitech integrated long-focusing optical microscope.

The method of determining the characteristics of the surface layer of materials allows determining and controlling the thickness of the gradient layer, the topology of the interface "gradient layer - the basis of the material", surface microrelief, etc. and is unique in essence, since it allows to obtain high-precision results of microgeometry values and characteristics of the surface layer with a thickness of 10 nm to 6 μm. To determine the characteristics of a gradient layer that forms on the surface of optical glass, an experimental-calculation technique is used based on a certain degree of probe slippage over the sample (in fact, complex bending and torsional moments occurring in the cantilever) as a result of friction forces [11].

In general, the preparation of AFM and samples for the research of thin surface structures on them, as well as the scanning of the surface in dynamic and static modes, are carried out similarly to the steps carried out for the integrated control of the characteristics of optical materials [11]. The main difference in the sample preparation procedure is that for gradient structures, the use of chemical-mechanical treatment is unacceptable because of the possibility of significant damage to surfaces [12].

In order to correctly select the parameters of load and delay in determining the mode of monitoring the characteristics at the first stage of research, it is necessary to establish the thickness of the gradient layer as accurately as possible [13].

For this, depending on the type of gradient layer (discrete or solid), you can apply two approaches. Determining the thickness of a discrete layer using the method of AFM is carried out in the following sequence.

after preparing the sample and installing it on the AFM stage, turning on the device and launching the "SurfaceScan" control program on the "Area" panel of the control program, select the scan area with a clearly defined feature of the applied coating;

departing from this boundary in the direction of the gradient at a distance of 1.5 – 2 microns, they automatically lead the probe to the surface in static mode by pressing the "Auto Z Approach" button on the "Main" panel;

fter the completion of the automatic summing process on the "Main" panel, pressing the manual up-down buttons with a minimum step of 0.2 nm reaches a value that is half the indications of the "Z" indicator on the "Indicators" panel;

conduct manual removal of the probe from the surface at 1000 steps (that is, at a distance of 0.2 μm);

moving the probe relative to the boundary of the applied coating towards the surface without a gradient layer (as in the previous case - at a distance of 1.5 - 2 microns from this boundary);

in manual mode, the probe is brought to the surface by 1000 steps (0.2 μm) and further, step by step, until the reading of the "Z" indicator on the "Indicators" panel changes its value (will correspond to the distance of the beginning of the action of the intermolecular interaction forces - the distance to the surface of the order of 0.5 –1 nm);

according to the formula: $h = m \cdot k$, where h – thickness of the studied structure, nm; m – the number of steps taken in manual mode by the operator when leading the AFM probe to the surface; k – minimum distance at which the probe approaches the surface in one step ($k = 0{,}2$ nm); calculate the probable thickness of the gradient layer.

The absolute error of determining the thickness of the layer by this method does not exceed 1 nm.

In the case of a solid gradient layer, its thickness is determined by the AFM method as follows.

– after preparing the sample and installing it on the AFM stage, turn on the device and run the "SurfaceScan" control program. In the "Area" panel of the control program, an area is selected and a point on it at which the determination of the layer thickness will be carried out;

– the spectroscopy procedure is selected at the point on the "Main" panel;

– the spectroscopy procedure is automatically performed at the point when the "Start" button is pressed on the "Main" panel;

– after completion of the procedure and graphical construction of the static power spectroscopy function in the visualization window of the measured data "View spectroscopy data" (Fig.1), the AFM device automatically stops working. The data obtained in the graph can be saved on disk in text or graphic format using the file save dialog;

– according to the graph (Fig.1) determine the possible thickness h of the researched gradient layer.

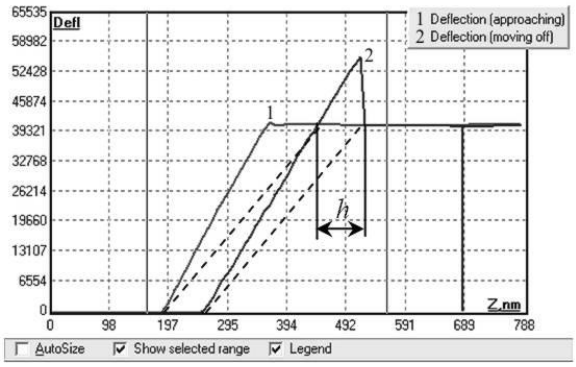

Fig.1. *Visualization window of static power spectroscopy*

The thickness of the coatings obtained is checked by the resonant-acoustic method [13] on the «ИТТП-1М» instrument, which confirms the high accuracy of the method for determining the thickness of the gradient layer in optical surfaces described in the work.

Determination of geometric parameters of gradient structures. To determine the geometrical parameters of the gradient structures, after sample preparation and AFM adjustment for operation, the surfaces to be examined are scanned to select the place of the tribological research. Further, by selecting the operation mode of the device "Tribological Line", the line for conducting the study is determined - a homogeneous surface without inclusions and abrupt differences in relief. At the same time, increasing load should be specified (0,3 – 1 mN), load time (1,5 – 6 ms) and the number of tribological lines (tracks) – from 3 to 5 [15].

According to the dependence of the force on the depth of penetration of the probe, displayed on the screen, the change in the density of the investigated materials is estimated by thickness. After that, the location of the tribological scanning line is scanned. As a result, the volume of the stamped material and the volume of the displaced material in the strain on the boundary of the scanning line are determined. Next, the refractive index is calculated as the ratio of the density change in the gradient layer over its thickness (on the

other hand, this is the ratio of multiplication of the wiping track width l by the probe load force P to the multiplication of its height h by the track surface area S and the effective Young's modulus of sample E): $n = (l \cdot P) / (h \cdot S \cdot E)$.

Thus, the above method for determining the geometric parameters of the gradient structures of optical materials using the AFM method allows determining the thickness of such gradient layers, refractive index, etc. with an accuracy of 8–12%.

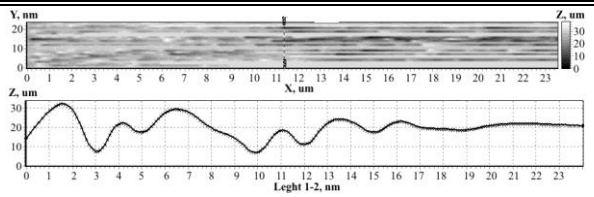

Fig 2. *AFM images (a) and Topogram (b) of the result of sclerometric determination of the thickness of the gradient structure on the K8 optical glass*

3. Results and discussion

As a result of the experiments conducted and the study of their results, the thickness was determined and the averaged value of the refractive index was calculated on samples of optical glass K8 and photographic plates. The thickness and refractive index of the gradient structure on the optical glass was determined by the sclerometric method under the following conditions: probe load when exposed to K8 glass – $6{,}2 \cdot 10^{-4}$ N; when acting on a photographic plate – $6{,}4 \cdot 10^{-4}$ N. The AFM images of the result of sclerometry on the K8 optical glass are shown in Fig.2.

As can be seen from Fig. 2, the intensity of the tracks obtained as a result of the action of the probe and the surface area of the surface increases and is continuous, which indicates the homogeneity of the density distribution of the material over the thickness of the optical glass (i.e., the gradient structure should gradually (not discretely) change the refractive index over its thickness), and, accordingly, the high accuracy of determining the refractive index n, which was confirmed by an alternative method for determining the refractive index, namely, by the goniometric method. (device: Г-5). In general, studies of single-type samples, which were carried out in series, showed a high convergence of the results of determining the refractive index, the value of which for different samples is given in tabl.1.

Tabl. 1. *The results of the study of gradient structures in optical glass K8*

Sample number	Estimated gradient layer thickness, μm	Refractive index (averaged value), n	
		Estimated value	The value is obtained by goniometric method (Г-5)
Sample 1	15,6	1,85	1,9
Sample 2	18,3	1,93	2,0
Sample 3	19,0	2,01	2,0
Sample 4	21,5	2,11	1,95
Sample 5	25,8	1,92	2,0
Reference sample	32,4	2,05	2,1

As can be seen from the data presented in table 1, the accuracy of determining the refractive index correlates with the values obtained by the goniometric method (the discrepancy between the calculated and goniometric values does not exceed 8%). Similar results have also taken place for researches carried out for photographic plates.

According to the results of the study, it is clear that the calculated values of the refractive index are somewhat higher than the goniometric ones. This may be due to the fact that for optical glass, the hardness of which is commensurate with the hardness of the indenter, the probe "sticks" on the surface and leads to a slight (about 3-8%) increase in the refractive index compared to goniometric data. However, taking into account the subjectivity of determining the refractive index (determined in arbitrary units), the discrepancy between the calculated and alternative method values of the refractive index can be considered as acceptable, and the data obtained by the proposed sclerometry method correspond to reality.

In parallel with determining the thickness of the gradient layer and calculating the refractive index of the gradient structures in optical glass, a connection was established between the modes of electron-beam modifying (specific power P, kW/m^2 and the speed of the electron flow V, sm/s) the optical glass surface and the thickness h (Fig.3) and the refractive index n of the gradient structure in the glass (Fig.4).

It has been established (Fig.3, Fig.4) that with an increase in the specific power, a nonlinear increase in the thickness of the gradient structure occurs, whereas the refractive index also increases with the increase in specific power, but almost linearly.

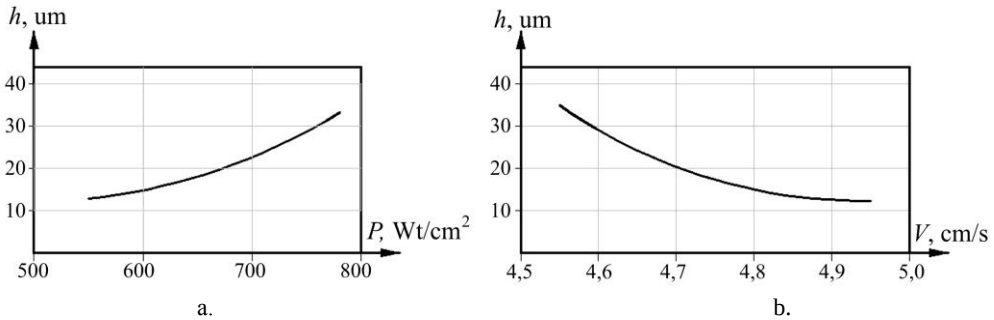

Fig. 3. *Dependence of the thickness h of the gradient structure in optical glass on the specific power P (a) and speed V (b) of the electron flow*

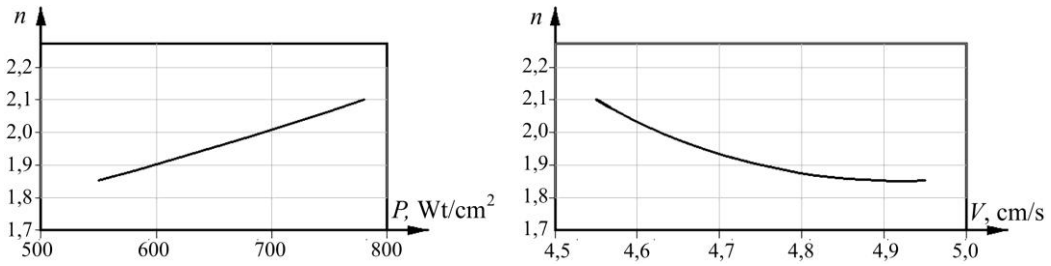

Fig. 4. *The dependence of the change in the averaged value of the refractive index n of the n gradient structure in optical glass on the specific power P (a) and speed V (b) of the electron flow*

At the same time, an increase in the electron flow rate leads to a nonlinear decrease in both the thickness of the gradient structure and the refractive index.

Such patterns (Fig.3, Fig.4), according to the authors, are associated with time and energy flow acting on the surface of optical glass. Thus, with an increase in heat flux, or a decrease in exposure time, the heating of optical glass increases, which leads both to a change in the chemical composition (volatile ions evaporate from the surface, while the concentration of heavy ions increases) and to change its physical characteristics (the melted glass layer, as well as the reduction of microdefects and pores in the surface layer). It should be borne in mind that, unlike metals, the heating of which takes place in a very short time, optical glass, having a relatively small thermal conductivity and a large heat capacity, warms up much slower. The selection of electron beam exposure modes allows you to control the penetration depth, as well as the law of heat distribution (respectively, the optical density of the material) across the thickness of the optical glass, is the basis of the theory of creating gradient structures in an optical material.

4. Conclusion

As a result of the research, the expediency of using the atomic force microscopy method to determine the geometric parameters of gradient microlayers formed in the surfaces of optical materials by the method of their electron-beam modifying was substantiated. To this end, the article presents a method for determining the basic geometric parameters (thickness of the gradient layer and refractive index) of gradient structures based on the atomic force microscopy method. The proposed method is based on the principle of the complex application of various modes of operation of an atomic-force microscope in one measurement cycle.

Regularities between changes in the refractive index and modes of conducting electron-beam modifying the surface of optical glass, as well as between the modes of electron-beam action and the geometric parameters of the gradient structure on glass (thickness and averaged value of the refractive index of the gradient structure) are established.

Comparison of the obtained results with the results of determining the thickness of the gradient layer and the averaged value of the refractive index obtained by the alternative method of goniometry on the Г-5 device showed high accuracy (the relative error between the results obtained by various methods did not exceed 8%) reliability (probability of failure-free determination of values by the method of AFM, not less than 0,95) and the adequacy of the proposed method.

5. Literature

1. Pokryttia u pryladobuduvanni (*Coatings in instrument making*) [Tekst]: monohrafiia / V.S.Antoniuk, H.S.Tymchyk, Yu.Iu.Bondarenko, Yu.I.Kovalenko, M.O.Bondarenko ta in. // K.: NTUU «KPI», 2016. – 360 s.

2. Tekhnolohichni osnovy otrymannia metalizovanykh pokryttiv na vyrobakh mikrooptyky ta nanoelektroniky elektronno-promenevym metodom (*Technological bases for obtaining metallized coatings on micro-optical products and nanoelectronics by electron-beam method*) / V.A.Vashchenko, H.V.Kanashevych, S.M.Vashchenko, M.O.Bondarenko i dr. // Zvit z NDR (MONU); № DR 0103U003689. – Kiyv, 2004. – 63 s.

3. Special'ni metodi obrobki optichnogo skla (*Special methods of optical glass processing*) [Tekst]: monohrafiia / G.V.Kanashevich, D.I.Kotel'nikov, V.A.Vashchenko; pid red. Profess. D.I. Kotel'nikova. – CHernigiv: “Sivers'ka dumka”, 2002. – 215 s.

4. Pryklady zastosuvannia fizychnykh metodiv doslidzhennia struktury poverkhni (*Examples of the application of physical methods for studying the structure of the surface*) [Tekst]: monohrafiia / H.M.Dubrovska, N.I.Bozhko, M.O.Bondarenko, H.V.Kanashevych ta in. // Silkhet: Shobuzh Biponi, Udoun Ofset Prynters, 2007. – 248 s.

5. Fynn A.M. Rekonstruktsyia ostatochnыkh napriazhenyi v hradyentnыkh sredakh pry prodolnom prosvechyvanyy (*Reconstruction of residual stresses in gradient media with longitudinal translucency*) [Tekst]: monohrafiia. - SPbHPU, 2005. – 77s.

6. Bondarenko M. *Peculiarities of metalized surfaces modification of silicon elements of microelectromechanical systems with low-power electronic flow* / M.Bondarenko, I.Bondarenko, V.Antoniuk [etc.] // Materials science. Non-equilibrium phase transformations. – 2017. – Year III. – Issue 2. – pp.53-55.

7. Yatsenko I., Antoniuk V., Bondarenko M., Vashchenko V. *Influence of parameters by electronic ray on properties of superficial layers of optical elements of exact instrument-making*, in Proc. Intern. scien.-tech. conf. “Innovations in ingeneering”, 9-12 september 2015. – Burgas, Bulgaria. – Vol. 20/183. – 2015. – pp. 64-66.

8. Kanashevich G.V. Tekhnologichni mozhlivost elektronno-promenevo obrobki optichnogo skla (*Technological possibilities of electron beam processing of optical glass*) / Visnik CHITI, 1998, No.3. – S. 48-55.

9. Lisochenko V.N. Razrabotka elementov integralno-opticheskikh skhem novymi metodami na osnove elektronno-luchevoi obrabotki

(*Development of elements of integrated-optical circuits by new methods based on electron-beam processing*) / V.N.Lisochenko, G.V.Kanashevich, V.A.Vashchenko i dr. // Otchet po NIR Cherkasskogo filiala KPI. – Cherkassy, 1993. – 205 s.

10. Yurkovych N.V., Mar'yan M.I. *The processes formation of thin-film heterogeneous structures based on Ge_2S_3 glass in dependence of the technologies conditions of their preparation*. – Uzhhorod University Scientific Herald. Series Physics. – Iss. 28, 2010. – pp. 64 – 69.

11. Diagnostics of functional layers in products of micro-optics and nanoelectronics obtained by electronic technologies (*Diagnostics of functional layers in the products of micro-optics and nanoelectronics obtained by electronic technologies*) / V.A.Vashchenko, H.V.Kanashevych, M.O.Bondarenko i dr. // Zvit z NDR (MONU); № DR 0106U004500. – Cherkassy, 2008. –192 s.

12. Kovalenko Yu.I., Bondarenko M.O., Bondaren-ko Yu.Iu., Vplyv rezhymiv ultrazvukovoho ochyshchennia p'iezoelektrychnykh elementiv na yakist sformovanykh na yikhnikh poverkhniakh sribnykh elektrodiv (*Influence of modes of ultrasonic cleaning of piezoelectric elements on the quality of silver electrodes formed on their surfaces*) // Visnyk Natsionalnoho tekhnichnoho universytetu Ukrainy "Kyivskyi politekhnichnyi instytut". Mashynobuduvannia, № 64, 2012. – s. 87-90.

13. Bondarenko M.O., Vashchenko V.A., Reva Y.A., Bondarenko Yu.Iu. Metodyka yzmerenyia tolshchyn tonkykh nesploshnykh pokrytyi na dyelektrycheskykh poverkhnostiakh metodom atomno-sylovoi mykroskopyy (*Method of measuring the thickness of thin non-permeable coatings on dielectric surfaces by atomic force microscopy*), na XVIII mezhdunar. konf. Sovremennye metody y sredstva nerazrush. kontrolia y tekhnycheskoi diahnostyky, Yalta, 2010, s. 209-212.

14. M.O. Bondarenko ta in. Otsinka adheziinoi mitsnosti na styrannia oksydnykh pokryttiv na optychnomu skli metodom atomno-sylovoi mikroskopii (*Estimation of adhesive strength for abrasion of oxide coatings on optical glass by atomic force microscopy*), na XII mizhnar. nauk.-tekhn. konf. Pryladobuduvannia: stan i perspektyvy, Kyiv, 2013, s. 207.

15. S.A. Bylokon, M.A. Bondarenko, V.A. Andryenko, ta V.S. Antoniuk Yssledovanye mykrotverdosty tonkykh plenok metodom nanoyndentyrovanyia s pomoshchiu atomno-sylovoi mykroskopyy (*Investigation of Microhardness of Thin Films by Nanoindentation by Nuclear Force Microscopy*), na XIII mezhdunar. nauchno-prakt. konf. Kachestvo, standartyzatsyia, kontrol: teoryia y praktyka. – Kyev, 2013. – s. 20-21.

16. Antoniuk V.S., Bondarenko M.O., Bondarenko Yu.Iu., Bilokin S.O. Sklerometrychna otsinka znosostiikosti tonkykh pokryttiv metodom atomno-sylovoi mikroskopii (*Scrollometric evaluation of wear resistance of thin coatings by atomic force microscopy*), na XV Mezhdunar. nauch.-tekhn. konf. Ynzheneryia poverkhnosty y renovatsyia yzdelyi. – Kyev, 2015, s. 17-19.

UNIVERSAL THERMAL MICROSYSTEMS BASED ON SILICON CARBIDE

Phd Student Eng Daniil Evstigneev [12], Prof. Grand PhD in Engeneers Science Eng . Vladimir Karachinov [12],
Master's degree courses Eng. AntonVarshavsiy [1 2] , PhD Applicant Eng. Petrov Dmitriy [1 2]

Specialty microelectronics - Novgorod state University named after Yaroslav the wise [1]
Open Society - OKB "Planeta", Velikiy Novgorod [2]

Abstract: *The results of modeling the thermal characteristics of microsystems, evaluated mutual thermal influence of the elements depending on the type of construction.*
KEYWORDS*: Heat-loss anemometr, thermal microsystem, wide-band semiconductor, modeling thermal performance, pyrometry.*

1. Introduction

At present, there is a tendency for development of various types of flowmeters and sensors for measuring the characteristics of gas flows. In general, the changes themselves undergo the design of the probes themselves and select materials with characteristics that exceed traditional values. As shown by the analysis of literature sources, one of several best technologies for investigating the properties of gas flows remains thermal anemometry and the method of television pyrometry. The authors note the high sensitivity of the methods and the considerable accuracy, in comparison with the known methods for measuring the characteristics of gas flows. These methods arc widely used in industry, oil and gas, laboratories, military science, etc.

2. Problem discussion

Currently, scientific and production technologies involve the use of high-temperature operations to produce refractory high-strength materials, diagnostics of various technical systems under extreme conditions, etc. For such operations, various energy sources (in particular propane-butane in burners) and their effective use are required. To achieve maximum efficiency, you need to know the speed and temperature of the gas flow.. [1,5] At the same time, in the field of thermal anemometry, as has been shown by the analysis of literature data, a thermoanemometric method (TAM) is currently a fairly common method for measuring the volumetric flow rate of gases. As a sensitive element in a thermoanemometric probe, thin electrically conductive wires and films with low thermal inertia are often used. The known disadvantages of TAMs are: a decrease in sensitivity with an increase in the flow rate of the measured gas, low mechanical strength, impossibility of burning (selfcleaning), as well as a change in graduation due to aging and re-crystallization of the wire material due to dynamic loads and high heating temperature [1]. The listed disadvantages limit the use of TAM based on traditional probe designs under extreme operating conditions, including high temperatures of the measured gas flow, the presence of radiation, etc.

3.Objective and research methodologies

The paper presents the results of a study of two directions, the method of television pyrometry and the method of thermoanemometric analysis of the characteristics of gas flows.

3.1 Method of television pyrometry for measuring the velocity of a gas stream.

For the experimental study, a technique was developed for measuring the flow velocity from the angle of deviation of the pendulum from the vertical. The option of technical implementation is as follows:

a) The pendulum and the holder are mounted in the positioner, and the gas flame region is placed;
b) The camera connected to the computer registers the image of the pendulum;
c) With the help of special software installed on the computer, the flow velocity along the angle of the pendulum deviation from the vertical is calculated.

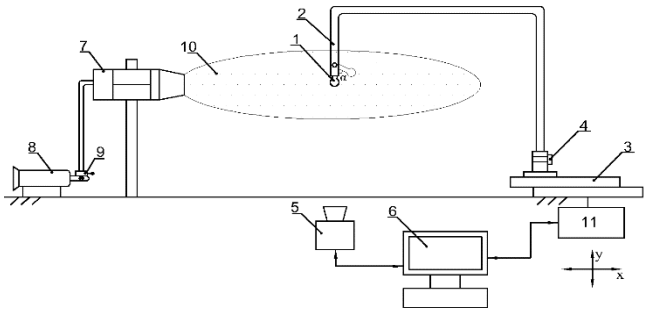

Figure 1 *- Schematic representation of the technical implementation of the flow velocity measurement technique: 1 - The pendulum; 2 - Holder; 3 - Positioner; 4 - Adjustment device; 5 - Camera; 6 - Computer with special software; 7 - Nozzle; 8 - Gas source; 9 - Rotameter; 10 - Gas flow; 11 - Positioner controller.*

To determine the velocity of the gas flame, it was required to obtain the dependence of the velocity of the gas flame on the angle of deviation of the pendulum from the vertical. For this purpose, a simplified physico- mathematical model was used. The obtained dependence is represented by the formula 1:

(1) $$\upsilon = \sqrt{\frac{m \cdot g}{\rho \cdot S \cdot \cos(\alpha)} \cdot tg(\alpha)}$$

where m - is the mass of the pendulum, g;
g - acceleration of gravity, m/s^2;
ρ - is the density of the gas flame, kg/m^3;
α - angle of deviation of the pendulum from the vertical, deg
The specificity of the flame is such that it has a definite structure [1]:

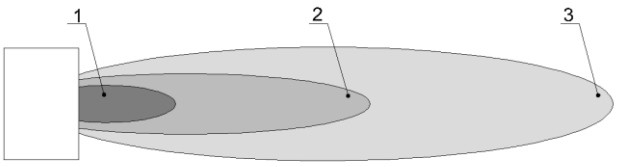

Figure 2 *- Structure of the flame: 1 - core; 2 - recovery area; 3 - area of the torch.*

When calculating the flame velocity, it must be taken into account that it consists of zones with different viscosities and temperatures. The values of temperature and viscosity in different zones of the flame are shown in Table 1:
Table 1 – gas flame characteristics

	Core flame	Flame retarding zone	Flame torch area
Temperature, °C	300-500	1200-1500	700-1000
Viscosity, $10^6\ m^2/s$	48-79	233-280	115-177

With the help of Matchcad 15, mathematical modeling was performed to obtain the range of possible velocities in different areas of the gas flame:

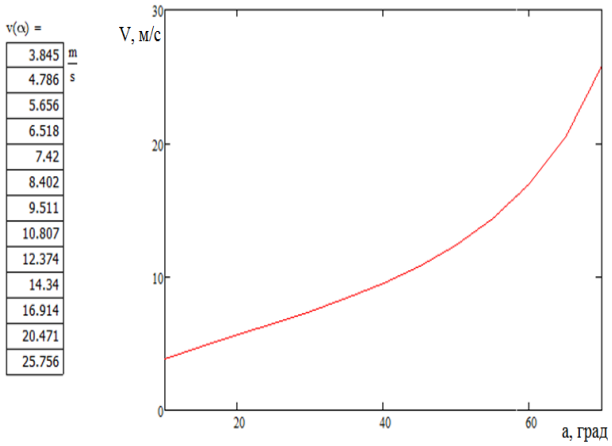

Figure 3 *– Velocity range and graph of velocity versus sensor deflection angle at ρ (500℃) = 0.456 kg/m*^{3}

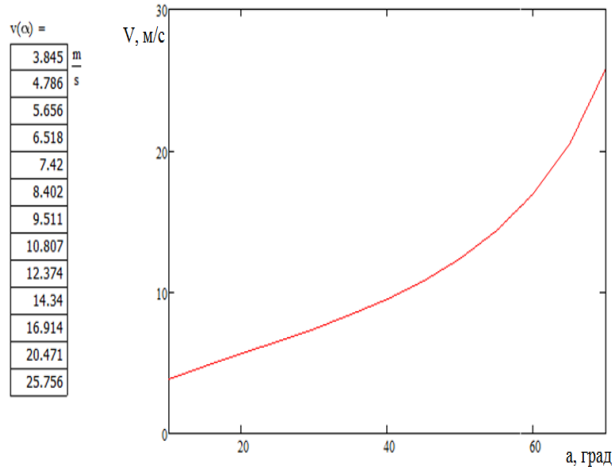

Figure 4 *– The speed range at the velocity versus the sensor deflection angle at ρ (900℃) = 0.301 kg/m*^{3}

3.2 Method of thermoanemometric analysis of the characteristics of gas flow.

The method involves determining the flow rate by changing the temperature of a thermistor probe heated by electricity placed in a controlled gas flow. The cooling of the thermistor probe depends on the flow rate, the physical properties of the gas (thermal conductivity, temperature and density) and the temperature difference between the thermistor probe and the gas.

As shown by the analysis of literature data, the thermoanemometric method (TAM) is currently a widely used method for measuring the volumetric flow rate of gases. As a sensitive element in a thermoanemometric probe, thin electrically conductive wires and films with low thermal inertia are often used. The known disadvantages of TAMs are: a decrease in sensitivity with an increase in the flow rate of the measured gas, low mechanical strength, impossibility of burning (self-cleaning), as well as a change in graduation due to aging and re-crystallization of the wire material due to dynamic loads and high heating temperature [1]. The above disadvantages limit the use of TAM based on traditional probe designs under extreme operating conditions, including high temperatures of the measured gas flow, the presence of radiation, etc.

The purpose of this work is to develop methods that allow the creation of a thermal microsystem with improved characteristics for measuring the velocity (flow rate) and temperature of gas streams, including under conditions of abrasive particles and radiation.

For the first time in work, the thermal micro-system layout in the thermistor probe of the anemometer and the temperature sensor in the form of a Schottky barrier made from a polytypic compound-silicon carbide is theoretically justified. It is shown that the use of single-crystal silicon carbide of certain polytype composition provides the following advantages of TAM:

1) A wide range of measured costs and high sensitivity (due to a controlled change in the electrophysical characteristics of the material);

2) High stability and reproducibility of the operating characteristics of the microsystem under extreme conditions (due to monocrystallinity, high Debye temperature and hardness, wide bandgap and erosion profiling capabilities);

3) The possibility of self-cleaning (due to high chemical and thermal resistance values). It is also worth mentioning that a patent for the invention of a thermal microsystem has been obtained.

The necessity of step-by-step solution of the problems of designing the SiC-thermal microsystem is pointed out, which, for example, is due, not to the study of the influence of conductive bonds, abrasive and radiation fluxes on the electrical properties of the elements of the microsystem.

4. The results of the study and their discussions

The study of the thermal regime of the microsystem, in which the thermal bonds between the elements are determined mainly by the conduction process, the properties of the material and the design features, is a model analysis of the distribution of the temperature field from a strongly heated element to a slightly heated one.. For comparison, 2 variants of the design and the thermal model of the microsystem, presented in Figure. 5, are proposed.

According to the obtained data, curves for the dependence of the electric current on the temperature of the model under study at two point (1), and the coldest point (2) itself, shown in the Fig.7, are plotted. Figure 7 shows that the thermal model this the though hole is preferable, in consequence of the fact that the temperature of the thermo – anemometer in working conditions has less effect on the thermometer located on the foot on the microsystem. In this case, the inverse thermal effect is excluded from the calculation since the working temperature of the thermometer is assumed to be equal to the temperature of medium being measure.

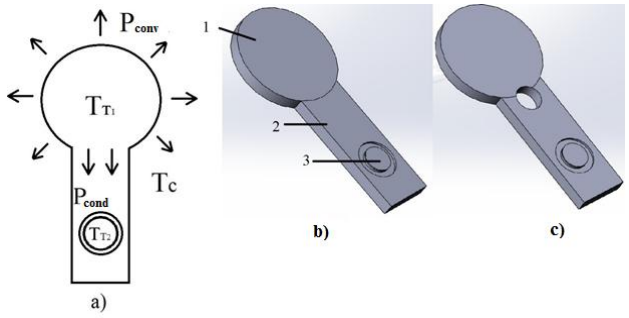

Figure. 5 *- Thermal model of microsystem (a), microsystem design without hole (b), microsystem design with hole (c). 1 - the site of the heat-loss anemometer; 2 - the leg; 3 - the site of the thermometer.*

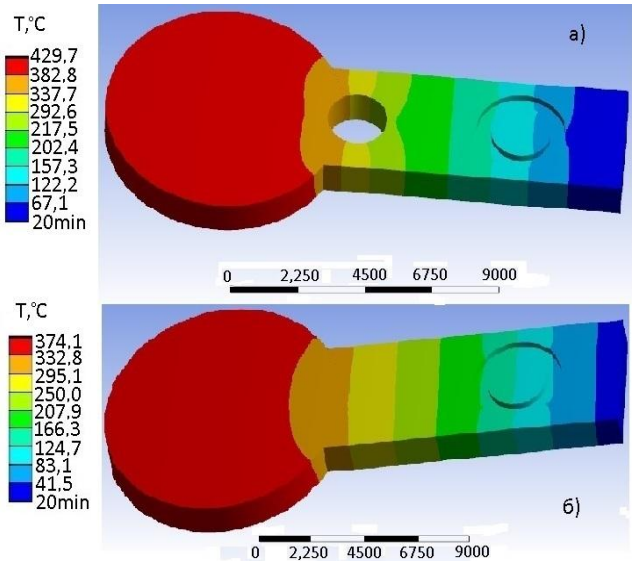

Figure 6 *– Temperature field in the microsystem.*

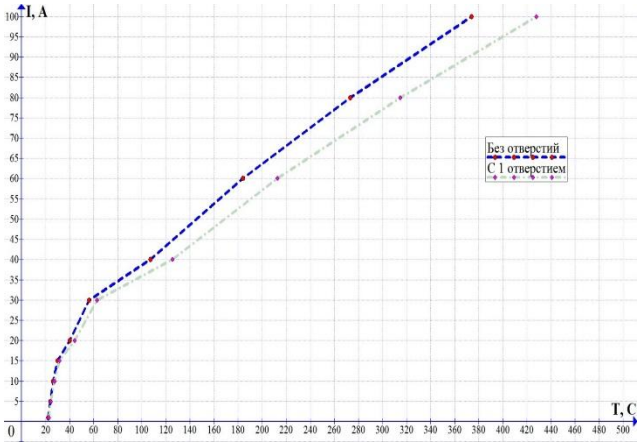

Figure 7 *- Graph of the temperature dependence of the microsystem at the "hot spot" itself on the magnitude of the electric current.*

5. Conclusion

In the course of the study, a method for calculating the micro-system was proposed, showing the mutual thermal effect of the elements. According to the data of the study, curves for the dependence of the electric current on temperature are plotted, as shown in Fig. 7.Based on the results of the simulation, it can be judged that the tested versions of the microsystem designs have significant temperature differences >50 ℃ in the presence of small design solutions

Reference

1. Baicar R.I., Varshava S.S., Potapchyk G.N., Chekyrin V.F.,// Pribori I tehnika exsperimenta. 1994. №3. C.158-163.

2. Karachinov V.A. Termoanemometr na osnove karbida kremnija // Trudy mezhdunar. Seminara «Poluprovodnikovyjj karbid kremnija i pribory na ego osnove». Novgorod, 1995.S.72-73.

3. Aljamovskijj A.A., Sobachkin A.A., Odincov E.V. Solid Works. Komp'juternoe modelirovanie v inzhenernojj praktike. SPb.: BVKh-Peterburg, 2005. 799 s.

4. Shlikhting.G. Teoria pogranichnogo sloya/ Per. c nem., M.: Nayka, 1974.C.70-72.

5. Lykov A.V. Teplomassoobmen: Spravochnik. M.: Ehnergija, 1978. 560 s.

DIAGNOSTICS OF THERMAL PIPES WITH SYMMETRIC STRUCTURE THERMAL IMPACT METHOD

Grand PhD in Engeneers Science Eng . Vladimir Karachinov [12] ,Phd Student Eng Daniil Evstigneev [12], Prof.,PhD in Engeneering sciences Eng. Alexander Abramov, , PhD Applicant Eng. Petrov Dmitriy [1 2]
Specialty microelectronics - Novgorod state University named after Yaroslav the wise [1]
Open Society - OKB "Planeta", Velikiy Novgorod [2]

Abstract: *On the basis of completed studies, including computer modeling of the morphology of the temperature field of heat pipes and thermal measurements in the framework of the experiment, a method was developed for diagnosing the quality of heat pipes with a symmetrical structure.*

KEYWORDS: diagnostics, heat pipe, temperature field, defect, visualization, simulation, thermal imaging system, isotherm.

1. Introduction

It is known that heat pipes (HP) historically belong to the class of special cooling devices and they can carry out high-speed transport of high-intensity heat flows beyond the localization of various heat sources within their own containment. Currently, HP's are widely used in various ground-based, airborne and space-based electronic systems, as well as in nuclear power engineering and, of course, in computer technology [1-5]. Therefore, high demands arc made on the reliability of HPs, and the methods and means of diagnosing them arc constantly evolving and improving. It should be noted that, along with ultrasound and X-ray methods, a certain scientific and practical interest in the quality control of products in the containment, within which phase transitions take place with absorption and heat release, are thermal methods. The greatest efficiency, reliability and sensitivity among them have thermal imaging, [6,7]. Despite the fact that in the scientific literature there is information about thermal imaging techniques for monitoring various objects, including pipelines, their direct transfer for diagnosing HP is fraught with a number of difficulties. They are caused, for example, by the variety of materials used for the manufacture of shells, wicks, heat transfer fluids, design solutions, etc. The work is devoted to approbation of the developed technique, including the use of field characteristics, for diagnosing HPs.

2. Research methodology

Experimental studies were conducted on a laboratory bench containing an IR - television system (KTP-326Ekh camera based on an uncooled thermal imaging module IR-113, $X = 8$
thermal receivers: (IR - pyrometer - Mastech MS6530; thermocouple XA) and PC with software. As the objects of study were selected profile aluminum pipes. The heat carrier in them was acetone or ammonia. Theoretical studies (modeling in the ELCUT and COSMOS environment) were performed using the finite element method [8, 9].

3. Research results and discussion

Analysis of the literature showed that the design of the TT mainly uses approximate engineering methods of thermal calculation, for example,

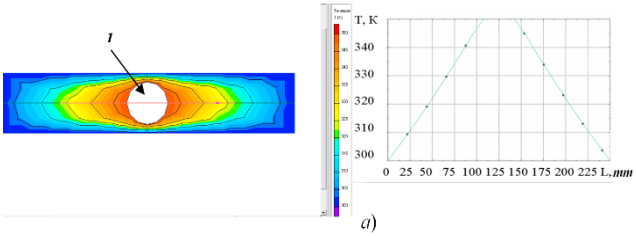

a)

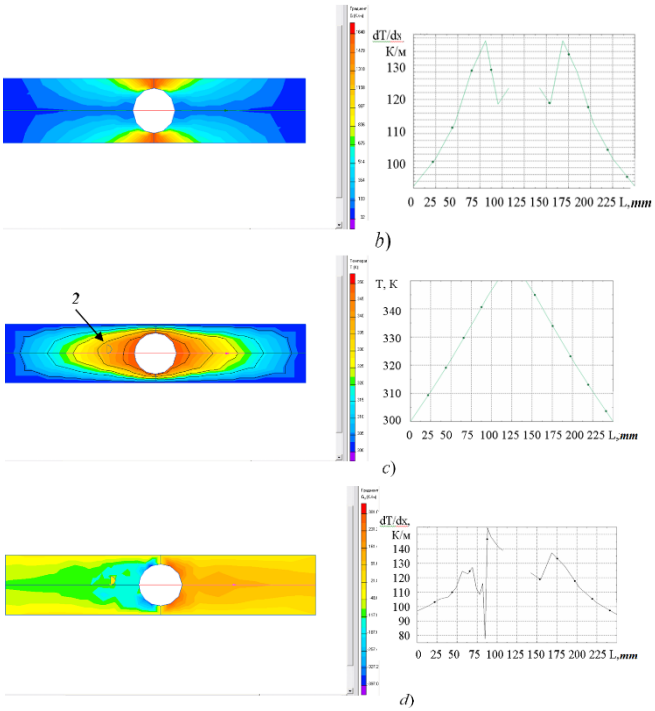

***Figure 1** - Features of the temperature field in an aluminum heat pipe. Method of field characteristics. Payment. (Pulsed Heat Source(PHS) operation time, τ = 100 s).*

a, *c - isotherms and temperature distribution along the selected circuit (1 - PHS; s -HP with defect: 2 - case defect, segment-air);*

b, *d - the field of temperature gradients and the distribution of the gradient along the selected contour (d-HP with a hull defect, segment-air).*

the basis of the theory of thermal circuits, and others. [1]. This is due to the complexity of accounting and descriptions of all phenomena occurring within the operating HP. As the initial thermal model of the profile HP, we have chosen the model of an anisotropic rod (Fig. 1) [1, 10]. A pulsed heat flow source (PHS) with insulated surfaces was located in the center on the surface of the rod. The studies used sources of round and rectangular shapes.

Taking into account the thermal inertia of the system, the maximum time of the PHS operation was x = 120 s. The thermal connection of the PHS with the HP surface was considered ideal. The original equation of heat conduction [10]:

(1) $$C_\rho \rho \frac{\partial T}{\partial t} = \lambda_x \frac{\partial^2 T}{\partial x^2} + \lambda_y \frac{\partial^2 T}{\partial y^2} + \lambda_z \frac{\partial^2 T}{\partial z^2} + q_0$$

where: *Cp* and p is the specific heat capacity and density of the material; *Xx, Xy, Xz* - thermal conductivity coefficients; ***q0*** - heat output per unit volume of sources of thermal energy; T is temperature; x, y, z - coordinates; within the framework of the formulated constraints, it was solved numerically (finite elements of a triangular shape were used) on a PC in the standard "ELCUT" environment.

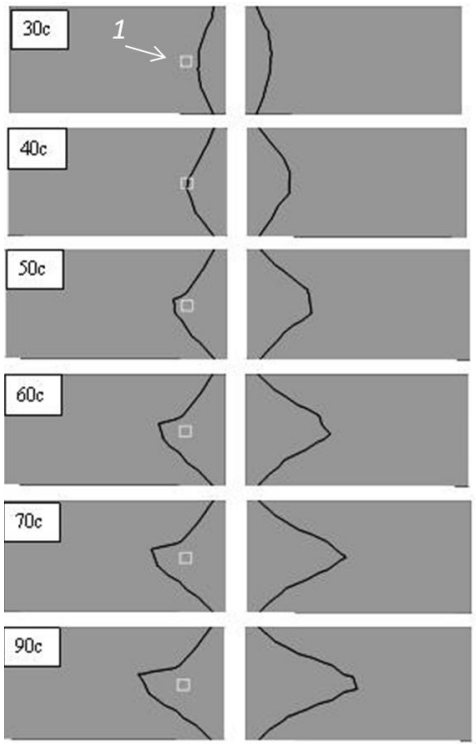

Figure 2 *- Changing the shape of the isotherm in time when there is a rectangular shape (air) in the body of the defect (1). Example: Aluminum HP, rectangular PHS. Calculation (isotherm scale, 90K).*

When constructing a mathematical model, initial and boundary conditions (of the first and third kind) [10], obtained from targeted experiments, were used:

1. At the initial moment of time, for the edges of all bodies included in the model, the temperature was constant:

(2) $$Ti,\tau = 0 = Ta = const$$

2. For all PHS edges, taking into account the isothermality of the surface, a condition of the first kind was set:

(3) $$T=Tp$$

On the edges of the HP model, a third kind conditions was specified, which in describes both convective and radiant heat exchange with the environment:

(4) $$\lambda_p \frac{\partial T}{\partial n} = -\alpha_k(T\text{-}Ta) - \beta(T^4\text{-}T_a^4)$$

Where: β - is a value equal to the product of the Stefan-Boltzmann constant (σ0 = 5.7 ■ 10-8 W $/m^2/K^4$) and the coefficient of radiation of the surface of the probe material; α_k- convection heat transfer coefficient. Heat flow diversion through conductive connections of HP fixture was not considered.
Qualitative analysis of the temperature field by color pictures, the shape and nature of the distribution of isotherms in HP allowed us to identify the following features (Fig. 1). The location of the PHS in the central part of the HP without a defect generates both the left and the right of the source a symmetrical structure of isothermal lines, as well as a symmetrical temperature distribution relative to the selected circuit (Fig. la). The specified value of the anisotropy of the thermal conductivity coefficient *X\ / Xy* = 40 led to the formation of isothermal lines with pointed tops. The nature of the temperature gradient change relative to the selected contour (Fig. lb) also emphasized the symmetric structure of the thermal field.

It is known that the magnitude and speed of transfer of heat flux in the HP depends on many factors, among which a significant role belongs to the defects of the wick structure, the body [1-3]. Most often, these defects may appear due to the imperfection of the HP manufacturing technology, and also be acquired during operation. Pores, cracks in the body of the HP significantly reduce the degree of tightness, and in terms of vibrations, shock can lead to early failure of the HP. Modeling the temperature fields of the HP with defects made it possible to understand the basic laws of change in the field characteristics, and therefore prepare the basis for the development of a diagnostic technique. Defects of regular geometric shape were chosen as the model: round, in the form of a segment, rectangular, triangular. The main variable physical characteristics of the defects were the thermal conductivity coefficient, as well as the density and specific heat capacity. Examples of simulation results of such systems are shown in Fig. lc, d and Fig. 2. It can be seen quite well that along with the change in the shape of isotherms, symmetry breaking with respect to the HP center, a defect with a low thermal conductivity coefficient most strongly changes the field of the temperature gradient.

3.2 Experimental studies

To create a pulsed local heating, a film resistive heater was used, which, through heat conductive paste (KPT-8), was attached to the IIP strictly in the center. Getting the original brightness contrast (image) was carried out with a horizontal position of the HP (on the edges), and to reduce the methodological errors, heat is removed from the surface of the pipe on both sides of the PHS occurred under conditions of free convection. It should be noted that well-known measures were taken, including shielding to reduce external illumination.

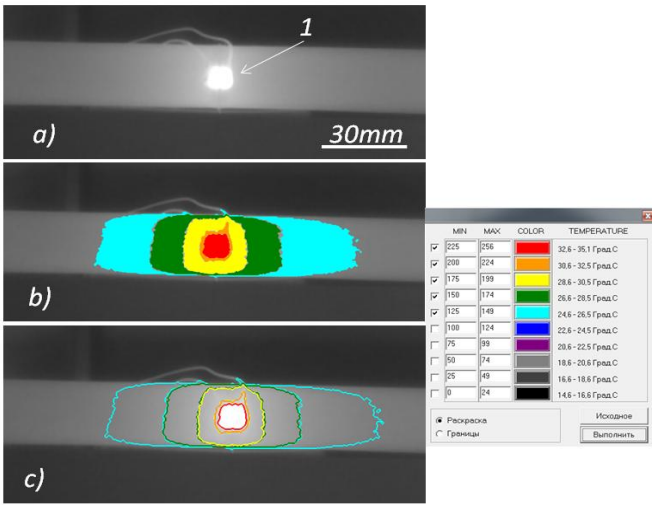

Figure 3 *- Visualization of the thermal field of an acetone heat pipe using the "Parus 5.0" program. Example. A photo. Experiment: (heating time, T = 45 s). a - the initial thermal brightness brightness contrast (1 - PHS); b - structure of thermal field zones (Thermogram mode, pseudo-coloring); c - evolution (slip) of isotherms (isoline mode).*

The transition from the image to the quantitative characteristics of the thermal state of the HP was implemented using the method of field characteristics (MFC) in the form of the developed universal software (software) ''Parus 5.0" [11]. It allowed to carry out image input (static and dynamic - video) both from a television camera via a video signal input board in a PC, and from a file in the "* .bmp" format. A typical example of visualization is shown in Fig.3. Considering that the experiment used a commercially available HP, without specially introduced defects, in the framework of this technique we can only talk about the features of the morphology of this temperature slice. The focal nature of its structure, which most likely can be associated with surface defects of the HP body, is quite clearly visible. And the asymmetry is most pronounced in the nature of the temperature distribution, relative to the PHS (it is difficult to transport heat to the left side of the IIP). It is clear that to establish the true causes of the asymmetry effect require additional research.

3. Conclusions

The method of the field characteristics, based on digital thermal imaging processing algorithms, allows you to create criteria for assessing the quality of the heat pipe.

4. Reference

1. Alekseev V.A., Arefyev V.A. Heat pipes for cooling and temperature control of electronic equipment M .: Energy, 1979. - 128 p.
2. Dan P.D., Ray D.A. Heat pipes: Trans. from English: M. Energy, 1979. - 272 p.
3. Karachinov V.A.Zashchita RES in extreme conditions. Special cooling devices. Tutorial. NovSU them. Yaroslav the Wise, Veliky Novgorod, 2007. - 176.
4. Lux, A.L., Matveev A.G. Investigation of high-performance ammonia heat pipes of energy-saving thermal control systems for large-sized spacecraft structures // Samara State University Bulletin. Natural science series. - № 6 (56). - 2007. - p. 401
5. Seryakov A.V., Karachinov V.A., Ilyin S.V., Ivshin K.A. Special cooling system for matrix photodetectors / 19th Int. scientific and technical conf. "Modern Television and Radioelectronics": Proceedings. - Moscow. FSUE MKB "Electron". 2011. - pp. 78-79.
6. Nondestructive Testing Handbook.V.3. Infrared and Thermal Testing. ASNT.2001. 714p.
7. Vavilov V.P. Infrared thermography and thermal control. 2nd edition. - M .: Publishing House "Spectr", 2013. - 544 p.
8. ELCUT. Simulation of two-dimensional fields by the finite element method. User's manual. Research and production cooperative "Tor". St. Petersburg, .1989 - 2006.
9. Zenkevich O. Method of finite elements in engineering. - M .: Mir, 1975. 544 p.
10. Lykov A.V. Heat and mass transfer. - M .: Energy. 1978. - 480 p.
11. Karachinov V.A., Ilyin S.V., Karachinov D.V., Dzherenov I.G. Application of the method of field characteristics for the study of microsystems with burning based on profiled silicon carbide crystals. Vestn. Novg. state un-that .. Ser Tech. science. 2011, №65. - p.23-28.

AN EFFICIENT COMBINATION OF WATER TREATMENT AND ELECTRICITY GENERATION BY DIFFERENT MICROORGANISMS

Assoc. Prof. PhD M. Nicolova[1], Assoc. Prof. PhD I.Spasova[1], Assoc. Prof. PhD P. Georgiev[1], Prof. PhD V. Groudeva[2] , Prof. DSc S. Groudev[1]
[1]University of Mining and Geology "St. Ivan Rilski"
[2]Sofia University "St. Kliment Ohridski"
spasova@mgu.bg

Abstract: *A sample of acid drainage waters generated after rainfall in a dump of low-grade copper ores and mining wastes was tested under laboratory conditions to combine the treatment of such waters with the subsequent generation of electricity. This combination was possible and efficient due to the fact that the same microorganisms participated in both processes, i.e. in the water treatment and in the electricity generation. These microorganisms were heterotrophs related to two main groups: of sulphate-reducing and iron-reducing bacteria. These bacteria were anaerobes, with efficient growth and activity at pH within 3.0 – 3.5 using the organic donors of energy and avoiding the precipitation of the trivalent iron*

Key words: *WATER TREATMENT, ELECTRICITY GENERATION, BACTERIA*

1. Introduction

The extraction of some valuable components (mainly non-ferrous and precious metals but also uranium, iron and some rare elements) from sulphidic ores, concentrates and even from some mineral wastes by means of different microorganisms, mainly chemolithotrophic bacteria and archaea, is largely and steadily increased in industrial-scale application in several countries located in the five continents. At the same time, most of these activities are connected with the generation of acid drainage waters, which apart from the sulphuric acid, contain several toxic elements, mainly heavy metals, radionuclides and arsenic. Some of these components are recovered and used as useful and valuable products. Apart from this, the treatment of the residual waste waters by adding some biodegradable organic substrates and suitable heterotrophic bacteria, mainly such using sulphates and/or ferric ions as electron acceptors, can be used for generation of electricity by means of constructed fuel cells (Rabaey and Verstraete, 2005; Du et al., 2007; Spasova et al., 2014, 2016; Groudev, 2015).

2. Materials and Methods

In this study drainage waters generated during the bioleaching of a polymetallic sulphide ore were subjected to treatment by means of lab-scale permeable reactive multibarriers. The multibarriers were plastic cylindrical columns 40 cm high, with an internal diameter of 10 cm. The columns were filled with a mixture of limestone (crushed to a particle size of minus 10 mm) and a biodegradable organic matter consisting of a mixture of spent mushroom compost, fresh leaf compost, animal manure and saw dust. The columns were inoculated by means of inocula of three types: of sulphate-reducing bacteria, of iron (III) – reducing bacteria and of mixed cultures of sulphate and iron-reducing bacteria. The microorganisms used in these experiments were preliminary adopted to grow and to be active at relatively low pH levels (within 3.4 – 4.0) to avoid considerably the precipitation of the ferric iron present in the pregnant solutions. These solutions were enriched in soluble organic compounds and portions of them were used separately from each other in the experiments for electricity generation by means of microbial fuel cells. These cells were also Plexiglas cylindrical columns 40 cm high, with an internal diameter of 10 cm. A perforated graphite – Mn^{4+} anode and a graphite – Fe^{3+} cathode were located in the bottom and in the top sections of the column, respectively. The two sections were separated by a permeable barrier of 5 cm thickness consisting of a 2.5 cm layer of glass wool and a 2.5 cm layer of glass beads. The feed stream, i.e. the effluents from the multibarrier, was supplied to the bottom anodic sections of the column and effluents passed through the cathodic section and continuously exited at the top. Air was injected during the treatment to the cathodic section.

The quality of the waters treated by means of the permeable reactive multibarriers and by the microbial fuel cells was monitored at the inlet and the outlet of these components of the system for the water cleaning and electricity generation. The parameters measured in situ included: pH, Eh, dissolved oxygen, chemical composition, and temperature. The isolation, identification and enumeration of microorganisms were carried out by the classical physiological and biochemical tests (Karavaiko et al., 1988) and by the molecular PCR methods (Sanz and Köchling, 2007; Escobar et al., 2008).

3. Results and Discussion

Data about the composition of the polluted waters before and after their treatment by means of sulphate-reducing bacteria, as well as by means of mixed populations of sulphate-reducing and iron (III)–reducing bacteria are shown in Table 1. The treatment by means of sulphate-reducing bacteria able to oxidize the organic substrates to CO_2 as a final product was the most efficient. These bacteria were related to the genera *Desulfovibrio, Desufobacter* and *Desulfococcus.* It must be noted that strains related to one and the same genus from their group can differ considerably from each other with respect to this ability. Another group of sulphate-reducing bacteria (related to the genera *Desulfomonas, Desulfobulbus* and *Desulfomicrobium*) were able to oxidize the organic substrates only partially to CO_2 and acetate and usually reduced the sulphates at lower rates than the sulphate-reducing bacteria related to the first group. However, some of the strains related to the species of this second group also differ considerably from each other with respect to their ability to oxidize the organic substrates.

The strains of iron (III)-reducing bacteria used in this study also can differ from each other with respect to their ability to degrade the organic sources to energy. These bacteria reduce the ferric iron to the ferrous state and in this way decrease considerably the pollution of their habitats, especially of these containing large amounts of sulphides.

Table 1. Treatment of polluted waters by means of different microorganisms

Parameters	Initial contents of the waters	Data about the water after treatment by:	
		Sulphate-reducing bacteria	Mixed population of sulphate and iron reducing bacteria
pH	1.85 – 3.74	6.80 – 7.21	6.84 – 7.25
Eh, mV	(+327)–(+541)	(-181)–(-268)	(-178)–(-284)
Total dissolved solids, mg/l	3580 - 5940	512 - 1380	532 - 1308
Dissolved O_2, mg/l	1.0 – 1.8	0.1 – 0.3	0.1 – 0.3
Dissolved organic carbon, mg/l	2.3 – 3.7	275 - 523	260 - 509
Sulphate, mg/l	710 - 1645	170 - 327	181 - 320
Cu, mg/l	9.5 – 8.2	9.5 - 82	<0.1 – 0.29
Zn, mg/l	14 - 97	14 - 97	<0.1 – 0.25
Co, mg/l	3.2 - 14	3.2 - 14	<0.1 – 0.21
Cd, mg/l	0.1 – 0.5	0.1 – 0.5	<0.1 – 0.3
Mn, mg/l	4.4 - 18	0.21 – 0.23	0.18 – 0.25
Fe, mg/l	954 - 1720	3.7 – 7.1	2.6 – 6.4

The treatment of the polluted waters by means of iron (III)-reducing bacteria was not very efficient. However, these bacteria were also able to transfer electrons from the dissolved organic substrates in the anoxic section of the microbial fuel cells via their own respiratory chains and extracellular matrix directly to the anode located also in this section of the microbial fuel cells. It must be noted that some mixed cultures of sulphate and iron reducing bacteria were very efficient not only for cleaning of the polluted waters but also for electricity generation (Table 2).

Table 2. Electricity generation by means of different microorganisms

Microorganisms	Power, mW/m^2
Pure culture of sulphate-reducing bacteria:	
Desulfovibrio desulfuricans	530 – 1040
Desulfobacter multivorans	374 – 780
Desulfobulbus elongates	358 – 695
Mixed cultures of sulphate-reducing bacteria	410 - 910
Pure cultures of iron (III)-reducing bacteria:	
Shewanella loihica	312 – 765
Geobacter metallireducens	215 – 615
Mixed cultures of iron (III) reducing bacteria	345 – 705
Mixed cultures of sulphate and iron (III)-reducing bacteria	307 - 810

It is also essential to be mentioned that some microorganisms related to one the same taxonomic species can differ considerably from each other with respect to their ability to generate electricity even from one and the same organic substrate under one and the same experimental conditions.

The microbial sulphate reduction in the multibarriers was efficient due to the large amount not only of sulphates but also of soluble biodegradable organic substrates generated from the initial organic matter by the action of the anaerobic heterotrophic bacteria present in this system. The high residual concentrations of such soluble organic substrates and sulphates in the multibarrier effluents, together with the very low residual concentrations of toxic heavy metals, the negative electrochemical potential, the neutral pH and the practical absence of dissolved oxygen , made these effluents very suitable for electricity generation by the microbial fuel cells.

Conclusion

Some mixed cultures of sulphate-reducing and iron (III)-reducing bacteria are very efficient for generation electricity by means of microbial fuel cells. The best strains from these bacteria are characterized to and efficient degradation of the organic substrates at relatively low pH (about 3.5 – 4.0) which is usually quite low for these bacteria

Acknowledgements: The authors expressed their gratitude to the National Science Fund of Bulgaria for the financial support connected with this study (Project T02/2/2014).

References

Du, Z., Li, H., Gu, T., 2007. A state of the art review on microbial fuel cells: A promising technology for wastewater treatment and bioenergy, Biotechnology Advances, 25, 464 – 482.

Escobar, B., Bustos K., Morales, G. and Salazar, O., 2008. Rapid and specific detection of *Acidithiobacillus ferrooxidans* and *Leptospirillum ferrooxidans* by PCR, Hydrometallurgy, 92, 102 – 106.

Groudev, S. N., 2015. Biohydrometallurgy in Bulgaria – achievements and perspectives, Acta Microbiologica, 1, 81 – 92.

Karavaiko, G.I., Rossi, G., Agate, A.D., Groudev, S.N. and Avakyan, Z.A. , 1988. Biogeotechnology of Metals. Mannual GKNT Center for International Projects, Moscow.

Sanz, J.L. and Köchling, T., 2007. Molecular biology techniques used in wastewater treatment: An overview. Process Biochemistry 42, 119–133.

Spasova, I., Nicolova, M., Georgiev, P., Groudev, S., 2014. Mine waters cleaning connected with electricity generation, Annual of the University of Mining and Geology, Sofia, 57 (II), 137 – 139.

Spasova, I., Nicolova, M., Georgiev, P., Groudev, S., 2016. Bioleaching of metals from a waste ore in connection with copper recovery, environment protection and electricity generation, Annual of the University of Mining and Geology, Sofia, 59 (II), 167 – 171.

Rabaey, K., Verstraete, W., 2005. Microbial fuell cells: novel biotechnology for energy generation, Trends in Biotechnology, 23 (6), 291 – 298.

AN EXPERIMENTAL STUDY ON CUTTING FORCES AND SURFACE ROUGHNESS IN MQL MILLING OF ALUMINUM 6061

B.Sc. Conger D.B.[1], M.Sc. Emiroglu U.[1], Assoc. Prof. M.Sc. Uysal A. PhD.[1], Prof. M.Sc. Altan E. PhD.[1]
[1] Yildiz Technical University, Department of Mechanical Engineering, Besiktas, Istanbul, 34349, Turkey

congerdervis@gmail.com

Abstract: *The minimum quantity lubrication (MQL) and dry machining operations are two types of environmentally friendly processes that have potentials to replace with conventional cooling methods. In recent years, the studies have been performed on the environment-friendly lubrication methods such as MQL method in machining operations. These studies have also focused on the usage of vegetable cutting fluids instead of mineral based oils due to increasing awareness to the environment and human health. In this experimental study, Aluminum 6061 was machined under dry and MQL conditions and the cutting force components and surface roughness values were measured. The experiments were carried out by CNC milling machine tool at three different cutting speeds and constant depth of cut and feed. The vegetable cutting fluid was pulverized to the rake face by using single nozzle and double nozzles at two flow rates during MQL milling. Cutting force components and surface roughness values were compared for minimum quantity lubrication and dry milling operations of Aluminum 6061.*

Keywords: CUTTING FORCE, SURFACE ROUGHNESS, MQL MACHINING, ALUMINUM 6061

1. Introduction

The challenge of modern machining industry is mainly focused on achievement of high quality in terms of workpiece dimensional accuracy, surface finish, high production rate, less wear on the cutting tools, economy of machining, reducing environmental impact etc. [1]. In machining of ferrous and other high strength materials, the temperature rises with the cutting speed and the tool strength decreases, leading to faster tool wear and failure [2]. In order to reduce the temperature in the cutting zone, traditional flood cooling strategies have been commonly used. However, there are critical needs to reduce the usage of cutting fluids in machining process in order to decrease their environmental and cost effects [3]. As is known, the majority of cutting fluids is based on mineral oils and contains heavy chemicals which are hazardous to the human health and environment [4, 5]. Therefore, the usage of cutting fluids needs to be limited. For this purpose, minimum quantity lubrication (MQL) technique is utilized which is a promising, attractive, efficient and environmental friendly technique of cooling and lubrication [6].

In MQL technique, a very small amount of lubricant/coolant is mixed with air to form aerosol, which is sprayed at a high pressure in the cutting zone with the help of a nozzle. This system consists of an atomizer, cutting fluid pump, discharge nozzle, etc. The atomizer works as an ejector in which high pressure air is used to atomize the coolant. Atomized coolant is then delivered to the machining zone by the air in a low-pressure distribution system. Due to the venturi effect in the mixing chamber, partial vacuum sucks the cutting fluid from the oil pump where it is maintained at a constant hydraulic load. The air passing through the mixing chamber atomizes the coolant stream into aerosol of micron-sized particles. When this aerosol is sprayed in the cutting zone as mist, it works as coolant as well as lubricant and penetrates deep into the tool-workpiece interface [2]. In MQL method, the cutting fluid can be pulverized in the range between 0.01-2 l/h instead of the 50-1000 l/h in the case of conventional lubrication/cooling systems. Some MQL advantages against other lubrication/cooling systems are: reduction of cutting fluid consumption, cost and tool wear, improvement of surface roughness, diminution decrease of the environmental and worker health hazards and improve lubrication than conventional lubrication/cooling system. The cutting fluid is used in such small quantities that it is practically consumed in the process, eliminating the fluid disposal problems. In addition, chips produced are nearly clean from cutting fluid, which are easily recyclable [7].

In literature, there are several studies on MQL machining. Mulyadi et al. [8] compared to dry, flood, and MQL conditions and pointed that selecting MQL environment can be an intermediate strategy for reducing direct electrical energy requirements, global warming potential, human toxicity, and acidification in machining processes. The MQL method provides a good compromise in terms of tool life, when compared to dry machining. Also it performance was very close to machining under flood coolant environment. Ginting et al. [9] presented an industrial situation in a local small to medium sized enterprise (SME) in Western Australia to determine the technical, economic and environmental benefits of the replacement of traditional flood cooling with MQL. The use of MQL reduced the greenhouse gas emissions and eco-toxicity associated with the disposal of the contaminated liquid. It was found that this alternative cooling method increased the performance of the metal cutting operation. Finally, the replacement of traditional fluid cooling with MQL cooling system can help attain the three pillars of sustainability: economic, environmental, and social. Another implementation example of MQL is that Ford Motor Company began applying MQL to aluminum transmission components in 2005, and by 2008 had over 200 MQL machining centers in operation machining Aluminum transmission cases, torque converter housings, and valve bodies at two plants in North America. MQL machining is Ford's current standard machining method for these components, and is being implemented in new high-volume machining lines globally. Ford began machining aluminum engine heads and cast iron engine blocks at two plants in Europe in 2011; as in the case of transmissions, MQL is now the primarily standard method for machining cast iron engine blocks and aluminum engine blocks

and heads, although wet machining is still used for some specialized operations. New engine MQL modules have been installed in Brazil and China [10]. Berzosa et al. [11] reached better surface roughness results in MQL method than that in dry drilling of magnesium alloy. Sun et al. [12] observed better surface roughness in MQL turning of Ti-5553 alloy when compared to flood coolant and cryogenic cooling. Kumar et al. [13] performed turning experiments on AISI 4340 stainless steel under dry, flood cooling, and MQL conditions. Researchers reported that the surface quality improved by 7% to 10% with MQL when compared with flooded supply of lubricants. In Ramana's study [14], turning of Ti-6Al-4V alloy was performed under dry, flood cooling and MQL conditions. Based on the experimental results, the cutting performance of MQL condition showed better results as compared to dry and flood cooling conditions in reduction of surface roughness. Oliveira et al. [15] compared the influence of cryogenic cooling, MQL method, and flood cooling on end milling of Inconel 718 alloy and it was concluded that the MQL method provided the lowest levels of tool wear at the same cutting conditions and the resulting force levels were similar in both methods flood and MQL using water based cutting fluid. Joshi et al. [16] conducted turning experiments on Inconel 800 under dry, flood cooling, and MQL conditions and compared the surface roughness and flank wear results with each other. The MQL method showed the best performance. Aslantas and Cicek [17] determined that the use of MQL provides important advantages in terms of tool wear, burr formation and surface roughness for micro-milling of Inconel 718 superalloy.

In this experimental study, dry and MQL milling processes were performed on Aluminum 6061 to evaluate and compare the cutting force components and surface roughness values. In MQL milling, the cutting fluid was applied to the rake face through single nozzle and double nozzles at two flow rates.

2. Experimental Study

In experimental studies, slots were machined on Aluminum 6061-T651 parts by a CNC milling machine which chemical composition is given in Table 1. The workpiece parts were prepared in the dimension of 140x170x30 mm.

Table 1. *Chemical Composition of Aluminum 6061-T651*

Si %	Fe %	Cu %	Mn %	Mg %	Cr %
0.76	0.63	0.3	0.15	0.99	0.17

In milling operations, APHT 100308FR-27P uncoated cutting inserts were used and mounted two inserts on a diameter of 16 mm end mill. The milling experiments were conducted at a constant deep of cut of 1.5 mm, feed of 0.1 mm/rpm and three different cutting speeds as 200 m/min, 250 m/min, and 300 m/min under dry cutting and MQL conditions. In MQL method, milling experiments were performed by applying the cutting fluid to the rake face at total 26 ml/h and 52 ml/h through single nozzle and double nozzles as seen in Table 2 and Fig.1 due to understanding the effects of cutting fluid distribution on surface roughness and cutting force components.

In MQL milling, a micro lubrication system was used and a commercial vegetable cutting fluid was selected. The global lubricant is expected to reach 43.9 million tons in 2022. Cutting fluids represent about 5% of the global lubricant market, with Asia as the largest consumer. Availability of mineral based oils is limited as they are finite source and decreasing steadily whereas vegetable based cutting fluids are sustainable. Vegetable oils are evolving as metalworking fluids due to its higher biodegradability and ability to minimize the waste treatment costs. It also reduces the health risks to operators which were quiet common with petroleum based mineral oils due to their lower toxicity [18].

Table 2. *MQL conditions*

Conditions	Flow rate (ml/h)	MQL pressure (bar)	Nozzle distance (mm)	Nozzle angle (°)
Dry	-	-	-	-
MQL with single nozzle	26	5	30	45°
MQL with single nozzle	52			
MQL with double nozzles	13 13			
MQL with double nozzles	26 26			

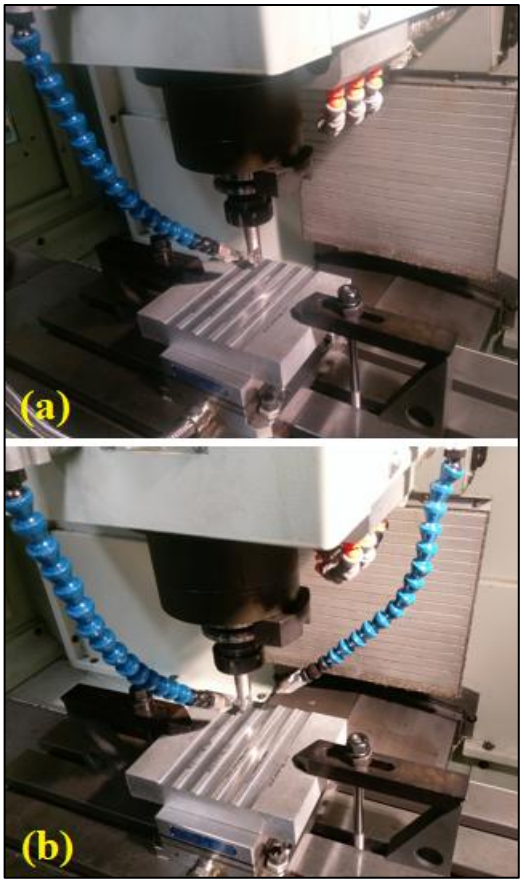

Fig.1. *Machine tool set-up for MQL milling with a) single nozzle and b) double nozzles*

Surface roughness (R_a) measurements of milled slots were performed by using Mitutoyo Surftest SJ-210 surface roughness tester. The dimension length was adjusted as 0.8 mm and the resolution of tester is 0.002 µm. During surface roughness measurements, 10 (ten) measurements were done on each surface and arithmetic means were calculated. The cutting forces were measured by Kistler 92578A dynamometer which the workpiece was mounted on.

3. Results and Discussion

3.1 Surface Roughness

Depending on the surface roughness measurement results, the minimum surface roughness was obtained at the cutting speed of 200 m/min in MQL milling with double nozzles at 26 ml/h of flow rate from each nozzle whereas the maximum surface roughness was measured in dry milling at the cutting speed of 300 m/min (Fig.2). The usage of MQL method gave better surface roughness results than that measured in dry milling. Additionally, it can be said that the surface roughness increased with increase of the cutting speed for all selected conditions.

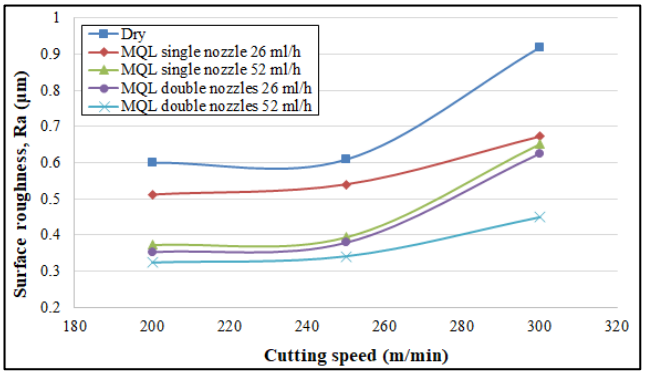

Fig. 2. *Variation of surface roughness with cutting conditions*

In MQL milling, the utilization of single nozzle or double nozzles affected the surface roughness. When the total flow rate is 26 ml/h, surface roughness decreased as 31%, 29.8% and 7% by using double nozzles at the cutting speed of 200 m/min, 250 m/min and 300 m/min, respectively as comparing with single nozzle. This is because of the reaching cutting fluid effectively to the cutting zone. Similarly, the effect of double nozzles on the surface roughness at the total flow rate of 52 ml/h, surface roughness decreased as 13%, 13.3%, and 31% at the cutting speed of 200 m/min, 250 m/min and 300 m/min, respectively, as comparing with single nozzle.

Additionally, surface roughness measurements showed that the flow rate of aerosol affected the surface roughness. In MQL milling by utilizing single nozzle, surface roughness decreased as 27.2%, 27.1%, and 3.2% at cutting speeds of 200 m/min, 250 m/min and 300 m/min, respectively, when the flow rate increased from 26 ml/h to 52 ml/h. At the same conditions, the decreases in surface roughness were determined as 8.2%, 9.9%, and 28.1% when the cutting speeds were 200 m/min, 250 m/min, and 300 m/min, respectively for double nozzles.

3.2 Cutting Force and Feed Force

As expected, the cutting force components decreased with increase of cutting speed. Based on the measurements, the minimum cutting forces and feed forces observed at the cutting speed of 300 m/min in MQL milling with double nozzles at flow rate of 13 ml/h from each nozzle whereas the maximum cutting forces and feed forces were measured in dry milling at the cutting speed of 200 m/min (Figs. 3, 4).

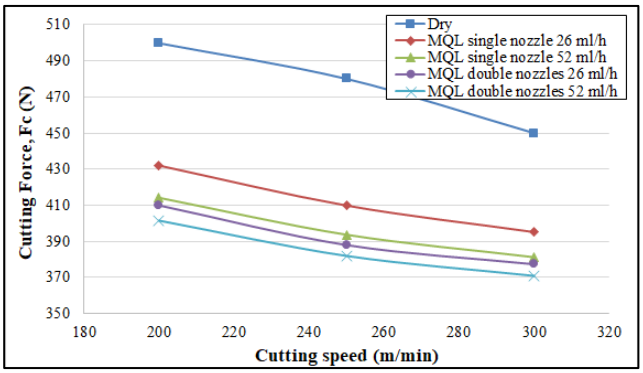

Fig. 3. *Variation of cutting forces with cutting conditions*

In MQL milling by utilizing double nozzles at the total flow rate of 26 ml/h, the feed forces decreased as 7.8%, 15.2%, and 18.2% at the cutting speeds of 200 m/min, 250 m/min, and 300 m/min, respectively when comparing the single nozzle. Under the same circumstances, the cutting forces decreased as 5.1%, 5.2%, and 4.5%. As investigating the effects of double nozzles on the cutting forces at the total flow rate of 52 ml/h, the cutting forces decreased by approximately 3% for the selected cutting speeds when comparing to single nozzle. In addition, the feed forces reduced by 14.4%, 17.5%, and 19.3% at the cutting speeds of 200 m/min, 250 m/min, and 300 m/min, respectively.

In MQL milling with single nozzle, the cutting force measurements showed that the cutting forces decreased as 4.1%, 3.9%, and 3.5% and the feed forces decreased as 3.5%, 7%, and 10% at the cutting speeds of 200 m/min, 250 m/min, and 300 m/min, respectively when the flow rate increased from 26 ml/h to 52 ml/h.

Regarding to the effects of aerosol flow rate on the cutting force components in MQL milling with double nozzles, the cutting forces decreased as 2.1%, 1.5%, and 1.7% whereas the feed forces reduced by 10.4%, 9.6%, and 11.6% at the cutting speeds of 200 m/min, 250 m/min, and 300 m/min, respectively when the flow rate increased from 26 ml/h to 52 ml/h.

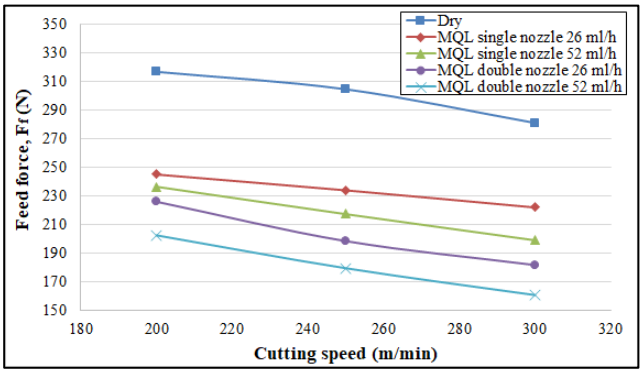

Fig. 4. *Variation of feed forces with cutting conditions*

4. Conclusion

In this experimental study, the effects of cutting conditions on the cutting force components and surface roughness were investigated in milling of Aluminum 6061. In experiments, three

different cutting speeds were selected while the depth of cut and feed rate were kept constant. Depending on the surface roughness and cutting force measurements, the conclusions could be expressed as follows;

- MQL milling gave lower surface roughness values than the dry cutting.
- In MQL milling, the increment of aerosol flow rate caused a reduction on surface roughness values.
- It was observed that lower surface roughness values were obtained by applying same total flow rate through double nozzles instead of single nozzle.
- The cutting force and feed force values were lower in MQL milling than those in dry cutting.
- In MQL milling, the cutting forces and feed forces decreased with increase of aerosol flow rate.
- Lower cutting forces and feed forces were observed by utilizing same total flow rate through double nozzles instead of single nozzle in MQL milling.

References

[1] R.K Suresh, G.Krishnaiah, P.Venkataramaiah. An Experimental Investigation with Minimum Quantity Lubrication and its Comparison with Various Vegetable Oil Based Cutting Fluids during Turning. Materials Today: Proceedings 4 (2017) 8758–8768.

[2] Anuj Kumar Sharma, Arun Kumar Tiwari, Amit Rai Dixit. Effects of Minimum Quantity Lubrication (MQL) in machining processes using conventional and nano fluid based cutting fluids: A comprehensive review. Journal of Cleaner Production 127 (2016) 1-18.

[3] Zhiqiang Liu, Qinglong An, Jinyang Xu, Ming Chen, Shu Han. Wear performance of (nc-AlTiN)/(a-Si3N4) coating and (nc-AlCrN)/(a-Si3N4) coating in high speed machining of titanium alloys under dry and minimum quantity lubrication(MQL) conditions. Wear 305(2013)249–259.

[4] Radoslaw W.Maruda , Grzegorz M.Krolczyk , Eugene Feldshtein, Piotr Nieslony ,Bozena Tyliszczak , Franci Pusavec. Tool wear characterizations in finish turning of AISI1045 carbon steel for MQCL conditions. Wear372-373(2017)54–67.

[5] O. Pereira, J.E. Martín-Alfonso, A. Rodríguez, A. Calleja, A. Fernandez-Valdivielso , L.N. Lopez de Lacallei. Sustainability analysis of lubricant oils for minimum quantity lubrication based on their tribo-rheological performance. Journal of Cleaner Production 164 (2017) 1419-1429.

[6] Anil Kumar, Sudarsan Ghosh, S. Aravindan. Grinding performance improvement of silicon nitride ceramics by utilizing nanofluids. Ceramics International 43 (2017) 13411–13421.

[7] E.Benedicto, D.Carouc, E.M.Rubio. Technical, Economic and Environmental Review of the Lubrication/Cooling Systems used in Machining Processes. Advances in Material & Processing Technologies Conference, Procedia Engineering 184 (2017) 99 – 116.

[8] Ismet Hari Mulyadi, Vincent Aizebeoje Balogun, Paul T. Mativenga. Environmental performance evaluation of different cutting environments when milling H13 tool steel. Journal of Cleaner Production 108 (2015) 110-120.

[9] Yogie Rinaldy Ginting, Brian Boswell, Wahidul Biswas and Nazrul Islam. Advancing Environmentally Conscious Machining.12th Global Conference on Sustainable Manufacturing. Procedia CIRP 26 (2015) 391 – 396.

[10] Bruce L. Tai, David A. Stephenson, Richard J. Furness, Albert J. Shih. Minimum Quantity Lubrication (MQL) in Automotive Powertrain Machining. 6th CIRP International Conference on High Performance Cutting, HPC2014, Procedia CIRP 14 (2014) 523 –528.

[11] F. Berzosa, B. de Agustina, E.M. Rubio. Tool Selection in Drilling of Magnesium UNSM11917 Pieces under Dry and MQL Conditions based on Surface Roughness. Advances in Material & Processing Technologies Conference, Procedia Engineering 184 (2017) 117 – 127.

[12] Y. Sun, B. Huang, D.A. Puleo, I.S. Jawahir. Enhanced Machinability of Ti-5553 Alloy from Cryogenic Machining: Comparison with MQL and Flood-cooled Machining and Modelling. 15th CIRP Conference on Modelling of Machining Operations, Procedia CIRP 31 (2015) 477 – 482.

[13] Sanjeev Kumar, Dilbag Singh, Nirmal S. Kalsi. Analysis of Surface Roughness during Machining of Hardened AISI 4340 Steel using Minimum Quantity lubrication. 5th International Conference of Materials Processing and Characterization (ICMPC 2016), Materials Today: Proceedings 4 (2017) 3627–3635.

[14] M.Venkata Ramana. Optimization and Influence of Process Parameters on Surface Roughness in Turning of Titanium Alloy under Different Lubricant Conditions. ICAAMM-2016, Materials Today: Proceedings 4 (2017) 8328–8335.

[15] Gleiton de Paula Oliveira, Maria Cindra Fonseca, Anna Carla Araujo. Residual stresses and cutting forces in cryogenic milling of Inconel 718. 8th CIRP Conference on High Performance Cutting (HPC 2018) Procedia CIRP 77 (2018) 211–214.

[16] Kamal Kishore Joshi, Ramanuj Kumar, Anurag. An Experimental Investigations in Turning of Incoloy 800 in Dry, MQL and Flood Cooling Conditions. 2nd International Conference on Materials Manufacturing and Design Engineering , Procedia Manufacturing 20 (2018) 350–357.

[17] K. Aslantas, A. Çiçek. The effects of cooling/lubrication techniques on cutting performance in micro-milling of Inconel 718 super alloy. 8th CIRP Conference on High Performance Cutting (HPC 2018), Procedia CIRP 00 (2018) 000–000.

[18] Kishor Kumar Gajrani, M. Ravi Sankar. Past and Current Status of Eco-Friendly Vegetable Oil Based Metal Cutting Fluids. 5th International Conference of Materials Processing and Characterization (ICMPC 2016), Materials Today: Proceedings 4 (2017) 3786–3795.

FLANK WEAR OF SURFACE TEXTURED TOOL IN DRY TURNING OF AISI 4140 STEEL

Mech. Eng. Eskizara H. B.[1], R. Assist. Emiroglu U.[2], Prof. Dr. Altan E.[3]
Department of Material and Manufacturing Technologies, Yildiz Technical University – Istanbul, Turkey[1,2,3]
E-mail: [1]huseyin.eskizara@gmail.com, [2]emiroglu@yildiz.edu.tr, [3]ealtan@yildiz.edu.tr

Abstract: *Surface texturing on a cutting tool is a process which can provide reduction in friction, improved performance of a contact interface and a better tool life. In this paper, influence of surface texturing on tool wear of both textured and non-textured tools were compared. Different textures were applied on coated carbide tools by Femtosecond laser to enchance the wear resistance. Dry cutting experiments on AISI 4140 (32 HRC) were carried out with conventional cutting inserts having parallel and perpendicular textured sufaces to the cutting edge on the flank face. Finally, results showed that surface texturing of cuttting insert was found to be beneficial to the decrease of the flank wear.*

KEY WORDS: SURFACE TEXTURED TOOL, NON-TEXTURED TOOL,FLANK WEAR, DRY TURNING

1. Introduction

Machining industries will change their processes as dry machining in the next years because of environmental protection laws for occupational safety and health regulations. For this reason, the importance of dry machining increasing day by day. The advantages of dry machining includes non-pollution of the nature, no residue on the swarf which will be rejected in reduced disposal and cleaning costs, no danger to health and is allergy free. Moreover, it offers cost reduction in machining. [1] On the other hand, at dry machining tool wear, adhesion between tool and chip, the friction forces and cutting temperature become more important.

Tool wear is the most important phenomenon for dry machining which effects the parts quality, surface roughness and production costs directly. Because of this significant effect, researchers are developing a variety of methods to reduce tool wear. Several authors have studied the surface texturing phenomenon and provided their justification for improving machinability with different techniques for performing surface texturing on the tool. In recent years, several studies have revealed that surface-textured cutting tools can effectively reduce the tool wear, thereby improving tool anti-wear performance, reducing the friction between the tool and chips, and lowering the cutting temperature and forces [2-4]. Most of the textures are accomplished by various authors in the rake face of the cutting tool using femtosecond laser, grinding wheel, Rockwell hardness tester, electric discharge machining etc. Lei et al. [5] have studied the impact of cutting tool which are textured with micro-pits, by comparison against the conventional cutting tool, and found that tool with the micro-pits could effectively reduce cutting forces 10~30%. Liu et al.[6] reported a few surface textured tools with different texture figures. The research results showed that application of the surface textured tools can reduce cutting forces and cutting temperature. Rajbongshi et al.[7] have found that texturing helps in reducing the formation of white layer thickness and micro-hardness as compared to the non-textured tool. Sugihara and Enomoto[8] found that surface texturing on cemented carbide tool at the rake and flank faces in parallel to cutting edge direction caused reduction of crater and flank wear while machining. Wu et al. [9] wrote the surface textured tool could reduce the surface roughness of workpiece, and the tool life of surface textured tool was improved by 15% or so compared with the conventional one. Ze et al. [10] mentioned the benefits of rake or flank face fabricated structures of carbide using molybdenum disulfide in the textured places in the dry cutting of Ti-6Al-4 V alloy. With this texturing the authors were able to get improved machining performances in terms of cutting forces, cutting temperature, chip thickness ratio, and tool wear. Jianxin et al. [11] reported the effect of three microstructures made by lasers created on the rake faces of the cutting tool in machining of AISI 45 steel. The authors wrote that with this kind of texturing, temperature, cutting forces and coefficient of friction could be reduced. Furthermore, as mentioned above, many papers applied this surface texturing process on the rake faces of the tools and very few studies that tried to presents textured surfaces into tool flank face have been carried out, despite the importance of the flank wear resistance of cutting tools.

This study stands on the comparison of non-textured and textured tool wear characteristics. In order to understand the performance of textured tools, a comparative study was carried out using one perpendicular(PPT), one parallel(PT) textured to main cutting edge and non-textured(NT) tool. Femtosecond laser processing technology was used to produce the samples. In addition we have seen that, surface texturing effectted the surface roughness of workpiece and chip formations.

2. Experimental set up

2.1. Workpiece and tool material

The main objective of this experimental work was to investigate the effect of surface textures on flank wear and to observe how texturing was effecting the surface roughness and chip formations in dry turning of AISI 4140 32HRC steel with CVD coated conventional semented carbide tool. An orthogonal turning operation was used with cylindrical AISI 4140 32HRC workpieces with length of 250 mm and diameter of 60 mm. The chemical composition of AISI 4140 is given in Table 1.

Table 1.
Chemical composition of AISI 4140 Steel

C	Mn	P	S	Si	Ni	Cr	Mo
0,38-0,43	0,75-1	0,035	0,04	0,15-0,35	-	0,8-1,10	0,15-0,25

Turning was performed on machining centre Goodway GA-230. Figure 1 showed the experimental set up for dry orthogonal turning. In the experimental study, coated (CVD Ti(C,N)+Al2O3+TiN) cemented carbide was used. The type of the tool was Sandvik CNMG 12 04 08 PM 4315 according to the standard ISO 1832 with chip breakers. Tool holder was ACLNL 25 25 M12.

For surface roughness measurement, surface roughness tester Mitutoyo SJ-210 was used. The cut off length (λ_c) was 0,8 mm and sampling length range was 2,5mm. SOIF model optical microscope and having 1.0μm precision OSM model ocular micrometer was used for flank wear measurement.

2.2. Surface texturing on cutting tool

Femtosecond laser was applied to produce textured tools on the flank face. The laser had a marking speed of 1000μm/s, skip speed of 125mm/s and repetation rate of 1000μm/s. The line gap was 100μm, pulse duration was 120fs. Laser had a wawelenght of 800nm and laser power was 50mW. Texture grooves were produced perpendicular (PPT) and parallel (PT) to main cutting edge. In order to specify the effect on flank wear non-textured (NT) tool were used

for the comparison. The microscope views of surface textures are shown in Fig. 2.

Fig. 1. Dry orthogonal turning experimental set up

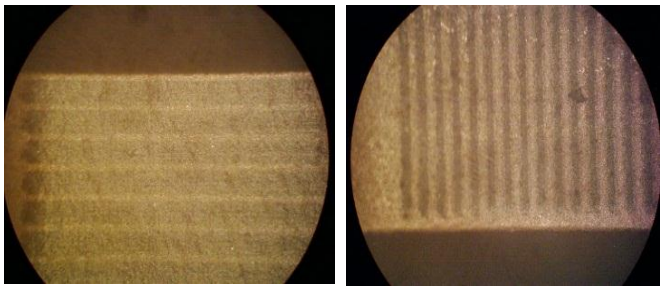

(a) PT tool (b) PPT tool

Fig. 2. Microscope views of surface textures, (a) parallel to maincutting edge, (b) perpendicular to main cutting edge.

2.3. Cutting conditions

Table 2.
Cutting condition parameters used in experiments

Workpiece	AISI 4140 32 HRC
Tool	Cemented carbide, CVD coated tool
	CNMG 12 04 08 PM 4315 (Sandvik Coromant)
Cutting velocity, Vc [m/min]	180
Feed rate, f [mm/rev]	0,2
Cutting depth, ap [mm]	1,5
Cutting fluid	Dry
Corner radius, rε [mm]	0,8
Rake angle, ɣ [°]	-7
Clearance angle, α [°]	0
Wedge angle, β [°]	80

The cutting parameters are summarised in Table 2. For the observation of the flank wear, the cutting speed, feed and depth of cut were selected as follows: Vc=180m/min, f=0,2mm/rev ap=1,5mm were selected for proper chip formation.

3. Results and discussion

3.1. Effect of surface texturing types on flank wear and its comparison with a non-textured tool

Flank wear of cutting tools is often selected as a tool life criterion because it determines the dimension accuracy of machining, its stability and reliability.[8] In the study, flank wear of PT, PPT and NT surface of coated carbide tool were measured, thus, the difference between them was revealed. Two types of surface textures have been developed with femtosecond laser which are perpendicular and parallel to main cutting edge.

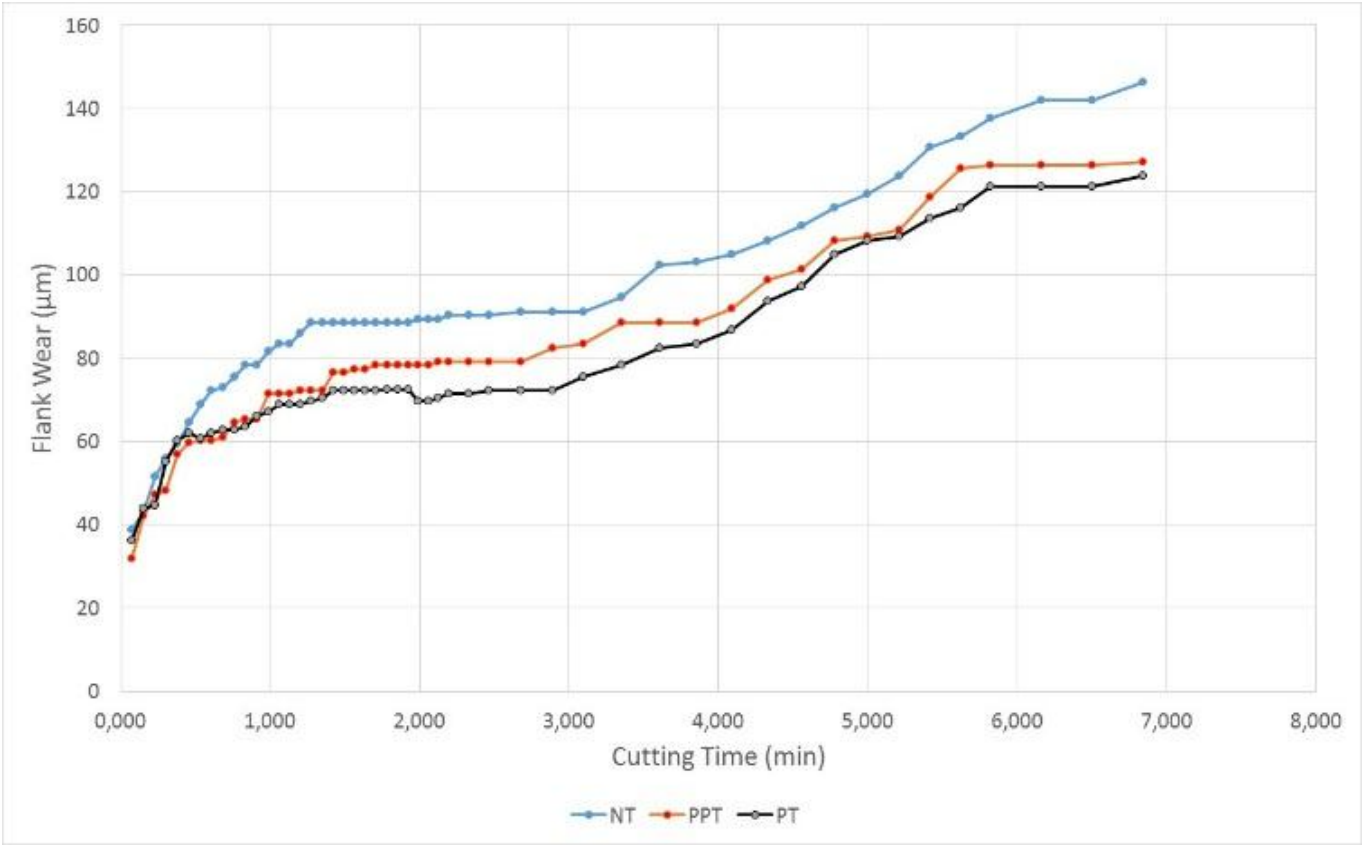

Fig. 3. Variation of tool flank wear with non-textured, perpendicular textured and parallel textured coated carbide tool.

Three samples per each test were used for the responses of flank wear and surface roughness and chip formation. The flank wear comparison of all samples is shown in Fig. 3. The tool wear was measured after every pass and all chips measured for after each of the experiment. Flank wear lenghts on the tools were observed at certain intervals and the wear conditions were compared for the same cutting times. Camera images were taken at certain time intervals of three samples (see Fig. 4.).

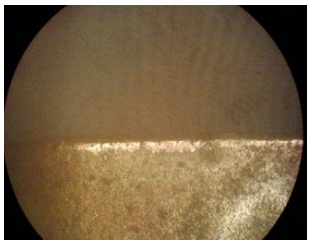

(a) NT tool wear: 68,8µm

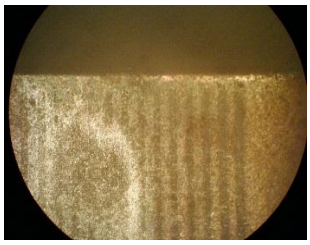

(b) PPT tool wear: 60,2µm

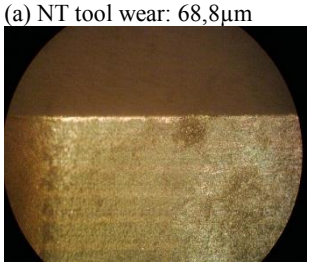

(c) PT tool wear: 60,82µm

Fig. 4.1. Flank wear values at cutting time 32 seconds.

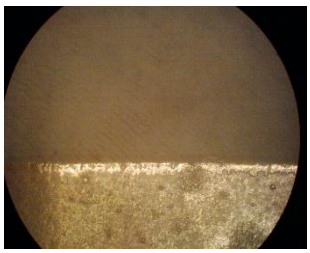

(d) NT tool wear: 88,58µm

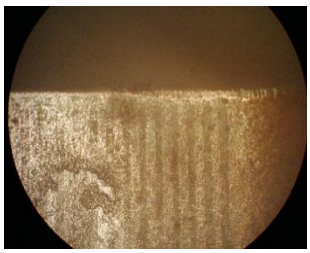

(e) PPT tool wear: 77,4µm

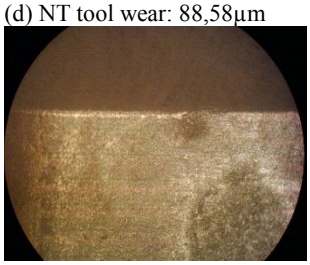

(f) PT tool wear: 72,24µm

Fig. 4.2. Flank wear values at cutting time 98,2 seconds.

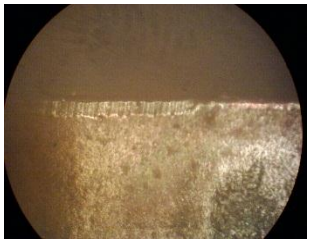

(g) NT tool wear: 146,2µm

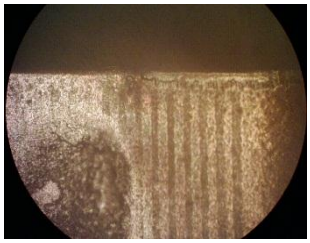

(h) PPT tool wear: 127,28µm

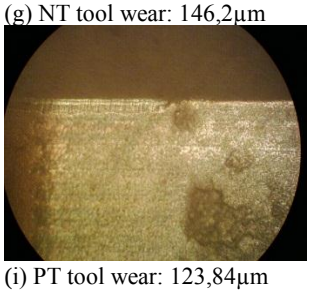

(i) PT tool wear: 123,84µm

Fig. 4.3. Flank wear values at cutting time 410,4 seconds.

As evident from the experimental data, a significant difference of flank wear for the all textured and non-textured tool was observed at same cutting conditions. The flank face textured tools with micro-scale grooves parallel to the main cutting edge (PT) had the most improved flank wear resistance (as shown in Figs. 3., 4.). The aim of the surface texturing is to decrease the contact area between the tool interface and workpiece area. On the occasion of the tool textured, the tool and workpiece friction reduced and consequently the adhesion and abrasion also decreased. Due to the less friction between tool and workpiece, the width of wear land at the flank face decreased. Hence, due to texturing on the flank face, the contact length of the cutting tool and tool wear reduced. As a result, the cutting forces generated during machining become less when it was compared to non-textured tool. In this regard, lower cutting forces, lower friction between tool and workpiece provided reduction in tool flank wear and the tool life improved. [11]

3.2. Effect of surface texturing types on surface roughness and chip formation and its comparision to non-textured tool

Fig. 5. showed the differences of avarage surface roughness on workpieces between textured and non-textured tools. From Fig. 5. It could be seen that PPT and PT tools have respectable effect on Ra. However, there has not been seen significant difference between PPT and PT.

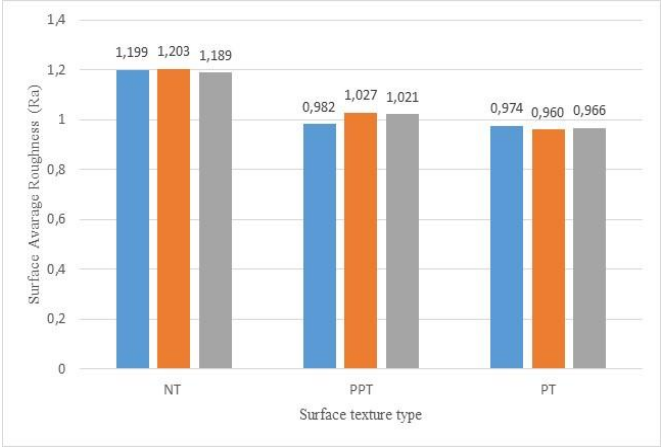

Fig. 5. Surface roughness (Ra) values of NT, PPT and PT tools

These data collected at the same cutting conditions which showed that lower flank wear that induced lower surface roughness values. In the light of all these experiments, the textured tool could reduce the surface roughness of the machined surface in comparison to that of the non-textured tool.

(a) NT tool chip form

(b) PPT tool chip form

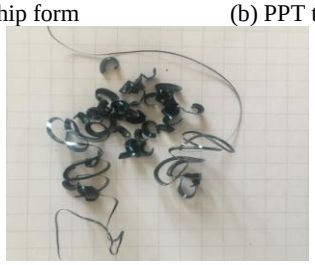

(c) PT tool chip form

Fig. 6. Chip forms of three samples, (a) NT tool chip form, (b) PPT tool chip form, (c) PT tool chip form.

On the other hand, in this paper the chip formation of all three samples were examined. As it is shown in Fig. 6., there has not been observed any visible changes on chip formation but it has seen that during cutting of the workpiece, on entering and exiting of PT tool, different chip formation occurred. Despite the tool has chip breaker, unbroken chip forms were seen on PT tool (Fig. 6.c).

4. Conclusions

In order to decrease tool flank wear and improve tool life in dry orthogonal cutting, two different types of surface texture were adopted. Surface textures were pretreated on flank faces of tools with femtosecond laser. All experiments completed under same cutting conditions with textured and non-textured coated cemented carbide tools in turning of AISI 4140 steel. Experimental results are summarized below:

- It was found that surface texturing on flank face reduced flank wear and tool life was improved. Due to the reduction of tool chip contact, friction forces and the stress on the tool decreased.
- Parallel textured tool hads more significant effect than that of perpendicular textured tool on the flank wear rate.
- It has been seen that, the decrease of flank wear improved the surface quality. But there has not been seen remarkable differences between surface roughnesses of the workpieces cut by PPT and PT tool.
- Additionally, it was observed that there was no visible changes on chip forms but during cutting of the workpiece, on entering and existing of PT tool, different chip formation occurred

5. Acknowledgements

All surface texture applications were performed at “Konya Selcuk University” with femtosecond laser technology.

References

[1] Ngoi B.K.A., P.S. Sreejith, Dry machining: machining of the future. Journal of Materials Processing Technology 101 (2000) 287-291.

[2] Enomoto T., T. Sugihara, S. Yukinaga, K. Hirose, U. Satake, Highly wear-resistant cutting tools with textured surfaces in steel cutting. CIRP Annals – Manuf. Technology, 2012, 61(1): 571-574.

[3] Dengn J. X., Z. Wu, Y. S. Lian, T. Qi, J. Cheng, Performance of carbide tools with textured rake-face filled with solid lubricants in dry cutting processes. Int. J. of Refractory Metals and Hard Materials, 2012, 30(1): 164-172.

[4] Qi B.Y., L. Li, N. He, W. Zhao, Z. Wang, Experimental Study on Orthogonal Cutting of Ti6Al4V with Micro-textured Tool. Tribology. 2011, 31(4): 346-351.

[5] Lei S, S. Devarajan, Z. Chang, A study of micropool lubricated cutting tool in machining of mild steel. J. Mater. Process Technol. 2009;209:1612–20.

[6] Liu Y., J. Deng, F. Wu, R. Duan, X. Zhang, Y. Hou, Wear resistance of carbide tools with textured flank face in dry cutting of green alumina ceramics. Wear 372-373 (2017) 91–103.

[7] Rajbongshi S. K., M. A. Singh, D. K. Sarma, A comparative study in machining of AISI D2 steel using textured and nontextured coated carbide tool at the flank face. Journal of Manufacturing Processes 36 (2018) 360–372.

[8] Sugihara T, T. Enomoto, Crater and flank wear resistance of cutting tools having microtextured surfaces. Precision Engineering 37 (2013) 888– 896.

[9] Wu Z., J. Deng, J. Zhao, Study on tool life of surface textured tool in dry cutting of Ti-6Al-4V alloys. Advanced Materials Research Vols. 538-541 (2012) pp 1245-1249.

[10] Ze W., D. Jianxin, C. Yang, X. Youqiang, Z. Jun, Performance of the self-lubricating textured tools in dry cutting of Ti-6Al-4V. Int. J. Adv. Manuf. Technol. (2012) 62:943–951.

[11] Deng J., W. Ze, L. Yunsong, Q. Ting, C. Jie, Performance of carbide tools with textured rake-face filled with solid lubricants in dry cutting processes. Int. Journal of Refractory Metals and Hard Materials 30 (2012) 164–172.

EFFECTS OF PROCESS PARAMETERS IN PLASMA ARC CUTTING ON STAINLESS STEELS AND STRUCTURAL STEEL

Erbilen M. 1*, Çakır O.1
1 Yildiz Technical University, Department of Mechanical Engineering, Besiktas, Istanbul, 34349, Turkey
*m_erbilen@hotmail.com

Abstract: *Plasma arc cutting is a non-conventional manufacturing process that has potential for modern day metal cutting demands with good dimensional accuracy and high-quality surfaces without any extra operation. In this experimental study, AISI 304, AISI 430 and EN S235JR sheet materials having 5 mm. thicknesses, has cut with plasma arc cutting. Each material has cut with 6 different variations. Current, cutting speed, arc voltage, gas pressure and gas flow rate have been changed as process parameters. The quality of the cut has been monitored by measuring the edge roughness, the hardness of the heat-affected zone (HAZ) and the results has compared.*
Keywords: STAINLESS STEEL; STRUCTURAL STEEL; PLASMA ARC CUTTING; HEAT-EFFECTED ZONE (HAZ)

1. Introduction

Modern manufacturing processes are widely employed for harder, stronger, and tougher materials those are known as "difficult to cut". Moreover these methods are capable to produce complex geometries with high dimensional and surface accuracies. Plasma cutting is a modern manufacturing method which can be applied for cutting wide range of materials. The inert gas is blown with high speed out of a nozzle; at the same time, an electrical arc is formed through that gas from the nozzle to the surface, reaching high temperatures that are ionizing atoms to plasma form. The formed plasma melts the material being cut and swiftly moves blowing molten metal away from the cut [1-4].

'Plasma', as a term, had been used firstly in 1920s, it was firstly realized in 1950s that material can cut with it. Cutting with plasma arc, one of the thermal cutting methods has been improved as an alternative method for mostly stainless steel, aluminium and non-ferrous metals being cut with oxy-acetylene. Plasma cutting of the workpiece is the result of melting/vaporizing of material through a very hot cylindrical (theoretical) plasma beam which burns and melts through the material (Fig. 1).

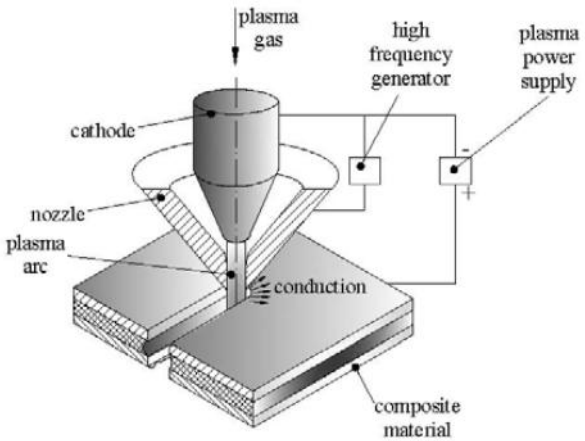

Fig.1. *Plasma cutting [2]*

One of the most important problems occurring as result of heat transfer from plasma column to the workpiece is the deformation of the cut edges after the material is cut and then cooled. During the cut operation, many physical phenomena occur in this process: heat conduction, convection, radiation effects, mechanical deformation, phase transition etc. The principle of plasma cutting means to focus a lot of power on a small area of workpiece surface, in this way producing an intense surface heating [2].

Nowadays, with the increasing of stainless steel, aluminium and metal and non- metal materials' consumption in industry, the importance of rapid, cheap and delicate cutting for these materials have scaled up. At initial application of plasma cutting, generally, argon and 35% hydrogen mixture was used as a plasma gas. However, this mixture is expensive and cutting operation will be costly. Reducing operation costs would be reached by changing mixture of gas to air as a plasma gas. Simply, plasma can be identified as a state of matter. The differences between states of matter is the energy that they have. For the transition from a state to another, it is required to supply energy and reverse transition is also possible [5]. The solid material can be turned into fluid state by supplying energy, the fluid material can be converted to gas with energy and gaseous material can be ionized and converted to plasma by supplying energy.

The plasma cutting technology is sometimes compared to laser and waterjet cutting methods. This technology seems providing more advantages over both cutting methods such as lower operation costs, widely used in cutting high-alloy steel and aluminium materials in medium and larger thickness, excellent performance in small and medium-sized thickness of steel (30 mm), high cutting speeds, high automation, etc [3-7].

Stainless steel is identified ferrous alloys having at least 10,5% chromium (Cr). The thin but dense chromium oxide layer on surface of stainless steel provides high resistance against corrasion and inhibits oxidation to move deeper [8,9].

There are five different types of stainless steels which are ranked from completely austenitic to completely ferritic varying in regard to additives that they contain. These are respectively:
Austenitic Stainless Steel
Ferritic Stainless Steel
Martensitic Stainless Steel
Dual phase Stainless Steel
Precipitation-hardened Stainless Steel

Austenitic Stainless Steel includes 200s and 300s quality series and 304 quality is the most commonly used which its basis element is chromium nickel. Ferritic Stainless Steel is an alloy that cannot be hardened and 405,409,430,422 and 446 quality stainless steels are Ferritic Stainless Steel. Martensitic Stainless Steel has almost the same chemical properties, yet it has high incidence of carbon and less chromium that's why they can be hardened with heat treatment. 403,410,416 and 420 qualities are Martensitic Stainless Steel. Dual phase Stainless Steel is obtained by forming a microstructure having almost equal austenite and ferrite and it definitively contains %24 chromium and %5 nickel. It doesn't include any of quality series from 200s, 300s and 400s.

Various studies have been reported regarding the application of plasma cutting in stainless steels using different process parameters [10-15]. These studies have provided useful and

applicable parameters, however, more efforts have been required to understand the process better.

In this experimental study, the plasma method is selected to cut some commonly used metals (AISI 304, AISI 430 and EN S235JR). CNC plasma cutting machine is used The selected cutting parameters were current, cutting speed, arc voltage, gas pressure and gas flow rate and the effects of these parameters on edge roughness, the hardness of the heat-affected zone (HAZ).

2. Experimental Study

In this experimental study, AJAN CNC 2x6m PP260A plasma cutting bench was used (Fig. 2.). 6 different experiment scenarios having different parameters were applied (Table 1.). 3 different materials shown in Table 2. having same thickness of 5mm were subjected to these experiments.

Fig. 2. *AJAN CNC 2x6m PP260A plasma cutting*

The materials were cut flat sided oval shape having 90mm length and 40mm width. Totally, 18 cutting operations were performed, yet it was not accomplished to cut S235JR material in 5st scenario.

Table 1. *Parameters of Experiment Scenarios*

	CURRENT (A)	PLASMA GAS	GAS PRESSURE (BAR)	GAS FLOW RATE(Lpm)	MATERIAL THICKNESS(mm)	VOLTAGE(V)	CUTTING SPEED (mm/min)
1. SCENARIO	30	O2	4,56	18,3	5	120	750
2. SCENARIO	40	O2	4,8	5,4	5	114	1300
3. SCENARIO	80	O2	6,53	9,6	5	120	3700
4. SCENARIO	130	O2	4,49	16,4	5	111	4500
5. SCENARIO	45	N2	5,51	9,7	5	129	1050
6. SCENARIO	80	AIR	6	28	5	151	2200

Table 2. *Materials subjected to the experiment*

	C%	Cr%	Ni%	Mn%	P%	S%	Si%
S235JR	0.17	-	-	1.4	0.035	0.035	-
AISI 304	0.08	18	8	2	0.045	0.03	0.75
AISI430	0.12	16	0.75	1	0.045	0.03	1

The surface roughness (R_z) of cut materials was measured with Mitutoyo SJ201P equipment. Then by, the materials were divided into 3 sections by bandsaw bench branded Mossner. The middle sections of materials is rubbed with P240 emery sheets by using Netkon and Forcipol 2V grinders. The hardness of material which its surfaces were polished and the hardness of heat affected zone(HAZ) were measured with HMV Sumadzu Micro Vickers Hardness test device.

3. Results and Discussion

3.1. Surface Roughness

Surface roughness is one of the major process outputs when metal is cut. This value will affect the dimensional accuracy as well as surface quality. In surface roughness measurement, for S235JR material, the least roughness was experienced in the 4th experiment scenario (2,385µm). The highest roughness value (6,7975 µm) was beheld in the 6th experiment scenario.

For AISI304 stainless steel, the least roughness (2,3175 µm) was seen in the 5th experiment scenario. The highest roughness value (41,125 µm) was experienced in the 1st experiment scenario. For AISI430 stainless steel, the least roughness (1,6925 µm) was met in the 5th experiment scenario. The highest roughness value (38,2725 µm) was observed in the 1st experiment scenario.
The surface roughness of 3 different materials resulted by 6 different experiment scenarios are indicated in Fig.3.

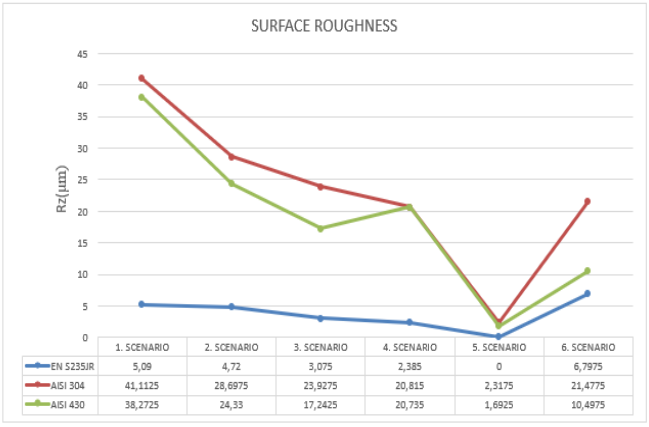

Fig.3. *Surface roughness of material after plasma cutting*

3.2. Hardness

The hardness of cut sections in plasma cutting application is examined and the results have been presented in Fig 4. The obtained minimum and maximum hardness results for the materials after plasma cutting operations are as follows:
For 235JR, between 130HV-150HV
For AISI304, between 190HV-225HV
For AISI 430, between 340HV-395HV

It was noticed that the hardness value has not changed with using different cutting conditions. The hardness of cut sections were similar in all cutting conditions.

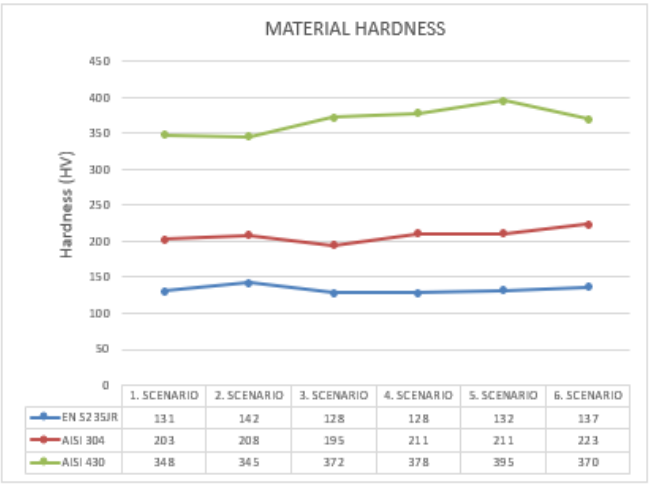

Fig.4. *Material hardness after plasma cutting*

3.3. Hardness of Heat Affected Zone (HAZ)

The Heat-Affected Zone (HAZ) presents to a non-melted area of cut metal that has experienced changes in its material properties as a result of exposure to high temperatures. The HAZ is identified as the area between the cut and the main metal. These areas can vary in size and severity depending on the plasma cutting parameters.

The height hardness for 235JR material was obtained in 6th experiment scenario and the least one was sought in 4th experiment. When it is compared roughness of HAZ and of the material, it is realized that HAZ roughness is higher than the one that the material has.

For the austenitic AISI 304 stainless steel, after the 6th experiment scenario, the highest hardness value was occurred.
The lowest hardness value was obtained after 4th experiment scenario. The HAZ hardness is higher than the one that material has.

Comparing to ferritic AISI 430 stainless steel, highest value was experienced in 3rd experiment scenario and the lowest value was observed after 6th experiment scenario. Contrast to other materials, the HAZ roughness is less than the roughness of material.

The Heat Affected Zone (HAZ) hardness of the materials cut with plasma cutting are shown in Fig. 5.

During plasma cutting operations, the depth of the HAZ is related to cutting speed, material properties, and material thickness. It is known that plasma cutting process that operates at high temperatures and slow speeds produce large HAZs. Furthermore, cutting processes that operate at high speeds tend to reduce the width of the HAZ.

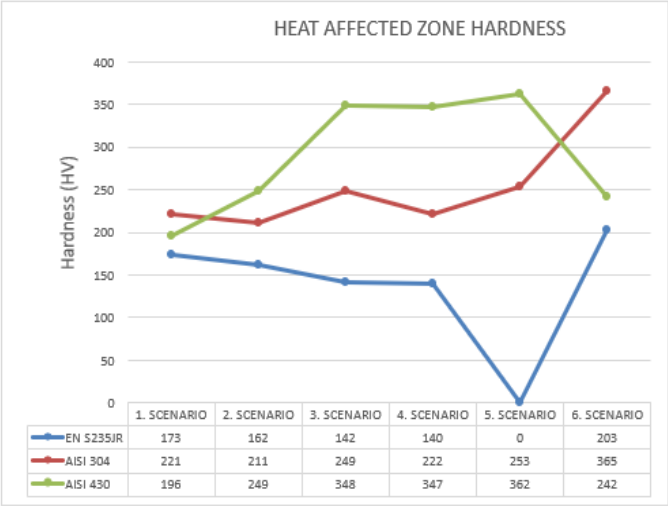

Fig.5. *HAZ hardness after plasma cutting*

Note: Due to that S235JR couldn't be cut with 5th experiment scenario, HAZ hardness was not measured.

4.Conclusion

Plasma cutting is one of the modern cutting methods that is applied for various materials. The process has different cutting parameters and these are should be examined to find optimum industrial application. In this experimental study, 5mm thick austenitic and ferrite stainless steels were cut by plasma method. The selected cutting parameters on surface roughness, hardness and HAZ were examined. The following conclusions are obtained:

- When oxygen was used as plasma cutting gas, the surface roughness value was higher than the other applications with different gases.
- The lowest surface roughness value (1,6µm) was observed when nitrogen is used
- The HAZ hardness of austenitic stainless steel increased after plasma cutting, whereas HAZ hardness of ferritic stainless steel decreased.

Industrial application of plasma arc cutting process presents many unique advantages and cost effective technology comparing to other cutting methods. It should be noted that more efforts put to optimize the process parameters in any industrial application of material cutting.

References

[1] Hassan El-Hofy, Advanced Machining Processes : Nontraditional and Hybrid Machining Processes, McGraw Hill, 2005
[2] A. Iosub, Gh. Nagit, F. Negoescu, "Plasma Cutting of Composite Materials", International Journal of Material Forming (2008) Suppl 1:1347 –1350
[3] B. Nedic, M. Jankovic, M. Radovanovic, G. G. Lakic, "Quality of plasma cutting", Proc. Of 13th International Conference on Tribology (SERBIATRIB '13), Kragujevac, Serbia, 15 – 17 May 2013, pp: 314-319
[4] Z. Cinar, M. Asmael, Q. Zeeshan, "Developments in Plasma Arc Cutting (PAC) of Steel Alloys: A Review", Jurnal Kejuruteraan 30(1) 2018: 7-16
[5]. K. V. Vasil'ev, "Plasma-arc-cutting- a promising method of thermal cutting," Welding International, Vol 17(2), pp. 147-151, 2003.
[6] S.M. Ilii, M. Coteata, "Plasma arc cutting cost", International Journal of Material Forming (2009) Vol. 2 Suppl 1:689–692
[7] C.Radu, E. Herghelegiu, C. Schnakovszky, "Comparative study on the effects of three unconventional cutting technologies on cut surface quality", Indian Journal of Engineering and Materials Sciences, 22(2), pp. 127-132, 2015
[8] Helmi A. Youssef, Machining of Stainless Steels and Super Alloys Traditional and Nontraditional Techniques, John Wiley & Sons, Ltd., 2016
[9] K. P. Maity & Dilip Kumar Bagal "Effect of process parameters on cut quality of stainless steel of plasma arc cutting using hybrid approach",
[10] K. Salonitis, S. Vatousianos, "Experimental Investigation of the Plasma Arc Cutting Process", Procedia CIRP, Vol 3, 2012, 287 – 292 (45th CIRP Conference on Manufacturing Systems 2012)
[11] A. Parthiban, J.P. Prasath, P.Vivek, R. Pugazhenthi, "Experimental investigation of plasma arc cutting for stainless steel sheet", International Journal of Mechanical and Production Engineering Research and Development, 8(1),IJMPERD, FEB, 2018110, pp. 907-914
[12] D.K. Naik, K.P. Maity, "An optimization and experimental analysis of plasma arc cutting of Hardox-400 using Taguchi based desirability analysis", Materials Today: Proceedings, 5(5), pp. 13157-13165, 2018
[13] A. Lazarevic, D. Lazarevic, "Investigations of material hardness and structural changes in the heat-affected zone during plasma cutting", Welding in the World, 61(6), pp. 1069-1075, 2017
[14] A. Lazarevic, "Experimental research of the plasma arc cutting process", Journal of Applied Engineering Science, 12(4), pp. 291-296, 2014
[15] H.R. Kumar, S. Thileepan, "Analysis in plasma arc cutting of 21Cr ferritic stainless steel", International Journal of ChemTech Research, 8(11), pp. 474-483, 2015

ГЛОБАЛЕН МАКСИМУМ – ПРАКТИЧЕСКИ ОЦЕНКИ В ОБЛАСТТА НА МЕТАЛУРГИЧНИЯ ДИЗАЙН

Йордан Калев, Николай Тончев [1]
[1] Висше Транспортно Училище „Тодор Каблешков“ – tontchev@vtu.bg

Abstract: *The paper present approach for the analysis and optimization of various processing parameters are applied numerical methods in the field of metallurgical design and properties of metal products. The proposed methods are associated with the theory of the experiment and using the concept of a multi-factor analysis of various selected parameters of quality. The topicality of such a study is conditioned by the fact that the growing role of product quality requires tools for automating experimental studies and that increasingly is carried out with numerical method. This is to absorb the need to increase the effectiveness of the experimental studies.*

Keywords: GLOBAL MAXIMUM, PRACTICAL EVALUATIONS ALGORITHM, MULTIOBJECTIVE OPTIMIZATION, STEELS, ALLOYS

1. ВЪВДЕНИЕ

Дългогодишната практика за развитие на сплавите се състояла в производството на многобройни проби с променящ се състав и вариации на елементите, както и режим на обработка, за да се определят състави с оптимални свойства [1]. Този подход води до високи разходи за експериментиране [2]. Численният металургичен дизайн е не само проектиране на основата с легиращи елементи по вид, брой и количество, но и отчитане на техния синергичен ефект. Необходимо е да се подбере такъв синергичен ефект по комбинация от елементи, в който по-скъпо струващите елементи да са в по-малки количества. Наред с изпълнението на тази задача, металургичният дизайн трябва да изпълни и търсения компромис между свойствата на продукта, зависещи от параметрите на обработка. Тези няколко групи параметри би трябвало да формират общо параметрите на обработката и състава. Сложността на така дефинираната задача се състои в големия брой на INPUT/входни/ - фактори, както и на обстоятелството, че химическият състав участва неявно чрез синергитичния ефект, в системата „състав – обработвания – структура – свойства – цена“. Оптимизацията е алтернативен и ефективен подход в който се използват свързани, като състав, обработка и свойства резултати от предишен опит, обработени до статистичен модел, в основата на който е голяма база данни. Във всеки случай с количествено изменящи се променливи, представлява интерес изследване влиянието на променливите върху крайния резултат.

Изменящи се променливи ще наричаме фактори, а крайния резултат, свойството ще наричаме изход.

Когато крайният резултат се оценява по няколко показателя, тогава за една и съща комбинация на факторите ще имаме няколко изхода. Проектирането на състава на сплавите и оптимизирането на параметрите на технологичния процес са пряко свързани с разрешаване на компромиса между стойностите на измерените величини, съотнесени към определени селектирани показатели на качеството, за множество материали от изследвана група или даден клас [3]. Най-характерното за тези подходи е, че те не използват принципите на металургията и физиката на металите. Разчита се предимно и само на априорна информация за връзката състав-обработване и влиянието им върху крайните свойства. Предимството на статистическите в сравнение с физическите модели, се крие в способността им да определят комплекс и по своевременен и ефективен начин да получат информация, дори когато не съществуват добре установени физични теории и модели [4,5,6]. Изследването е част от серия подходи и методики, които в етапа на генериране на решението не се използват знания, натрупани от областта на металургията. Позовавайки се на богатата информация от компаниите, на различни бази от данни при изследване на зависимостите от тях е възможно да се направят ценни предложения подобряващи параметрите на създаваните изделия и технологии. С това се проследява влиянието и взаимодействието между легиращите елементи и техния синергичен ефект, върху свойствата на сплави и по-конкретно върху техните якостни и експлоатационни свойства.

2. СЪСТОЯНИЕ НА ПРОБЛЕМА

В експерименталните изследвания съществува връзка между технологичните фактори на количество, брой и вид легиращ елемент, като управляващи комбинации от една страна и стойности на механичните показатели, като комплекс, от друга.

Необходимо е да се съберат експериментални данни. Да се обработят с цел получаването на математичен модел, годен за предсказване. Накрая с оптимизационна процедура се намира глобалния максимум на математичния модел.

2.1 Експериментални данни:

Използва се пасивен експеримент с 80 „опита”. Фактори са осемте компоненти на химическия състав на конструкционни стомани [3] – C, Si, Mn, Ni, S/P, Cr, Mo и V. Изходите са Re – граница на провлачване [MPa], A – относително удължение [%] и HB – твърдост по Бринел.

В таблица 1 са дадени факторите, техните номера, минимални и максимални стойности между които се изменят. В таблица 2 са посочени изходите с минималните и максимални стойности между които те се изменят.

Табл. 1. *INPUT/входни/ -фактори на експерименталното изследване.*

№	Символ	Min %	Max %
1	C	0,125	0,52
2	Si	0,027	1,4
3	Mn	0,35	1,75
4	Ni	0	4,22
5	S/P	0,015	0,035
6	Cr	0,15	3,25
7	Mo	0	1,5
8	V	0	0,15

Табл.2.*OUTPUT-изходи на експерименталното изследване*

№	Изход	Min	Max
1	Rm	300	1375
2	A	7	22
3	HB	179	235

2.2. Обработка на експерименталните данни.

За всеки изход Re, A, HB са пресметнати математичен модел от вида:

$$Y(X) = C_0 + \sum C_i X_i + \sum C_{ij} X_i X_j + \sum C_{ii} X_i^2$$

Този модел при 8 фактора има 45 коефициента. Направен е статистически анализ на всеки модел. Коефициента на множествена корелация за всеки изход се оказа значим, от

което следва, че математичния модел може да се използва за предсказване [7].

2.3. Цифрова оптимизация.

В [7], [8] и [9] са описани методи за цифрова оптимизация на математични модели. Бе използван модифициран метод на Хук и Дживс [10]. Метода на Хук и Дживс, подробно е описан [8].

Методът на Хук и Дживс е един от най добрите, а и броя на факторите, допълнително предопредели, неговия избор.

Коефициентите на математичния модел са цитирани със седем значещи цифри – вж. приложение 1, 2, 3. Максимумите са цитирани там с две цифри след десетичната точка.

2.4. Избор на начална точка.

При всяка задача като разглежданата тук, крайната цел е намирането на по добър в някакъв смисъл краен резултат. Това най общо се формулира като „усъвършенстване".

Когато се каже „усъвършенствувам нещо" то се рабира, че това „нещо" го има и то съществува реално.

Всеки алгоритъм за екстремум започва с „избира се начална точка". Единствените изисквания до момента към нея е да бъде в границите на допустимото за факторите. Точно тук се забравя че се усувършенствува нещо и за да го усъвършенстваме трябва да тръгнем от него. Правило е че крайния резултат при търсенето на екстремум зависи много от началната точка. Това ще се види по-нататък.

Изхождайки от това се реши да се направят 80 търсения на максимум, като във всеки отделен случай за начални точки се използват стойностите на факторите от експерименталните данни.

3. АНАЛИЗ НА ПОЛУЧЕНИТЕ РЕЗУЛТАТИ

Получените резултати са показани в приложение 1, 2 и 3. Приложение 1 – Изход Re, Приложение 2 – Изход А, Приложение 3 – Изход НВ.

И за трите приложения – горе в ляво коефициентите на математичния модел с пресметнати стойности на коефициента на множествена корелация R и изчислена стойност на F критерий. В дясно сортираните в нарастващ ред, получени стойности на максимумите. Долу в ляво на фигурата – хистограма на сортираните максимуми.

Получените стойности на максимумите не са различни за всеки случай, а се групират около отделни стойности. За изход Re, (таблица 3) те са 14 броя. За изход А , (таблица 4) те са 7 броя и за изход НВ (таблица 5) те са 8 броя. Там стойностите на максимумите са сортирани в нарастващ ред. До тях е посочен броя на случаите , когато е получена тази стойност и в дясно са стойностите на отделните фактори.

За всеки случай, стойностите на получените максимуми на изходите са по големи от съответните им в експерименталните данни. За някой от тях стойностите на отделните фактори съвпадат с границите в които те се изменят. Това т.н. условни максимуми. За изход Re, те са за стойност: 5638.2, 6333.8 и 9601.3. За изход А те са за стойност 32.3, 91.6, 96.2 и 122.88. За изход НВ за стойност 590.8, 932.4 и 1156.7. В останалите случай имаме поне един фактор който се намира вътре в интервала в който се изменя. Те оформят т.н. безусловни максимуми.

Обръща се внимание на това защото стойностите на факторите на условните максимуми, не позволяват използването им като начални точки за търсене на по-голяма от тях стойност на максимума.

Табл.3. *Числени стойности за границата на провлачване, максимуми и стойности на факторите при тези максимуми.*

Стойност	Броя	X_1	X_2	X_3	X_4	X_5	X_6	X_7	X_8
4113,9	1	0,52	0,027	0,35	0	0,035	3,25	0	0,09
4370,2	1	0,125	0,027	0,35	0	0,035	0,15	0	0,1
4425,6	5	0,52	0,027	0,35	0	0,035	2,03	0	0,117
5638,2	4	0,125	0,027	0,35	0	0,035	3,25	0	0
5969,6	2	0,52	1,4	0,35	0	0,015	0,15	0	0,071
6333,8	1	1,25	0,027	1,75	0	0,035	3,25	0	0
6423,7	4	0,52	0,027	0,35	0	0,035	0,15	1,5	0,15
7473,9	38	0,52	1,4	0,35	0	0,035	0,15	0	0,1
7478	2	0,52	1,4	0,35	0,0078	0,035	0,15	0	0,1
8774,1	10	0,52	0,027	1,75	0	0,035	0,15	1,5	0,15
9564,6	1	0,125	0,027	1,75	0	0,035	1,27	1,5	0,15
9601,3	1	0,125	0,027	1,75	0	0,035	0,15	1,5	0,15
10032,98	5	0,125	0,027	1,75	0	0,035	1,85	1,5	0
10094,42	5	0,125	0,027	1,75	0	0,035	1,71	1,5	0,038

Табл.4. *Числени стойности за относителното удължение, максимуми и стойности на факторите при тези максимуми.*

Стойност	Броя	X_1	X_2	X_3	X_4	X_5	X_6	X_7	X_8
32,3	15	0,125	0,027	0,35	0	0,015	0,15	0	0
35,2	34	0,486	0,027	0,35	0	0,015	0,15	0	0
80,3	4	0,125	1,4	0,35	4,22	0,015	3,25	0	0,15
91,6	7	0,125	1,4	1,75	4,22	0,015	3,25	0	0,15
93,06	1	0,52	1,4	1,75	4,22	0,015	3,25	1,03	0,15
96,2	2	0,125	1,4	0,35	4,22	0,15	3,25	0	0,15
122,88	17	0,52	1,4	0,35	4,22	0,015	0,15	0	0

Табл.5. *Числени стойности за твърдостта, максимуми и стойности на факторите при тези максимуми.*

Стойност	Броя	X_1	X_2	X_3	X_4	X_5	X_6	X_7	X_8
421,6	2	0,52	1,4	0,35	0,49	0,015	0,15	0	0
439,8	22	0,52	1,4	0,35	0	0,015	2,39	0	0
441,4	3	0,52	1,13	0,35	0	0,015	3,25	0	0
590,8	4	0,125	0,027	0,35	0	0,015	3,25	0	0,15
932,4	1	0,52	1,4	1,35	0	0,035	0,15	1,5	0
944,9	1	0,52	1,4	1,35	0,35	0,035	0,15	1,5	0
1156,7	26	0,52	0,027	1,75	0	0,035	0,15	1,5	0,15
1160,516	21	0,52	0,027	1,75	0,19	0,035	0,15	1,5	0,15

Полученото до тук показва основно, че резултатът зависи много от началната точка и подхода с използването за начална тока, стойностите на факторите от опита е оправдано. Най – големите стойности на максимумите дадени най – отдолу в таблица 3, табл.4 и табл.5 са желаните в случая кандидати за глобален максимум.

Ако може те да бъдат потвърдени, това ще помогне да бъдат обявени за „глобални".

Реши се да се продължи търсенето, като за начална точка се използват стойностите на факторите от получените безусловни максимуми.

Резултатите са дадени в табл. 6,, табл. 7., и табл. 8.

Табл.6. *Численни стойности на максимума за границата на провлачване, и решения от ново търсене.*

Максимуми от които са използвани стойностите на факторите за начална точка	Получена стойност на максимума. Стойностите на факторите са използвани за ново търсене на максимуми	Стойност На максимума
4113.9	**9597.98***	**10094.42****
4370.2	**9597.98***	**10094.42****
4425.0	**9597.98***	**10094.42****
5638.2**		
5969.6	**7478.0**	
6333.8**		
6423.7**		
7473.9	**7478.0**	
7478.0	**7478.0**	
8774.1**		
9564.6	**10094.42*****	
9601.3**		
10032.42	**10094.42*****	
10094.42	**10094.42*****	

* Новополучена стойност на максимум с координати:
$X_1 = 0.125$, $X_2 = 0.027$, $X_3 = 1.75$, $X_4 = 0$, $X_5 = 0.035$, $X_6 = 3.25$, $X_7 = 1.5$, $X_8 = 0$
** Условен максимум, не позволява по нататъшно търсене
*** Потвърдена най - голяма стойност на максимум

Както се вижда математичния модел на този изход предлага сложна много екстремална функция. Тръгвайки с начални точки от максимуми 4113.0, 4370.2 и 44250 се стига до нов новополучен максимум със стойност 9597.98. Използвайки неговите фактори за начални стойности при търсене на максимум се достига максимум със стойност 10094.42. С тази стойност се потвърждава три пъти получената най – голяма стойност.

По нататък фактурите на максимуми 5969.6, 7473.9 и 7478.0 използувани като начални точки, водят до максимум със стойност 7478.0.

Накрая, тръгвайки от максимум 7478.0, получаваме пак същата стойност, т.е. не може да бъде подобрена. Това налага препоръката , че тези стойности на факторите не трябва да се използуват опри една бъдеща експериментална проверка.

Следващите стойности на факторите от максимуми 956.4. 10032.42 и 10094.42 използвани като начални точки, водят до максимум със стойност 10094.42.

Резултатите от първите два потвърждават най – голямата получена стойност, а третият случай потвърждава, че няма по – голяма от тази най – голяма стойност.

След този резултат, получената най – голяма стойност 10094.42 може да бъде обявена за глобален максимум. Тя може да бъде получена , тръгвайки от 13 точки (виж табл.3), от използваните 80. При евентуални експериментални проверки това е от значение.

Направеното до тук наподобява изкачване по стълба. Като се стъпи на ново стъпало се прави нов опит на това ниво и т.н. до достигане на най – голямата стойност, като при това се потвърждава убедително, че тя е най – голяма.

Табл.7. *Численни стойности на максимума за относителното удължение, и решения от ново търсене.*

Максимуми от които са използвани стойностите на факторите за начална точка	Получена стойност на максимума. Стойностите на факторите са използвани за ново търсене на максимуми	Стойност На максимума
32.3**		
35.2	**35.2**	
80.3**		
91.6**		
93.06	**122.88*****	
96.2**		
122.88**		

** Условен максимум, не позволява по нататъшно търсене
*** Потвърдена най - голяма стойност на максимум

При този изход, картината е подобна на описаната вече. Вторият по ред максимум имащ стойност 35.2, позволява факторите му да бъдат използувани за начална точка. Тръгвайки от нея, крайния резултат е същата стойност на максимума. Това показва, че този резултат не може да бъде подобрен.

При максимум 93.06 стойностите на факторите използувани за начална точка, водят до стойност на максимума 122.88, което е потвърждение на получената до момента най – голяма стойност. Това позволява тази стойност да бъде обявена за глобален максимум. Получен е в 18 случая.

Не цитираните максимуми са условни и не позволяват търсене на максимуми.

И тук е валиден аналога със стълбата.

За случая с твърдостта, посочена в табл. 8. може да се каже, че използвайки стойности на факторите от максимуми 421.6, 439.8 и 441.4, водят до получаване на максимум със стойност 590.8, който съвпада с четвъртия след тях. При него стойностите на факторите вече са определели условен максимум.

Факторите на максимум със стойност 944.9 използвани за начална точка, водят до максимум със стойност 1160.5, което потвърждава до момента получената най – голяма стойност.

Накрая използвайки факторите на максимум 1160.5 за начална точка, водят до стойност 1160.5, което показва че няма по голяма от нея.

Това позволява стойността 1160.5 да бъде обявена за глобален максимум, получен в 22 от случаите. И тук е валиден аналога със стълбата.

Табл.8. *Численни стойности на максимума за твърдостта, и решения от ново търсене*

Максимуми от които са използвани стойностите на факторите за начална точка	**Получена стойност на максимума. Стойностите на факторите са използвани за ново търсене на максимуми**	**Стойност На максимума**
421.6	**590.8****	
439.8	**590.8****	
441.4	**590.8****	
590.8**		
932.4**		
944.9	**1160.5*****	
1156.7**		
1160.5	**1160.5*****	

** Условен максимум, не позволява по нататъшно търсене
*** Потвърдена най - голяма стойност на максимум

4. РЕЗУЛТАТИ ОТ ИЗСЛЕДВАНЕТО.

При търсене на глобален максимум на даден математичен модел най-правилно е това да започне с използване за начални точки стойностите на факторите във всеки отделен случай. По този начин продължава да се използва информацията заложена в експерименталните данни.

Сортирането и групирането около отделни стойности е следващата стъпка. Най – голямата от тях е желания глобален максимум.

Следващия етап ако е възможно се използват стойностите на факторите от получените максимуми за начални точки за последващо търсене на нови максимуми.

Това продължава до изчерпване на тази възможност. Най – голямата от тях се обявява за глобален максимум.

Факта, че до глобалните максимуми се достига от малък брой начални точки, предлага че това може да се постигне с едно сканиране на изходните данни , без да се намесват други методи за определянето им, например вероятностни методи и т.н..

Получените по този начин, стойности на факторите при отделните търсения може д се използват при експериментална проверка за тези резултати.

5. ЗАКЛЮЧЕНИЕ

Доказано е ,че ползването на стойностите на факторите от експерименталните данни за начални точки при търсене на глобален максимум е правилно и оправдано. Така се улеснява намирането му. Продължава ползването на информацията заложена в експерименталните данни.

Глобалният максимум е сред намерените.

Правилно е групирането на максимумите около отделни стойности.

Правилное използването на факторите на тези максиму и за начални точки за следващо търсене на максимум.

Получените при това най – големи стойности могат да бъдат обявени за глобални.

Счита се задължителна тази процедура при търсене на глобален максимум.

В случай за търсене на глобален минимум трябва само да се замени „максимум” с „минимум”, „ по-голямо” с „по-малко” и „най-голямо” с „най-малко”.

Новият подход е създаден така, че да предлага реална възможност за значително намаляване на разходите и времето за предсказване на химични концентрации за множество свойства на клас от сплави на желязна основа, така, че новите сплави ще имат по-добри свойства.

Постигнатите резултати показаха, че предложената методика може напълно удачно да бъде използвана за определяне на съществените връзки между екстремалните стойности на механичните параметри.

ЛИТЕРАТУРА:

1. Campbell C.E., G.B. Olson, “System design of high performance stainless steels I, Conceptual and computational design”, Journal of Computer-Aided Materials Design 2001, 7:145-170.
2. VitosL., P.A. Korzhavyiand B. Johansson, "Stainless steel optimization from quantum mechanical calculations", Nature Materials 2003, 2:25-28.
3. Tontchev N. Materials Science, Effective solutions and Technological variants, 2014/3/3, LAMBERT Academic Publishing
4. RajanK., “Materials Informatics Part I: A Diversity of Issues”, JOM 2008, 60:50-50.
5. Liu Z.K., L.Q. Chen and K. Rajan, "Linking length scales via materials informatics", JOM 2006, 58:42-50.Borst R. de, “Challenges in computational materials science: Multiple scales, multi-physics and evolving discontinuities”, Computational Materials Science 2008, 43:1-15
6. Koppen, M., Teunis, M., Nicholay, B., A Neural Network that uses Evolutionary Learning. Proc. of 1997 IEEE International Conference on Evolutionary Computation, ICEC’97, Indianapolis, IN, April, 1997, pp. 635-639
7. Иван Н. Вучков, Стоян К. Стоянов: Математическо моделиране и оптимизация на технологични обекти. 1980 г.;
8. Стоян К. Стоянов: Методи и алгоритми за оптимизация. 1990 г.;
9. Стоян К. Стоянов: Оптимизация на технологични процеси. 1993 г.;
10. Brian D. Bunday: Basic optimization methods. 1984 г.

№	Coefficient		№	Coefficient		№	Coefficient	
1	free	-4452.059	17	$X_2 X_3$	-1060.607	33	$X_5 X_7$	34576.83
2	X_1	8326.12	18	$X_2 X_4$	777.9031	34	$X_5 X_8$	133024.4
3	X_2	943.8401	19	$X_2 X_5$	-35124.73	35	$X_6 X_7$	-695.8329
4	X_3	-1868.801	20	$X_2 X_6$	-2324.508	36	$X_6 X_8$	-1760.739
5	X_4	229.4068	21	$X_2 X_7$	-3567.716	37	$X_7 X_8$	6238.599
6	X_5	162116.7	22	$X_2 X_8$	-3532.844	38	X_1^2	-2559.821
7	X_6	3373.654	23	$X_3 X_4$	157.4631	39	X_2^2	1536.74
8	X_7	34.32774	24	$X_3 X_5$	71579.5	40	X_3^2	60.02069
9	X_8	-432.2255	25	$X_3 X_6$	-21.16535	41	X_4^2	28.28497
10	$X_1 X_2$	3871.064	26	$X_3 X_7$	1664.799	42	X_5^2	-1935699
11	$X_1 X_3$	-1346.121	27	$X_3 X_8$	-5660.557	43	X_6^2	-224.8435
12	$X_1 X_4$	18.60078	28	$X_4 X_5$	-8071.432	44	X_7^2	486.6123
13	$X_1 X_5$	-133223.6	29	$X_4 X_6$	-281.8229	45	X_8^2	-45761.34
14	$X_1 X_6$	-2005.801	30	$X_4 X_7$	20.84207			
15	$X_1 X_7$	-2831.251	31	$X_4 X_8$	-80.51182	R = 0.8748619		
16	$X_1 X_8$	23344.15	32	$X_5 X_6$	-32668.01	E = 2.59499 > 1.705517		

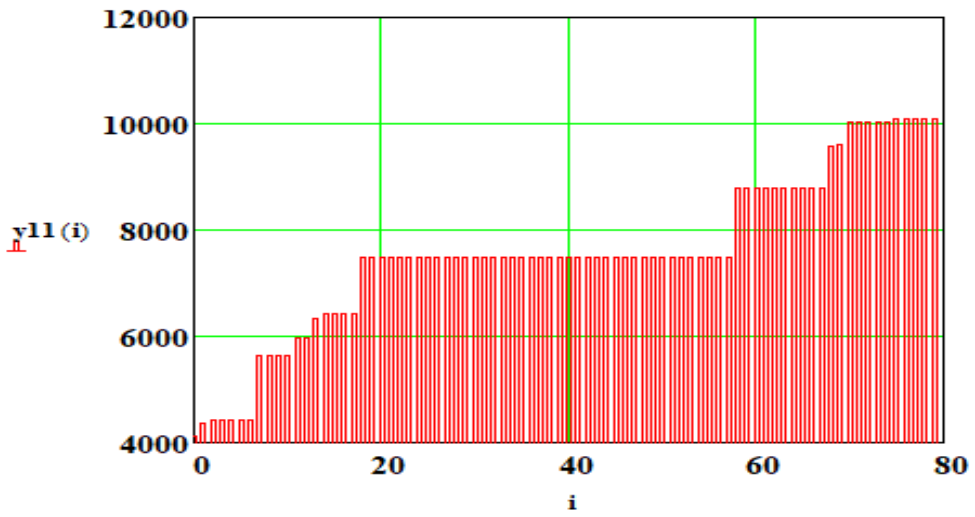

R - z		27	7742.95	54	7742.95
1	4734.6	28	7742.95	55	7742.95
2	4734.6	29	7742.95	56	7742.95
3	4734.6	30	7742.95	57	7742.95
4	5508.39	31	7742.95	58	7742.97
5	5892.9	32	7742.95	59	7747.19
6	5892.9	33	7742.95	60	9591.41
7	6100.14	34	7742.95	61	9591.41
8	6100.14	35	7742.95	62	9591.41
9	6100.14	36	7742.95	63	9591.41
10	6100.14	37	7742.95	64	9591.41
11	6100.14	38	7742.95	65	9591.41
12	6100.14	39	7742.95	66	9591.41
13	6100.4	40	7742.95	67	9591.41
14	6553.79	41	7742.95	68	9591.66
15	6553.8	42	7742.95	69	9591.66
16	6674.63	43	7742.95	70	9852.62
17	6674.63	44	7742.95	71	9992.68
18	6674.63	45	7742.95	72	10465.08
19	6674.65	46	7742.95	73	10465.08
20	7742.95	47	7742.95	74	10465.08
21	7742.95	48	7742.95	75	10465.08
22	7742.95	49	7742.95	76	10465.08
23	7742.95	50	7742.95	77	10465.08
24	7742.95	51	7742.95	78	10526.7
25	7742.95	52	7742.95	79	10526.7
26	7742.95	53	7742.95	80	10526.7

Приложение 1. *Коефициенти на модела и екстремални стойности за границата на провлачване*

№	Coefficient		№	Coefficient		№	Coefficient	
1	free	88.76084	17	$X_2 X_3$	-.548418	33	$X_5 X_7$	1009.666
2	X_1	30.8836	18	$X_2 X_4$	1.76884	34	$X_5 X_8$	1151.242
3	X_2	-12.15175	19	$X_2 X_5$	145.5527	35	$X_6 X_7$	17.68249
4	X_3	-18.70191	20	$X_2 X_6$	16.15557	36	$X_6 X_8$	24.2967
5	X_4	-4.422863	21	$X_2 X_7$	-.9981771	37	$X_7 X_8$	-22.4125
6	X_5	-3292.067	22	$X_2 X_8$	34.43759	38	X_1^2	-21.76391
7	X_6	-34.90053	23	$X_3 X_4$	-1.493248	39	X_2^2	-3.435944
8	X_7	-48.72969	24	$X_3 X_5$	354.9381	40	X_3^2	-.1078764
9	X_8	-21.01403	25	$X_3 X_6$	5.905782	41	X_4^2	-0.0196199
10	$X_1 X_2$	-12.86883	26	$X_3 X_7$	-20.4766	42	X_5^2	47704.26
11	$X_1 X_3$	2.852018	27	$X_3 X_8$	61.61046	43	X_6^2	2.900727
12	$X_1 X_4$	-4.159557	28	$X_4 X_5$	44.36152	44	X_7^2	-4.169527
13	$X_1 X_5$	-806.7738	29	$X_4 X_6$	3.888098	45	X_8^2	-342.9059
14	$X_1 X_6$	11.53828	30	$X_4 X_7$	-.3586056			
15	$X_1 X_7$	51.47882	31	$X_4 X_8$	6.280846	R = 0.884035		
16	$X_1 X_8$	-127.617	32	$X_5 X_6$	187.6339	E = 2.884035 > 1.705517		

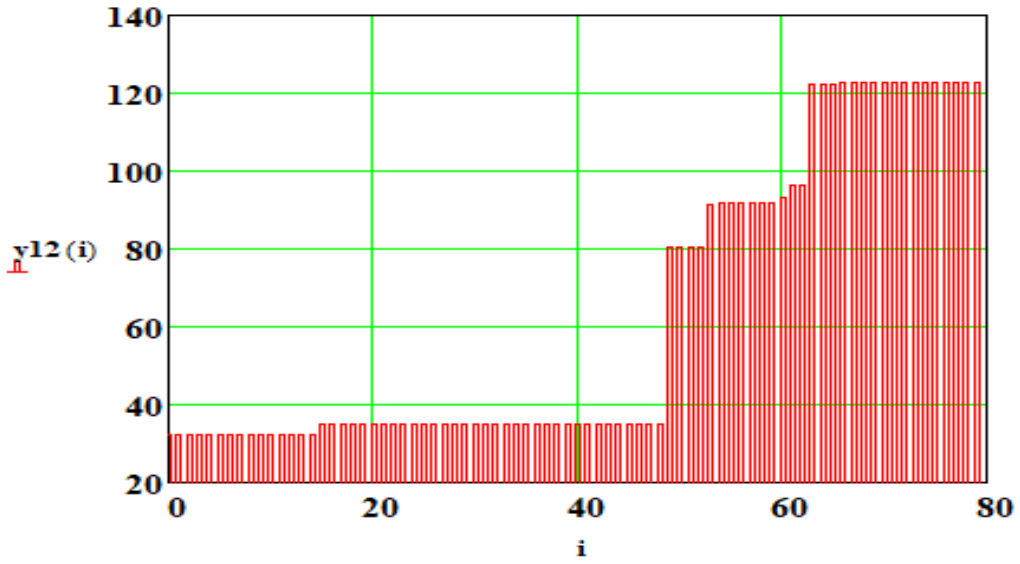

A		27	35.16	54	91.36
1	32.34	28	35.16	55	91.63
2	32.34	29	35.16	56	91.63
3	32.34	30	35.18	57	91.63
4	32.34	31	35.18	58	91.63
5	32.34	32	35.18	59	91.63
6	32.34	33	35.18	60	91.63
7	32.34	34	35.18	61	93.06
8	32.34	35	35.18	62	96.2
9	32.34	36	35.18	63	96.2
10	32.34	37	35.18	64	122.17
11	32.34	38	35.18	65	122.17
12	32.34	39	35.18	66	122.17
13	32.34	40	35.18	67	122.89
14	32.34	41	35.18	68	122.89
15	32.37	42	35.18	69	122.89
16	35.16	43	35.18	70	122.89
17	35.16	44	35.18	71	122.89
18	35.16	45	35.18	72	122.89
19	35.16	46	35.18	73	122.89
20	35.16	47	35.18	74	122.89
21	35.16	48	35.18	75	122.89
22	35.16	49	35.18	76	122.89
23	35.16	50	80.26	77	122.89
24	35.16	51	80.26	78	122.89
25	35.16	52	80.26	79	122.89
26	35.16	53	80.26	80	122.89

Приложение 2. *Коефициенти на модела и екстремални стойности за относителното удължение*

№	Coefficient		№	Coefficient		№	Coefficient	
1	free	-0.690552	17	$X_2 X_3$	-40.38304	33	$X_5 X_7$	5277.579
2	X_1	748.1019	18	$X_2 X_4$	12.01228	34	$X_5 X_8$	-603.9802
3	X_2	145.4783	19	$X_2 X_5$	-1194.606	35	$X_6 X_7$	-32.70389
4	X_3	-285.5187	20	$X_2 X_6$	-29.56228	36	$X_6 X_8$	17.64212
5	X_4	30.64575	21	$X_2 X_7$	-65.76683	37	$X_7 X_8$	548.8279
6	X_5	2772.399	22	$X_2 X_8$	-1981.146	38	X_1^2	-425.6137
7	X_6	213.4684	23	$X_3 X_4$	24.56322	39	X_2^2	-68.41123
8	X_7	-338.4433	24	$X_3 X_5$	7293.218	40	X_3^2	26.36744
9	X_8	502.9206	25	$X_3 X_6$	7.744653	41	X_4^2	2.029414
10	$X_1 X_2$	263.7722	26	$X_3 X_7$	284.951	42	X_5^2	-41440.31
11	$X_1 X_3$	-49.1374	27	$X_3 X_8$	-70.65888	43	X_6^2	-4.532439
12	$X_1 X_4$	-63.89705	28	$X_4 X_5$	-115.1166	44	X_7^2	-54.07746
13	$X_1 X_5$	-6435.193	29	$X_4 X_6$	-17.95414	45	X_8^2	3670.276
14	$X_1 X_6$	-187.5298	30	$X_4 X_7$	14.09137			
15	$X_1 X_7$	446.3832	31	$X_4 X_8$	-104.2053	R = 0.9429393		
16	$X_1 X_8$	-895.1897	32	$X_5 X_6$	-3710.575	E = 6.379504 > 1.705517		

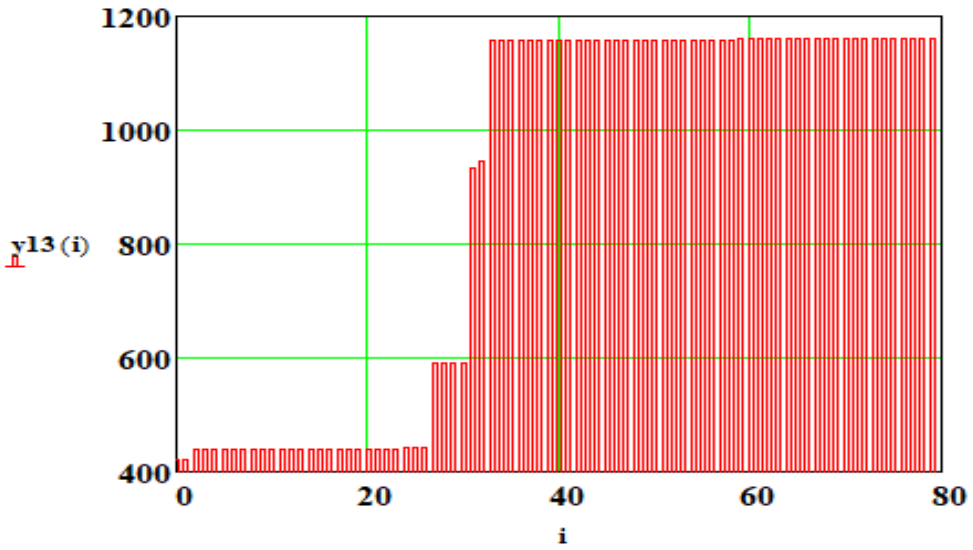

HB		27	442.6	54	1156.7
1	421.6	28	590.8	55	1156.7
2	421.6	29	590.8	56	1156.7
3	439.7	30	590.8	57	1156.7
4	439.7	31	590.8	58	1156.7
5	439.7	32	932.4	59	1156.7
6	439.7	33	944.9	60	1160.5
7	439.7	34	1156.7	61	1160.5
8	439.7	35	1156.7	62	1160.5
9	439.7	36	1156.7	63	1160.5
10	439.7	37	1156.7	64	1160.5
11	439.7	38	1156.7	65	1160.5
12	439.7	39	1156.7	66	1160.5
13	439.7	40	1156.7	67	1160.5
14	439.7	41	1156.7	68	1160.5
15	439.8	42	1156.7	69	1160.5
16	439.8	43	1156.7	70	1160.5
17	439.8	44	1156.7	71	1160.5
18	439.8	45	1156.7	72	1160.5
19	439.8	46	1156.7	73	1160.5
20	439.8	47	1156.7	74	1160.5
21	439.8	48	1156.7	75	1160.5
22	439.8	49	1156.7	76	1160.5
23	439.8	50	1156.7	77	1160.5
24	439.8	51	1156.7	78	1160.5
25	441.4	52	1156.7	79	1160.5
26	441.4	53	1156.7	80	1160.5

Приложение 3. *Коефициенти на модела и екстремални стойности за твърдостта*

TECHNOGENIC RAW MATERIALS FOR THE PRODUCTION OF MAGNESIUM AND SILICON-CONTAINING COMPOUNDS

Candidate of technical sciences Shayakhmetova R.A. [1],1st year PhD student Mukhametzhanova A.A.[1,2], Candidate of geological and mineralogical sciences Samatov I.B.[1], doctor of chemical sciences, assoc. prof. Akbayeva D.N.[2]
[1]RSE «National Center on complex processing of mineral raw materials of the Republic of Kazakhstan», Laboratory of Rare Metals, 050036 Almaty, 67 Zhandosov str.
[2]Al-Farabi Kazakh National University, Department of Physical Chemistry, Catalysis and Petrochemistry, Faculty of Chemistry and Chemical technology, Republic of Kazakhstan, Almaty 050040, Al-Farabi Avenue 71
e-mail: narike.91@gmail.com

Abstract: *This work considers technogenic waste from chrysotile asbestos production as a source of magnesium and silicon-containing compounds. The products obtained by hydrochloric acid dissection of chrysotile asbestos wastes were studied by chemical, scanning electron microscopy, thermogravimetric analysis.*
KEY WORDS: *CHRYSOTILE-ASBESTOS, TECHNOGENIC WASTES, LEACHING, SILICA, MAGNESIUM*

1 Introduction

The anti-asbestos campaign launched in the countries of Western Europe and the USA, which is mainly competitive in nature and aimed against the use of amphibolite asbestos, has significantly reduced chrysotile-asbestos export opportunities. For this reason, many asbestos mining and processing plants in the world have created additional capacity for the production of nonmetallic building materials demanded by consumers. Complex processing of chrysotile asbestos raw materials, as well as industrial wastes from their enrichment has become very relevant for many mining and processing enterprises associated with asbestos under market conditions and a crisis situation around asbestos [1-3].

There are various mineral classes of asbestos, including amphiboles and serpentinites. In Kazakhstan and in Russia, the deposits of the latter are widespread.

During the processing of chrysotile asbestos raw materials, only 6-8% is extracted into the commodity fiber, the rest, which is a serpentine raw material $3MgO{\cdot}2SiO_2{\cdot}H_2O$, is irretrievably lost as waste. With the enrichment of serpentinite the target product - asbestos fiber (Fig. 1a) and waste (Fig. 1b) are obtained. Fibrous type of serpentinite - asbestos has an independent technical value. Waste from the production of the asbestos industry is a source of environmental pollution and at the same time represents a mineral reserve of mineral raw materials practically prepared for processing for metallurgy and the construction industry [4].

а б

Fig. 1 *– Products of serpentinite enrichment*

The total reserves of the main useful components contained in industrial wastes are comparable to the reserves of a fairly large polymetallic deposit.

2 Results and discussion

The subject of the research was the sand fraction -1.25 + 0.25 mm technogenic wastes from the serpentinite enrichment of the Zhitikara deposit.

Every year thousands of tons of high magnesium content waste are generated at Kostanay Minerals JSC, which occupy a huge area and carry an environmental hazard to the region (Fig. 1b). The question of the need to recycle the enterprise's waste with the release of new products that are in demand, competitive with high value-added products is relevant for Kazakhstan, as well as for countries producing asbestos fiber.

Chemical, scanning electron microscopy, thermogravimetric analysis methods were used to perform the studies.

Thermal analysis of the samples was carried out on a Q-1000/D derivatograph of the F.Paulik, J.Paulik and L.Erdey systems from MOM (Budapest) company. The survey was carried out in air, in the temperature range of 20–1000 °C, the heating mode was dynamic (dT/dt = 10), the reference substance was calcined with Al_2O_3, and the sample weight was 500 mg. X-ray phase analysis on a DRON-4 diffractometer, micro-X-ray fluorescence analysis on an EDAX tsl ametek instrument. Chemical analysis data obtained using certified methods.

The mineral base of chrysotile asbestos production wastes, according to X-ray phase analysis, is serpentine-$3MgO{\cdot}2SiO_2{\cdot}2H_2O$, containing silica in crystalline and amorphous states (Table 3). Of the other components, up to 5-7 % of iron oxides in the form of hematite and magnetite are present in the feedstock.

Table 3 *– X-ray phase composition of asbestos waste*

Component	Formula	Mass composition, %
Serpentine	$3MgO{\cdot}2SiO_2{\cdot}2H_2O$	61
Talcum	$3MgO{\cdot}4SiO_2{\cdot}H_2O$	19
Brucite	$Mg(OH)_2$	5
Forsterite	Mg_2SiO_4	4
Magnesium oxide	MgO	3

Figure 2 *shows the results of the analysis of the initial waste obtained on a scanning electron microscope.*

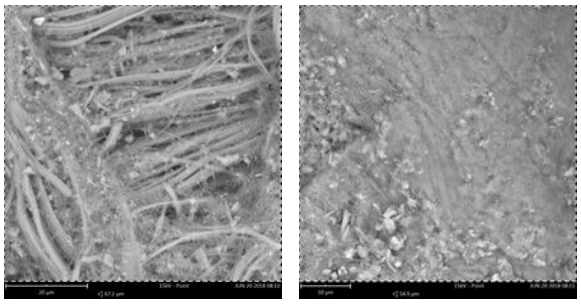

a b

Figure 2 – *Electron microphotograph of chrysotile asbestos waste*

In electron microphotographs, chrysotile asbestos wastes are represented by particles of different sizes with inclusions of asbestos filamentous fibers (Fig. 2).

Table 1 *– The average composition of chrysotile asbestos waste*

Element Symbol	Atomic. %	Oxide Symbol	Stoich. wt %
O	66,17		
Mg	19,87	Mg	41,25
Si	9,29	Si	33,43
Fe	0,35	Fe	2,75
Ca	0,46	Ca	1,35
C	0,25	C	0,38
Al	0,13	Al	0,23

Table 2 *– Chemical composition of technogenic wastes*

Fraction size, mm	MgO	SiO_2	Al_2O_3	CaO	Fe_3O_4	NiO
-1,25 +0,25	39,0	36,5	0,79	0,46	4,87	0,22

As can be seen from the data of Tables 1 and 2, the main components of chrysotile asbestos waste are (in %): MgO – 39.0-41.3; SiO_2 – 33.4-36.5; CaO – 0.5-1.4; Fe_2O_3 – 2.7, Fe_3O_4 – 4.9. According to chemical analysis Nickel is present in small amounts..

Sulfuric acid and hydrochloric acid methods of processing waste of this type are known [5-10]. The low level of the market consumption of magnesium sulfate in Kazakhstan should be attributed to the risk factors for the development of sulfuric acid technology [5, 6]. The hydrochloric acid opening of asbestos wastes allows obtaining the marketable products of magnesium and silicon [7-10].

The technology of hydrochloric acid dissection of chrysotile asbestos technogenic raw materials consists in transferring magnesium into solution, two-stage purification of productive solutions from impurities, crystallization of bischofite.

As a result of this work, bischofite was obtained from chrysotile asbestos wastes. Thermograms of the sample $MgCl_2 \cdot nH_2O$ at a heating rate of 10 °C/min are presented in Figure 3.

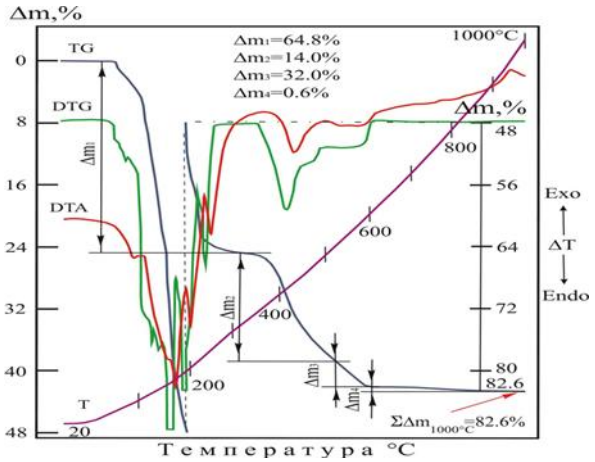

Fig. 3 – Derivatogram of sample $MgCl_2 \bullet nH_2O$

The DTA curve captures a number of endothermic effects associated with the dehydration of the system. According to the literature, the first endoeffect (at T = 132 °C) corresponds to the melting of $MgCl_2 \cdot 6H_2O$ with water splitting. The second thermal development (at T~213 °C) according to the change in mass characterizes the removal of 3.03 mol of water, the third effect (246 °C) corresponds to the removal of 1.55 mol of water from the system, and the next stage of dehydration (291 °C) is associated with loss 1.18 mole of water. In our case, these endothermic effects are caused by a 64.8 % decrease in sample mass, which corresponds to a loss of ~ 9.7 moles of water.

The endoeffect at 480 °C corresponds to the decomposition of the products of hydrolysis of magnesium chloride and the formation of anhydrous magnesium oxide MgO. The decomposition of magnesium hydroxochloride is accompanied by a change in mass of 14.0 % in the first sample and 15.7 % in the second. This process ends at 635 °C and leads to a loss of 3.2 % by weight.

The endoeffect at 720 °C corresponds to the beginning of the melting of anhydrous $MgCl_2$. and weight loss of 0.6 % and 0.5 %, which can also be explained by evaporation or decomposition of magnesium chloride.

The chemical composition of the resulting product is, wt.%: $MgCl_2 \cdot 6H_2O$ 97.5; Mg^{2+} 11.8; sulfate ions SO_4 0.8; alkali metal ions (Na^+, K^+) 0.1; water insoluble residue 0.15.

Electron micrographs of the silicon-containing residue obtained in the process of hydrochloric acid leaching of chrysotile asbestos wastes with the following process parameters: the concentration of acid used is 18–20 %, S:L 1: 3, the process temperature is 85–90 °C, time is 120 min and four-stage washing is shown in Figure 4. The average composition of the silicon-containing residue is shown in Tables 3 and 4.

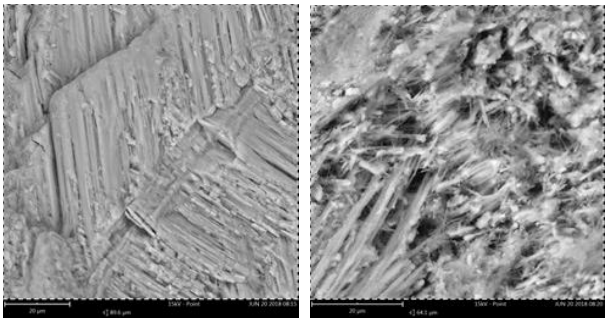

a b

Fig. 4 *– Electron microphotograph of silicon-containing residue*

Table 3 *– The average composition of the silicon-containing residue after leaching*

Element Symbol	Atomic. %	Oxide Symbol	Stoich. wt%
O	74,69		
Si	17,46	Si	75,29
Mg	4,88	Mg	13,02
Al	0,51	Al	1,98
Fe	0,55	Fe	3,88
C	0,67	C	2,03
Cl	0,35	Cl	1,56

Table 4 *– The results of chemical analysis of silicon-containing cake after leaching*

Content, wt. %						
Cr_2O_3	MgO	FeO	MnO	SiO_2	Ni	Cl
0,52	7,58	3,41	0,044	75-78	-	0,35

Silica cake after processing contains up to 13 % of magnesium oxide contaminated with impurities of iron, aluminum, chromium, manganese. This product will be of limited use.

In order to reduce the loss of magnesium, complete its transfer into the solution and obtain pure silica, the second stage of leaching with 18% hydrochloric acid at S:L rate 1: 3, temperature 85-90°C.

Electron microphotograph of the silicon-containing residue after the second stage of acid treatment and two-stage washing with water is shown in Figure 5. The average composition of the silicon-containing residue is shown in Tables 5 and 6.

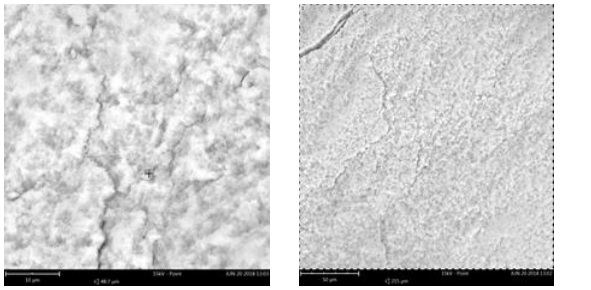

FOV: 215 μm, Mode: 15kV - Point, Detector: BSDFu FOV: 48.7 μm, Mode: 15kV - Point, Detector: BSDFull

a b

Figure 5 *– Electron microphotograph of the silicon-containing residue after the second stage of acid treatment at different magnifications*

Table 5 *– The average composition of the silicon-containing residue after the second stage of acid treatment*

Element Symbol	Atomic. %	Oxide Symbol	Stoich., wt%
O	75,39		
Si	19,39	Si	98,11
Mg	0,33	Mg	1,20
Fe	0,06	Fe	0,13
Cl	0,11	Cl	0,59

Table 6 *– The results of chemical analysis of the silicon-containing residue after the second stage of acid treatment*

Content, wt.%				
MgO	FeO	MnO	SiO_2	Cl
1,92	0,08	0,046	90-95	0,33

From the presented results it can be seen that the resulting amorphous silica contains almost no iron and other impurities, the magnesium content has decreased by 4 times.

3 Conclusion

Thus, according to the results of an electronic scanning microscope and chemical analysis data, it follows that with complex processing of chrysotile-asbestos wastes using hydrochloric acid technology, in addition to bischofite, amorphous silica with an SiO_2 content of 97-98%, which is recommended for use in as a filler in the rubber industry, in the production of paints, varnishes, silicate adhesives, the starting material for the production of high-purity silicon.

4 References:

1 Ivanov V.A. Anti-asbestos company and the situation with the use of chrysotile in the world // Source book of the Fifth Intern. scientific and practical conf. “Geologists 2010: Problems and ways of industrial-innovative development of mining industries” Zhitikara. – 2010. – p.83-91.

2 Yizmerov N.F., Kovalevsky E.V. A brief overview of the documents of international organizations on chrysotile // Source book of the Fifth Intern. scientific and practical conf. “Geologists 2010: Problems and ways of industrial-innovative development of mining industries” Zhitikara. – 2010. – p.143-146.

3 Dzhafarov F.N., Dzhafarov N.N. Complex utilization of waste from the Dzhetygara deposit of chrysotile asbestos as a source of increasing production efficiency // Mining and Geological Journal – 2003. – № 3. – p. 3-7.

4 Ratsen V.Z., Strelnikova V.Ya., Kolomiytsev V.V. Waste from the processing of asbestos-containing ores and their characteristics as a mineral material for road construction / Uralasbest: Asbestos. – 2005.

5 Bedelova Zh.D., Tabylganova A.N., Homyakov A.P., Dagubaeva A.T. Developing the technology of waste sulfuric acid leaching of chrysotile asbestos production // International journal for science, technics and innovations for the industry. – 2017. – Issue 7. – p. 350-352.

6 Khomyakov A., Tabylganova A., Nurkhodzhaev E., Bedelova J., Dagubaeva A. Obtaining of magnesium sulphate from chrysotile - asbestos waste // Industry of Kazakhstan. – 2015, № 2. – P. 72.

7 Figara P., Chin E., Walker T. Magnola. New Industrial Process of Magnesium Production // The Canadian Mining and Metallurgical Bulletin. – 1998. – V. 91, № 1019. – P. 214.

8 Shayakhmetova R.A., Nurkhozhaev E.S., Stepanenko A.S., Baygenzhenov O.S., Osipov P.A., Zhumataev B.A. Obtaining magnesium chloride and carnallite from chrysotile asbestos wastes // Proceedings of the international scientific-practical conference “Mining sciences in the industrial-innovative development of the country”, Almaty. – 2015. – p. 423-427.

9 Baigenzhenov O.S., Kozlov V.A., Luganov V.A., Mishra V.A., Shayahmetova R.A., Aimbetova I.O. Complex Processing of Wastes Generated in Chrysotile Asbestos Production // Mineral Processing and Extractive Metallurgy Review. – 2015. – № 36. – p. 242–248. DOI: 10.1080/08827508.2014.955610

10 Shayakhmetova R, Stepanenko A., Osipov P., Zhumakynbay N. Obtaining carnallite from technogenic chrysotile asbestos wastes // Industry of Kazakhstan. – 2016. – № 4. – p. 83-85.

GEOMETRIC METHOD FOR DETERMINIG RADIANT HEAT EXCHANGE IN VACUUME FURNACE

PhD Eng. Angelova E, Assoc.Prof. PhD Eng. Ronkova V., Assoc.Prof. PhD Eng. Faculty of Transport, University of Ruse, Bulgaria
E- mail: eangelowa@uni-ruse.bg

Abstract: *Heating chamber in vacuum furnace is closed thermal system where heat exchange is predominantly radiant. Conductive heat exchange is defined by well-known formulas. In order to determine the temperature condition of the object during heating (cooling), it is necessary to determine the angular coefficient of radiant exchange on every other objects. The known in the literature methods, including the geometrical once, have a solution for heat exchange only between two objects. The applications for real heat systems is partial and limited. It is presented a geometric model for calculation the angular coefficients of radiant interchange for closed thermal system. Heat exchange is taking place between an unlimited number of objects and a free-standing arrangement between them. The model allows solutions for objects of different geometric form in the presence of intermediate objects, as well as barriers for heat radiant from their own surfaces. The paper has been verified by a solution of thermal problems for vacuum furnaces.*

Keywords: *vacuum furnace, heater, angular coefficient, radiant heat*

1. Introduction

In vacuum furnaces the heat exchange is predominantly radiant as in diluted gas environment the convection heat transfer can be neglect.

In order to determine the temperature condition of the object during heating(cooling), it is necessary to determine the angular coefficient of radiant interchange. In the litreture [2], it is derived dependancies for calculating angular coefficient between two objects in predetrmiend geometrical surface and position.

In real-life thermal systhem those dependancies can have only partial application. The reason for that is the existance of various restrictions in the radiant intechange between two objects.

For example, on Fig. 1 it becomes clear that not all of the rays from p. A of radiating sutface of Object 1 reach the surface of Object 2.

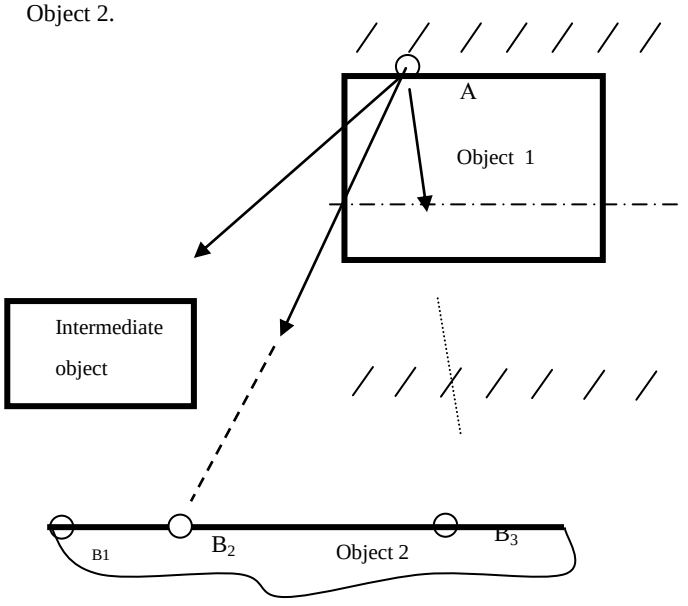

Additional constraint that is area from objects surface where heat exchange with another object is through conduction. These areas are not included in radiating surface.

In radiation theory determining the angular coefficients between two objects is accomplished through geometric task and it is represented mathematically with certain/insignificant dependences(1) [],[], (Fig. 1). With restrictions in free irradiation in variety in geometric surfaces as well as positioning of objects, solutions in (1) in most cases can not be found.

$$\phi_{1,2} = 1/F_1 \int_{F_1} \int_{F_2} \frac{\cos\beta_1 \cos\beta_2}{\pi . S^2} dF_1 dF_2 \quad ;$$

$$\phi_{1,2} . F_1 = \phi_{2,1} . F_2 \qquad (1)$$

, where $\phi_{1,2}$ and $\phi_{2,1}$ -angular coefficients of heat exchange, respectively:

Object 1 to Object 2 and Object 2 to Object 1;

F_1 и F_2 - the overall area of surfaces` objects;

$\cos\beta_1$ и $\cos\beta_2$ - cosine of angle between ray and a normal to the relevant surface;

S - length of the ray between dF_1 и dF_2;;

n1 и n2 - normal to surfaces dF1 and dF2.

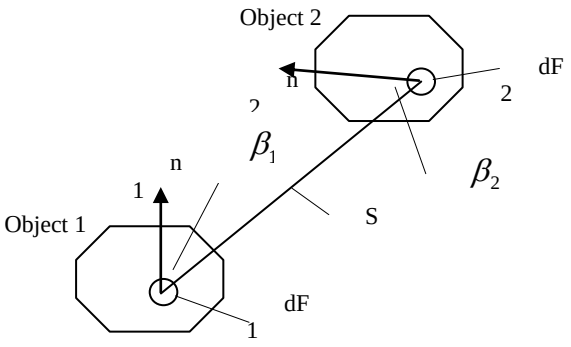

Fig.1. *Scheme relating to determine angular coefficient of heat exchange to (1).*

Calculations are undertaken through sequential solution of elementary integral parts on every object in respect to the rest. The result is average angular coefficient with acceptable margin of error for solution of practical tasks.

2. Solution of the problem

In [1] are summed up the possible types of tasks and restricting conditions for heat exchange between two objects.

In order for calculations to be done in (1), in any moment with every position of elementary integration parts, it must be determined: the length of the ray (S) and angles β , between it and the normals to them.

$$S^2 = \Delta X^2 + \Delta Y^2 + \Delta Z^2 \quad \text{, where} \qquad (2)$$

$$\Delta X = X_{A_{внш}} - X_{A_{обк}}; \Delta Y = Y_{A_{внш}} - Y_{A_{обк}};$$

According to [1], the possible positions of the surfaces that $\cos\beta$ is determined are:

- Plane with a normal parallel to one of the coordinate axes;
- Plane parallel to coordinate axe "X":
- Cylindrical outer and inner surfaces with a geometric axis parallel to X.
- Cylindrical outer surface with a geometric axis perpendicular to X.
- Obstruction object with a planar shape
- Obstruction object with cylindrical surface

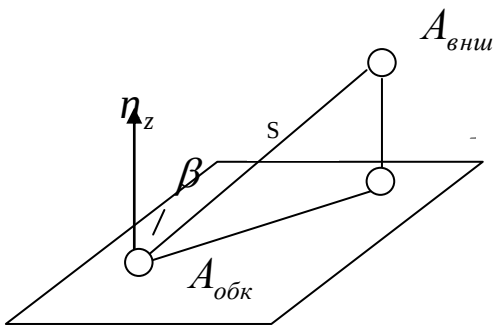

a

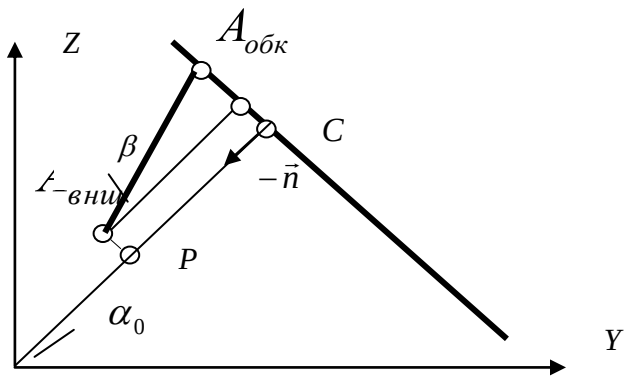

b

Fig. 1. *Scheme for calculating* $\cos\beta$ *:*
a) for plane with normal that is parallel to 'Z'($A'A_{внш} = \Delta Z$*)*
б) for plane parallel to coordinate axe "X".

With dependencies it is calculated $\cos\beta$ respectively for plane with normal parallel to X, Y or Z. With $A_{внш}$ and $A_{обк}$ stands for current area of radiation "external" and the object being irradiated.

$$\cos\beta = |\Delta X| / S; \qquad \cos\beta = |\Delta Y| / S;$$
$$\cos\beta = |\Delta Z| / S;$$

In the second case (Fig 1 b), the plane is defined with p. S between it and angle α_0 that intersect with the normal "$-\vec{n}$" with axe "Y". $\cos\beta$ is calculated with dependencies 4b.

$$Zp = \frac{Zc - (Yc - Y_{A_{внш}})tg\alpha_0 + tg^2\alpha_0 Z_{A_{внш}}}{1 + tg^2\alpha_0};$$
$$Yp = Y_{A_{внш}} - (Zp - Z_{A_{внш}})tg\alpha_0;$$
$$PC = \sqrt{Y_c^2 + Z_c^2} - \sqrt{Y_p^2 + Z_p^2};$$
$$\cos\beta = PC / S$$

On Fig.2 it is shown method for calculating $\cos\beta$ for cylindrical surface with geometrical axe parallel to 'X'. The normal to the surface in point $A_{обк}$ is continuation of $O'A_{обк}$=R and lay in the plane of a triangle $O'A_{обк}A_{внш}$, and O's coordinates $X_{обк}$, $Y_{ос}$, $Z_{ос}$ lies in a cross-section of the surface through the current crawl point $A_{обк}$. After calculating $O'A_{внш}$ as a distance between two points in space and a substitution in a cosine theorem, for $\cos\beta$ the result is (3) . The plus and minus characters refer respectively to the outer and inner surfaces and are obtained due to the different direction of the normal.

$$O'A_{внш}{}^2 = R^2 + S^2 - 2R\cos(180 - \beta)$$

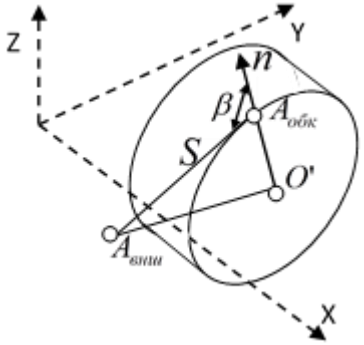

Fig.2 Method for calculating $\cos\beta$ for cylindrical surface with geometric axis || X

$$\cos\beta = \pm\frac{O'A_{внш}{}^2 - (R^2 + S^2)}{2RS}$$

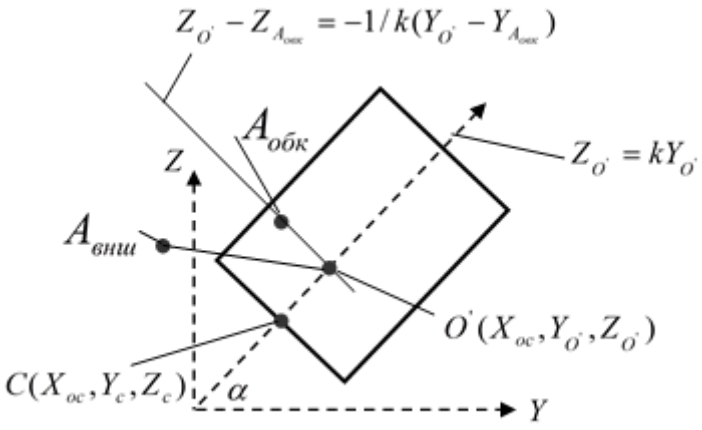

Fig.2 Method for calculating $\cos\beta$ for cylindrical surface with geometric axis $\perp$ X

On an outer cylindrical surface with a geometric axis perpendicular to 'X' and rotated at an angle $(X_{A_{внш}}, Z'_{A_{внш}})$ according to OY (fig.3) the solution is analogical. $\cos\beta$ is calculated with (3) , and $O'A_{внш}$ with dependencies (4). Point C

is center of cylinder base, point O' is the center of the cross section through the $A_{обк}$.

$$O'A_{внш}^{\ 2} = (X_{A_{овк}} - X_{oc})^2 + (Y_{A_{овк}} - Y_{O'})^2 + (Z_{A_{овк}} - Z_{O'})^2 \quad (4)$$

,where

$$k := Z_c / Y_c;$$

$$Z_{O'} = k(kZ_{A_{овк}} + Y_{A_{овк}})/(k^2 + 1);$$

$$Y_{O'} = Z_{O'} / k;$$

In relation to the analogy in the algorithms for solving two tasks have been provided:

Irradiation of external cylindrical surface with an axis || 'X' from a point outside of it.

The possible direction of irradiation from p. $A_{обк}$ are derived from tangent surface through cylindrical surface. The requirement for irradiation of p. $A_{внш}$ from $A_{обк}$, is for it to be in the zone of irradiation of point $A_{обк}$. On fig. 4 it is shown a solution with a plane that is perpendicular to the axe of the cylinder. The angular coefficient is determind κ on a straight line $OA_{обк}$as well as the point of intersection P between it and a straight line though point $A_{внш}$ perpendicular to$OA_{обк}$.

For т. $A_{обк}$ a requirement must be met (point that lay on the section) where irradiation between two points has to be ensured. The coordinates Y_P иZ_P are calculated according to (5).

$$\text{If } Y_{A_{обк}} = Y_{oc}: \quad Y_P = Y_{oS}; \quad Z_P = Z_{A_{внш}}; \quad \text{If } Y_{A_{обк}} \neq Y_{oc}: \ \kappa := (Z_{A_{obk}} - Z_{oc})/(Y_{A_{obk}} - Y_{oc});$$

$$Z_P = \left[Z_{oc} + \kappa^2 . Z_{A_{внш}} + k.(Y_{A_{внш}} - Y_{oc})\right]/(\kappa^2 + 1);$$

$$Y_P = (Z_P - Z_{oc})/\kappa + Y_{oc} \quad (5)$$

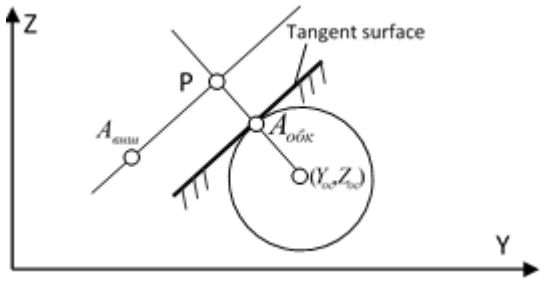

Fig. 4 Irradiation of an external cylindrical surface with axe || X from a point outside of it.

Obstruction object - planar figure.

Every object is an obstacle if the point intersection of the ray (p. P) is inner for section $A_{внш}$ $A_{обк}$ as well as it is in the contour of the object in the projection plane that is perpendicular to the normal. The coordinates X_P, Y_P и Z_P for different positions of the geometric normal are calculating through derived formulas and ΔX, ΔY и ΔZ with (3). On fig.5 it is given a clarification for conditions that fulfill obstacle "circle" и 'ring' with normal through X. For geometric normal that is perpendicular to X the solution is taking into an account object "circle" with rotated coordinate system XY'Z' (fig. 6). The coordinates $Y'_{A_{внш}}$, $Z'_{A_{внш}}$ и $Y'_{A_{обк}}$, $Z'_{A_{обк}}$ and for the center of the circle Y'_C, it is calculated through derived formulas in different, ΔX, $\Delta Y'$ и $\Delta Z'$ with (3) for recalculated coordinates with point index $A_{внш}$ and$A_{обк}$. The coordinates of p. P are calculated according to (7).

Fig.5. Conditions for irradiation with given obstacles "circle" and "ring" with W|| X.

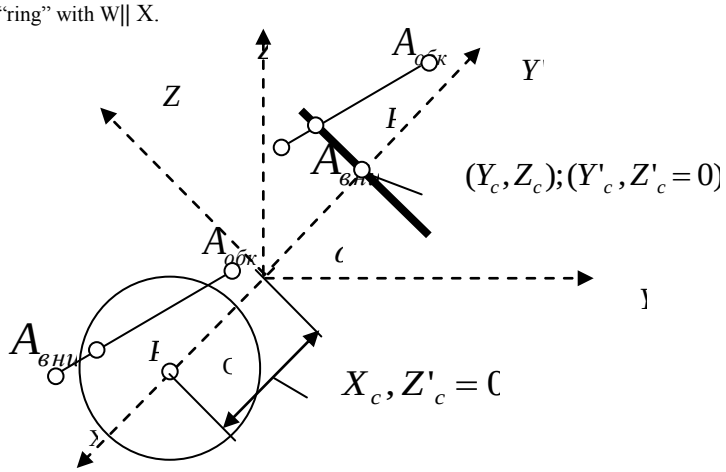

Fig.6. Conditions for irradiation with given obstacles "circle" with geometric normal $\perp$ X.

Coordinates of p.P, respectively for geometric normal || X,Yor Z:

$$Z_P = (X_C - X_{A_{обк}}).\Delta Z / \Delta X + Z_{A_{обк}};$$

$$Y_P = (X_C - X_{A_{обк}}).\Delta Y / \Delta X + Y_{A_{обк}}$$

$$Z_P = (Y_C - Y_{A_{обк}}).\Delta Z / \Delta Y + Z_{A_{обк}};$$

$$X_P = (Y_C - Y_{A_{обк}}).\Delta X / \Delta Y + X_{A_{обк}}$$

$$X_P = (Z_C - Z_{A_{обк}}).\Delta X / \Delta Z + X_{A_{обк}};$$

$$Y_P = (Z_C - Z_{A_{обк}}).\Delta Y / \Delta Z + Y_{A_{обк}} \quad (6)$$

Coordinates of p.P for geometric normal X:

$$Z'_P = (Y'_C - Y_{A_{обк}}).\Delta Z' / \Delta Y' + Z'_{A_{обк}};$$

$$X'_P = Z'_{A_{обк}}.\Delta Z' / \Delta X + X_{A_{обк}} \quad (7)$$

4. Conclusion

It is presented a geometric method for calculation the angular coefficients of radiant interchange for closed thermal system. Heat exchange takes place between an unlimited number of objects and a free-standing arrangement between them. The model allows solutions for objects of different geometric form in the presence of intermediate objects, as well as barriers for heat radiant from their own surfaces. The paper has been verified by a solution of thermal problemss for vacuum furnaces.

L I T E RA TU R E

1. Зигел Р., Дж. Хауел. . Теплообмен излучением, Мир, Москва.,1975
2. Angelova, Evg., Trifonov, Tr., Geometric Approach for Determining the Angle Irradiation Coefficients in the Vacuum Furnace, Scientific papers of University of Ruse, 2004

HOME PAGES, DEFINITION AND CLASSIFICATION OF THEIR ELEMENTS AND THEIR DISPLAY ON THE USERS' COMPUTERS

Asst. Prof. Bidjovski Goran PhD.
Faculty of Computer Science – International Slavic University "G. R. Derzhavin", Macedonia

bidjovskigoran@yahoo.com

Abstract: *The subject of the research in this scientific paper is a description of the home pages in websites, with special emphasis on definition and classification of elements, which are necessary for the proper functioning of a home page, from the aspect of functionality and creativity. The important part of my paper is an analysis of technical methods of their displaying on various users' computers. Here the comparative analysis of similarities and differences between a home page and other pages of the same website is made. A special overview is made for the correlation between home pages and all the other pages on the website from a point of view of visual harmony and functionality of those websites. Additionally, here I give overall directions for using home pages when designing websites, and also a description of some opinions and advice on the same topic. After that, I analyze six problems which arise from displaying home pages on the user's computer and topics connected with that. I will come across a few solutions for all of them, as well as recommendations for when to choose which solution.*

Keywords: HOME PAGES, DEFINITION AND CLASSIFICATION OF ELEMENTS OF A HOME PAGE, THE COMPOSITION OF THE WEBSITES, WEB DESIGN

1. Introduction

The basic four rules of design that need to be considered when designing a website are:
- Contrast. The rule of contrast means that the placement of similar elements on the same page should be avoided. If the elements (font, color, size, line thickness, contour, interval, etc.) are not exactly the same, but only similar, then they should be shaped differently. Very often, initially the contrast attracts the attention of users of the site.
- Repetition. The elements of the design should be repeated through the entire edition. Colors, contours, textures, mutual relations, line thickness, fonts, proportions, graphic concepts, etc. can be repeated. Repetition helps for better structuring and enhances the sense of integrity.
- Alignment. Nothing should be placed on the page by chance. Each element should have a visual connection with the other elements. This gives to the page a clean, sophisticated and fresh look.
- Closeness. Elements that are in some way related to each other should be close to each other. So these elements represent one unity and not just a few fragments. It helps information's to be well organized and reduces overcrowding, providing the reader with a clear structure.

Although the four basic rules apply also in the web design, repetition is the basic rule when shaping a website. The other three rules also help, but repeating is what shows visitors that they are still on the same site. There must be consistency in the navigation and the style of graphic design, repetition of the color scheme, the use of the same fonts, the placement of one styled graphic elements in the same way on each page, etc. [1]

A well-organized website should have: a logical structure, constant navigation, and clear inscriptions.

When determining the style for websites, it's good to know these two rules: there should be consistency in using the features of the design, and in the overall style of the site less is better (sometimes the most effective design is simple but elegant).

Good websites are designed with the ability to increase so to meet the new needs of their users, as these needs change over time.

An important rule regarding the structure of the website is to have a structure built in a way that reflects the user's view of the site and its information and/or services. The basic mistake is the structure of the site to reflect the organization of the company, rather than the user's point of view. [15]

Good websites are more than just random collected pages. They have to create a coherent overall impression on the visitor. [18]

When visitors move from page to page, they should always feel that they are on the same site. Although small decorative changes are good, the style and structure of the page should not be changed at once. Especially recommended are permanent background and unchangeable color scheme. Although the content of the pages is changed, the "containers" will be the same. On good sites, passing from page to page is unnoticeable.

Information that is repeated on many pages should be displayed in one and the same position. The structure and order of pages in a website should be logical. [17]

Each web page should have a clear visual hierarchy. Pages with a clear visual hierarchy are distinguished by three distinctive features:
- the more important a given element is, the easier it is to notice it (the most important titles should be larger, written in bold font, colored with a striking color, fenced with more than the usual blank space or placed close to the top of the page).
- elements that are logically connected, should be also visually connected (certain elements which are similar, when grouped under one title, will be displayed on a screen in a similar visual style or will be put together in a clearly defined area).
- it is good for some elements to be visibly put inside one another to see which is from what part (if a book is part of a given section, it is appropriate that the title of the section is located above the title of the book, encompassing visually the whole area for the content of the page).

Also, the good visual hierarchy saves time. [6]

Every page should have a focus (attention center), from which the reader should start. This focus is created by implementing visual contrasts, for example: large and small elements, dark and bright, rectangular and round, many and just a few, etc. [2] Websites are a set of different types of pages, but the home page is an inevitable part of all sites.

2. Study Area

The home page of a website can be considered as a "facade" of that site. Facade of the site should always be carefully thought about. The face of the website should be attractive and unforgettable in order to gain visitors attention. Business people say "the first impressions sell". [7]

Creating a good first impression is more than just looking good to everyone. The home page should seductively suggest the content of the site. [14]

The immediate goal of every home page is to answer the questions "Where am I?" and "What is this site for?"
The home pages are relatively permanent places that do not change their position, and with that, they help the orientation of the visitors on the site. [9]

Everyone wants a "piece" of the home page. This is the page that almost every visitor sees, and for some users, it remains the only seen page. Everything that is clearly emphasized on the home page is visited a lot more times. [13]

An attractive presentation of some of the content on the home page is an essential part of the information architecture because it

allows visitors to immediately find new contents instead of having to search for them.

Without it being a binding rule, most home pages tend to cover all content in one screen, which is without vertical scrolling. It is often a difficult task. [11]

The content of the home page should be regularly renewed. If the success of the site depends on whether it will be visited often, the home page will, in every probability, have to contain content that will often be updated.

The home page can be designed in a way that differs from that of the other pages. Of course, the home and the other pages should have the same style, but sometimes, depending on the conditions, there may be some differences.

However, the most common communication weaknesses on the home pages due to the growing need for increasing the information density, including "on the input", are excessive overload with elements, as well as poor architecture or complicated site structure, whereby users feel helpless as in front of an impossible intellectual task.

To achieve that all communication functions on the home pages are enabled is a complex task that requires excellent professionalism by editors, designers, and developers. Not only should the space constraint be overcome in online communication, especially in the design of the home pages, but also the time limitations. And not only in terms of the duration of the loading of the optical forming factors but also in terms of the limited capacity of absorbing information and the resource of attention by the user. [3]

3. Related Research

Defining all the elements of the home pages of websites is a very large task. Here are presented the most necessary elements and their possible different characteristics from the same elements in other pages of the same site:

- **Basic information about the functionality of the site**. It is needed to increase the efficiency of the pages by adding personal and contact information for the web designer. The basic information also includes the date of creation and the date of the subsequent or last update of the site.

- **Logo**. The logo of a website is usually placed in the upper left corner of the screen. The logo on the home page may sometimes be (but not necessarily) larger than on the following pages. I find it better if the size of the logo is the same for the whole website. From the aspect of advertising, less well-known websites can make the name and logo a bit larger compared to those of popular sites.

- **A characteristic phrase**. One of the most valuable parts on the home page is the space next to the site logo. When a phrase is visible, visibly related to the logo, it is known that it is a characteristic phrase, motto, and is therefore considered a feature of the entire site. In websites, a characteristic phrase stands directly under, above or next to the logo. [8]

The characteristic phrase should be a meaningful text that characterizes the whole venture - summarizes what it is about and what makes it so wonderful. Characteristic phrases are not from yesterday - for a long time they are involved in ads, entertainment and in printed editions.

Characteristic phrases are a very effective way to convey the message because they are the only place on the page where users expect to see a concise presentation for the purpose of the website and the company as a whole.

When selecting a characteristic phrase, the following thing should be taken into consideration:

- the good phrases are clear and informative;
- badly selected phrases are unclear;
- the good phrases are exactly as long as necessary.

Six to eight words are enough to express a complete thought and at the same time - just enough, so that they can be easily understood and remembered ("Let's make things better" - PHILIPS).

- **Something influential (impressive)**. In order to attract the attention of the user, "something impressive" can be placed on the home page: graphics, animation, interesting textual content, background music, sound effects, video... They enrich users' experience, effectively direct attention, emphasize certain moments of communication, define the beginning and end of important phases, create an impression of the unity of the composition...

Using all of these "tricks" to attract visitors' attention is not necessary, but they add to the attractiveness and clarity of web pages and because of that it is often recommended to use them, normally in adequate proportions.

- **An informative title**. As has been said before, the immediate goal of each home page is to answer questions about where the user is located and what is the purpose of the visited website. The answers to both questions require a clear and extended version of the site's name. The name of the company or site should be mandatorily placed in a prominent place. It may also be recommended to use a domain address and an adequate window title.

The most visible and most obvious element of the design on the home page should be the name of the company or the site. This does not mean that the name should be the largest element, but at least it should be in a place where it is easy to see. Most often it's on the upper left side on the web page.

If the name of the site and the relevant company is of no significance or its significance is not related to what is done in the company, more efforts will have to be made to help users understand it.

Websites, which are less well-known, need to put a small amount of additional identification information on each of the internal pages. [8]

- **Navigation**. Navigation is the most important element of the home page. The way how the site is divided and the section names in it can in large amount suggest its functionality.

For those who visit the site for the first time, the answer to the question "What does this site do?" is perhaps the most important feature on the home page, but for most other visitors the most important function on the home page is to serve as the starting point for the site navigation scheme. [16]

The navigation itself can be done in a variety of ways. In order to increase navigation efficiency, it is accustomed to a greater number of different types of navigational elements that suit the needs of a wide range of visitors. Navigation links and buttons should be easily visible and consistent in place. Text links usually appear at the bottom of the page. They are usually written in a small font and contain only the most important links. The text links that are put that way are usually the second set of navigation elements.

Some authors believe that the home page does not need to have a "Home" button because it is quite uncomfortable to press a button that doesn't lead to another page. [4] This recommendation should be accepted conditionally because preserving the design composition and no-disrupting the convenience of surfing for the users (easier to get used to the placement of links) suggests that it is better to keep the navigation the same. In other words, it's better the "Home" button to be on the home page as well.

Often, the question arises as to how the navigation on the home page should be the same as in the rest of the site. It may be different, but not too much. Common differences may be the following: section descriptions, different orientation, drop-down menu, and logo size.

Also on the home page, more often than on the internal pages, pop-up windows can also be found by clicking on a specific link. [3]

- **An emotional effect**. Emotional effect on users is achieved by means of words, color, font and other elements. The home page and internal pages should have the same style. The colors chosen are of great importance both for the definition of the brand as for creating a mood for the site. Standard, easily readable fonts should always be used).

A very significant feature of the home page is that it is one and the same for all tastes. Unlike the lower-level pages, the home page should appeal to anyone who visits the site, no matter how diverse their interests are.

- **Subheadings**. The subheadings divide long text, if it's necessary.

- **Search tools**. For most sites, it's good to have an easily visible search field on the home page. Most home pages require an option for searching in a prominent place because most users are prone to search and do not want to work hard to get to the connection they need, a link by link. For sites where a search is the main access mechanism, it makes sense to include a search field at the top of the home page).

- **Registration**. If a particular site is working with registrations, the home page should have links enabling new visitors to register, and old ones to gain access. It should also be clearly visible whether the user has entered the system. On websites where registration is necessary, if it is a new user, or if you need to enter with a username and password in the case of already registered users, the appropriate registration and logging places should be clearly visible).

- **Suggestions**. The home page should include all prepared advertisements, promotions, and offers. [12] Everyone wants a "piece" of the home page. It should not be forgotten that this is the page that almost every visitor sees, and for some users, it remains the only one seen. Everything that stands out clearly on the home page is visited a lot more times. Anyone who participates in a particular site wants to have an ad on the home page or a link to his section. The battle for territory on the home page can sometimes be quite fierce.

Unfortunately, the need to advertise "everything" sometimes leads to hiding and darkening important input points. The problem with advertising on the home page is that it works too well. The advertised section is pleased with a large number of visits, while from the overall loss of efficiency on the home page as a result of its overcrowding, all sections suffer.

Also, the home page is the place where all news or special promotions should be deployed, which is intended to attract visitors' attention.

- **Choice of language**. Many websites use manual language selection options. The main ways to implement language selection are: using an entry (introductory) page, by placing a language menu on the home page or with a language menu that will be on all pages.

It may be decided to use an entry page only when there is no easy way to make a decision to choose the default (standard) language on the home page. In the end, if a good default language is selected, anyone who prefers that language will be able to continue browsing the site without delay. Given slow navigation on the Internet space, everything that saves users from viewing an extra page is in favor of ease of use. Another argument regarding the standard language of the home page is that it often allows users who do not prefer this language, at least get an idea of what's on the site. So they can take a more objective decision whether they like the site and whether they are ready to wait for a page to be loaded in their language. When there is a choice between small numbers of languages, it may be advised to indicate the names of languages as words, by writing their names in their language, for example - English and Français. The most commonly used visual symbol for language is the flag.

Whether the initial language selection is made on the entry page or on the home page, the user should always be able to change his choice on the following pages. The main reason for this is that many people enter the site through its internal pages and not from the home page (whether from a search engine or because they follow a link from a bookmark or from another site). Users may also want to change their language if they are multilingual and feel that the translation of a particular page is not well made in the appropriate language. In general, bad translations should be avoided, but in practice users often prefer to read technical materials in their original language rather than in translation.

- **Social media icons**. With the development of social media practically we can very rarely encounter a website that is not accompanied by a profile in one of them. The right place where you need to have links to the additional site profiles in social media is the home page. Very often these links appear on all other pages too, but their existence at the home page is almost obligatory. [5]

The listed and analyzed elements are the most important for one home page. Of course, there are always possible exceptions, but for them, there should be a clearly defined reason. In web design, as with all other types of design, written rules and recommendations should be considered flexible and, therefore, sometimes they don't have to be strictly respected.

Taking into consideration everything the home page needs to accomplish and fulfill, in one already complicated website, it is simply not possible to satisfy each of the above requirements. Creating the home page is inevitably linked to compromises.

4. Findings/Results

In this part of the scientific paper are six problems that arise from the displaying of home pages and their elements from websites on users computers. There are several solutions to the problems and making recommendations for when to choose which solution.

4.1. Problems with Lack of Knowledge that the Site Logo Serves as a Link that Leads to the Home Page

The unwritten rule that the logo of the site also serves as a button, leading to the home page is increasingly imposed. This is a useful idea, which is good to be accepted from every website. That way it will be much easier to navigate through the site because users will always be able to go to the home page and start all over again. [10]

But a surprising number of users do not know about this rule. To improve that, the word "Home" (home page) should be discreetly added to the logo on the site everywhere. In this way, users will know that they can click on the logo. While this unwritten rule becomes common knowledge, there should be a link to the home page in sections and/or tools.

4.2. Problems with the Different Navigation on the Home Page and all other Pages in the Websites

One of the main rules for deploying navigation on all pages on one website is that it should be consistently equal. This rule has two possible exceptions. The first is the home page. It is not like other pages - it is burdened with other responsibilities and should be held to other promises. Sometimes it does not include permanent navigation.

The usual differences are the following:

- sections descriptions. Since the home page should show as much as possible from that what is behind it, it's not a bad idea to add a descriptive phrase to the name of each section, and even specify the subsections - something that not every page has space for.
- different orientation. The home page often requires a radically different layout compared to all others. This means that it may be more appropriate to use horizontal instead of the usual vertical navigation on site, or vice versa.
- more space for the logo. The site logo on the home page is sometimes larger than in the permanent navigation. It's good next to the logo to have a little free space for a characteristic phrase, which is not mandatory to appear on every page.
- drop-down menus. Because the space on the home page is severely restricted, web designers are constantly looking for ways to increase it. One of the most common ways to do this is by using drop-down menus.

It is also important not to make unnecessary changes. The home page navigation and permanent navigation should have enough common features so that visitors can immediately understand that it's about two different versions of the same thing. The most important thing is to preserve the same names of sections everywhere - sequencing, specific words, and grouping should not be different. It is also good not to change the visual features - the same font, colors, and registers of the letters.

4.3. Problems with the Visual Presentation of the Language on the Web Pages

The most used visual symbol for language is a flag, but, unfortunately, flags represent states, not languages. The problem

with the use of the flag as a symbol for language selection is that some languages are spoken in more than one country, and in some countries, the official languages are more than one. The example can be used with the English language. Using the US flag to mark the English language is the obvious insult for English people (they are in fact its creators), but that also irritates Canadians and many others. Of course, the use of the Canadian flag is also not appropriate, because they speak English and/or French.

Alternative icons with national stereotypes can be set as well, but there is a risk that they will be offensive (for example, not all Americans wear cowboy heats). It is usually the best to avoid icons and simply write languages with words. However, flags can be used that correspond to the geographical location of the service and its primary target audience. As an example, one tourist website in continental Europe can use United Kingdom flag for the English language, except if the website is primarily targeted for American tourists, and on the other hand, one tourist website in America could be using the USA flag if their primary targets are not European tourists. An English flag can be used, but it is not recommended, because not many people outside the UK know regional flags of England, Scotland, Wales, Northern Ireland, etc.

The other possible solution is using two flags in the size of one so that each flag will take half of the space. The separation can be made horizontally in the middle, vertically or diagonally.

4.4. The Dilemma with Presenting the General Information about the Site on the Internal Pages

The site name should be repeated on all internal pages because users can enter the site from anywhere, not only from the home page. Users entering the site using a search engine or tracking a link from another site should be able to clearly define which site they have entered. At the same time, however, the internal pages should focus attention on the particular content rather than presenting a general greeting or describing the site (these two goals should be reserved for the home page).

It is clear that there is a contradiction - on the one hand, between the need to make a presentation to people who have entered from any page, and on the other - the need to isolate general information and higher levels of navigation only on the home page. The solution to the problem depends on how often is expected users to enter the site from the internal pages and how much the site is impressive and popular. If the site is unmistakably recognized by most users, it is not necessary to place general information on internal pages. Only, each page should have a clearly visible link to the home page. It is recommended this link to be located in the upper left corner of the page, which is the recommended place for the name and logo of the site.

4.5. Problems with Overloading the Home Page with Ads

The problem with advertising on the home page is that it works too well. Everything that has a clearly visible hyperlink on the home page will surely have more visits (many more), which makes site owners think: "Why not add another hyperlink again?". The problem is that the advantages and disadvantages of adding more items to the home page are not distributed equally. The advertised section is impressed by a large number of visits, while from the overall loss of efficiency of the home page as a result of its overcrowding, all the other sections suffer)

Preventing that the home page doesn't get ad overload requires constant care, as it usually happens gradually, with the slow, but the unyielding addition of just one more thing. All website owners should be aware of the danger of overloading the home page and they need to use other methods to increase visits to their site, for example, their ad placed on other popular websites or rotating ads that use the same space on the home page.

4.6. Problems with Sounds on the Websites

An increasing lack of sound in web space is a complaint that is often met among media professionals. Some of them think that sound is the most powerful means of creating mood and manipulating emotions. The real environment of the users should never be forgotten. Unexpected sounds are frightening and violate the sense of privacy and control. However, many websites play with the idea of integrating audio - to give the mood, to follow the action, to advertise the site, and so on.

Adding sound to the website (whether it's an easy-to-use surround sound for moods or sounds from the interface) is very often chasing users away, especially when they cannot turn off the sound. Of course, there are exceptions - certain types of sites are expected to have sound (like for example, congratulations online). But the ability to turn off the sound should always be available. Therefore, a visible On/Off switch should be placed so that users can get rid of the sound without having to leave the page.

Most often, the problem with audio on websites occurs upon first entering a specific site (usually home page). The user is not familiar with the sound component of the website and a variety of inconveniences can arise during its use. It's good the "On/Off" switch to be on every page of a certain website, but its existence should be mandatory on the home page. The sound settings (will the user hear the sound or not) should remain as same as it was at the first choice (it's usually made on the home page) while surfing the entire website, with the possibility to it change on each page.

5. Conclusion

Modern website design allows designers themselves to decide if and when will they use standard rules for a home page, of course, together with all the other standards and norms that exist when we want to shape one stylishly designed site.

The conclusion that can be made from all of the above mentioned is that this area is extensive and offers many opportunities for research and analysis. Due to a large number of problems which occur in this area, usually, there is not only one correct solution.

For the most appropriate solution to be chosen, a lot of data should be collected about desires and habits of potential users, as well as the technical features of their computers. The solution needs to be found based on those information's. Sometimes, depending on the situation, it is possible to apply a combination of multiple solutions simultaneously.

One of the decisions that will qualify the quality of that site and its aesthetics and technical aspects is how good the quality of the home page will be. The need to find the appropriate balance between designer visions, users' expectations, and technical possibilities is one of most common problems which all website designers meet.

Web designers must be aware of market needs and business expectations of a site owner if they wish to create a visually perfect website implementing all their ideas and imagination. The other segment of this problem is users and their needs and requirements when using the Internet. And at the end here are technical parameters and limitations that very often can represent a key factor in the decision if and which website should be visited and used.

Today, when there are millions of sites with the same or similar topics, the downloading time is one of the main parameters when choosing which website to visit.

All these aspects should be considered when deciding which solution to choose to resolve these problems.

The conclusion is that there is no universal solution for all the possible problematic situations. It should also be noted that the abundance of a variety of program languages and codes allows other solutions too, depending on the used languages and codes.

This subject, as well as everything else with web design, is very progressive. Some other possible solutions to the problems in this science area will be undoubtedly produced using many various new innovations and opportunities.

6. Literature

[1] Williams R.; "The Non-Designer's Design Book, third edition"; *Peachpit Press*, USA, 2008.

[2] McWade J.; "Before and After Graphics for Business"; *Peachpit Press*, USA, 2005.

[3] Valkanova V.; "Design of the Newspaper"; *Publishing Sofia University "St. Kliment Ohridski"*, Bulgaria, 2008.

[4] Nielsen J.; "Designing Web Usability: The Practice of Simplicity"; *New Riders*, USA, 2000.
[5] Toms J., Georgiev Denislav; "Successful Online Marketing"; *Ciela Soft and Publishing Corp.*, Bulgaria, 2010.
[6] Zeldman J.; "Designing with Web Standards"; *New Riders*, USA, 2003.
[7] Gray D.; "Looking Good on the Web"; *Coriolis Group LLC.*, USA, 1999.
[8] Krug S.; "Don't Make me Think: A Common Sense Approach to Web Usability, 2nd edition"; *New Riders*, USA, 2006.
[9] Cohen J.; "Unusually Useful Web Book, 1st edition"*; New Riders*, USA, 2003.
[10] Millhollon M.; "Faster Smarter Web Page Creation"*; Microsoft Press*, USA, 2003.
[11] Toms J., Belogusheva Gorica; "Website, the Mission Obligatory"; *Ciela Soft and Publishing Corp.*, Bulgaria, 2009.
[12] Niederst J.; Web Design in a Nutshell, second edition; *O'Reilly & Associates, Inc*, USA, 2001.
[13] SoftPres publishing team; "Creating Web Pages"; *SoftPres Ltd.*, Bulgaria, 2001.
[14] Wiedemann Ed. J.; Web Design: Navigation; *Taschen*, Germany, 2009.
[15] Parker C. R.; "Looking Good in Print"; *Coriolis Group LLC.*, USA, 1999.
[16] Karbo M.; "HTML"; *Forlaget Libris*, Denmark, 2004.
[17] Stauffer T.; "Absolute Beginner's Guide to Creating Web Pages"; *Que Publishing*, USA, 2002.
[18] Newcomer E.; "Understanding Web Services: XML, WSDL, SOAP and UDDI"; *Addison Wesley Professional*, USA, 2002.

DAMAGE FUNCTIONS EVALUATION COHERENT TO WEAPON TARGET INTERACTION

Assistant M.Sc. Ing. Katsev I., Prof. PhD. Evlogiev S.
"Artillery, air defense and CIS" Faculty – "Vasil Levski" National Military University, Veliko Tarnovo, Republic of Bulgaria

katsev.i@abg.bg; sevl@abv.bg

Abstract: The interaction between weapon and target is through the "damage function" which is defined to be the probability that the target is killed by a weapon, damage function analysis is major factor in evaluating weapon effectiveness.

KEYWORDS: DAMAGE PROBABILITY, DAMAGE FUNCTION, NORMAL DISTRIBUTION, COOKIE CUTTER, DIFFUSE GAUSSIAN DAMAGE FUNCTION.

1. Introduction

Success in modern operations is achieved by those forces and means of counter-fighting combatants that use reliable fire support. Recognizing that fire support includes strikes and fires with lethal and non-lethal effects of fire and impact systems of land, airborne, naval components and special operations forces executed under operative scenario with attracted operational forces, it is necessary to analyze the individual components of this complex system. In this article, we are limited to examining only the effectiveness of artillery fire systems. The analysis of the electronic fire operations at the end of the 90s shows that the proportion of MLRS and Artillery's damage in the operations is 50-60%, which is distributed: 30-40% when the enemy damaged at near depth and 15 - 20% in case of a long range fire support [1].

The fire support of military formations is carried out by fire formations and firing systems and its effectiveness depends to a large extent on the efficiency of the used artillery systems.

A primary indicator in assessing the efficiency of fire systems is the probability of damage the target (object) using the damage function. Damage function is an essential part of the mathematical apparatus for determining the efficiency of fire support systems

2. Results of discussion.

Damage function comparison.

2.1. **Purpose:** Presenting a theoretical analysis of damage functions used in evaluation of artillery fire support effectiveness.

2.2. Objectives:

- to analyze damage functions and artillery weapon systems effectiveness using them;

- to determine differences in damage functions and their appropriate usage.

The damage function determines the percentage impact of the weapon (system) on the target. It has two main components: distribution of the mean point of impact to the target center (the point of measurement) and the likelihood of target damage as a result of the deviation from the center of the target.

The mean point of attack can be characterized as a random value with bivariate normal distribution, range error probable (**REP**) and deflection error probable (**DEP**) and the probability density function $\boldsymbol{f(x,y)}$:

$$(1)\ \boldsymbol{f(x,y)} = \frac{1}{2\pi\sigma_x\sigma_y} e^{-\left[\frac{(x-\mu_x)^2}{\sigma_x{}^2}+\frac{(y-\mu_y)^2}{\sigma_y{}^2}\right]} \quad [5]$$

And cumulative density function:

The cumulative density function (continuous probability distribution) is determined by the formula:

$$(2)\ \boldsymbol{F(X,Y)} = \int_{x=-\infty}^{x=X}\int_{y=-\infty}^{y=Y} \frac{1}{2\pi\sigma_x\sigma_y} e^{-\left[\frac{(x-\mu_x)^2}{\sigma_x{}^2}+\frac{(y-\mu_y)^2}{\sigma_y{}^2}\right]} [5]$$

where $\boldsymbol{\sigma_x, \sigma_y}$ standard deviations in range and deflection, $\boldsymbol{x, y}$ mean deviations of the random value in range and deflection, $\boldsymbol{\mu_x, \mu_y}$ mathematical expectations.

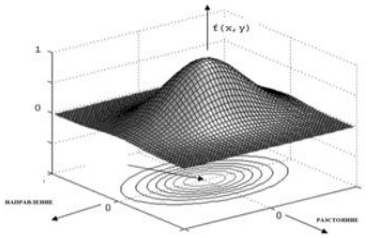

Fig.1 *Probability density function (PDF) of random value, distributed by a bivariate normal law.*

In different cases, the distribution of the mean point of impact may also be different. For example, when the numerical value of standard deviation of the two dimensions is equal, and the mathematical expectation of the mean point of impact equals zero, then it is a normal circle-like distribution, which is characterized by a circular error probable (CEP) and a function of distribution, which can be calculated using the formula:

$$(3)\ \boldsymbol{(x,y)} = \frac{1}{2\pi\sigma^2} e^{-\left[\frac{x^2}{\sigma^2}+\frac{y^2}{\sigma^2}\right]} \quad [4]$$

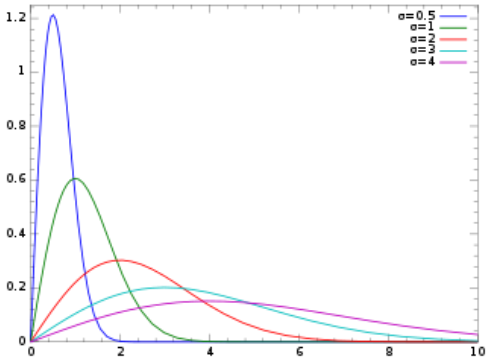

Fig.2 *Graphic representation of a Probability density function (PDF) of a random value distributed by radial law.*

In most cases, mean errors in distance and direction are not of equal value, making use of formula (3) impossible. In such a hypothesis, it is expedient to convert a bivariate normal distribution into a radial one:

$$(4)\ \boldsymbol{r^2 = x^2 + y^2} \quad [4]$$

where $\boldsymbol{x, y}$ mean deviations of the random value in range and deflection, $\boldsymbol{r}$ radial variance of the random value.

As a result of the assumption of radial distribution of the mean point of attack, the properties of the random magnitude will change.

One of the methods for determining the distribution function of a random variable with radial distribution is using Rayleigh distribution.

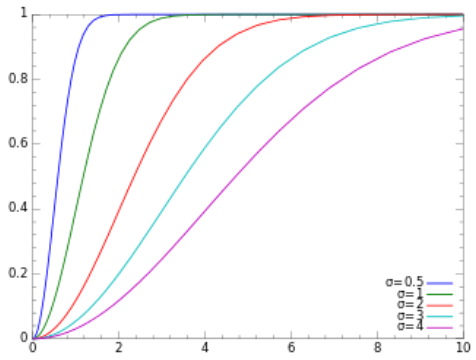

Fig.3 *Graphic representation of a Cumulative density function (CDF) of a random value distributed by radial law.*

The Rayleigh distribution is used to characterize the radial random variable with the distribution function shown in Fig. 2. These are defined by formulas:

$$(5)\ \boldsymbol{f(r)} = \frac{r}{\sigma^2} e^{-\left[\frac{r^2}{2\sigma^2}\right]}\ [3]$$

And cumulative density function $\boldsymbol{F(R)}$(Fig.3):

$$(6)\ \boldsymbol{F(R)} = \mathbf{1} - e^{-\left[\frac{R^2}{2\sigma^2}\right]}\ [3]$$

where $\boldsymbol{r}$ radial variance of the random value., $\boldsymbol{\sigma}$ standard deviation in range (deflection).

Models defining artillery fire support effectiveness are based on the distribution of the mean point of impact and the likelihood of target damage as a result of the deviation from the center of the target and the projectile dispersion. It is possible to use two models to calculate the damage function: Carleton - von Neumann (K) and Cookie - Cutter (CC).

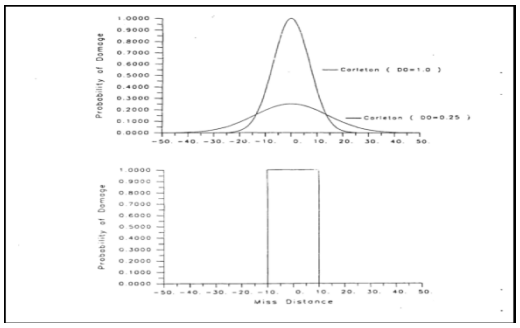

Fig.4 *Carleton damage function (up) and Cookie-cutter function.*

The "Cookie-Cutter" model characterizes the damage effect of fire support systems that have a constant radius of damage or impact area equal to $\boldsymbol{\pi R^2}$. If the error in the fire data preparation is a mean circular error and the point of measurement is the center of the target, the distribution function is determined by the formula:

$$(7)\ \boldsymbol{f(x,y)} = e^{-\frac{1}{2}\left(\frac{x^2+y^2}{\sigma^2}\right)}\frac{1}{2\pi\sigma^2}\ [5]$$

The probability of damage can be determined by the formula:

$$(8)\ \boldsymbol{PD} = \mathbf{1} - e^{-\frac{1R^2}{2\sigma^2}}\quad [2,3,4]$$

It is evident that this model can be used effectively in fire systems having random errors equivalent to one another or equal in value. This assumption does not allow the use of the model in any case and makes it specific rather than universal. Practice shows that the error value in range in the majority of cases has a higher numerical value than the errors in deflection. This is the result of the fact that the sum of random errors is characterized by an asymmetric bivariate normal distribution law rather than a bivariate normal distribution law (circular) (symmetrical). Numerous integration, approximate formulas and other assumptions are used to solve this problem.

In some cases, the following formula may be used:

$$(9)\ \boldsymbol{PD} = \mathbf{1} - \mathbf{0.5}^{\frac{R^2}{CEP^2}}\ [2,3]$$

$$(10)\ \boldsymbol{CEP} = \mathbf{1.1774}\boldsymbol{\sigma}[2,3]$$

where $\boldsymbol{R}$ radial variance of the random value, $\boldsymbol{CEP}$ circular error probable, $\boldsymbol{\sigma}$ standard deviations in range and deflection.

The other model that is primarily used to determine the effectiveness of fire systems for various purposes is the Carleton damage function or the diffuse Gaussian damage function.

$$(11)\ \boldsymbol{D(r)} = e^{-\frac{1r^2}{2b^2}}[2,3,5]$$

where $\boldsymbol{b}$ a damage factor dependent on fire system, $\boldsymbol{r}$ radial variance of the random value.

This model for determining the efficiency of the damage can be used in any case because it defines the covered area individually for each fire system. This makes the model more realistic about effectiveness evaluation.

In case the distribution law is asymmetric, the mathematical apparatus for calculating the probability of damage is as follows:

$$(12)\ \ \boldsymbol{PD} = \frac{b_x b_y}{\sqrt{(b_x^2+\sigma_x^2)(b_y^2+\sigma_y^2)}} e^{-\frac{1}{2}\left[\frac{\mu_x^2}{b_x^2+\sigma_x^2}+\frac{\mu_y^2}{b_y^2+\sigma_y^2}\right]}\quad [2,3,5]$$

where $\boldsymbol{b_x b_y}$ damage factors dependent on fire system in range and deflection, $\boldsymbol{\mu_x, \mu_y}$ mathematical expectations if random errors in range and deflection, $\boldsymbol{\sigma_x, \sigma_y}$ standard deviations in range and deflection.

To analyze the damage functions, the Monte Carlo simulation modeling method is used.

When initializing an analysis, it is necessary to calculate the damage area. In the first case, the damage factor of the fire system and the covered area will have a bivariate normal distribution:

$$(13)\boldsymbol{A_l(CC)} = \boldsymbol{\pi R^2}\quad [2,3,4]$$

$$(14)\boldsymbol{A_l(K)} = \boldsymbol{\pi b^2}\quad [2,3,5]$$

The next stage of the analysis covers the calculation of the probability of damage. In the first case, the damage functions will have the type:

$$(15)\ \boldsymbol{PD(CC)} = \mathbf{1} - e^{-0,5\frac{R^2}{\sigma^2}}\quad [2,3,4]$$

$$(16)\boldsymbol{PD(K)} = \frac{b}{\sqrt{b^2+\sigma^2}}\quad [2,3,5]$$

Using the statistical modeling method, we will analyze a series of mean points of impact away from the center of the target, respectively:

Input data for the analysis: $\boldsymbol{A_l = 2500m^2}$, $\boldsymbol{\sigma_x = 0 \div 50m}$, $\boldsymbol{\sigma_y = 0 \div 50m}$, $\boldsymbol{b = 28,2m}$, $\boldsymbol{R = 28,2m.}$

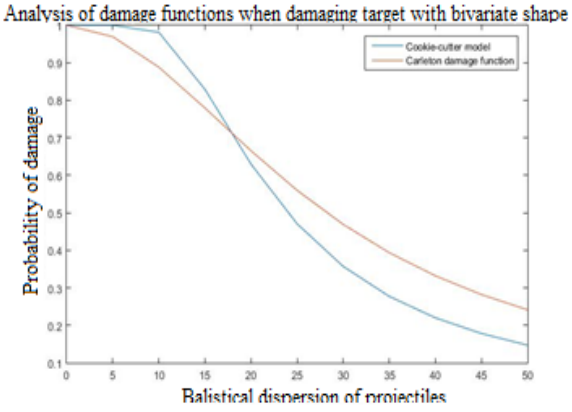

Fig.5 *Analysis of damage functions when damaging target with bivariate shape.*

Target with a bivariate shape, the Cookie-cutter model with little ballistic dispersion values provides a higher probability of damage, which is explained by the pattern distribution function. The Carleton damage function, with increase of standard deviation of ballistic dispersion, the probability of damage is gradually reduced.

In the second case, the damage factor of the fire system and the covered zone will have a rectangular shape and is determined by the formula::

$$(17) A_l(CC) = \pi R^2 \, , R = \sqrt{x^2 + y^2} \quad [2,3,4]$$

$$(18) A_l(K) = 2\pi b_x b_y \quad [2,3,5]$$

where R radial variance of the random value, $b_x b_y$ damage factors dependent on fire system in range and deflection.

The second step to determine the effectiveness of fire support of artillery is to determine the probability of damage on target. In the second case considered, the damage functions will have the type:

$$(19) PD(CC) = 1 - e^{-0,5\frac{R^2}{\sigma^2}} \quad [2,3,4]$$

$$(20)\ PD(K) = \frac{b_x b_y}{\sqrt{(b_x^2+\sigma_x^2)(b_y^2+\sigma_y^2)}} e^{-\frac{1}{2}\left[\frac{\mu_x^2}{b_x^2+\sigma_x^2}+\frac{\mu_y^2}{b_y^2+\sigma_y^2}\right]} \quad [2,3,5]$$

where R radial variance of the random value, $b_x b_y$ damage factors dependent on fire system in range and deflection, μ_x, μ_y mathematical expectations if random errors in range and deflection, σ_x, σ_y standard deviations in range and deflection..

Using the statistical modeling method, we can determine the mean point of impact and its deviation from the target center.

To illustrate the second case and perform the analysis, we use the following input data: $A_l = 2500m^2$, $\sigma_x = 0 \div 50m$, $\sigma_y = 0 \div 50m$, $b = 28,2m$, $R = 28,2\text{m}$

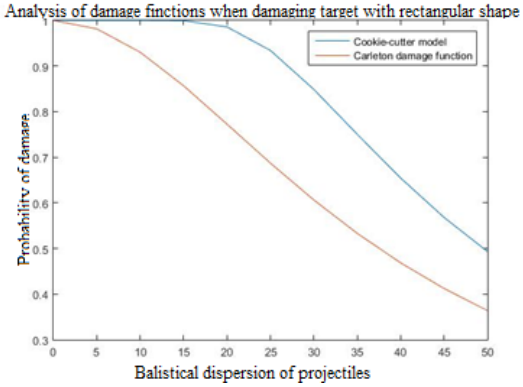

Fig.6 *Analysis if damage of damage functions when damaging target with rectangular shape.*

When target have rectangular shape, the "Cookie-cutter" model shows a higher probability of damage than Carleton damage function. In both models the probability of damage decreases exponentially with an increase in ballistic dispersion.

3. Conclution.

The results of this study allow us to draw the following conclusions:

1. The Cookie-cutter model shows a higher probability of damage than the Carleton damage function due to differences in the determination of the covered area.

2. The Cookie Cutter model does not account for changes in the angle of impact, so the shape of the covered area will always be round, which for most systems and impact angles does not fit the truth.

3. A more useful model of use is the Carleton damage function, because a small part of the fire system has a circle-impact area. In most cases, the covered area is determined by the impact angle and takes the shape of a rectangle, square or circle.

4. The Carleton damage function model gives a realistic view of the fire covered zone, taking into account the angle of impact. The numerical meanings of the target area in range and deflection allow the determination of the fire system's effectiveness.

Литература:

1. Evlogiev, S. Characteristic features of modern combat operations. „V. Levski“, National Military University Collection of scientific papers, ISBN-10:954-9681-19-X; ISBN-13: 978-954-9681-19-2, p.136-144, Shumen, 2005.

2. Driels M et al., Explicit exact solution of damage probability for multiple weapons against a unitary target, American Journal of Operations Research, 2016, 8. 450-467.

3. Fann, Ch.,adv. Driels, M. Development of an artillery accuracy model, Naval postgraduate school, Monterey, 2006.

4. Klopcic J.T., A comparison of damage functions for use in artillery effectiveness codes, Aberdeen proving grounds, 1990.

5. Washburn A., Diffuse Gaussian multiple-shot pattern, Military operations research, vol8, n3, 2003.

СТЕГАНАЛИЗ НА ИЗОБРАЖЕНИЯ ЧРЕЗ ИЗПОЛЗВАНЕ НА МУЛТИ-КЛАСИФИКАТОР

STEGANALYSIS OF IMAGES BY USING A MULTI-CLASSIFIE

Диан Велев[1], Ст. Павлова[2], полк. проф. д-р инж. И.Лилов[3], И. Кичуков[4]
НВУ "Васил Левски", факултет „Общовойскови"[1,2,3], Факултет „Артилерия, ПВО и КИС"[4]България
dianvelev@gmail.com

Abstract: *Traditional image steganalysis techniques for classification of steganograhic algorithms are conducted with respect to the entire image. In this work, we aim to design a multi-classifier which classifies stego images depending on their steganographic algorithms in addition to distinguishing stego images from cover images. This classification is based on steganalysis results of decomposed image blocks. As a natural image often consists of heterogeneous regions, its decomposition will lead to smaller image blocks, each of which is more homogeneous.*

Keywords: STEGANOGRAPHY, MULTI-CLASSIFIER, STEGO IMAGES, COVER IMAGES.

1. Въведение

Стеганализа е наука обратна на стеганографията и той се опитва да диференцира стегоизображенията от прикриващото изображения без знанието на използваните стеганографски алгоритми за вграждане [1]. Използвайки характеристиките, извлечени от прикриващото и стегоизображенията при еднократни опити, класификаторът научава характеристиките на прикриващото и стегоизображенията в многомерното пространство. Повечето от разработките в тази област се фокусират върху извличането на характеристики от изображения за целите на стеганализа с бинарен класификатор, който диференцира стегоизображенията от прикриващи такива [2], [3], [4].

В този доклад се представя мулти-класификатор, използващ блоково базиран стеганализ на изображения [5]. Предложеният подход за мулти-класификатор започва с разделянето на изображенията на прикриващи и стегоизображения от различни стеганографски алгоритми, в комплект за обучение на по-малки хомогенни блокове. След това се третира всеки блок като основна единица на изображението и се извличат характеристиките на Markov и DCT [4] от блоковете на изображението за блоково базиран стеганализ. Въз основа на характеристиките на блоковете, избрани чрез случайна извадка, техниката приема за класифициране блокове от множество класове. За всеки клас, специфичен класификатор може да бъде обучен като се използват блокови характеристики, които представляват характеристиките на този тип блок.

2. Преглед на изследванията.

2.1.Анализ на слепите стеганализи

2.1.1. Двоичен класификатор

Предишните изследвания в тази област са фокусирани върху извличането на характеристики от изображенията за целите на стеганализа [2], [3], [4]. Коефициентите в DCT областта са използвани за извличане на характеристики. DCT-базираните характеристики са предложени в [2] за стеганализ, като се използва факта, че междублочната зависимост между съседни блокове често е засегната от стеганографски алгоритми.

2.1.2. Мулти-класификатори

При използване на няколко класификатора, слепия стеганализ първо се опитва да реши дали дадено тестово изображение е прикриващо или е стегоизображение. Освен това, ако определеното тестово изображение е определено като стегоизображение, този класификатор трябва да реши кой стеганографски алгоритъм е бил използван за вграждане на тайното съобщение.

2.2*. Изпълнение на сляп стеганализ.*

2.2.1. Двоичен класификатор

Основната цел на слепия стеганализ е да реши дали данните, изпратени от потребител Алис на потребителя Боб, съдържат тайно съобщение или не. С други думи, да се направи точно решение дали непознатото тестово изображение е прикриващо или стегоизображение. Преди да се обясни процедурата за изчисляване на вероятността за грешка, се въвеждат два вида грешки, направени в процеса на вземане на решение от статистиката: фалшиви положителни резултати и фалшиви негативни. Слепият стеганализ се опитва да минимизира тези две грешки, за да получи по-висока точност на откриване. Фалшиви положителни сигнали (фалшиви аларми) се случват, когато се открие тайно съобщение от дадено прикриващо изображение. Обратно, фалшиви негативни (пропускания) се появяват, когато тайно съобщение не се открива от дадено стегоизображение.

Таблица 1*. Матрица на объркване на двоичен класификатор*

Решение	Реално	
	Прикриващо изображение	Стего изображение
Прикриващо изображение	Истински отрицателни сигнали	Фалшиви негативни сигнали
Стего изображение	Фалшиви положителни сигнали	Истински позитивни сигнали

2.2.2. Мулти-класификатор

Когато L различните стеганографски алгоритми се използват за създаване на стегоизображения вместо един стегонографски алгоритъм, трябва да се реши кой стеганографски алгоритъм е бил използван за вграждане на тайното съобщение.

2.2. Изпълнение на сляпа стегализа

2.2.1. Двоичен класификатор

Основната цел на слепия стеганализ е да реши дали данните, изпратени от потребител Алис на потребителя Боб, съдържат тайно съобщение или не. С други думи да се направи точно решение дали непознатото тестово изображение е прикриващо или стегоизображение.

Преди да се обясни процедурата за изчисляване на вероятността за грешка, се въвеждат два вида грешки, направени в процеса на вземане на решение от статистиката: фалшиви положителни резултати и фалшиви негативи. Слепия стеганализ се опитва да минимизира тези две грешки, за да се получи по-висока точност на откриване. Фалшиви положителни сигнали (фалшиви аларми) се случват, когато се открие тайно съобщение от дадено прикриващо изображение. Обратно, фалшиви негативи (пропускания) се появяват, когато

тайно съобщение не се открива от дадено стегоизображение (вж.табл. 1).

2.2.2. Мулти-класификатор

Когато L различни стеганографски алгоритми се използват за създаване на стегоизображения вместо един стеганографски алгоритъм, трябва да се реши кой стеганографски алгоритъм е бил използван за вграждане на тайното съобщение в дадено стегоизображение.

3. Блоково базиран стеганализ на изображения чрез използване на мулти-класификатор.

3.1. Общ преглед на системата

Блок-схемата на блок-базирана система за стегагализ на изображния за класификация на множество стеганографски алгоритми е показана на фигура 1. Състои се от процес на обучение и процес на тестване.

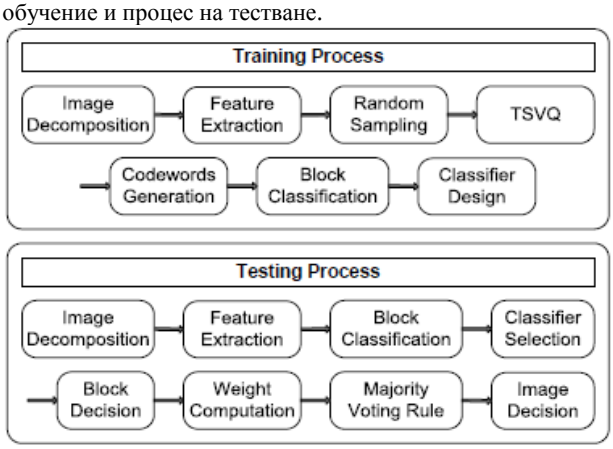

Фиг. 1. *Блок-диаграма на предложеното блоково изображение стеганализираща система*

3.2. Процес на обучение

3.2.1. Блоково разлагане, извличане на функции и случайно вземане на проби

За всеки от *L*-стеганографските алгоритми, се вгражда тайното съобщение в прикриващо изображение, за да се получи съответното стегоизображение. Този процес се прилага за всички изображения, за да се получат набори от изображения, състоящи се от прикриващи изображение и съответните стегоизображения. След това се разлагат всички изображения с размер ***MxN*** в комплекта за обучение на по-малки хомогенни блокове с размер ***BxB*** (като B=*8b; b = 2,3, ..., min (M, N)/ 8*). , Обединените DCT и Markov характеристики [4] се извличат от всеки блок от изображения в набора от изображения.Ако броят на декомпозираните блокове изображения е твърде голям, може да се използва метод на случайна извадка, за да се избере подмножество от блокове на изображението, за да се намали сложността на класификацията.

Например, за изображение с размер ***MxN,*** ако има около ***A=MN=B2*** блокове с размер ***BxB***. Ако ***A*** е твърде голям, може да се избере подмножество от размер ***K*** на случаен принцип. Този процес е обозначен като "случайна извадка". За да се получи равен брой пробни блокове от ***L1*** типове изображения, ***K=(L +1)*** пробни блокове се избират произволно от прикриващите изображения, заедно с ***K=(L + 1***) примерни блокове, които съответстват на същото място на стегоизображенията, създадени от ***L*** различни стеганографски алгоритми. Най-общо казано, случайната извадка е по-добра от извадката в пространствен ред, тъй като позволява да се събират блокове с по-голямо разнообразие, така че да могат да се използват по-представителни пробни блокове в процеса на класификация на блоковете.

3.2.2. Класифициране на изследвания блок

Базирайки се на обединените характеристики от блоковете ***BxB***, може да се направи обичайна класификация на ***K*** блокове в ***C*** различни класове,където всеки клас се състои от хомогенни блокове. Блок класификацията е разгледана в различни контексти за обработка на изображения. Техниката на Tree-Structured Vector Quantization (TSVQ) се използва за класифициране на блоковете на изображението, използвайки двоична дървовидна структура на базата на блоково подобие. Като се взамства тази идея и се приложи към дадено приложение се получава основна разлика, че блоковото сходство се измерва от Eulidean разстоянието между пикселни различия на два блока на изображението в контекста на векторното квантуване.

3.3. Критерий за оценка.

3.3.1. Класификация на блоковете и избор на класификатор.

За дадено тестово изображение може да се извърши точно същото разграждане и извличането на характеристиките, както е описано в процеса на обучение. Всеки блок от тестовото изображение се класифицира в клас, като се използва минимална стойност на изкривяване. В зависимост от класа на всеки блок, се прилага класификаторът получен от процеса на обучение. Може да се нарича класификатори зависещи от съдържанието, тъй като те се подбират адаптивно според класовия блок. Зависимите от съдържанието класификатори са полезни, тъй като промяната на стойностите на характеристиките след стеганографско вграждане има по-висока корелация с блокове от същия клас от тези на различни класове.

3.3.2. Изчисляване на теглата

Преди да приложите правилото за гласуване с мнозинство, два вида тежести може да направи блокови решения по-точни: 1) тегла, които зависят от различни блокови класове, и 2) тегла, които зависят от различни типове изображения. Тези два вида тежести за блокове се използват, за да се получи теглото за всяко решение за блок.

4. Експериментални резултати.

4.1. Експериментална настройка

В експеримента, се разглежда обучение и тестване на изображения с размери ***MxN➪ 384x512*** и се разлага всяко изображение на **48** блока с размер ***BxB ➪ 64x64.*** След извличане на **274** обединени характеристики от всеки блок, **K=20 000**. Блоковете за проби са избрани от прикриващите изображенията и съответните стегоизображения с ***L=3*** различни стеганографски алгоритми в набора за обучение чрез случайна извадка. Тези пробни блокове са класифицирани в ***C=8*** класове. За дизайна на класификатора са получени 8 различни линейни класификатора на Байес за 8 класа с параметър на регулиране ***R = S = 0.001***.

4.1.1. База данни с изображения

Некомпресирана база данни за цветни изображения (UCID) [6] е използвана като прикриващи изображения в комплекта за обучение. В тестовия комплект е използван комплект данни на INRIA Holidays [7] за прикриващо изображение. Базата данни за изображения на UCID се състои от 1338 изображения, а обогатената базата данни за изображенията има 1491 изображения, които имат различни обекти, като естествени сцени и изкуствени обекти. Въпреки че оригиналните изображения са цветни изображения с различни размери, всички изображения са променени в 384x512 изображения в сиво и са запазени като JPEG файлове с фактор за качество 85 JPEG компресия.

4.1.2. Стеганографско вграждане.

След избиране на прикриващи изображенията от базите данни за изображения, L=3 различни стеганографски

алгоритми са използвани за вграждане на тайно: Out Guess (OG) [8], F5 [9] и модел на основата на стеганография (MBS).

Фиг.2. *Примерни изображения от база за данни от некомпресирани цветни изображения(UCID) и набор от данни на INRIA Holidays*.

Тъй като различните изображения могат да имат различен капацитет на вграждане, степента на вграждане за всяко изображение се измерва в единици BPC (битове за ненулеви DCT AC коефициенти). За експериментите са тествани две различни скорости на вграждане (а именно 0.2, 0.3 BPC) за OutGuess, F5, MBS.

4.2. Резултати

За да се сравни и подобри методът и точността за откриване от многокласификатор, се използва [4] (линеен класификатор на Байес). Този подход, базиран на изображения се нарича метод на Penvy. Стратегията max-wins не е използвана за метода на Penvy, който се използва за да се направи сравнение с разглеждания метод. Мулти-класификаторът и за двата метода имат четири възможни класификационни резултата: прикриващо изображение и стегоизображение, създадено от OutGuess (OG), F5 и MBS.

Табл. 2 Матрици на объркване на метода на Penvy и разглеждания метод в случай на BPC = 0.2.

Действия	Реално			
	Прикриващо изображение	OG	F5	MBS
Методът на Penvy, $A_{засече}$=63,63%				
Прикриващо изображение	72.30	16.16	10.12	28.71
OG	2.41	57.14	2.55	5.77
F5	5.70	3.76	67.61	8.05
MBS	19.58	22.94	19.72	57.48
Предложен метод, $A_{засече}$=70.93%				
Прикриващо изображение	63.25	0.27	21.93	4,63
OG	2.35	83.03	3.49	8.05
F5	20.39	2.01	58.82	8.72
MBS	14.02	14.69	15.76	78.60

Докато точността на детекция на покритото изображение и стего изображенията от F5 намаляват с около 10% с предложената методика, а стего изображенията, създадени от OutGuess и MBS се подобряват повече от 20%. Когато тестовите изображения се вграждат с OutGuess, точността на откриване се подобрява най-много с 25,9%. Общата точност на детекция се подобрява от 63,63% до 70,93% с предложения метод, което е 7,3% подобрение.

Наблюдава се, че цялостната точност на откриване е по-висока за случая на BPC = 0.3, тъй като става по-лесно да се класифицират тестовите изображения в четири различни класа, когато е вградено тайно съобщение с по-голяма дължина. В зависимост от блоковите класове, различните класификатори са предназначени да използват характеристиките на блоковете в различни класове.

Табл.3 *Матрици на объркване на метода на Penvy и разглеждания метод в случай на BPC* = 0.3.

Действия	Реално			
	Прикриващо изображение	OG	F5	MBS
Методът на Penvy, $A_{засече}$=76.79%				
Прикриващо изображение	81.76	6.84	5.90	20.46
OG	1.48	76.73	0.94	3.82
F5	3.55	2.15	78.67	5.70
MBS	13.21	14.29	14.29	70.02
Предложен метод, $A_{засече}$=86.23%				
Прикриващо изображение	77.33	0.00	8.58	3.02
OG	1.01	94.90	1.01	4.43
F5	16.30	0.74	86.32	6.17
MBS	5.37	4.36	4.09	86.38

Точността на откриване на всички стегоизображения се подобрява с 8 - 18% в разглеждания метод. Подобно на случая с BPC = 0.2, точността на откриване се подобрява най-много с 18: 2%, когато тестовите изображения са с вградени данни за използване на Out-Guess. Общата точност на детекция се подобрява от 76,79% на 86,23% в разглеждания метод, което е с 9,4% подобрение (вж. табл.2 и табл.3). Както е показано в експерименталните резултати, предложеният метод има значително подобрение спрямо метода на Pevny за двата случая на BPC. Това е възможно, защото блоково-базирания подход се възползва от характеристиките на изображенията, които се разлагат на по-малки хомогенни блокове.

5. Заключение.

В този доклад е предложен блокова базиран стеганализ на изображения чрез използване на мулт-класификатор като са приети различни класификатори на базата на техните характеристики. Експерименталните резултати показват, че предложеният метод предлага значително подобрение в точността на откриване в сравнение с предишните опити, използвайки подход базиран на изображения.

Използвана литература:

[1] Stoyanova V., Steganography System that uses the LSB method of embedding information in images, INTERNATIONAL SCIENTIFIC CONFERENCE, Defense Technology forum 2015, Shumen, p.186-193, ISSN 2367-7902, http://www.aadcf.nvu.bg/scientific_events/papers/NS_2015.

[2]Stoyanova, V. , Компютърна реализация на стеганографските методи в изображения, Сборник доклади от Годишна Университетска научна конференция, Изд.комплекс на НВУ ”В.Левски” В. Търново,2015, т.12, с.128-135, ISSN 1314-1937.

[3] Stoyanova, Veselka T. Steganography System Using LSB Methods. In: 2018 ENTRENOVA Conference Proceedings. 2018, Vol. 4, No. 1, pp.381-385, ISSN 1849-7950 https://papers.ssrn.com/sol3/papers.cfm?abstract_id=3283729.

[4] T. Pevny and J. Fridrich, “Merging Markov and DCT features for multi-class JPEG steganalysis,” in Proc. SPIE Conf. Security, Watermarking, and Steganography, San Jose, California, February 2007.

[5] S. Cho, B.-H. Cha, J. Wang, and C.-C. Jay Kuo, “Block-Based Image Steganalysis: Algorithm and Performance Evaluation,” in Proc. IEEE Int’l Sym. Circuits and Systems, Paris, France, May 2010, to be published.

[6] G. Schaefer and M. Stich, “UCID - An Uncompressed Colour Image Database,” SPIE Storage and Retrieval Methods and Applications for Multimedia, vol. 5307, pp. 472–480, 2004.

[7] H. J´egou, M. Douze, and C. Schmid, “Hamming embedding and weak geometric consistency for large scale image search,” in European Conf. Computer Vision, Marseille, France, October 2008.

[8] N. Provos, “Defending against statistical steganalysis,” in 10th USENIX Security Symposium. Citeseer, 2001, vol. 10,pp. 323–336.

[9] A.Westfeld, “F5-a steganographic algorithm: High capacity despite better steganalysis,” in Proc. ACM Int’l Workshop on Information Hiding, Pittsburgh, PA, April 2001.

INCREASE IN STRENGTH PROPERTIES OF LOW-CARBON STEELS DUE TO STRUCTURAL TRANSFORMATIONS AT DEFORMATION BY ROTARY SWAGING

Prof., Dr.Sci. Dobatkin S.V.[1,2],Dr. Rybalchenko O.V.[1,2], Tokar A.A.[1,2], Prof., Dr.Sci. Odessky P.D.[3], Lunev V.A.[1,2], Morozov M.M.[1], Dr.Sci. Yusupov V.S.[1]

[1]A.A. Baikov Institute of Metallurgy and Materials Science of RAS, Moscow, Russia
[2]National University of Science and Technology "MISIS", Moscow, Russia
[3]Kucherenko Central Research Institute for Structural Construction, Moscow, Russia

dobatkin.sergey@gmail.com

Abstract: *Mechanical properties of low-carbon St.20 and 07G2MFB steels after rotary swaging (RS) were studied. It was established that an increase in strain ratio and decrease in temperature increase strength but decrease plasticity. The ultimate tensile strength of 867-927 MPa was obtained in both steels after deformation at temperature of 400 °C with a true strain ratio of 2.3 at good ductility of 15-17%.*

Keywords: LOW-CARBON STEEL, ROTARY SWAGING, ULTRAFINE-GRAINED (UFG) STRUCTURE, THERMAL STABILITY OF STRENGTHENING, MECHANICAL PROPERTIES

1. Introduction

It is well known that methods of severe plastic deformation (SPD) such as high-pressure torsion and equal-channel angular pressing lead to significantly refinement of structure and improve the strength and service properties of low-carbon steels [1,2]. But at the present time, SPD methods are difficult to embed into the industrial production. Therefore, it is important to obtain low-carbon alloys with ultrafine grained (UFG) structure by industrial deformation methods, such as rotary swaging [3].

The purpose of this research is to establish a possibility of producing ultrafine-grained (nano- and submicrocrystalline) structures of low-carbon steels by rotary swaging and to study of its mechanical behavior.

2. Materials and experiment

The deformation of St.20 (0.19%C, 0.49%Si, 0.21%Mn, 0.03%Ni, 0.25%Cr, 0.19%Cu, 0.05%As, and Fe as a balance in wt.%) and 07G2MFB (0.073%C, 0.252%Si, 1.58%Mn, 0.242%Ni, 0.007%P, 0.005%S, 0.151%Cu, 0.22%Cr, 0.037%Al, 0.018%V, 0.195%Mo, 0.015%Ti, 0.02%W, 0.08%Nb, 0.0029%N, and Fe as a balance in wt.%) low carbon steels was carried out by rotary swaging (Fig.1). St.20 was subjected to quenching in water from a temperature of 880°C (1 hour) and high-temperature tempering at 600°C (1 hour). The 07G2MFB steel was subjected to quenching in water from a temperature of 920°C (1 hour) and high-temperature tempering at 680°C (1 hour).

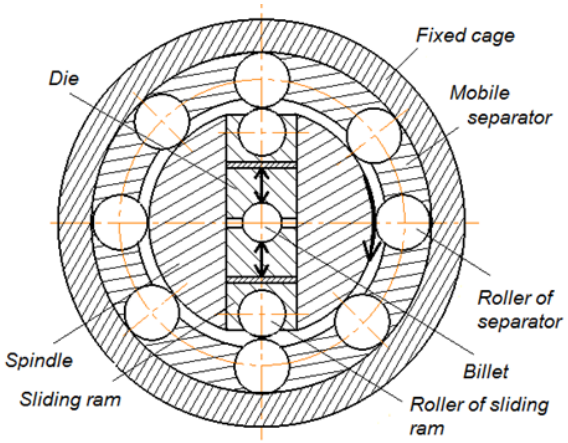

Fig. 1 *Schematic of the rotary swaging ($\mu = A_0/A_f$, where A_0 and A_f are the initial and the final cross-sectional area of the billets, respectively)*

The initial structure of both steels was similar. It was a polyhedral (globular) ferrite with pearlitic colonies, and also oriented products of quenching (Fig. 2). Transmission electron microscopy (TEM) revealed that the quenching products are acicular ferrite and tempered martensite.

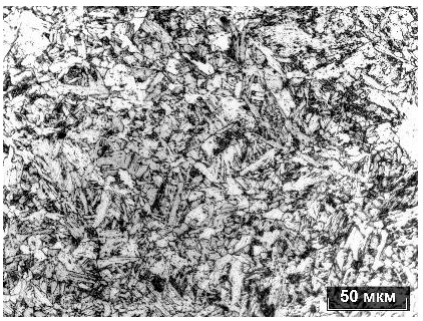

Fig. 2 *The structure of 07G2MFB steel after quenching and high-temperature tempering (optical microscopy)*

Rotary swaging of 07G2MFB steel was carried out in two modes with a decrease in the deformation temperature: 650°C (true strain ratio – 0,6) – 575°C (total true strain ratio –1,2) – 500°C (total true strain ratio –2,3) and 600°C – 500°C – 400°C with the same strain ratio. Rotary swaging of St.20 was carried out according to the second mode. The limited facilities of equipment and size of specimens did not allow an increase in the strain ratio during RS.

The microstructure was investigated using an Olympus PME 3 optical microscope and a JEM- 1400 transmission electron microscope operated at 120 keV. Static tensile tests were performed using an INSTRON 3380 tensile testing machine with a load capacity of 100 kN. Measurements of microhardness were taken by means 402 MVD Wolpert Wilson with loading 1N.

3. Results and discussion

The structure of 07G2MFB steel after rotary swaging (RS) was studied in two modes with a decrease in the temperature of deformation: 650 ° C - 575 ° C - 500 ° C and 600 ° C - 500 ° C – 400 ° C. The structure after RS at 650 ° C with a true strain ratio of 0.6 does not practically differ from the structure of this steel after quenching and tempering (Fig.2, 3a). Decreasing the temperature of RS to 575 ° C and increasing the strain ratio to 1.2 led to the orientation of the initial grain structure (Fig. 3b). The final stage of

the RS at 500 ° C with a total true strain ratio of 2.3 led to the formation of considerably oriented initial structure judging by the metallographic analysis (Fig. 3c). The TEM analysis revealed the formation of a submicrocrystalline structure with an average grain size of 343 nm inside this highly oriented initial structure. The metallographic analysis of 07G2MFB steel after RS by the mode of 600 ° C - 500 ° C - 400 ° C with a total true strain of 2.3 revealed an even more oriented structure due to a decrease in the strain temperature (Fig.4).

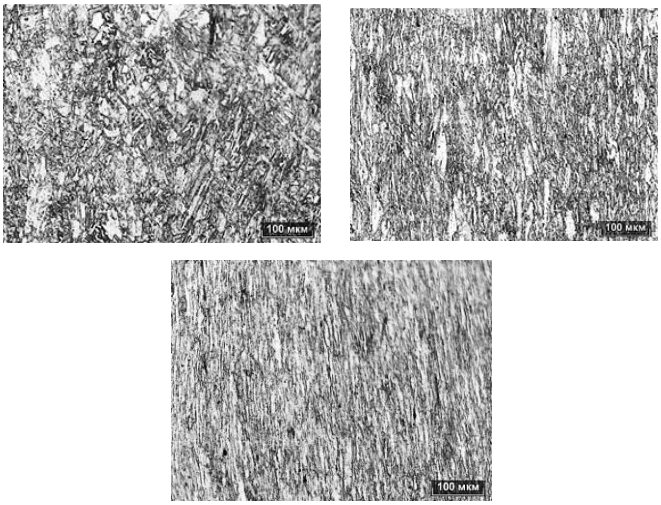

***Fig. 3**. The structure of 07G2MFB steel after rotary swaging with a decrease in temperature of deformation: 650 ° C (true strain ratio - 0.6) (a) - 575 ° C (1.2) (b) - 500 ° C (2.3) (c) (optical microscopy)*

It can even metallographically observed the substructure inside highly elongated initial grains (Fig.4b). In this case, the TEM analysis revealed a submicrocrystalline structure with a smaller average grain size of 312 nm (Fig. 5).

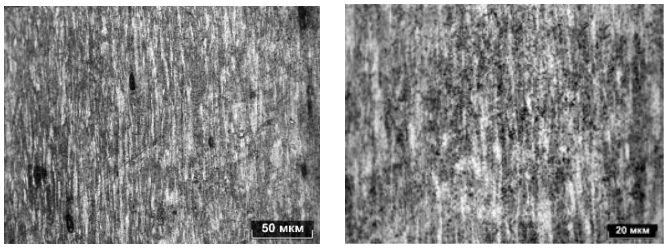

***Fig. 4** The structure of 07G2MFB steel after rotary swaging with a decrease in temperature of deformation: 600 °C (true srainratio - 0.6) - 500 ° C (1.2) - 400 ° C (2.3) (optical microscopy).*

The metallographic analysis of St.20 after RS by the 600 ° C - 500 ° C - 400 ° C mode (true strain ratio - 2.3) also revealed a highly oriented initial structure (Fig.6a). The TEM analysis revealed a submicrocrystalline structure with an average grain size of 285 nm (Fig.6b).

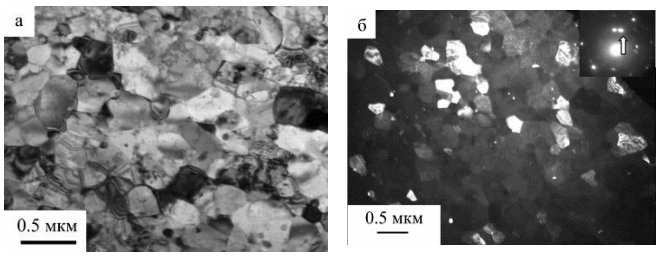

***Fig. 5** The structure of 07G2MFB steel after rotary swaging with a decrease in the temperature of deformation: 600 ° C - 500 ° C - 400 ° C (true strain ratio - 2.3):(a) bright-field; (b) dark-field image obtained in [110]* $_{\alpha\text{-Fe}}$.

Thus, the selected modes of rotary swaging of St.20 and 07G2MFB steels made it possible to obtain a predominantly submicrocrystalline structure with grain sizes ranging from 285 to 375 nm in these steels.

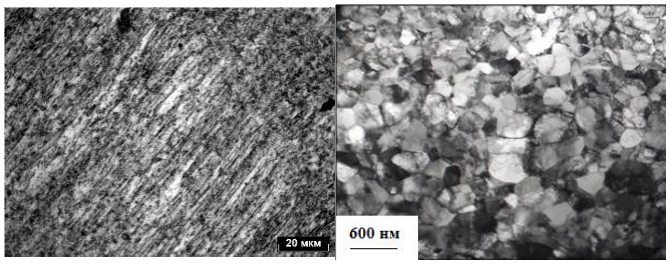

***Fig. 6** The structure of St.20 after rotary swaging with a decrease in deformation temperature: 600 °C - 500 °C - 400 °C (true degree of deformation - 2.3): (a) - optical microscopy, (b) - TEM*

The thermal stability of strengthening of St.20 and 07G2MFB steels after RS was studied according to the microhardness vs annealing temperature. The values of microhardness increase with decreasing temperature of RS and increasing strain ratio (Fig.7 and 8). After RS, the microhardness of 07G2MFB steel as compared with St.20 steel is higher (Fig.8).

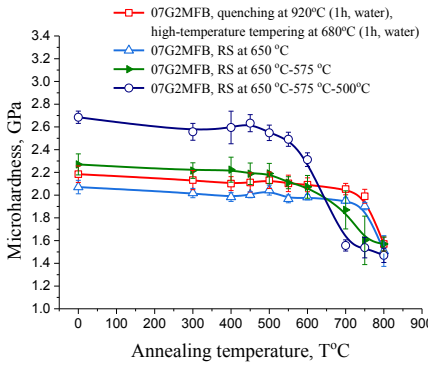

***Fig. 7** The thermal stability of strengthening of 07G2MFB steel after quenching and tempering and RS by mode of 650 ° C - 575 ° C – 500 °C*

The thermal stability for these steels of both treatments is about the same, but lower than that after quenching and tempering, despite a significantly higher level of strengthening.

For example, the thermal stability of the strengthening of 07G2MFB steel after the final stage of the RS at 400 °C is 400-450 °C, and after quenching and tempering it is 700 °C, but the microhardness level is 2.9 and 2.2 GPa, respectively (Fig.8a).

The mechanical properties of low-carbon St.20 and 07G2MFB steels after rotary swaging were studied. With a decrease in temperature and an increase in the strain ratio, the strength properties increased, and plasticity declined only slightly, which is observed both on 07G2MFB steel (Fig. 9 a, b, Table 1), and on St.20 (Fig. 9c, Table 1).

Acknowledgements

The work was carried out within the governmental task 075-00746-19-00 and supported by RFBR (grant 18-08-00321-a).

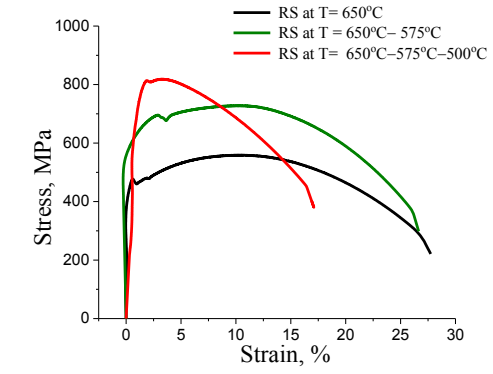

a

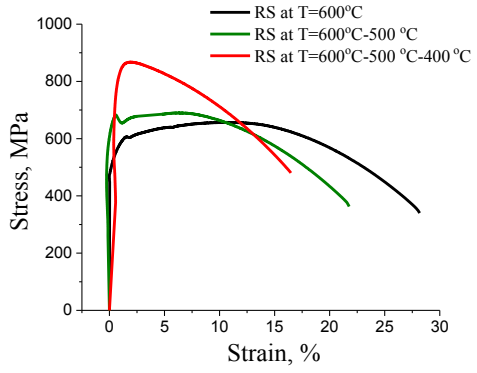

b

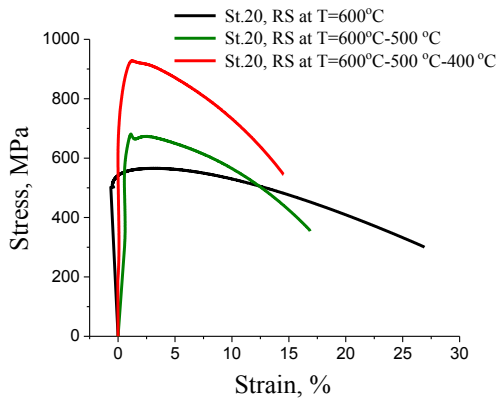

c

Fig. *9 Mechanical properties of low-carbon 07G2MFB (a, b) and St.20 (c) steels*

Comparing the ultimate tensile strength both of steels, deformed by the second mode of 600 °C – 500 °C – 400 °C, it can be seen that swaging at 600 °C with a true strain ratio of 0.6 leads to a slightly greater tensile strength in 07G2MFB steel, and swaging at 400 °C with a true strain ratio of 2, 3 - in St.20 (Fig. 9b, c, Table 1). But it should be noted in this case rather close values of the ultimate tensile strength. Therefore, it can be argued that the ultimate tensile strength of 867-927 MPa was obtained for both steels at the final stage of the RS at 400 ° C and with a true strain ratio of 2.3 at good ductility of EL = 16-17%.

Table 1: *Mechanical properties of low-carbon 07G2MFB and St.20 steels*

	Treatment /T_{def}°C,	Ultimate Tensile Strength σ_{UTS}, MPa	Yield Stress σ_{YS}, MPa	EL, %
07G2MFB	Quenching at 920°C (1h) → high-temperature tempering at 680°C (1h)	594	481	27
	RS / T=600°C	654	604	28
	RS / T=600°C→500 °C	690	654	22

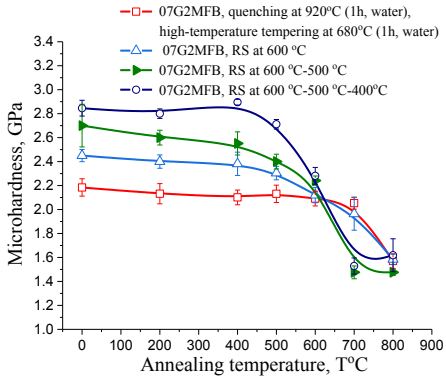

a

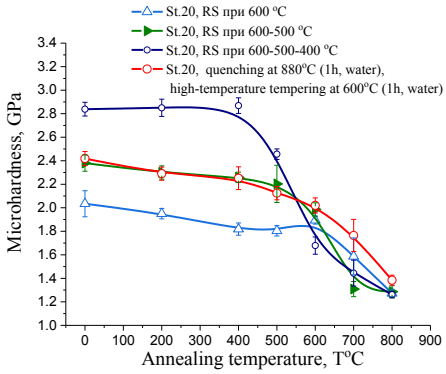

b

Fig. 8 *The thermal stability of strengthening of steels after quenching and tempering and subsequent RS by mode of 600°C – 500°C – 400°C: (a)- 07G2MFB steel;(b)- St.20*

	RS/T=600°C→500 °C→400 °C	867	846	17
	RS / T=650°C	558	460	28
	RS / T=650°C→575 °C	728	678	27
	RS / T=650°C→575 °C→500 °C	819	808	17
St.20	Quenching at 880°C (1h) → high-temperature tempering at 600°C (1h)	600	460	21
	RS / T=600°C	565	505	27
	RS / T=600°C→500 °C	673	664	17
	RS / T=600°C→500 °C→400 °C	927	923	15

4. Conclusions

1. Rotary swaging of 07G2MFB steel was carried out by two modes with a decrease in the deformation temperature: 650 ° C (true strain ratio - 0.6) - 575 ° C (1.2) - 500 ° C (2.3) and 600 ° C - 500 ° C – 400 °C with the same strain ratio. Rotary swaging of St.20 was carried out according to the second mode.
2. Rotary swaging of low-carbon St.20 and 07G2MFB steels at the final stage of the RS at 400 ° C with a true strain ratio of 2.3 leads to the formation of an ultrafine-grained (UFG) structure with a size of structural elements 285-312 nm.
3. The ultimate tensile strength in the range from 867 to 927 MPa with a true strain ratio of 2.3 and with good ductility EL = 16-17% was obtained in both steels at the final stage of the RS at 400 ° C.

5. References

[1] R.Z. Valiev, A.P. Zhilyaev, T.G. Langdon. Bulk nanostructured materials: fundamentals and applications, Wiley, Hoboken, 2014.

[2] R. Z. Valiev, Y. Estrin, Z. Horita, T.G. Langdon, M.J. Zehetbauer, Y. Zhu. Producing bulk ultrafine-grained materials by severe plastic deformation: ten years later, JOM 68(4) (2016), 1216 - 1226.

[3] Yu. S. Radyuchenko. Rotary swaging. Processing of parts on rotary swaging crimping machines. MASHGIZ, Moscow, 1962 (in Russian).

FEATURES OF STRUCTURE FORMATION AND MECHANICAL BEHAVIOR OF METALLIC MATERIALS UNDER CONDITIONS OF APPLICATION OF GRADIENT DEFORMATIONS

A.G. Raab[1,2] - Ph.D., A.P. Zhilyaev [2,3]– Dr. Sci, I.S.Kodirov[1], G.N. Aleshin [1]- Ph.D.
[1] Ufa State Aviation Technical University, IPAM, Ufa, Russia
[2] Nosov Magnitogorsk State Technical University, Magnitogorsk, Russia
[3] Institute for Metals Superplasticity Problems, RAS, Ufa, Russia

Abstract. *The study of technological methods of plastic structure formation is an urgent task. Taking into account that structure formation depends on many factors and, first of all, on the deformed state, studies of the deformed state and structural studies involving TEM were carried out in the work. It is known that reliable data of the structural state allows predicting the mechanical and operational properties of the obtained semi-finished products and products. In this regard, the analysis of the effect of the processing route (C, Bc) on the structural changes after high-cycle active bending was carried out. A numerical simulation of the active bending process was also carried out, and the accumulated strain values were determined for 8 processing cycles. Established patterns of structure formation, depending on the level of accumulated deformation and processing route.*

KEYWORDS*: PLASTIC STRUCTURE FORMATION, ACTIVE BENDING, MODELING.*

1.Introduction

In the context of expanding industrial production, the need for new materials and for improving the physico-mechanical properties of known materials increases. Researches in this direction are conducted by many scientific centers all over the world. Great efforts are aimed at studying the features of the structural states of materials and their connection with the stress-strain state and other factors [1,2]. In this regard, there is an increasing need for the creation of promising industrial methods that allow to achieve improved properties of materials [3-5].

One of them is the method of active bending, which makes it possible to act on the initial structure under conditions of a continuous gradient under conditions of a strain gradient. In this regard, the aim of the work was to study the effect of the deformed state with two copper processing routes on the type of structure being formed.

2.Concept of process

A schematic diagram of the active bending used in research is presented in Figure 1. The proposed development is based on the well-known ECAP- "Conform" scheme, while in the deformation process, the workpiece 3 is pushed into the stationary bending matrix consisting of two elements of the matrix 1 and 2.

The method allows to combine the high-performance process "Conform" with bending deformation, which leads to a significant intensification of the hardening process of the deformable material due to the formation of a gradient structure. Active friction forces ensure process continuity

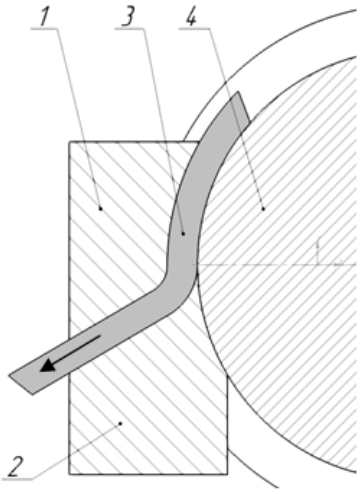

Figure. 1. *A schematic diagram of the bending of samples due to active friction forces according to the "Conform" scheme in a stationary bending matrix: 1, 2 - two matrix elements for bending; 3 – sample; 4 - drive roller with engraving*

For the simulation, the Deform 3D program was used to analyze the three-dimensional (3D) behavior of the metal during pressure treatment. This made it possible to obtain important information about the nature of the material flow in the forming tool, as well as about the stress-strain state and the temperature distribution during the deformation process.

When modeling the bend according to the "Conform" scheme at an angle of 90°, a square section sample with a size of 10x10 mm and a length of more than 150 mm was used for the first deformation cycle, a bend radius of 10 mm. For the subsequent cycles, a sample obtained by modeling on the previous cycle was used in order to obtain generalized data after passing through four sample processing cycles.

3. Results and discussion

Description of the structure of copper (M1) after bending on a horizontal installation ECAP-Conform

After 8 passes of active bending along the Bc route, a fragmented, close to equiaxed microstructure with misoriented fragments with sizes of ~ 0.3-0.5 μm was formed in the alloy. In the body and the boundaries of a significant part of the fragments, dislocation clusters with a scalar dislocation density ρ_d are observed, reaching values ρ_d in individual fragments of ~ 10^{11} cm^{-2}. With a further increase in the number of passes (degree of deformation), the dislocation density practically does not increase, i. e., it reaches saturation after 8 passes.

The estimate of the dislocation density, determined from the results of X-ray structural analysis, corresponds to the maximum value of ρd obtained by electron microscopic studies of thin foils.

Analysis of microdiffraction patterns obtained on thin foils from deformed flexible materials, as well as EBSD analysis, indicates a significant disorientation of the fragments after four passes. In general, these studies showed that in the process of bending along the V-route, medium- (5–15 °) and high-angle (~ 15 °) boundaries of deformation type are formed in copper.

At the same time, eight passes, which are flexible along route C, lead to the formation of a microstructure with lengths stretching in the direction of ~ 35–45 ° to the rod axis with sizes of ~ 1–3 μm in length and 0.2–0.6 μm in thickness. In many elongated fragments and boundaries between them there are clusters of dislocations with a scalar density ρd exceeding 10^{11} cm^{-2}. EBSD analysis showed the presence of a whole ensemble of fragment boundaries with different misorientations, among which medium- and high-angle deformation boundaries predominate.

The definition of microhardness in cross section of samples after bending is shown in Fig. 2 and 4. The magnitude of microhardness in the cross section varies in accordance with the character of the formed gradient structure, the features of which are higher HV values in the central rod area and a decrease in the HV value in near-surface areas for both bending paths (Fig. 2 and 4).

Obviously, such a dependence of the microhardness variation is due to the heating of the rods in the process of bending and the possible redistribution of dislocations and a decrease in their density in the near-surface region of the rods.

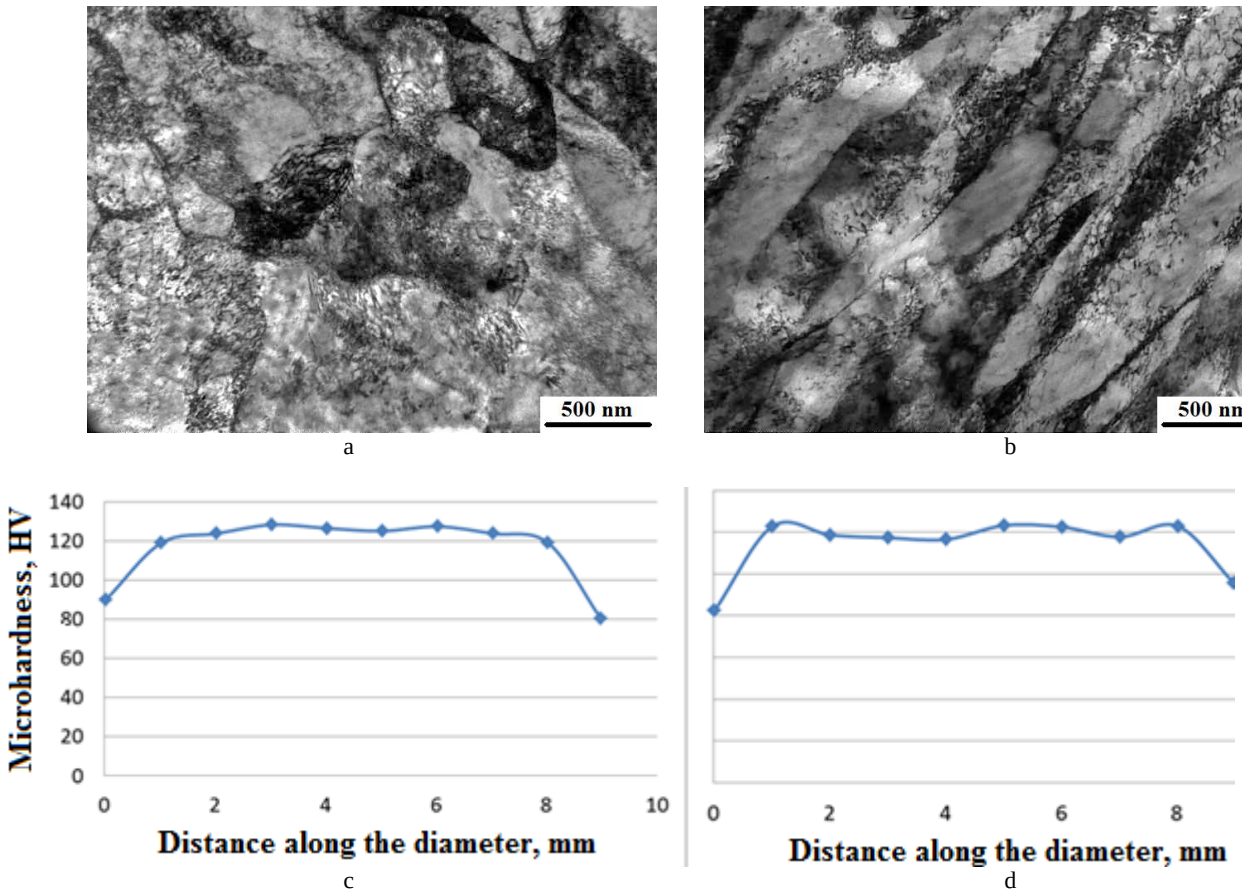

Figure 2. *8 passes are flexible: a - route Bc; b - route C; c, d – the dependence of the microhardness HV on the distance along the diameter of the rod, respectively, for routes Bc and C*

4. Conclusion

1. Using numerical simulation, it is established that active bending provides, after 8 processing cycles, the level of accumulated deformation e = 4.2 in the middle region and e = 5.0 in the near-surface cross-sectional area of the workpiece.

2. It has been established that when using the method of active bending along the Bc route, a grain-subgrain equiaxial structure with an average grain size of ~ 0.3-0.5 μm is formed in a deformed copper sample; a cross section of ~ 0.2–0.6 μm and a length of ~ 1–3 μm. UMP range.

Acknowledgements: the authors acknowledge the financial support by the Ministry of Education and Science of Russian Federation under Grant agreement acknowledge the financial support from the Grant

5. References

1. F. Z. Utyashev, G. I. Raab, Deformation Methods for Producing and Processing Ultrafine-Grained and Nanostructured Materials, Gilem, Ufa, 2013 (in Russian).

2. R. Z. Valiev, A. P. Zhilyaev and T. G. Langdon / Bulk Nanostructured Materials: Fundamentals and Applications // Wiley STM, USA 2014, p. 440.

3. G. I. Raab, A. G. Raab. Sposob polucheniya ul'tramelkozernistykh polufabrikatov volocheniem so sdvigom [Method for production of ultrafine-grained semi-finished products by shear drawing]. Russian Federation Patent No. 2347633, IPC B 21, C 1/00. Publ. 27.02.2009 (in Russian).

4. K. Lu, J. Lu, Nanoctructure surface layer on metallic materials induced by surface mechanical attrition treatment, Mater. Sci. Eng. A 375–377 (2004) 38-45.

5. E.I. Fakhretdinova, G.I. Raab1, M.M. Ganiev / Development of a Force Parameter Model for a New Severe Plastic Deformation Technique – Multi-ECAP-Conform // Applied Mechanics and Materials Vol. 698 (2015) pp 386-390.

6. G. I. Raab, L. A. Simonova, G. N. Alyoshin, Tailoring the gradient ultrafine-grained structure in low-carbon steel during shear drawing, Metalurgija 55 (2016) 177-180.

7. G.I. Raab, R.Z. Valiev, V.M. Kapitonov, A.G. Raab. Patent 2345861 Russian Federation, IPC B21J5 / 06, B21J13 / 00. Device for continuous angular pressing /; Applicant and patent holder of the "Ufa State Aviation Technical University" // - No. 2006145916/02; declare 12/22/2006; publ. 27.06. 2008. - 3s

TRIBOLOGICAL PROPERTIES OF COMMERCIALLY PURE COPPER AND A LOW-ALLOYED CHROMIUM BRONZE

ТРИБОЛОГИЧЕСКИЕ СВОЙСТВА ТЕХНИЧЕСКИ ЧИСТОЙ МЕДИ И НИЗКОЛЕГИРОВАННОЙ ХРОМОВОЙ БРОНЗЫ

Lead. Res., Dr. Semenov V.I.[1, +], PhD Stud. Alemayehu D.B.[2], Prof., Dr. Lin H.-C.[3], Lead. Res., Prof. Raab G.I.[1], Prof., Dr. Huang S.-J.[2], Prof., Dr. Chun Chiu[2]

[1]Ufa State Aviation Technical University, Ufa, Russia
[2] National Taiwan University of Science and Technology, Taipei, Taiwan
[3] National Taiwan University, Taipei, Taiwan
[+]corresponding author, e-mail: semenov-vi@rambler.ru

Abstract. *In this paper, we present the results of the tribological studies of commercially pure copper (99.9% Cu) and a low-alloyed chromium bronze (Cu-0.5%Cr), contacting a graphite-containing material. The samples under study were produced with two types of microstructures: a coarse-grained (CG) one, having an average grain size of 100-130 μm after annealing, and a submicrocrystalline (SMC) one, having an average grain size of 0.30-0.50 μm after multi-cycle severe plastic deformation (SPD) processing via equal-channel anglar pressing (ECAP) combined with Conform. It is shown that for the samples produced by ECAP-Conform, having an SMC structure, the friction coefficients are 12 - 20% lower than for the as-annealed samples, having a CG structure.*

KEY WORDS: *TRIBOLOGICAL PROPERTIES, FRICTION COEFFICIENT; SHEAR STRENGTH OF ADHESIVE BONDS, COMMERCIALLY PURE COPPER AND A LOW-ALLOYED CHROMIUM BRONZE, SEVERE PLASTIC DEFORMATION.*

Introduction

In the last 4 decades of the 20th century, the high-speed passenger transportation systems were under intensive development. Such systems allow for motion speeds of up to *300 – 400 km/h*, while the average speeds are only up to *160 – 200 km/h*. In order to ensure the operation of high-speed railway lines, structural materials, and in particular, the materials for contact wires, must meet a whole range of special requirements which are difficult to provide when using conventional technologies.

In the case of regular electrified railway lines, the stress of a contact wire does not exceed *100 MPa*, and in the case of high-speed railway lines, the tension stress of a contact wire is *250 MPa* (2.5 times higher than in the case of regular railway lines). The highest allowable temperature of long-term heating is *150°C* [1]. In this connection, a problem arises, related to the tribological parameters of the contact between copper wires and graphite-containing current collectors.

It is known that materials with a higher hardness ensure lower wear and friction coefficient [2]. In most cases, there are various ways to increase the hardness of alloys by means of heat treatment [3, 4]. However, a heat treatment aimed at hardness enhancement does not always enable achieving the desired effect. For this reason, the use of copper alloys in friction units is very limited. For such materials, various types of thermochemical [5 - 7] and surface plastic treatment [6 - 8] are used, which enable increasing the surface strength of the materials under treatment. The drawback of these methods is the relatively small depth of the strengthened surface layer, therefore they can be used only as a finishing treatment or for relatively simple and low-loaded parts of tribocouplings.

There are works evaluating the effect of the structural and phase compositions of metallic materials on their tribological properties [6, 7, 9 - 11]. In these works, tribological studies were performed on materials subjected to various types of heat treatment, resulting in microstructural changes.

To date, a technology has been developed, providing an efficient and manifold increase in strength, while preserving a high technological plasticity. This technology is based on severe plastic deformation (*SPD*) processing and enables producing high-strength bulk billets from metallic materials [12]. Among the *SPD* processing techniques is equal-channel angular pressing (*ECAP*) [13], used, in particular, for the fabrication of long-length billets and effected in several deformation cycles. The essence of this method for the strength enhancement of a material lies in the maximum refinement of grain structure down to submicrocrystalline (*SMC*) and nanocrystalline (*NC*) sizes [14]. Therefore, comprehensive tribological studies of copper in different structural states (as-annealed and *SPD*-processed) are of scientific and practical interest.

Methods for the evaluation of the integral value of the friction coefficent and its molecular component

In the tribological studies, we used two test configurations shown in Fig. 1.

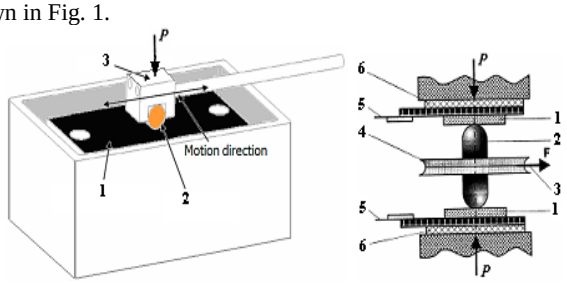

a *b*

Fig. 1. *Tribological test configurations: a) 1 – the lower sample (graphite-containing plate); 2 – the upper sample (under testing); 3 – holder; b) 1 – samples under testing; 2 – spherical indenter; 3 – cable; 4 – disc with a groove; 5 – current-carrying buses; 6 – electrically-insulating pads.*

The first test configuration under reciprocating motion (fig. 1, *a*) was used to evaluate the friction coefficient in the pairs «*M1* commercially pure *Cu – EK-40* graphite-containing plate» and «*Cu-0.5%Cr* chromium bronze – *EK-40* graphite-containing plate».The testing conditions were as follows: the normal load *P* was *80 N*, the relative sliding velocity was *0.1 m/s*, the time of each test was *60 min*. The normal load was selected based on the maximum force of pressing of a contact wire to a graphite-containing current collector in railway transport. The speed regime of the testing was determined by the capabilities of the employed tribometer. Time was set on the basis of the previous experience of such tests. The testing was performed at room temperature.

The second test configuration (Fig. 1, *b*) was used to evaluate the shear strength of adhesive bonds and the adhesive component of the friction coefficient. Since the graphite-containing plate is a brittle material and an indenter made thereof cannot withstand normal loads while the strength of adhesive bonds is determined, it was proposed to coat an indenter from the *Fe-18%W-4%Cr-0.8%C* tool steel with a graphitic compound (graphitize) with a subsequent

drying at a temperature of *100-120°C*. Hereinafter we will use the abbreviation «*GTS*» standing for «*graphitized tool steel*». Thus, the testing according to the second test configuration was conducted in the contacting pairs «commercially pure copper – *Fe-18%W-4%Cr-0.8%C GTS*» and «*Cu-0.5%Cr* chromium bronze – *Fe-18%W-4%Cr-0.8%C GTS*». For this purpose, samples were prepared from commercially pure *Cu* and the chromium bronze in the initial (*CG*) structural state (after annealing), and in the *SMC* and *NC* states after 4 cycles of *SPD* processing by *ECAP-Conform*. The samples under testing had the shape of a disc with a diameter of *10 mm* and a thickness of *3 mm*. The spherical indenter had a sphere radius of *2.5 mm*, and the thickness of the graphitic material applied onto the indenter's spherical surfaces was about *50 μm*. The testing was performed at temperatures of *20; 150; 250 and 450°C*, using a one-ball adhesion tester [15]. There is a physical model underlying this method, which in a first approximation reflects the actual friction conditions in a local contact.

According to this model, a spherical indenter 2, imitating a single asperity of the contact spot between the rubbing solid bodies, compressed by two plane-parallel samples 1 (with a high precision and cleanliness of the contacting surfaces), rotates under a load around its axis. The force *F* expended on the indenter rotation and applied to the cable 3, laid in the groove of the disc 4, is primarily related to the shear strength τ_n of adhesive bonds. In order to use this method at elevated contact temperatures, a special apparatus has been designed that enables producing the electric-contact heating (through the buses 5 isolated from the body by pads 6) of the contact zone.

The initial roughness of the contact surfaces of the tested samples and the indenter in both test configurations was *0.06 – 0.16 μm* in the *Ra* scale. The roughness of the samples was measured using an *SE-3500K 2D-3D* profilometer-profilograph.

The shear strength of adhesive bonds τ_n (*MPa*) was determined from the relation:

$$\tau_n = 0{,}75 \cdot \frac{M}{\pi \cdot \left(\frac{d_{1,2}}{2}\right)^3}, \quad (1)$$

where $d_{1,2}$ are the diameters of the impressions on the tested samples, *mm*; *M* is the moment of indenter rotation, *N mm*.

The adhesive component of the friction coefficient was determined as:

$$f_a = \frac{\tau_n}{p_n}, \quad (2)$$

where $p_n$is the normal pressure, *MPa*,

$$p_n = \frac{P}{\pi \cdot \left(\frac{d_{1,2}}{2}\right)^2} \quad (3)$$

where *P* is the force of compression of the samples, *N*.

Before and after the tribological tests in accordance with the first test configuration (Fig. 1, *a*), the tested samples from commercially pure *Cu* were studied to determine the microhardness *Hμ*, using a *Micromet-5101* device under a load of *0.98 N* with exposure to the load for *15 s*.

Results of finding the friction coefficient and the strength of adhesive bonds under elastic contact conditions

The results of the tribological tests performed in accordance with the first test configuration (Fig. 1, *a*) in the friction pairs «commercially pure *Cu – EK-40* graphite-containing plate» and «*Cu-0.5%Cr* chromium bronze – *EK-40* graphite-containing plate» are presented in Fig. 2.

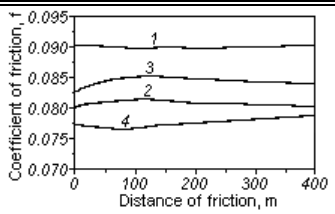

Fig. 2. *Friction coefficent as a function of the distance of friction: 1 – commercially pure Cu with a CG structure; 2 – commercially pure Cu with an SMC structure; 3 – Cu-0.5%Cr chromium bronze with a CG structure; 4 – Cu-0.5%Cr chromium bronze with an SMC structure.*

As revealed by the presented diagram, the friction coefficient values obtained for the as-annealed samples from both commercially pure *Cu* (curve *1*) and the *Cu-0.5%Cr* chromium bronze (curve *3*), are higher than those for the samples from the same materials processed by *ECAP-Conform* and having an *SMC* structure (curves *2* and *4*). It should be noted that after the friction coefficient grows, as the distance of friction increases, the samples from the chromium bronze having a *CG* microstructure demonstrate a tendency for a slight decrease in the friction coefficient. It should be mentioned that the results obtained for the samples from the low-alloyed chromium bronze *Cu-0.5%Cr* having a *CG* structure (curve *3*) show a slight decrease in the friction coefficient with increasing distance of friction. This fact can be attributed to a further increase in strength resulting from work hardening and a local structure refinement on the friction surface, followed by a transfer of chromium particles to the graphite-containing material used as a counterbody. The local structure refinement promotes activation of grain boundaries and enhancement of the diffusion interaction between the components of the *Cu-0.5%Cr* chromium bronze, having a *CG* structure, and the carbon in the graphite-containing material. This assumption requires further study.

As a result of finding the strength of adhesive bonds, it was established that in the case of commercially pure *Cu*, as the testing temperature is increased from room temperature to *150°C*, the adhesive component of the friction coefficient practically does not change and equals *0.082* for the *CG* material and *0.061* for the *SMC* material. As the temperature increases further, from *150°C* to *250°C*, there is observed a steady growth in the adhesive component of the friction coefficient from *0.082* to *0.09* for the material with a *CG* structure and from *0.061* to *0.069* for the material with an *SMC* structure. The observed change is evidently related to the structural and phase transformations, as well as the diffusion processes occurring at grain boundaries in a temperature range of *150 – 250°C*. Thus assumption requires further studies. As the temperature is further increased to *450°C*, the values of the adhesive components of the friction coefficients practically do not change.

In the case of the samples from the low-alloyed chromium bronze *Cu-0.5%Cr*, with increasing temperature the ahesive component of the friction coefficient monotonically grows in both structural states, and there is some stabilization of the values in a temperature range of *350 – 450°C*.

Fig. 3 presents the curves illustrating the results of the evaluation of the friction coefficient's adhesive component as a function of the temperature of testing performed using a one-ball tribometer according to the test configuration shown in Fig. 1 *(b)*.

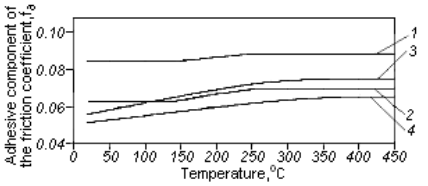

Fig. 3. *The adhesive component of the friction coefficient as a function of temperature: 1 – commercially pure Cu with a CG structure; 2 – commercailly pure Cu with an SMC structure; 3 – Cu-0.5%Cr chromium bronze with a CG structure; 4 – Cu-0.5%Cr bhromium bronze with an SMC structure.*

From the analysis of the results of finding the shear strength of adhesive bonds in the contact pairs «commercially pure *Cu – Fe-18%W-4%Cr-0.8%C GTS*» and «chromium bronze *Cu-0.5%Cr – Fe-18%W-4%Cr-0.8%C GTS*», it was established that the adhesive component of the friction coefficient is higher for the *CG* samples than for the samples with an *SMC* structure in the whole range of temperatures under investigation.

Table 1 lists the experimentally found values of the adhesive and deformation components of the friction coefficient at room temperature for commercially pure *Cu* and the *Cu-0.5%Cr* chromium bronze in different structural states.

Table 1. *Values of adhesive and deformation components of the friction coefficient at room temperature*

Material	Adhesive component of the friction coefficient (f_a)	Deformation component of the friction coefficient (f_d)*
$Cu_{(CG)}$	0.082	0.080
$Cu_{(SMC)}$	0.061	0.010
$Cu\text{-}0.5\%Cr_{(CG)}$	0.055	0.028
$Cu\text{-}0.5\%Cr_{(SMC)}$	0.051	0.024

* The deformation component of the friction coefficient was determined as: $f_d = f - f_a$ [5].

It can be seen from table 1 that in the studied friction pairs in a dynamic contact an essential role is played by the adhesive component both for the materials with a *CG* structure and for the materials with an *SMC* structure. However, it was noted that for the commercially pure *Cu* samples there is a large difference between the deformation components of the friction coefficient, depending on the material's structure. For the *Cu* samples with a *CG* structure the value of f_d is 8 times higher than the corresponding value for the *SMC* material. Apparently, this is related to the fact that commercially pure *Cu* with an *SMC* structure has a greater tendency for sticking. No such difference has been found in the *Cu-0.5%Cr* chromium bronze.

The values of the adhesive and deformation components of the friction coefficient for the chromium bronze samples have a small difference in the case of different microstructures. This observation is apparently an indirect evidence of the greater tendency of the commercially pure materials (in our case, *Cu*) for strain hardening.

The obtained results are in good correlation with earlier studies [17, 18].

Analysis of the friction surfaces of the as-annealed samples prior to and after the tribological tests

Prior to conducting the tribological tests according to the reciprocating-motion test configuration and afterwards, we performed chemical analysis of the investigated copper, bronze and graphite-containing samples (the graphite-containing samples were studied only in the condition after the tribological tests). For this purpose, we used an *S-3500N* scanning electron microscope with an *EDS* attachment for chemical analysis.

The analysis results show that the friction surface of the commercially pure *Cu M1* in the process of its frictional interaction with a graphite-containing plate becomes saturated with carbon and oxygen.

Fig. 4, *a)* shows the friction path formed as a result of the frictional interaction between the investigated sample from the commercailly pure Cu *M1* and the graphite-containing plate. From the analysis of the topography of the surface shown in Fig. 4, *b)*, it has been established that carbon is present on the furface in a free state, in the form of particles flaked from the graphite-containing plate. Oxygen is apparently in a bound state, in the form of oxides. Previously, it was noted elsewhere [17, 18] that the frictional interaction and structural changes initiate the process of oxygen content growth on the friction surfaces of metallic materials.

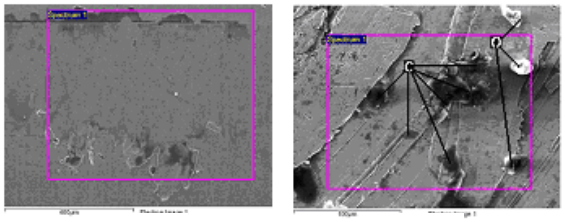

a) *b)*

Fig. 4. *Images of the friction surface of the commercially pure Cu M1: a) – general view of a portion of the friction path; b) – topography of the friction surface with marked carbon and oxide particles.*

The chemical analysis of the friction surface of the graphite-containing plate reveals that during the frictional interaction of the investigated pair in the conditions of the experiment, there is observed a transfer of copper particles onto the friction path. The chemical analysis results are presented in Fig. 5.

Graphite-containing plate

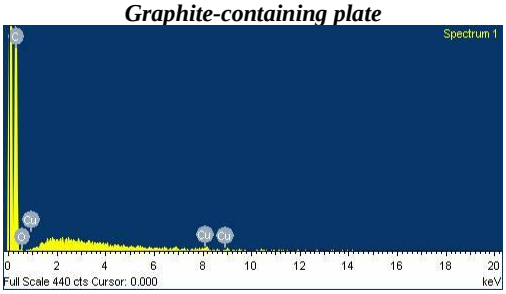

Fig. 5. *Spectrum of chemical element distribution on the friction surface of the graphite-containing plate after the frictional interaction with commercially pure Cu.*

The spectrum of the friction surface shows such chemical elements as carbon (the basis of the graphite-containing plate), oxygen and copper. The latter two are in the form of traces.

Approximately the same results were obtained as a result of the tribological studies of the low-alloyed chromium bronze.

It should be noted that the chromium content on the friction surface of the chromium bronze is 1.5 times lower, as compared to the initial state prior to the tests. This could be related to the fact that the chromium-containing compounds were coagulated in a limited volume and in the process of friction partially transported onto the friction surface of the graphite-containing plate.

Fig. 6, *a)* shows the friction path on the chromium bronze after its frictional interaction with the graphite-containing plate. It is assumed that chromium and the chromium-containing compounds are present on the friction surface in the form of narrow bands, positioned along the direction of friction (Fig. 6, *b*).

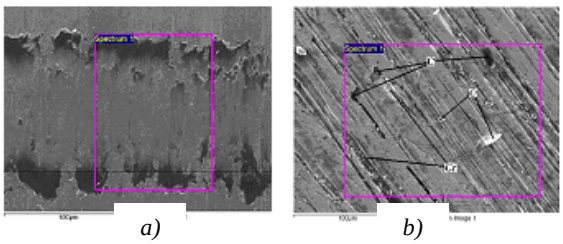

a) *b)*

Fig. 6. *Image of the friction surface of the Cu-0.5%Cr chromium bronze: a) – general view of a portion of the friction path; b) – topography of the friction surface with the marked dispersed particles of carbon, chromium and oxides.*

The chemical analysis, the results of which are presented in Fig. 7, reveals that the chromium particles, in the form of traces, have also been transferred from the chromium bronze surface onto the graphite-containing plate.

Graphite-containing plate

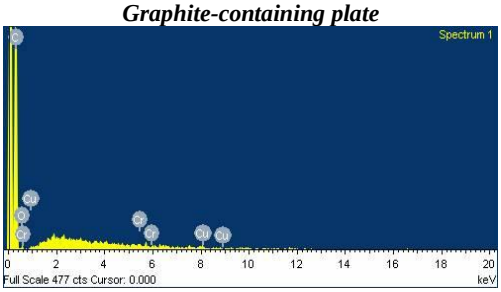

Fig. 7. . *Spectrum of chemical element distribution on the friction surface of the graphite-containing plate after the frictional interaction with the chromium bronze.*

Main conclusions

1. As a result of a comprehensive evaluation of the tribological properties of commercially pure *Cu* and the low-alloyed chromium bronze, having different microstructures, it has been found that in the investigated contact pairs, regardless of the structural state of *Cu* and chromium bronze, the adhesive component of the friction coefficient has a considerable value. In the commercially pure *Cu* samples, there is observed a large difference between the adhesive and deformation components of the friction coefficient, depending on the material's structure – for the *Cu* samples with a *CG* structure the values of f_d are 8 times higher than the respective values for the *SMC* material;

2. We have obtained the correlation dependencies, considering the different structural states of the investigated materials, for the contact pairs «*M1* commercially pure *Cu – EK-40* graphite-containing plate» and «*Cu-0.5%Cr* chromium bronze – *EK-40* graphite-containing plate» (for the evaluation of the friction coefficient's integral value at room temperature), and the contact pairs «commercially pure *Cu – Fe-18%W-4%Cr-0.8%C* GTS» and «*Cu-0.5%Cr* chromium bronze – *Fe-18%W-4%Cr-0.8%C* GTS» (for the evaluation of the friction coefficient's adhesive component at different temperatures). We have established that for commercially pure *Cu* and the low-alloyed bronze, the integral values of the friction coefficient and their adhesive components are structurally sensitive parameters, and their values are lower for the samples with an *SMC* structure than for the samples with a *CG* structure;

3. The chemical analysis of the friction surfaces of the samples and the graphite-containing plate has shown a mutual transfer of chemical elements, as well as an increase in the oxygen content, which is an evidence of the activation of the friction surface, resulting from the frictional interaction, and structural transformations in the near-surface layers.

ACKNOWLEDGEMENTS

This research was supported by the Ministry of Science and Higher Education of the Russian Federation under grant agreement No. 14.586.21.0059 (unique project identifier RFMEFI58618X0059).

Literature

[1] Yu.E. Kuptsov. Conversations about Current Collection. — Moscow: «Modern-A», 2001. - 256 p. (in Russian).

[2] Friction, Wear and Lubrication (Tribology and Triboengineering)/ A.V. Chichinadze, E.M Berliner, E.D. Brown et al., ed. by A.V. Chichinadze. – Moscow: Mashinostroenie, 2003. – 576 p. (in Russian).

[3] Yu.V. Futoryanskiy, Efficient Methods for the Hardening of Steel Products. Kuibyshev: Kuibyshev Book Publisher. 1978. 87 p. (in Russian).

[4] V.Ya. Kirshenbaum. Mechanical-Thermal Formation of Friction Surfaces. Moscow: Mashinostroenie, 1987. 230 p. (in Russian).

[5] D.G. Gromakovskiy, N.D. Kuznetsov et al. Increasing the life of friction units through the use of carbon fluorides//Vestnik Mashinostroeniya, 1987, № 8 (in Russian).

[6] A.V. Belyi, G.D. Karpenko, N.K. Myshkin. Structure and Methods for the Formation of Wear-Resistant Surface Layers. Moscow: Mashinostroenie, 1991. 208 p. (in Russian).

[7] D.N. Garkunov. Triboengineering. Moscow: Mashinostroenie, 1989. 327 p. (in Russian).

[8] L.G. Odintsov. Strengthening and Finishing of Parts Using Surface Plastic Deformation: Reference book. Moscow: Mashinostroenie, 1987. 327 p. (in Russian).

[9] Pearlite in Carbon Steels / V.M. Schastlivtsev, D.A. Mirzaev, I.L. Yakovleva et al. Ekaterinburg: the Ural Branch of RAS, 2006. ISBN 5-7691-1713-3 (in Russian).

[10] V.M. Schastlivtsev, V.I. Zeldovich, D.A. Mirzaev et al. Developing the Ideas of Academician V.D. Sadovskiy. Collection of papers. Ekaterinburg, 2008. ISBN 5—900474—58—5 (in Russian).

[11] L.M. Rybakova, L.I. Kuksenova. Structure and Wear Resistance of Metal. Moscow: Mashinostroenie, 1982. 212 p. (in Russian).

[12] R.Z. Valiev, I.V. Alexandrov. Nanostructured Materials Produced by Severe Plastic Deformation. Moscow: Logos, 2000. 272 p. (in Russian).

[13] G.I. Raab, R.Z. Valiev. Equal-channel angular pressing of long-length billets // Izvestiya Vuzov. Tsvetnaya Metallurgiya -2000 -№5, p.50-53 (in Russian).

[14] Equal-channel angular pressing of metallic mateials: achievements and areas of development (Thematic collection of papers, ed. by V.M. Segal, S.V. Dobatkin and R.Z. Valiev)// Russian Metallurgy (Metally) 2004, Nos. 1, 2.

[15] L.Sh. Shuster. Adhesive Interaction of Solid Metallic Bodies. - Ufa: Gilem, 1999. 198 p. (in Russian).

[16] V.I. Semenov, L.Sh. Shuster, S.V. Chertovskikh, G.I. Raab. The effect of the complex parameter of the plastic friction contact and the material structure on the strength of adhesive bonds // Trenie i Iznos. 2005. Vol. 26. № 1. P. 74 – 79 (in Russian).

[17] Song-Jeng Huang, Yeau-Ren Jeng, V. I. Semenov and Yo-Zhi Dai Particle Size Effects of Silicon Carbide on Wear Behavior of SiC_p-Reinforced Magnesium Matrix Composites//Tribology Letters (2011), V. 42, No. 1, p. 79-87.

[18] V.I. Semenov, L.Sh. Shuster, S.-J. Huang, P.-Ch. Lin Tribological Behavior of Low-Carbon Steel Depending on Treatment and Structural State//Journal of Friction and Wear, 2011, Vol. 32, No. 3, pp. 205–211.

COMPARATIVE TRIBOLOGICAL PROPERTIES OF AZ91D MAGNESIUM ALLOY AFTER STRENGTHENING BY SiC POWDER AND AFTER SEVERE PLASTIC DEFORMATION

СРАВНИТЕЛЬНЫЕ ТРИБОЛОГИЧЕСКИЕ СВОЙСТВА МАГНИЕВОГО СПЛАВА AZ91D ПОСЛЕ УПРОЧНЕНИЯ ПОРОШКОМ КАРБИДА КРЕМНИЯ И ПОСЛЕ ИНТЕНСИВНОЙ ПЛАСТИЧЕСКОЙ ДЕФОРМАЦИИ

Lead. Res., Dr. Semenov V. I.[1+], Prof., Dr. Lin H.-C.[2], Prof. Shuster L.Sh.[1], Prof. N. Tontchev[3], Prof., Dr. Chun Chiu[4], Prof., Dr. Huang S.-J.[4]

[1]Ufa State Aviation Technical University, Ufa, Russia
[2]National Taiwan University, Taipei, Taiwan
[3]Todor Kableshkov Higher School of Transport, Sofia, Bulgaria
[4]National Taiwan University of Science and Technology, Taipei, Taiwan
[+]corresponding author, e-mail: semenov-vi@rambler.ru

Abstract. *The paper presents the results of studies of tribological properties of the contact of the tool steel composition Fe-18W-4Cr-1,2V with the magnesium alloy AZ91D strengthened by submicron powder filling out of SiC and severe plastic deformation (SPD), namely equal-channel angular pressing (ECAP). It is stated that introduction of SiC powder filling to the magnesium alloy the friction coefficient on the moving frictional contact increases, the wear rate reduces. These tribotecnical characteristics are influenced by the size and volume of the particles of powder filling, normal loading force and slip rate. SPD of the initial material results in reduction of the adhesion constituent of the friction coefficient.*

KEYWORDS: *MAGNESIUM ALLOY; METALLIC COMPOSITE MATERIAL; POWDER FILLING; SEVERE PLASTIC DEFORMATION; EQUAL-CHANNEL ANGULAR PRESSING; SILICIUM CARBIDE; FRICTION COEFFICIENT; ADHESIVE BOND SHEAR STRENGTH ; WEAR RATE.*

Introduction

In modern mechanical engineering, in particular in friction knots, one of the ways to reduce the weight of cars is to apply light alloys with enhanced mechanical properties. Magnesium is attractive to be applied as structural material due to attractive strength-to-weight ratio that exceeds the one for aluminum and other light metals and alloys [1-3]. High damping capacity of magnesium alloys allows using them effectively to manufacture automobile and aircraft wheels, various components for motor-and-tractor and aerospace engineering, rollers for cargo conveyors [6, 7] etc. The strength of magnesium could be enhanced without significant change in the strength due to addition of small amount of submicron powder filling of SiC [3-5]. Besides, severe plastic deformation is known to effectively increase the strength of bulk metals due to fabrication of ultrafine-grained structure [8, 9]. SPD techniques can be considered as alternative techniques to dispersion strengthening of composite materials.

However, tribological behavior of these materials is studied insufficiently for application in friction knots [10, 11].

In this paper the results of definition of wear rate of the magnesium alloy, the friction coefficient and its molecular constituent depending on the content of the powder filling are given. Comparative evaluation of the adhesive bond shear strength and molecular constituent of the friction coefficient of the magnesium alloy *AZ91D* strengthened by *ECAP* in the slipping tribological contact with the tool steel composition *Fe-18W-4Cr-1,2V* is presented.

Experimental procedure and materials

Magnesium alloy *AZ91D* (*89.89%Mg-9.0%Al-0.68%Zn-0.13%Mn*) was used as material for study. In comparative tests there were employed matrix composite materials, containing submicron powder filling out of *SiC*, and the magnesium alloy *AZ91D* after *2 ECAP* passes.

The variants of investigated composite materials differing in dispercity and amount of added powder of *SiC* and strain-hardened magnesium alloy of the initial state are the following: *AZ91D* in the initial state*; AZ91D + 3% SiC* with an average particle size of *5 μm; AZ91D + 3% SiC* with an average particle size of *11 μm; AZ91D + 6% SiC* with an average particle size of *11 μm; AZ91D + 3% SiC* with an average particle size of *15 μm; AZ91D* after 2 *ECAP* passes.

Tribological tests of the initial alloy and dispersion-strengthened composite materials were carried out on the friction machine "Timken". Fig. 1 presents the set and the processing scheme.

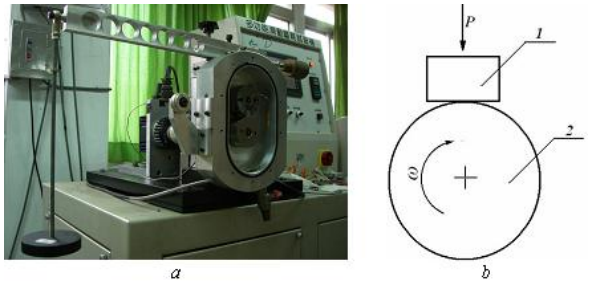

Fig. 1. *Machine of friction "Timken" (a) and testing scheme (b): 1 – tested sample; 2 – rotating steel disk.*

Testing of the initial and dispersion-strengthened materials was conducted under normal loading of *10N* and *50N* and a disk rotation speed of *250 min*$^{-1}$ and *1000 min*$^{-1}$, the slip distance was *1650 m* in all the tests.

Friction force *(F)*, loss of sample mass *(Q)* and geometric area of the contact *(S_c)* were recorded during tests. The wear rate *(J_h)* value was defined with the help of the mentioned parameters.

The diameter of the disk out of tool steel composition *Fe-18W-4Cr-1,2V* was *70 mm*, the thickness was *20 mm*. The wear of the disk quenched to the hardness of *HRC58…65* was neglected due to its low value as compared to the wear of the tested samples.

The friction coefficient *f* was calculated according to the formula:

$$f = \frac{F}{P}, \qquad (1)$$

where *F* – friction force, *N*; *P* – normal loading force, *N*.

The wear rate J_h value was defined according to the formula:

$$J_h = \frac{Q}{qS_cL}, \quad (2)$$

where Q – sample mass loss, g; q – material density, g/cm^3; S_c – geometrical area of the contact, cm^2; L – slip distance, *cm*.

Fig. 2 presents the *ECAP* scheme that was chosen for strain hardening of the initial material [12, 13].

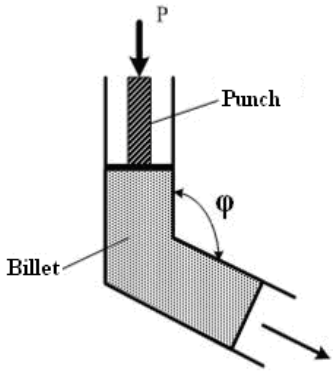

Fig. 2. *ECAP scheme.*

The employed scheme allows achieving high degrees of accumulated strain as a result of shear in the conjugating channels. In this case the angle between the conjugating channels φ was 120^o.

Studies on the evaluation of the adhesive bond shear strength and molecular constituent of the friction coefficient were carried out on the one-ball machine of friction at temperatures of *20, 150* and *300 °C* according to the scheme that is presented in Fig. 3 [14].

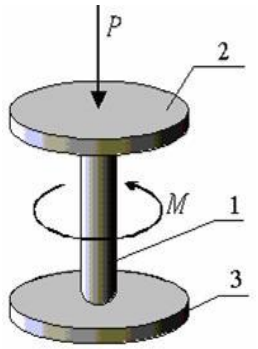

Fig. 3. *Scheme of testing of molecular constituent of the friction coefficient: 1 – tool steel R18 indentor; 2 – tested samples.*

Adhesive bond shear strength τ_n was defined from the ratio:

$$\tau_n = 0{,}75 \cdot \frac{M}{\pi \cdot \left(\frac{d_{1,2}}{2}\right)^3}, \quad (3)$$

where $d_{1,2}$ – diameters of prints on the tested samples, mm; M – indentor rotary moment, *N mm*.

Adhesive (molecular) constituent of the friction coefficient was defined as:

$$f_M = \frac{\tau_n}{p_r}, \quad (4)$$

where p_r – normal pressure, *MPa*

$$p_r = \frac{P}{\pi \cdot \left(\frac{d_{1,2}}{2}\right)^2} \quad (5)$$

where P – force of sample compression, *N*.

Results of experiments and their discussion

Figs. 4 and 5 present the charts with the results of tribological tests conducted according to the scheme "block-disk" (Fig.1).

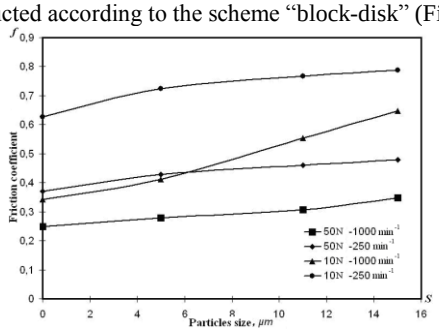

Fig. 4. *Dependence of the friction coefficient on the size of SiC particles*

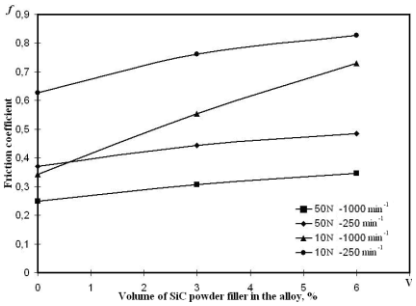

Fig. 5. *Dependence of the friction coefficient on the volume of powder filling*

It is seen from the charts that addition of powder filling of *SiC* to the magnesium alloy increases the friction coefficient. The lower the normal loading force and the slip rate, the higher friction coefficient.

In order to explain these results, let us consider the data received with the help of the one-ball machine of friction.

Fig. 6 demonstrates that the dependence of the adhesive bond shear strength τ_n on the normal pressure p_r is described by the binomial dependence:

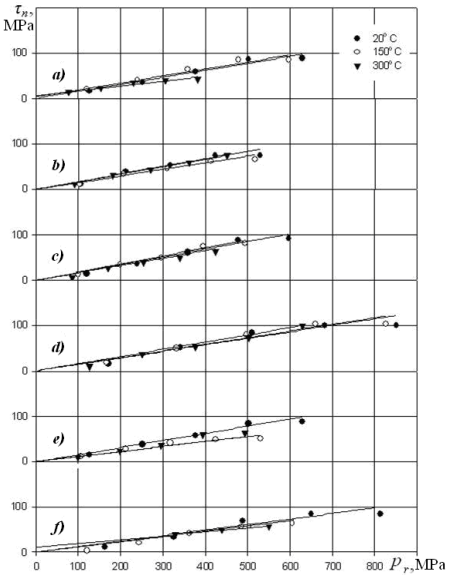

Fig. 6 *Dependence of adhesive bond shear strength on the normal pressure in the contact with tool steel composition Fe-18W-4Cr-1,2V: a) - AZ91D in the initial state; b) - AZ91D + 3% SiC with an average particle size of 5 μm; c) - AZ91D + 3% SiC with an average particle size of 11 μm; d) AZ91D + 6% SiC with an average particle size of 11 μm; e) AZ91D + 3% SiC with an average particle size of 15 μm, f) AZ91D after 2 ECAP passes.*

$$\tau_n = \tau_o + \beta p_r \quad (6)$$

where τ_o – adhesive bond shear strength without normal loading force; β – piezocoefficient.

The molecular constituent of the friction coefficient f_M can be defined as:

$$f_M = \frac{\tau_n}{p_r} = \frac{\tau_o}{p_r} + \beta \quad (7)$$

It is seen from formula (7) that the molecular constituent of the friction coefficient increases, when the normal pressure p_r decreases. This fact explains the enhancement of the friction coefficient when the normal loading force reduces (Figs. 4 and 5).

Decrease in the slip rate reduces the temperature of the friction contact, which according to the data in Fig. 7 enhances the molecular constituent f_m and the total friction coefficient f (Fig. 4 and 5).

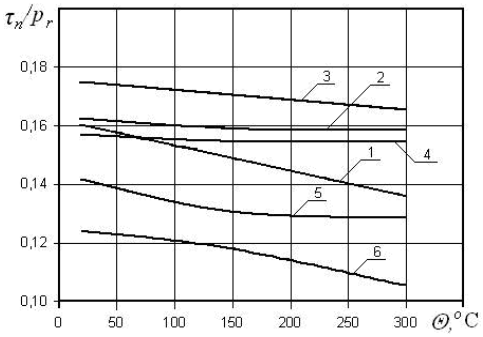

Fig. 7. *Dependence of molecular constituents of the friction coefficient on the temperature for friction couples: 1) AZ91D – Fe-18W-4Cr-1,2V; 2) AZ91D + SiC (S = 5 μm; V = 3%) – Fe-18W-4Cr-1,2V; 3) AZ91D + SiC (S = 11 μm; V = 3%) – Fe-18W-4Cr-1,2V; 4) AZ91D + SiC (S = 11 μm; V = 6%) – Fe-18W-4Cr-1,2V; 5) AZ91D + SiC (S = 15 μm; V = 3%) – Fe-18W-4Cr-1,2V, 6) AZ91D after 2 ECAP passes – Fe-18W-4Cr-1,2V.*

Increase of the friction coefficient after addition of *SiC* powder filling into the magnesium alloy can be explained by enhancement of the deformation constituent of the friction coefficient f_d (Figs. 4 and 5). It is known that in accordance with the mechanical and molecular friction theory [15] the deformation constituent of the friction coefficient is formed by the resisting forces of the deformation roller that runs in front of introduced irregularities to the surface of the softer contacting slipping bodies. The value of the deformation constituent of the friction coefficient f_d depends on the amount of introduced irregularities and their relative introduction can be defined analytically [15] or experimentally as:

$$f_d = f - f_m \quad (8)$$

The calculations of the values of the molecular constituent of the friction coefficient f_m conducted in the comparable conditions on the basis of experimental data given in Figs. 4, 5 and 7 demonstrate that addition of the *SiC* powder filling to the magnesium alloy enhances the value of the deformation constituent f_d from 0.09 to 0.20. The higher the f_d value, the higher the volume and size of *SiC* particles in the magnesium alloy. These particles characterized by high hardness are added to the contact surface of the counterbody, and the deformation constituent and total friction coefficient increase.

Solid *SiC* particles in the form of powder filling provide reduction of the wear rate of the dispersion-strengthened magnesium alloy (Fig. 8 and 9).

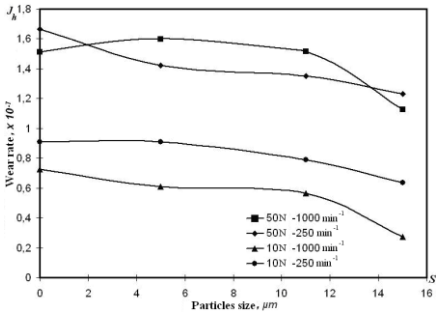

Fig. 8. *Dependence of the wear rate on the size of SiC particles*

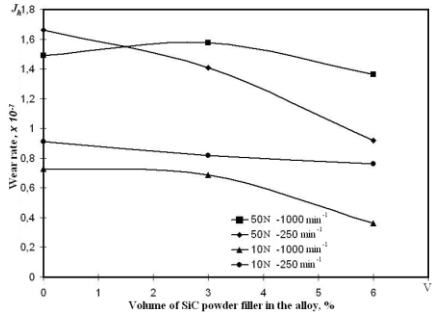

Fig. 9. *Dependence of the wear rate on the volume of powder filling*

It should be noted that the wear rate decreases with the increasing size and volume of the filling particles in the magnesium alloy, as in this case the areas containing hard-wearing *SiC* particles increase. This effect can be observed on babbit bearings. The solid filling is added to the soft matrix of bearings.

The experimental data given in Figs. 6 and 7 testify to the fact that the magnesium alloy *AZ91D* after 2 *ECAP* passes is quite alternative to the composite magnesium alloy strengthened by the powder filling out of *SiC*. The preliminary deformation treatment of the initial magnesium alloy provides lower value of the adhesive constituent of the friction coefficient at a rather high bearing capacity of the frictional contact [16]. As the research results showed (Fig. 6), the bearing capacity of the frictional contact of the material processed by *SPD* technology is comparable with the composite material on the basis of the magnesium alloy *AZ91D* that contains *3% SiC* with an average particle size of *15 μm*.

Conclusion

1. Addition of the powder filling of *SiC* to the magnesium alloy results in enhancement of the integral value of the friction coefficient, as in this case its deformation constituent increases. In the investigated range the normal loading force and the rate of relative slip impact the total value of the friction coefficient as the factors that change its molecular constituent.
2. Addition of the powder filling of *SiC* to the magnesium alloy *AZ91D* results in reduction of the wear rate, as in this case the areas containing hard-wearing *SiC* particles increase.
3. Employment of the magnesium alloy after *ECAP* in the friction knots is promising. The molecular constituent of the friction coefficient reduces significantly with the enhanced bearing capacity of the frictional contact.

References

1. W.C. Harrington Metal matrix composites applications. In: Ochiai S, editor. Mechanical properties of metallic composites. New York: Mercel-Dekker; 1994. 759–73.

2. J.W Kaczmar, K Pietrzak, W. Wlosinski The production and application of metal matrix composite materials// J Mater Process Technol – 2000. V. 106: 58–67.

3. W.M. Yeong Influence of types of reinforcements on properties of magnesium alloy.// Eng. Thesis, National University of Singapore; 2000.

4. S.U. Reddy, N. Srikanth, M Gupta, S.K. Sinha Enhancing the properties of magnesium using SiC particulates in sub-micron length scale// Adv Eng Mater 2004. V. 6. (12):957–64.

5. R.A Saravanan, M.K. Surappa Fabrication and characterization of pure magnesium K30 vol.% SiC particle composite// Mater Sci. Eng – 2000. V. 276. 108–16.

6. N.M. Galdin Color Casting: Reference Book - M.: Mashinostroenie. - 1989.

7. D.N. Reshetov Mechanical Engineering. Vehicle components. Structural strength. Friction, wear, lubrication. V. IV-1- M.: Mashinostroenie. - 1995.

8. R.Z. Valiev, I.V. Alexandrov Bulk Nanostructured Metallic Materials: processing, structure and properties. M.: "Akademkniga", 2007. 398 p.

9. R.Z. Valiev, Y. Estrin, Z. Horita, T.G. Langdon, M.J. Zehetbauer, Y.T. Zhu Producing bulk ultrafine-grained materials by severe plastic deformation. // JOM-2006. 58, No4, p33.

10. S.-J. Huang and H.-W. Liu, 2003, Viscoelastic Analysis for Adhesive Layer of Composite Sandwich Plates//The Chinese Journal of Mechanics. - 2003. Vol. 19. No. 2. pp. 57-68.

S.K Sinha, S.U. Reddy, M. Gupta Scratch Hardness and Mechanical Property Correlation for Mg/SiC and Mg/SiC/Ti Metal–Matrix Composites//Tribology International, 39 (2006), pp.184-189

11. R.Z. Valiev Fabrication of nanostructured metals and alloys with unique properties by severe plastic deformation. Rossiyskiye Nanotechnologii – 2006, V. 1, No. 1-2, pp. 208-216.

12. G.I. Raab To the problem of industrial production of bulk ultrafine-grained materials. High pressure physics and techniques. 2004, V. 15, No. 1 pp.72-80.

13. L.Sh. Shuster Adhesive interaction of metallic solids. - Ufa: Gilem, 1999. 198 p.

14. I.V. Kragelskiy Basis of calculation of friction and wear/ I.V. Kragelskiy, M.N. Dobychin, V.S. Kombalov/ - M.: Mashinostroenie, 1977. 526 p.

15. V.I. Semenov, L.Sh. Shuster, S.V. Chertovskikh, G.I. Raab Influence of the parameter of plastic friction contact and structure of the material on the adhesive bond shear strength // Friction and wear- 2005. V. 26. No.1. pp. 74-79.

PREPARATION AND PROPERTIES OF CARBON ADSORBENTS BASED ON PLANT RAW MARERIALS AND POLYMERIC WASTE

РАЗРАБОТКА ОСНОВ ТЕХНОЛОГИИ АКТИВНЫХ УГЛЕЙ НА ОСНОВЕ ОТХОДОВ ПОЛИМЕРОВ И РАСТИТЕЛЬНОГО СЫРЬЯ

Доц. к.т.н. Нистратов А.В., проф. д.т.н. Клушин В.Н.
alvinist5@gmail.com
Факультет биотехнологии и промышленной экологии –
Российский химико-технологический университет им. Д.И. Менделеева, Россия

Реферат: *Объектом исследования являются отходы полиэтилена, полипропилена и полиэтилентерефталата, поливинилхлорида и полиуретана, подвергаемые утилизации методом пиролиза с растительным сырьём в качестве носителя. Цель исследования – термическая переработка названных отходов в углеродные адсорбенты и анализ их адсорбционных свойств. Комбинации наиболее распространённых полимерных отходов и растительного сырья (древесины, торфа, каменного угля и его кокса) изучены в качестве сырья для получения углеродных адсорбентов. На основе термографического анализа установлен температурный режим пиролиза растительного сырья. Оценено влияние вида сырья и полимерных отходов на выход и показатели пористой структуры результирующих адсорбентов, среди которых определены наиболее качественные образцы.*

КЛЮЧЕВЫЕ СЛОВА: *РАСТИТЕЛЬНОЕ СЫРЬЕ, ПОЛИМЕРНЫЕ ОТХОДЫ, УТИЛИЗАЦИЯ, ПИРОЛИЗ, АДСОРБЕНТЫ*

1. Введение

Настоящие исследования направлены на реализацию государственной стратегии в области утилизации отходов производства и потребления [1], в частности, отходов упаковочных полимеров. Объём образования полимерных отходов в России по разным оценкам составляет 700-900 тыс. т в год, причём в их составе преобладают упаковочные материалы из полиэтилена (ПЭ, 34 %), полиэтилентерефталата (ПЭТФ, 20 %) и полипропилена (ПП, 14 %). Поливинилхлорид ПВХ (пластиковая посуда) и пенополиуретан ППУ (наполнитель мягкой мебели) также составляют заметную часть твёрдых коммунальных отходов. Внедрение с 2019 г. системы раздельного сбора коммунальных отходов будет стимулировать их утилизацию, однако загрязнённая и смешанная часть их не подлежит рециклингу и будет выводиться из оборота.

Утилизация полимерных отходов возможна по нескольким направлениям: механическая, химическая, термическая переработка (пиролиз и сжигание), причём последние целесообразны для неоднородных и загрязнённых полимерных отходов. В отличие от сжигания, пиролиз позволяет получать из таких отходов ещё и жидкое топливо. Перспективным представляется получение углеродсодержащих адсорбентовпутём пиролиза указанных отходов в присутствии минеральных и углеродных носителей, способное повысить рентабельность такой утилизации.

Перечисленные полимерные материалы относятся к термопластичным, не образующим твёрдого остатка при полном термическом разложении. Возможность вовлечения органических отходов в производство композиционных адсорбентов обеспечивает метод ГФХО – пиролиз прекурсора, сопровождающийся «газофазным физико-химическим осаждением» и карбонизацией его продуктов (пиролитического углерода) на пористых минеральных носителях – силикагелях, глинах, цеолитах [2]. Применительно к полиуретановым отходам описанный процесс, названный «гетерогенным вторичным пиролизом» [3], исследован в присутствии активного угля и твёрдого продукта пиролиза самого полиуретана как носителей. Результатом явились изменение состава жидких продуктов пиролиза и образование дополнительного количества угля на поверхности носителей, однако полученные материалы не рассматривались как адсорбенты. С этой целью возможно использование и богатых углеродом материалов из растительного сырья – древесины, торфа, каменного угля и кокса.

2. Экспериментальная часть

Изучаемые отходы (прекурсоры) включают нарезанные на полосы фасовочные пакеты из прозрачного полиэтилена марки ПЭНП, куски посуды из полипропилена и бутылок из полиэтилентерефталата размером до 2 см, а также стружку белого ПВХ и порошок ППУ. В качестве носителей в работе использованы достаточно дешёвые материалы растительного происхождения: сосновые опилки, верховой осоковый торф месторождения «Красный мох» Тверской области, каменноугольная шихта АО «Москокс», металлургический (ГОСТ 3340-88) и пековый коксы (ГОСТ 3213-91).

Термографический (термогравиметрический) анализ изучаемых растительных материалов был произведён с целью обоснования режима их пиролиза. Измерения выполнены на дериватографе Q-1200 фирмы МОМ (Венгрия) при нагревании измельчённых воздушно-сухих образцов до 900 °С в течение 100 мин в атмосфере азота (чувствительность гальванометров ДТГ и ДТА – 1/10). Масса образцов и диапазон шкалы массы G указан в дериватограммах на рис. 1.

Исходя из распространённой на практике конструкции пиролизной печи с ретортой (камерой) в лаборатории подобные условия смоделированы в закрытом негерметично фарфоровом тигле в муфельной электропечи с регулированием температуры.

Предварительно взвешенное сырьё (высушенный растительный материал сырьё + полимерный отход в массовом отношении 1 : 1) загружают в виде смеси в закрытый фарфоровый тигель. Его устанавливают в муфельную печь и задают прараметры пиролиза (скорость нагрева, конечную температуру и время выдержки), запускают установку, работающую автоматически. После завершения пиролиза тигель с продуктами остужают до комнатной температуры. Затем твёрдый продукт взвешивают и по отношению его массы к массе сырья вычисляют выход адсорбента. Также оценивают содержание пиролитического углерода как изменение массы адсорбента в присутствии в сырье полимерного отхода.

3. Результаты и их обсуждение

3.1. Термографический анализ растительного сырья

Дериватограммы и количественные параметры выполненных исследований приведены на рис. 1*а-е* и в табл. 1.

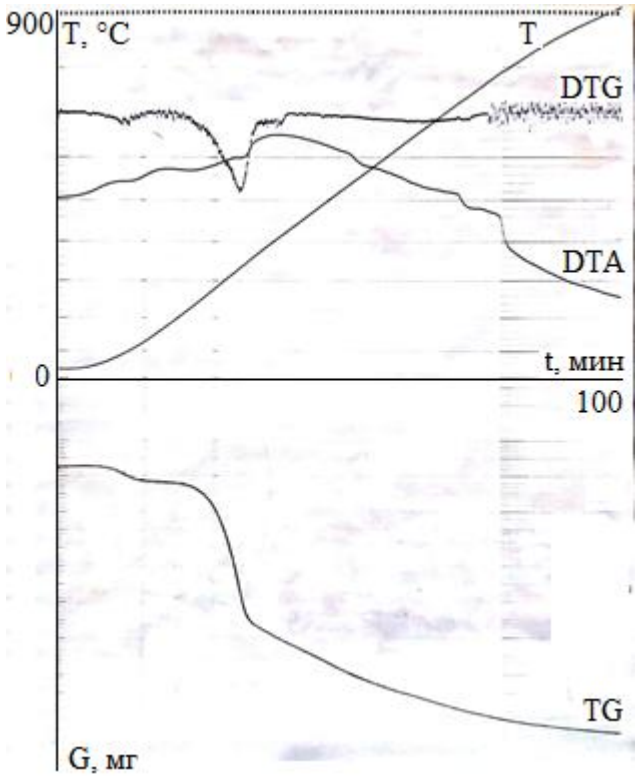

а – сосновые опилки:
навеска 141 мг, шкала G 200 мг

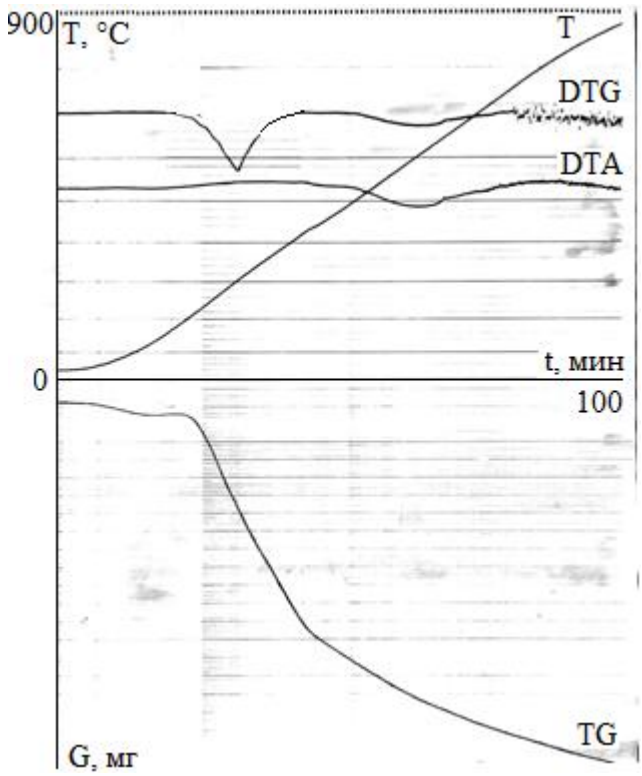

б – торф:
навеска 323 мг, шкала G 200 мг

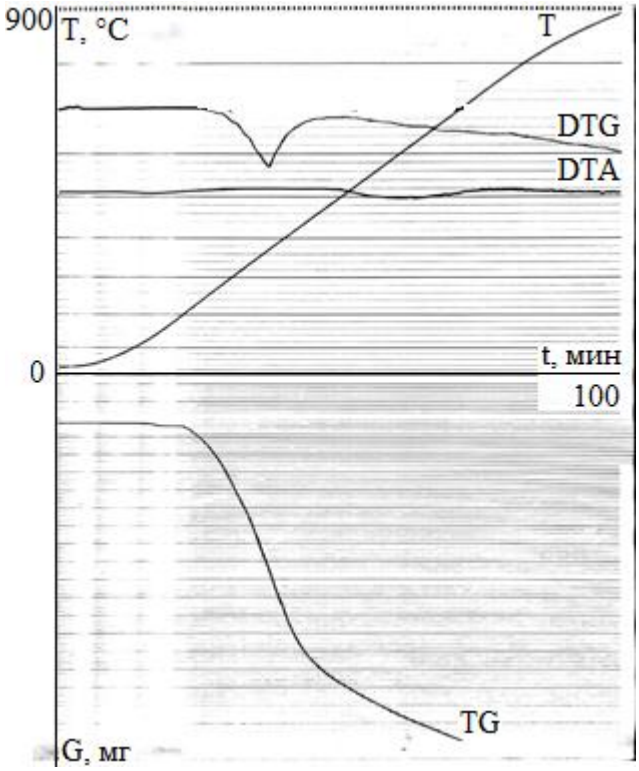

в – бурый уголь:
навеска 364 мг, шкала G 200 мг

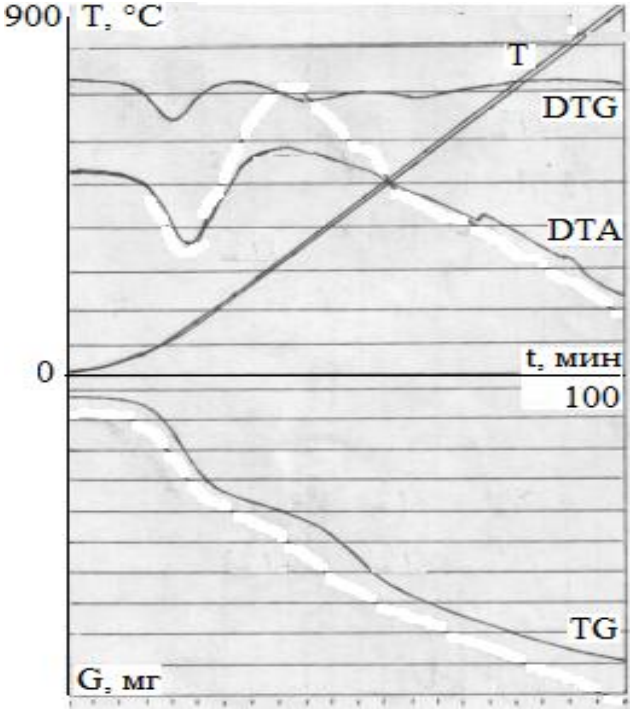

г – каменный уголь
(Мьянма):
навеска 821 мг, шкала G 500 мг

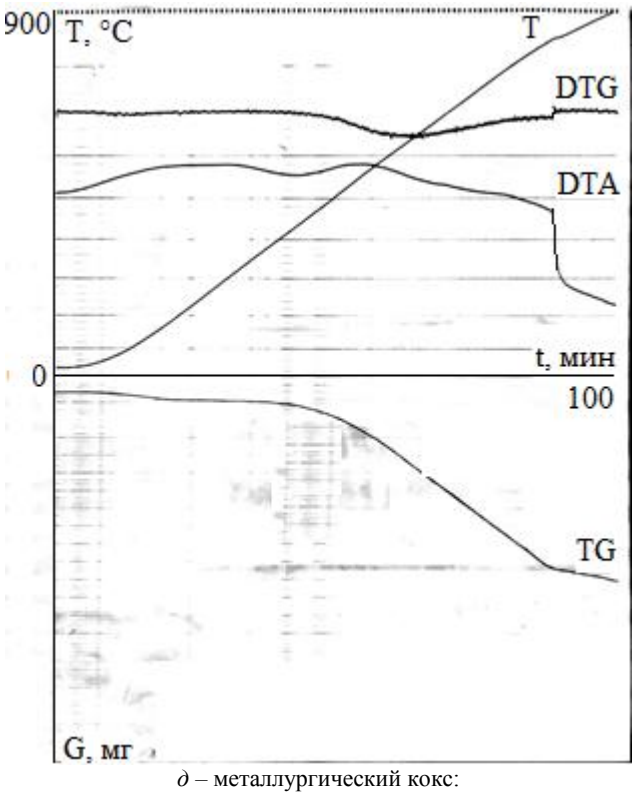

д – металлургический кокс:
навеска 749 мг, шкала G 200 мг

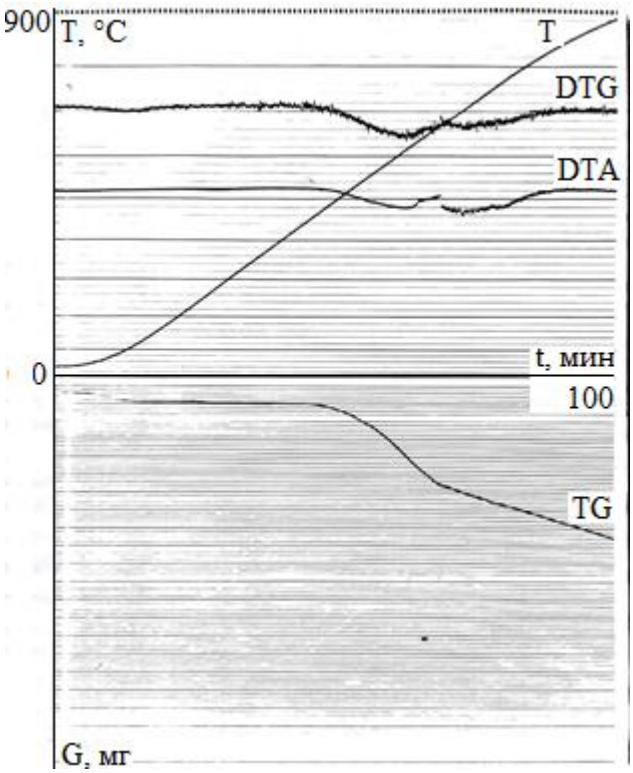

е – пековый кокс:
навеска 619 мг, шкала G 200 мг

Рис. 1. *Дериватограммы пиролиза растительных материалов*

Таблица 1 *– Данные термографического анализа растительного сырья*

Сырьё	Масса, мг		Остаток(%) при температуре ,°С				Температуры наиболее интенсивной потери массы,°С	Вид остатка в тигле прибора при остывании
	начальная	конечная	300	500	700	900		
опилки	141	0,4	73	22	6,4	0,3	200-370	чёрные пылинки
торф	323	6,1	78	53	44	1,9	160-420	коричневые рассыпчатые комки
бурый уголь	364	37	90	59	50,5	10	240-460	коричневые частицы и порошок
каменный уголь	821	391	80,5	65,5	52,5	47,6	60-240 и 260-500	чёрные твёрдые частицы
металлургич. кокс	749	638	99	98	92	85	450-820	чёрный рыхлый порошок
пековый кокс	619	395	99	98	90,5	64	430-650	чёрный рыхлый порошок с усадкой

Изучаемые материалы различаются характером термического разложения при пиролизе в инертной среде. Следует отметить, что термостойкость (выход твёрдого остатка при данной температуре) их ожидаемо повышается по мере превращения растительной массы в углеродный материал. Для всех материалов кроме каменного угля характерна одна ступень разложения, т.е. интервал интенсивной потери массы, но при переходе от древесины к коксу он смещается к большим температурам. Обычно эти процессы сопровождаются поглощением тепла (отрицательные пики DTA), но в случае опилок – выделением (рис. 1*а*). Констатировано, что основные превращения не коксованных материалов происходят до 500 °С, выход карбонизатов при этом за исключением опилок превышает 50 масс. %, при 700 °С он ниже на 9-15,6 %. Дальнейшее нагревание сопровождается плавной потерей массы без выраженных тепловых эффектов.

Полученные промышленно из каменного угля виды кокса, естественно, относятся к термостойким материалам, заметное разложение которых (потеря массы более 2 %) протекает лишь при 500-900 °С (табл. 1). Карбонизат каменного угля имеет наиболее практичную зернёную форму, остальные материалы образуют порошковые продукты.

Рекомендуемые [4] температуры пиролиза (карбонизации) весьма сходны для каменного угля, торфа и древесины – 500-750 °С. Температуры деструкции изучаемых полимеров, наоборот, различны [5]: для ПЭ, ПП, ПЭТФ, ПВХ составляют >300, 200-300, >800, >400 °С соответственно. Поэтому получение адсорбентов из смесей данных материалов проведено при фиксированной температуре 500 °С (для ППУ - 350 °С). Скорость нагрева для медленной карбонизации задана 5 °С/мин, выдержка при конечной температуре – 0,5 ч.

Пиролиз древесины и торфа хорошо изучен [например, 6], парогазовые продукты пиролиза представлены водой, диоксидом углерода, метаном, алкенами, спиртами, кислотами, смолами. Каменные угли при пиролизе (коксовании) образуют полиароматические соединения, бензол и его производные, а также воду, метан и водород.

3.2. Выходы углеродных адсорбентов

Внешний вид полученных адсорбентов на основе названного сырья и полимерных материалов изображен на рис. 2. Согласно фотографиям рис. 2 наиболее макропористыми материалами после пиролиза являются опилки и кокс. Изучение их пористой структуры приведено ниже в табл. 4.

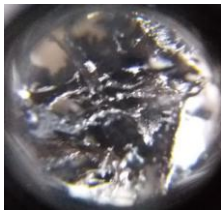

а - опилки

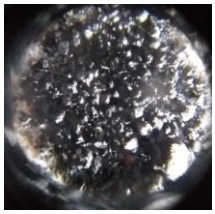

б – торф

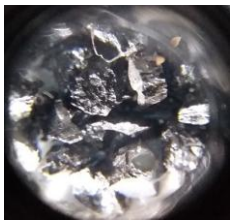

в – каменный уголь

г –кокс

Рис. 2. *Изображения углеродных адсорбентов на основе растительного сырья (увеличение х60)*

Табл. 3 *– Показатели выхода адсорбентов*

Сырье	Масса сырья, г	Масса адсорбента, г	Выход адсорбента, %	Выход адсорбента от массы носителя, %	Изменение массы адсорбента, %
Опилки	1,5	0,37	24	24	-
Опилки + ПЭ	1,5	0,26	17	34	10
Опилки + ПП	1,45	0,24	16	32	8
Опилки + ПЭТФ	1,47	0,38	26	52	28
Опилки + ПВХ	5,07	1,72	34	68	44
Опилки + ППУ	1,66	0,75	45	90	66
Торф	3,1	1,54	50	50	-
Торф + ПЭ	2,72	0,87	32	64	12
Торф + ПП	1,66	0,35	21	42	-
Торф + ПЭТФ	1,57	0,45	27	54	4
Торф + ППУ	2	1,30	65	130	80
Металл. кокс + ПЭ	3,08	1,61	52	104	4
Пековый кокс + ПЭ	3,08	1,7	55	110	10
Каменный уголь	2,32	2	84	84	-
Уголь + ПЭ	3,08	1,85	60	120	36
Уголь + ПП	3,08	1,77	57,5	115	31
Уголь + ПЭТФ	3,08	1,68	54,5	109	25
Уголь + ППУ	3,08	1,90	62	124	40
Уголь + ПВХ	3,08	1,85	60	120	36

Выходы целевых продуктов пиролиза сырья – адсорбентов – охарактеризованы в табл. 3 отношениями их массы к массам самого носителя, его смеси с отходами и изменением массы адсорбента в присутствии в сырье различных полимеров (последний показатель оценивает содержание в адсорбенте пироуглерода из прекурсора). В условиях опыта оба вида кокса не меняют массу, каменный уголь разлагается лишь на 16 %, торф теряет 50, а древесина – 76 % массы. Содержание в полученных адсорбентах пироуглерода, нанесённого на них при разложении полимеров, варьируется в широких пределах (табл. 3). Так, каменный уголь осаждает 25-40 % массы полимера, торф – от 4 до 80 %, опилки – от 8 до 66 %; остальная часть образует парогазовые продукты. Заметно, что термопластичные полимеры (ПЭ, ПП, ПЭТФ) обеспечивают привес адсорбентов гораздо меньший, чем термореактивные ПВХ и ППУ. Т.е. последние способствуют образованию целевого продукта, но надо иметь в виду пониженную температуру пиролиза (350 °С для ППУ).

3.3. Пористая структура адсорбентов

Характеристики пористой структуры материалов отражены в табл. 4 в виде объёмов пор, сорбирующих вещества с различным размером молекул: H_2O (субмикропоры) $<C_6H_6$(микро- и мезопоры) $<CCl_4$ (мезопоры).

Анализ показателей исходного и карбонизованного при 500 °С сырья без добавок выявляет, что при пиролизе развиваются преимущественно микро- и мезопоры, сорбирующие органические вещества. Микропоры, сорбирующие воду, наиболее развиты у образца из опилок, мезопоры, поглощающие CCl_4 – у образца из торфа. Карбонизат каменного угля и коксов остаётся низкопористым.

Совместный пиролиз сырья и полимеров в большинстве случаев приводит к развитию их пористой структуры. Предположительно это происходит по механизму сужения существующих пор носителя за счёт покрытия их слоем пироуглерода [7]. Для адсорбентов на основе опилок и термопластичных полимеров появляются новые микропоры, объём которых рекордный для ПП (табл. 4), для ПЭТФ и ПВХ – также мезопоры. Наилучший образец из опилок и ПП по объёму микропор (0,523 – 0,025 = 0,498 $см^3/г$) превосходит активный уголь из берёзовой древесины БАУ (0,22-0,25 $см^3/г$). Однако на примере ППУ видно, что эффект отложения пироуглерода может быть избыточным – объёмы всех пор соответствующего адсорбента уменьшены относительно карбонизата опилок.

Таблица 4 *– Показатели пористой структуры адсорбентов*

Сырье	Объем сорбирующих пор ($см^3/г$) по парам		
	H_2O	C_6H_6	CCl_4
Исходные опилки	0,152	0,032	0,014
Опилки	0,144	0,102	0,049
Опилки + ПЭ	0,17	0,314	0,047
Опилки + ПП	0,361	0,523	0,025
Опилки + ПЭТФ	0,320	0,241	0,118
Опилки + ПВХ	0,328	0,238	0,146
Опилки + ППУ	0,025	0,039	0,024
Исходный торф	0,077	0,114	0,011
Торф	0,103	0,136	0,169
Торф + ПЭ	0,052	0,073	0,065
Торф + ПП	0,195	0,104	0,069
Торф + ПЭТФ	0,052	0,261	0,075
Торф + ППУ	0,058	0,082	0,023
Каменный уголь	0,056	0,031	0,018
Уголь + ПЭ	0,018	0,032	0,021
Уголь + ПП	0,017	0,018	0,021
Уголь + ПЭТФ	0,029	0,033	0,027
Уголь + ППУ	0,021	0,020	0,023
Металл. кокс + ПЭ	0,010	0,008	0,011
Пековый кокс + ПЭ	0,017	0,018	0,016
Уголь + ПВХ	0,015	0,024	0,029

Для адсорбентов на основе торфа результирующая структура зависит от строения полимера: максимальный объём субмикропор обусловлен добавкой ПП, микро- и мезопор по бензолу – добавкой ПЭТФ. Последний образец обладает способностью преимущественно поглощать органические растворители по сравнению с водой (табл. 4). Взаимодействие торфа с ППУ при пиролизе также снижает показатели продукта. Положительные изменения пористой структуры адсорбентов на основе древесины и торфа соотносятся с содержанием в них пироуглерода 4-28 % (табл. 3).

Все адсорбенты на основе каменного угля и полученных из него коксов несмотря на макропоры (рис. 2*г*) и осаждение 4-40 % пироуглерода обладают низкими показателями пористой структуры, часто уступающими карбонизованным материалам. Их единственное преимущество – более высокая прочность зёрен.

4. Заключение

В данной работе изучено пиролитическое разложение древесины, торфа, бурого и каменного угля и кокса, обоснован температурный режим их переработки с полимерными отходами при 500 °С, найдены выходы целевого продукта пиролиза, определены показатели пористой структуры сырья и его карбонизатов.

Выявлено влияние совместного пиролиза сырья и полимеров в соотношении 1 : 1 на показатели пористой структуры адсорбентов: добавки полиэтилена, полипропилена, полиэтилентерефталата обеспечивают повышение объёмов сорбирующих пор по H_2O, C_6H_6, CCl_4. Максимальный объём пор по бензолу образца на основе опилок и полипропилена (0,52 $см^3/г$) превосходит таковой большинства промышленных активных углей. Каменный уголь и кокс не образуют пористых адсорбентов в сочетании с любыми полимерами.

Нахождение наилучших условий синтеза изучаемых адсорбентов требует варьирования соотношения компонентов и температуры пиролиза. Для низкопористых адсорбентов на основе угольных материалов можно рекомендовать парогазовую активацию.

5. Ссылки

1. Стратегия развития промышленности по обработке, утилизации и обезвреживанию отходов производства и потребления на период до 2030 года. Распоряжение Правительства РФ от 25.01.2018 № 84-Р.

2. Елецкий П.М. Дисс. к.х.н. Новосибирск: Институт катализа им. Г.К. Борескова СО РАН. 2009. 115 с.

3. Takamoto D.Y., Petrich M. A. Effect of Heterogeneous Secondary Pyrolysis Reactions on the Thermal Decomposition of Polyurethane Scrap. Ind. Eng. Chem. Res. 1994. V. 33. P. 3004-3009.

5. Мухин В.М., Клушин В.Н. Производство и применение углеродных адсорбентов: учеб. пособие. М.: Российский химико-технологический университет им. Д. И. Менделеева, 2012. 308 с.

5. Устинов В.А., Козлита А.Н., Люлькин М.С. Выбор температурного режима в аппарате пиролиза на основе химии процесса. Нефтегазовое дело. 2011. № 3. С. 208-214. Электронный журнал: http://www.ogbus.ru.

6. В.И. Касаточкин, Н.К. Ларина. Строение и свойства природных углей. М.: Недра 1975. 160 с.

7. Dabrowsky A., Tertykh V.A. Adsorbtion on new and modified inorganic sorbents. Amsterdam, 1996. P. 115-146.

GEOPOLYMERS BASED ON BULGARIAN RAW MATERIALS – PRELIMINARY STUDIES

Ass. Prof. Dr. Eng. Nikolov A.[1]
[1]Institute of Mineralogy and Crystallography, Bulgarian Academy of Science (IMC-BAS), Sofia, Bulgaria
E-mail: drsashko@imc.bas.bg

Abstract: *The geopolymers are novel class of inorganic polymer materials consist of chains, sheets or networks made of covalently bonded mineral molecules. The main precursors of the geopolymers are reactive alumosilicate material and hardener solution. Various suitable raw materials are located in Bulgaria. The present paper shows successful examples of geopolymers based on Bulgarian raw materials – fly ash, metakaolin, natural zeolite and iron-rich waste from copper industry. The properties and structure of the prepared geopolymers greatly depend on the composition and type of the raw material, as well as concentration and type of the activator solution. The results show the potential of geopolymers based on Bulgarian raw materials as building materials.*

Keywords: GEOPOLYMER, METAKAOLIN, FLY ASH, IRON-SILICATE FINES, IRON-RICH, NATURAL ZEOLITE, CLINOPTILOLITE, MICROSTRUCTURE

1. Introduction

Geopolymers are novel class of inorganic materials consist of chains or networks of mineral molecules linked with co-valent bonds. The geopolymer is an X-ray amorphous material at ambient and medium temperature [1]. The geopolymers have also been described in the academic literature as 'mineral polymers', 'inorganic polymers', 'inorganic polymer glasses', 'alkali-bonded ceramics', and a variety of other terms [2]. First the French scientist Joseph Davidovich coined the term 'geopolymer" in 1978 when he mixed sodium hydroxide and kaolin clay. The actual breakthrough was done years later when metakaolin was used for the first time. Since then up to nowadays, metakaolin is the most common geopolymer precursor [3]. The geopolymers are two component system. The main precursor is usually (but not always) alumosilicate powder material. The three most common raw material classes used in geopolymerization are metakaolin, slags and coal fly ashes. In addition to the reactive solid components a hardening solution, so called 'activator', is required to initiate the geopolymerisation reaction. The mechanism of geopolymerisation is described in several overlapping stages: dissolution of the precursor; special equilibrium, gelation, reorganization, polymerization and hardening [4]. The main difference between Portland cement hardening mechanism is the role of the water. In conventional cements the water react with the cement particles and the main products of the reaction are hydrates (C-S-H). Other hand, in geopolymerisation the water provides workability and ensures the contact between the particles. After condensation water is out of the structure or stays into the pores. The hardened geopolymer material possess properties similar to Portland cement and ceramic products. The wide variety of potential application includes: fire-resistant materials, thermal insulations, cements, concretes, resins, low-tech building materials, low-energy ceramic tiles, refractory and foundry items, high-tech composites, radioactive and toxic waste immobilization, decorative elements, etc.

Important characteristics of the raw materials in order to prepare geopolymers are: high Si and Al content, and their reactivity - the rate of dissolution of the Si and Al in the first stage of geopolymer process. The reactivity correlates with the structure– amorphous structure more easily dissolves and reorder, while crystalline structure stays inert. The reactivity also depends on the size and type of the particles, which are important features that govern also the rheology of the fresh mixture and water demand. Many raw materials and industrial by-products with Bulgarian origin meet the criteria above. Kaolin clay deposits are located near Vetovo and Kaolinovo. A few years ago Kaolin AD started production of calcined clay – metakaolin. Huge deposits of natural zeolite, perlite and bentonite are located in East Rhodope Mountain. Additionally, vast amount of industrial waste has been generated by local plants and metal producers. The biggest copper producer in South-East Europe (Aurubis) is located in Bulgaria. After flotation process fine iron-rich tailing remained and disposed in landfills. The former steel producing plant Kremikovtsi generated huge amount of blast furnace slag. Many thermal power plants are still operating and produce fly ashes – TPP Maritsa East, TPP Bobov dol, Brikel, TPP Ruse, TPP Sliven, etc. Some of the industrial by-products find application mostly in cement industry, road pavement and embankments. Still huge amount stay unutilized and disposed in landfills. There economic, environmental and social benefits of utilization of industrial waste.

The present paper describes results with geopolymers prepared from Bulgarian raw materials – metakaolin, iron-silicate fines, fly ash and natural zeolite.

2. Experimental

3.1. Method of analysis

The powder XRD patterns were obtained by Bruker D-2 Phaser diffractometer with Bragg-Brentano geometry using a CuKα source. SEM images were obtained with different magnification by using electron microscope – SEM 515 Philips.

2.2. Materials

The metakaolin was provided by Kaolin AD, Bulgaria. The wet residue of the material was 0.40% on 45μm. The iron-silicate fines are industrial by-product from local copper plant (Aurubis, Bulgaria). The iron-rich precursor was dried to constant mass in oven at 105°C. Fly-ash class F from TPP Maritsa East 2, Bulgaria. The chemical composition of the used precursor is presented in table 1.

Table 1 *Chemical composition of the geopolymer precursors*

	SiO_2	Al_2O_3	CaO	K_2O	MgO	Fe_2O_3	Na_2O	TiO_2	MoO_3	PbO	SO_3
Metakaolin	53.9	43.2	0.15	0.62	0.09	1.14	0.11	0.74	-	-	0.014
Iron-silicate fines[5]	29.34	4.4	2.66	0.71	0.89	58.2	0.58	0.3	0.27	0.37	-
Fly ash [6]	52.66	23.37	5.75	-	2.75	8.72	-	-	-	-	5.75
Natural Zeolite	69.4	10.3	3.02	2.72	0.99	0.98	0.39	0.17	-	-	-

The activator solutions were prepared by using solid KOH pellets, sodium silicate ($SiO_2/Na_2O=3$) and tap water. The ingredients were mixed by magnetic stirrer and tempered prior usage as activator

2.3. Geopolymer synthesis

The geopolymer precursor and activator solution were mixed and homogenized with mechanical stirrer for 1 min. The mixtures were rested to mature for 5 min, then mixed again for 30 seconds. The fresh geopolymer paste was moulded in polypropylene cylindrical moulds (50x30mm). The samples are stored in plastic bags and cured at laboratory conditions (20^{o}C).

3. Results and Discussion

3.1. Geopolymer based on metakaolin

Five series of geopolymer specimens were prepared. The samples were demoulded after 24 hours of curing and placed in laboratory conditions (20^{o}C and 65% relative humidity). At 28-th day compressive strength was determined by using three specimens of each series. The composition and results from compressive strength is presented in Table 2. Series MM1 showed maximal strength.

Table 2 Molar composition and compressive strength (28-th day) for geopolymers based on metakaolin

	MM1	MM2	MM3	MM4	MM5
SiO_2/Al_2O_3	3.55	3.55	3.55	3.55	3.29
H_2O/M_2O	15	13	17	11.6	14.6
M_2O/Al_2O_3	1	1.2	0.85	1	1
Compressive strength, MPa	33.7	27.8	31.5	30.3	20.6

The metakaolin and geopolymer series MM1 was examined by Powder X-ray diffraction. The results are presented in Fig. 1. Both metakaolin and geopolymer MM1 showed amorphous structure with inclusion of quarts. The amorphous halo shifted after geopolymerisation from 15-30 2θº to 22-35 2θº, which is typical for geopolymers. The crystalline quarts stayed inert.

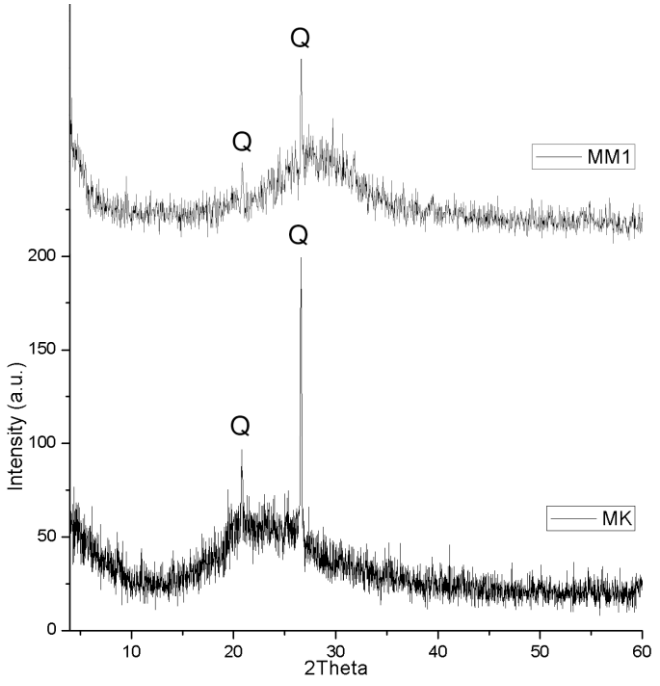

Fig. 1 *Powder X-ray diffraction patterns of metakaolin (MK) and obtained geopolymer (series MM1). Q- quarts*

The chemical purity of metakaolin is very high, represented almost entirely by SiO_2 and Al_2O_3, which helps to investigate the ongoing reactions in the synthesis of geopolymers and the analysis of the results. Bulgarian Metakaolin from Kaolin AD has sufficient reactivity and is a potential raw material for the production of geopolymers.

3.2. Geopolymer based on iron-rich waste from copper industry

Five series of geopolymer specimens were prepared with water to solid ratio equal to 0,15. The samples were cured at laboratory conditions in plastic bags until 10^{-th} day, when were placed in oven for 12 days at 80^{o}C. At 22^{-th} day the specimens were demoulded and placed at laboratory conditions (20^{o}C and 65% humidity). At 90^{-th} day compressive strength was determined by using three specimens of each series. The composition and results from compressive strength is presented in Table 3. Series 15F2 and 15F3 showed highest strength. Both results are similar, but 15F3 was obtained by lower concentration of the activator solution.

Table 3 *Molar composition and compressive strength (90-th day) for geopolymers based on iron silicate fines*

	15F1	15F2	15F3	15F4	15F5
Al_2O_3/M_2O	0.32	0.32	0.5	0.22	0.22
H_2O/M_2O	7.59	7.64	11.4	5.46	5.36
Fe_2O_3/M_2O	2.5	2.5	4	1.75	1.75
Compressive strength, MPa	19.36	27.96	27.53	3.87	3.5

The results from powder X-ray diffraction showed the mineral composition of the iron-silicate fines. It contains mostly fayalite and magnetite (Fig. 2). Minor changes between raw material and obtained geopolymer (series 15F3) were observed.

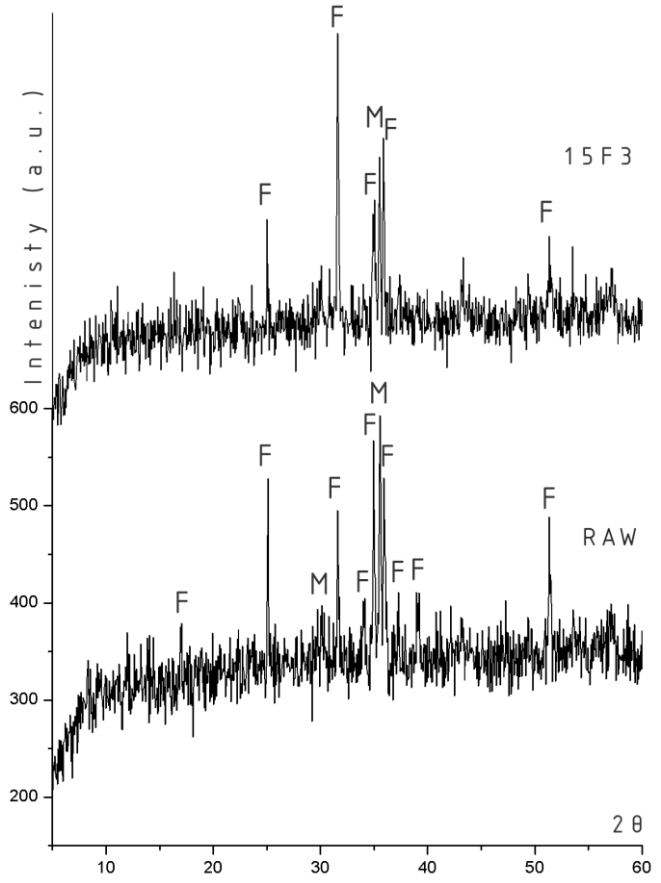

Fig. 2 *Powder X-ray diffraction patterns of iron silicate fines (RAW) and obtained geopolymer (series 15F3). M- Magnetite, F – fayalite.*

The presented studies showed that geopolymer technology is capable to reduce the huge amounts of fayalite slag generated for the last decades as a result of copper production.

3.3. Geopolymer based on fly ash

In previous study [7] four series of geopolymers were prepared using different concentration of the alkaline hardener solutions and water to solid ratio equal to 0.40 (w/w). The series B1 with following molar ratio: $M_2O/Al_2O3=1.4$, $H_2O/M_2O=10$ showed lowest absorption to water – 20.0%. Thus the obtained geopolymer showed high porosity which motivated the research team to develop highly porous lightweight geopolymer by addition of 1% by mass H_2O_2 as gas forming agent (***Fig. 3***). The decomposition of the peroxide produce oxygen, which form small interconnected pores. The resulted porous geopolymer was characterized by 0.44 g/cm^3 density, 2.64 g/cm^3 absolute density and 83.3% relative porosity. Preliminary fire-resistance test of the material was examined. Simple jet-torch test was conducted to observe the behavior of the porous geopolymer at high temperature and direct fire. The lightweight geopolymer was exposed to direct fire from butane jet-torch for 3 minutes at 5 cm distance. During the fire exposure the color of the specimens in the hottest area turned into red-orange, which is associated to temperature about 1000^{o}C. After the fire test the specimen preserved its integrity, which indicates its potential as fire-resistance materials.

The raw fly ash, light-weight geopolymer and fired samples were examined with SEM. The fly ash contained cenosphere, which contributed to better workability of the fresh geopolymer mixture (*Fig. 4*). There were cracks on the hardened geopolymer before and after the fire test (*Fig. 5**Fig. 6***). The particles of the fly ash contains small micron-sized pores. The presence of such micro pores provides a road of escape for hot gases generated by the elevated temperature.

It can be concluded that mixing fly ash from Maritsa TPP with a suitable activating solution lead to formation of geopolymer material characterized relatively large porosity. Lightweight geopolymers could be also successfully prepared by using suitable gas forming agent. The fire torch test indicates the potential as fire-resistance materials.

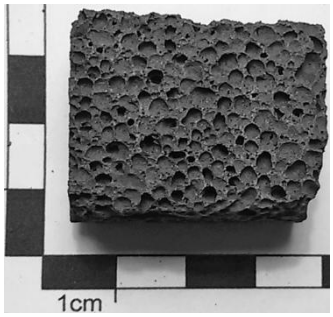

Fig. 3 *Lightweight geopolymers based on fly ash*

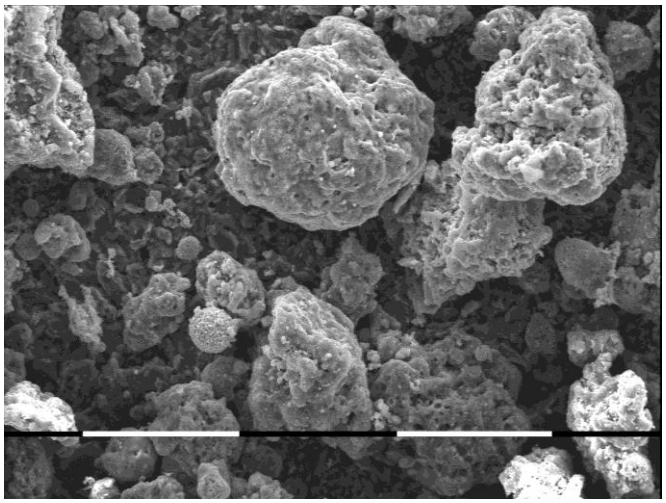

Fig. 4 *SEM image of used fly ash from Maritsa East 2 (marker- 100μm)*

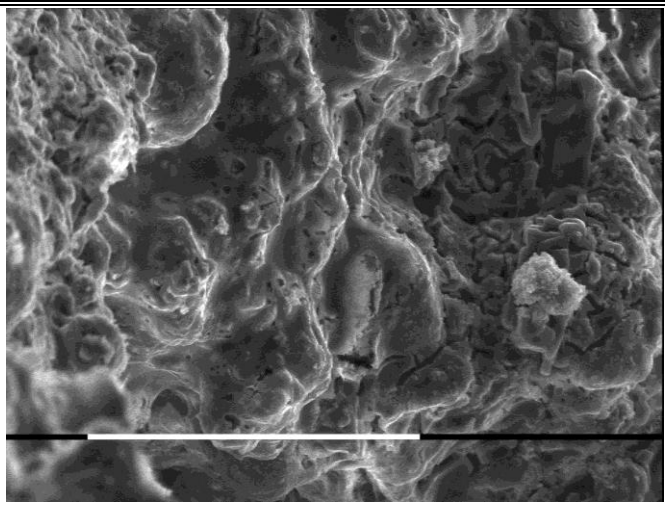

Fig. 5 *SEM image of geopolymer based on fly ash from Maritsa East 2 (marker- 10μm)*

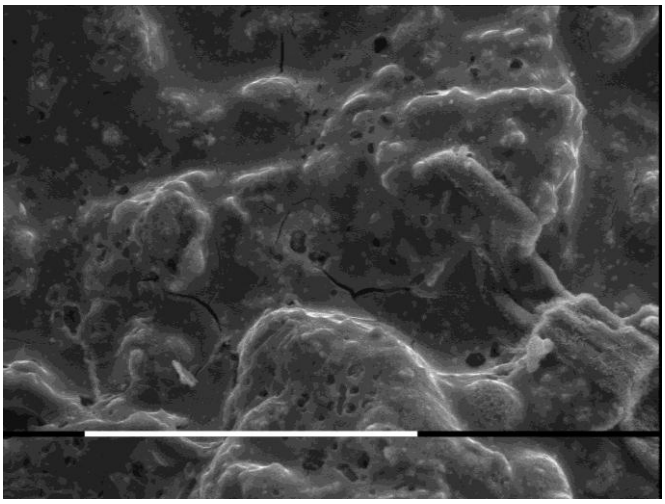

Fig. 6 *SEM image of fired geopolymer based on fly ash from Maritsa East 2 (marker- 10μm)*

3.4. Geopolymer based on natural zeolite (review)

In-depth studies on possibility of using natural zeolite clinoptilolite from local large deposit Beli Plast were done within the PhD thesis of Nikolov, A. [8]. The optimal results were obtained using activator solution - mixture of potassium hydroxide, sodium silicate (molar ratio modulus $MR=SiO_2/Na_2O=3$) and water. However, the obtained material hardens slowly at normal temperature. Demoulding was possible after at least one week at 20^{o}C. The hardened geopolymer activated with silicate activators showed high shrinkage. However, applied in thin layers as coating the material did not showed shrinkage cracks. The adhesion to concrete was significant – over 2MPa [9]. Thus geopolymer based on natural zeolite are suitable for plasters or coatings.

The effect of modulus of sodium silicate was investigated. Using higher modulus of water-soluble sodium silicate (WG3) leads to bigger rate of strength gain. Geopolymers obtained with WG2 showed higher final strength and slightly higher degree of geopolymerization. However, due to the crystallinity of the natural zeolite the alkali concentration of the used sodium silicate reagents solution (MR= 2÷3) were not sufficient to dissolve the raw material. Thus, using sodium silicate solution with MR above 2 leads to certain quantity unreacted clinoptilolite, which preserves the beneficial properties of the clinoptilolite per se.

The calcination of the natural zeolite at 900 °C leads to full dehydroxylation of the clinoptilolite structure thus transforming the natural zeolite into 'metazeolite'. The shrinkage of the hardened geopolymer was reduced twice and the compressive strength

increase 3 times when calcined zeolite (metazeolite) was used as a geopolymer precursor instead of natural zeolite [10].

4. Conclusion

The presented studies showed that Bulgarian raw materials could be successfully used as geopolymer precursor. The properties and structure of the prepared geopolymers greatly depend on the composition and type of the raw material, as well as concentration and type of the activator solution. Further more detailed studies are needed to develop materials with practical application.

5. Acknowledgement

The results in this work have been achieved in fulfilment of a project financed by the National Science Fund of Bulgaria under contract No. DM17/3 from 12.12.2017.

6. Literature

[1]. Davidovits, J., Geopolymer chemistry and applications, 2011.
[2]. Provis, J.L. and J.S.J. Van Deventer, Geopolymers: structures, processing, properties and industrial applications, Elsevier, 2009.
[3]. Davidovits, J., Chemistry of Geopolymeric Systems, Terminology, Proceedings of 99 International Conference. eds. Joseph Davidovits, R. Davidovits & C. James, France, 1999.
[4]. Duxson, P., et al., Geopolymer technology: the current state of the art. Journal of materials science, 2007. 42(9): p. 2917-2933.
[5]. A. Nikolov, R.T., N. Velinov, Z. Delcheva, B. Chen, Characterization of a novel acid-activated geopolymers based on fayalite slag from local copper industry, Sofia, Seventh National Crystallographic Symposium with International Participation. 2018, p. 54–61.
[6]. Zgureva, D. and S. Boycheva. Comparative studies on the zeolitization of fly ash from different Bulgarian power plants TPP "AES Galabovo" and TPP "Maritza East 2", Proceeding of XXth International Conference of Faculty of Power Machines and Power Engineering. 2015, p. 54–61.
[7]. Nikolov, A. and B. Barbov, Lightweight geopolymer based on fly ash, Review of the Bulgarian Geological Society, 2018. 79(part 3), p. 23-24.
[8]. Nikolov, A., Geopolymers based on natural zeolite for construction applications, composition, structure, properties 2016, Sofia ,University of Architecture, Civil Engineering and Geodesy.
[9]. Nikolov, A., I. Rostovsky, and H. Nugteren, Geopolymer materials based on natural zeolite. Case Studies in Construction Materials, 2017, 6, p. 198-205.
[10]. Nikolov, A., I. Rostovsky, and H. Nugteren, Natural and calcined zeolite (metazeolite) based geopolymers. Peer reviewed short communications of the national conference with international participation, 2017, p. 31-32.

CRACK RESISTANCE EVALUATION FOR Al+3.5% Mg ALLOYS BY MEASURMENTS OF ULTRASONIC VELOCITIES AND HARDNESS

Assoc. Prof. PhD Alexander Popov[1], PhD. Eng. Georgy Dobrev[2],

[1] Institute of Mechanics - BAS, Sofia, Bulgaria
[2] Institute of Metal Science, Eqipment, and Technologies - BAS,Sofia, Bulgaria,
E-mail: alpopov@abv.bg ; dobrevbg@mail.bg,

Abstract: *The crack resistance in fracture mechanics is defined as critical value of stress intensity factor in the plane-strain fracture toughness. A mechanical test is used to assess it under certain conditions. This is a complicated, long and expensive procedure. In practice, it is of interest to determine the crack resistance for construction elements by means non-destructive evaluations (NDE).*
KEY WORDS*: CRACK RESISTANCE, Al + 3,5 % Mg ALLOYS, ULTRASONIC VELOCITIES, HARDNESS*

1. Introduction

The ability of the material to resist of the cracks propagation in the body is called crack resistance - K_{Ic}

Conventional crack resistance testing

In the fracture mechanics [1-5] the value of crack resistance K_{Ic} is named "fracture toughness" for plane deformation [1-5]. The value of K_{Ic} by means mechanical testing [1,2], according , ASTM E 399:2017 (USA) or GN 25.506–85 (Russia) is determined. For aluminum alloys, ASTM B 645-10:2015 (USA), is used. The condition for mechanical testing is

(1) $$B \geq \chi.\left(\frac{K_{Ic}}{\sigma_{YS}}\right)^2,$$

where *B* (fig.1.) is the minimum thickness that specimen a condition where plastic strain energy at the crack tip in minimal , σ_{YS} is yield stress of the material, χ is the empirical coefficient, According ASTM B 645-10:2015 (USA) for the parameter there is χ ~ 5.0. A most commonly used specimen for mechanical testing are given on fig.1.

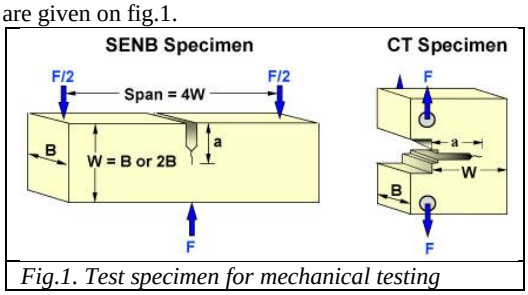

Fig.1. Test specimen for mechanical testing

The mechanical testing to obtain of K_{Ic} is difficult to realize, due to the large size *B* is needed. This testing is destructive. Often, it is not possible to prepare a test sample from the subject who is tested. It is needed of methods for non-destructive evaluation (NDE) of crack resistance to develop. These methods must be directly applicable to the test subject. The test specimen for NDE of K_{Ic} is not needed.

NDE of crack resistance - K_{Ic}

In practice there is interest for NDE of crack resistance K_{Ic} in directly on constructive elements manufactured by aluminum alloys. Such an approach does not require the preparation of test specimens from the test material. In this case a relationships are looking [1-7]

(2) $$K_{Ic} \Leftrightarrow \left(\overline{D}; E; \nu; \psi; \sigma_{YS}; \sigma_{UTS}\right)$$

where respectively average grain size, elasticity modulus, relative contraction, yield stress, ultimate tensile stress). There are also the relationships are known [3, 8, 9]

(3) $$\left(E; \nu; \psi; \sigma_{YS}; \sigma_{UTS}\right) \Leftrightarrow \overline{D}$$

In addition, deterministic or stochastic the relations [8-10] are view

(4) $$\left(\overline{D}\right) \Leftrightarrow \left(V_L; V_T : HB\right)$$

where $\left(V_L; V_T\right)$ are velocity of longitudinal and transverse ultrasonic waves, *HB* is Brinell's hardness. In this case the norms ASTM E 494:2015 and ASTM E 10:2018 are used.

2. NDE of grain size - $\overline{D}$

An important stage of NDE of K_{Ic} is NDE of $\overline{D}, mm$.

To obtain a dependency for $\overline{D}$ the following relationships are considered:

A/ Hall–Petch's dependency [8,9]

(5) $$\sigma_{YS}, MPa = \sigma_0 + K_y\left(\overline{D}, mm\right)^{-1/2},$$

where the reference values for Al+3,5%Mg alloys [5,6] is $\sigma_0 \sim 50{,}0 MPa$, $K_y \sim 8{,}5 MPa.mm^{1/2}$.

B/ Bussinesq's dependency [10]

(6) $$\sigma_{YS}, MPa = k_{Buss}.\varphi(\nu).\left(HB, kgf/mm^2\right)$$

where $\varphi(\nu) = \frac{1}{2}(1-2.\nu) + \frac{2}{9}(1+\nu).\left[2.(1+\nu)\right]^{1/2}$,

$\nu = \frac{0.5-(V_T/V_L)^2}{1-(V_T/V_L)^2}$, for Al+3,5%Mg, according BGN EN 1706,

$k_{Buus} \in (2.12-3.53), med.k_{Buss} \approx 2.8$.

After excluding σ_{YS}, MPa from (5), (6) equation for $\overline{D}, mm$ is obtain

(7) $$K_y.\left(\overline{D}\right)^{-1/2} + \left[\sigma_0 - k_{Buss}.\varphi(\nu).HB\right] = 0$$

The equation (7) is non-linear, regarding $\overline{D}, mm$, by set $\left(k_{Buss}; \nu; \sigma_0; K_y\right)$ and $\left(V_L; V_T\right)$, $HB, kgf/mm^2$ are measured. To solve the equation (7) a bisection method, ZEROIN algorithm [11] and on-line compiler for C++ are used. The rots is searching in the interval (0;1]. The accuracy 10^{-6} is set. The number of iteration is $N \sim \log_2^2\left[\left(X_R - X_L\right)/TOL\right]$, where $(X_R : X_L)$ is searching interval. In this case *N* ~ 170 (time of work is ~ 3-4 seconds).

3. NDE of K_{Ic}^T, according Tetelman

In [5] a relation $K_{Ic} = K_{Ic}\left(\overline{D}; \sigma_{YS}\right)$ is considered. The Tetelman's model [6] is

(8) $$\left(\frac{K_{Ic}^T}{\sigma_{YS}}\right)^2 = 25{,}23.\chi\left(\frac{\sigma_C}{\sigma_{YS}}\right).\left(\overline{D}\right),$$

where $\chi\left(\frac{\sigma_C}{\sigma_{YS}}\right)=\left[\exp\left(\frac{\sigma_C}{\sigma_{YS}}-1\right)-1\right].\left(\overline{D}\right),\sigma_C$ is critical value of stress in crack tip. For Al alloy witch 3.5%Mg (BGN EN 1706) there are $\sigma_{\max}\equiv\sigma_C\sim\sigma_{UTS}\approx 2.\sigma_{YS}$ (fig.2.) .

After necessary conversions of (8) is done

(9) $\left(\frac{K_{Ic}^T}{\sigma_{YS}}\right)^2\approx 43.\overline{D}$,

where $\overline{D}=\overline{D}(V_L;V_T;HB,K_y;\sigma_0;k_{Buss})$,calculated by (7).

.

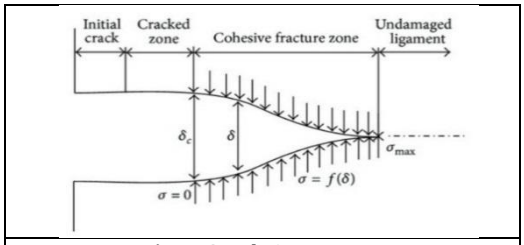

Fig.2. *Crack tip geometry*

.

4. NDE of K_{Ic}^A, *according Andreykiv*

Andreev's relationship [7] is a model includes not only $\left(\overline{D};\sigma_{YS}\right)$, but also the mechanical properties of the material - $(E;\nu;\psi)$. Andreev's relationship can by write as

(10) $\left(\frac{K_{Ic}^A}{\sigma_{YS}}\right)^2\approx.\xi\left(\overline{D}\right).\frac{E}{1-\nu^2}.\psi$,

where

$\xi\left(\overline{D}\right)$ - structural function is defined as

$\xi\left(\overline{D}\right)=\frac{\sqrt{3}}{3}.\overline{D}.\left[\sigma_0+K_y\left(\overline{D}\right)^{-1/2}\right]^{-1}$;

$\overline{D}=\overline{D}(V_L;V_T;HB,K_y;\sigma_0;k_{Buss})$,calculated by (7).

$\frac{E}{\rho.V_T^2}=\frac{3-4(V_T/V_L)^2}{1-(V_T/V_L)^2}$, $\nu=\frac{0.5-(V_T/V_L)^2}{1-(V_T/V_L)^2}$, where $(V_L;V_T)$ are velocity of longitudinal and transverse ultrasonic waves and obtain by means ASTM E 494:2015. $(\psi,\%/100)=m.(V_L,mm/\mu s)+b$,

R^2 ~ 99.9 %, for Al + 3,5% Mg alloy $m=0{,}1016;b=0{,}0038$.

5. Experiment

For samples from Al + 3,5% Mg alloys [13], BGN EN 1706:2010, measurements have been made.

5.1. Equipment.

For NDE measure the following equipment are used:

1. Leeb hardness tester M – 295, WILCON, Germany, for measure of $HB,kgf/mm^2$;

2. Digital ultrasonic flaw detector, SONATEST, England and transducers for L and T waves are used,

for measures of $V_L,mm/\mu s$ and $V_T,mm/\mu s$;

3. Digital micrometer DIGIMATIC, Mitutoyo, Japan, for thickness measures.

In Table 1. the images of Leeb hardness tester and digital ultrasonic flaw detector and transducers are given.

Table 1. *Devices for NDE*

$V_L,mm/\mu s$ $V_T,mm/\mu s$	$HB,\ kgf/mm^2$
SITESCAN 150 S with transducers for L and T waves	*M – 295 with spherical impact device*

.

5.2. Measurements

For Al alloy witch 3.5 % Mg (BGN EN 1706).

Velocity, $(V_L;V_T).mm/\mu s$, ASTM E 494:2015

$(6{,}36\pm 0{,}030)$; $(3{,}15\pm 0{,}015)$.

Note: Minimum thickness of test object is 5 mm.

Hardness, $HB,kgf/mm^2$, ASTM E 10:2018

$(90\div 120)\pm 10$.

Note: Minimum weight of test object is 5 kg.

6. Calculations

According BGN EN 1706 for Al + 3,5% Mg alloy, the average value $\overline{\sigma_{YS}}$, MPa ~ 70 is accept.

The results of calculations and reference values, are presented in Table 1. and Table 2.

Table 2. *NDE of constants*

Characteristic	According Tetelman 1971 year	According Andreykiv 1982 year
$(K_{Ic}/\sigma_{YS})^2$,mm $NDE.\lvert Err.\rvert,\%$	~ 2,90 ~ 7 %	~ 2,95 ~ 5 %
$K_{Ic},MPa.m^{1/2}$ $NDE.\lvert Err.\rvert,\%$	~ 27,5 ~ 9 %	~ 29,0 ~ 4 %

The results of calculations are need correction by $\left(\frac{K_{Ic}^A}{\sigma_{YS}}\right)^2\approx\left(\frac{K_{Ic}^{CALC}}{\sigma_{YS}}\right)^2$ and $K_{Ic}\approx\frac{1}{3}.K_{Ic}^{CALC}$. This coefficient takes into account the difference in dimensions of the quantities participating at calculated of the values.

Table 3. *Reference values of constants*

Characteristic	[Wikipedia 2,3,4]
$(K_{Ic}/\sigma_{YS})^2$,mm	3,1 – 3,3
$K_{Ic},MPa.m^{1/2}$	30 – 33

7. Example

One of most important applications of the conception for crack resistance K_{Ic} is the condition for fracture [1,3]. The head of a diesel engine (aluminum alloy) with semi-elliptical crack between the cylinders, fig.3. is considered.

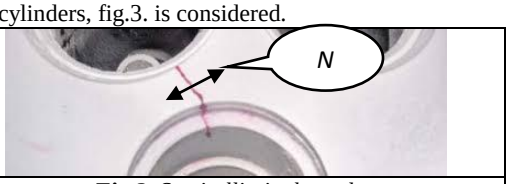

***Fig.3**. Semi-elliptical crack between cylinders in the diesel engine*

.

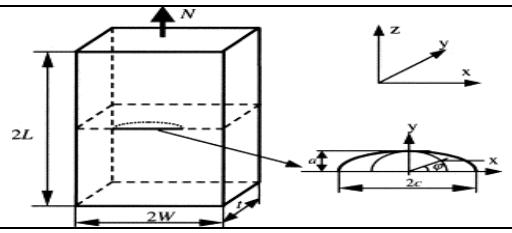

***Fig.4.** Model of semi-elliptical crack in the diesel engine*

The diesel engine does not break if provided [1,5]

(9) $K_I(\sigma_\infty; a; c) \le K_{Ic}(E; \nu; \psi; HB)$,

where $\sigma_\infty \equiv \sigma_C \equiv \sigma_{\max}$ - mechanical stress;

$a \equiv a_{UT}$ - depth of the semi-elliptical crack, fig.5. by means ultrasonic testing, method TOFD (ASTM E 2373:2014) is determined;

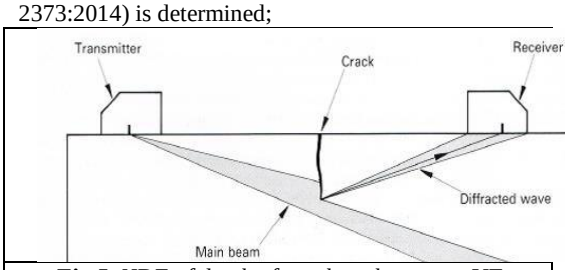

***Fig.5.** NDE of depth of crack - a by means UT*

2c - length of the semi-elliptical crack, fig.4. , by means lens (10X optical zoom) with measurement scale is determined.

$K_I(\sigma_\infty; a; c)$ is stress intensity factor of semi - elliptical crack in infinite plain, [12] fig.4.

(10) $K_I = M_K.\sigma_\infty.\sqrt{\pi.a} / E_2(a/c)$,

where correction factor $M_K = M_K(a/t; a/(2.c))$ by means Table 4. [13] is obtain.

Table 4.

$M_K(a/t; a/(2.c))$ at $\varphi = \pi/2$				
a/t \ $a/2c$	0.2	0.4	0.6	0.8
0.2	1.173	1.359	1.642	1.851
0.4	1.138	1.225	1.370	1.447
0.6	1.110	1.145	1.230	1.264
0.8	1.049	1.062	1.107	1.112

$E_2(a/c)$ is full elliptical integral, 2-nd kind [12].

A/ If $a << t$, then

$$E_2(a/c)) = \sum_{j=0}^{j=2} \beta_j (a/c)^{2-j}$$,where

$(\beta_0 / \beta_1 / \beta_2) \equiv (0.2959; / 0.2933 / 0.9886)$,

coefficient of determination R^2 = 99.8%.

B/ If $a \le 0.3t$, then

$E_2(a \le 0.3t)$ = (0.9 -1.1). $E_2(a/c))$.

After carry out the necessary transformations of (9), for the computing depth of crack a_{CALC}, the inequality is obtain

(11) $$K_{Ic} \cdot \sum_{j=0}^{j=2} \beta_j \left(\frac{a_{CALC}}{c_{VT}} \right)^{2-j} - K_{VT} \cdot \left(\frac{a_{CALC}}{c_{VT}} \right)^{1/2} \ge 0,$$

where $c_{VT} \equiv c$, fig.4.; c_{VT} by means magnifying glass (10x optical zoom) with measuring scale is obtained.

$K_{VT} = M_K(a/t; a/(2.c_{VT})).\sqrt{\pi}.\sigma_\infty.c_{VT}^{1/2}$,where correction factor M_K by means Table 4. is obtained,

$a \equiv a_{UT}$; a_{UT} by means ultrasonic method TOFD (ASTM E 2373:2014) is obtained; $\sigma_\infty = \sigma_\infty(T^0 C)$.

$K_{Ic} = K_{Ic}(E; \nu; \psi; HB)$ by means (10) is obtained.

The inequality (11) by equation (12) is solved

(12) $$K_{Ic} \cdot \sum_{j=0}^{j=2} \beta_j X^{2-j} - K_{VT}.X^{1/2} = 0.$$

where $X = a_{CALC} / c_{VT}$.

The non-linear equation (12) by bisection method, algorithm ZEROIN [11] and on-line compiler for C++ is solved.

Making a decision for the acceptability of the crack depth - a_{ACC} is according $a_{ACC} \le a_{CALC}$.

Therefore the condition for a_{ACC} is

(13) $a_{ACC} \le X.c_{VT}$,

where *X* and c_{VT} respectively by means solution of (12) and method VT are obtain.

8. Conclusion

This article describes the NDE of crack resistance by means ultrasonic velocities and hardness. The calculated of value $K_{Ic}^K(\sigma_{YS}; \overline{D})$, is simply, but does not produce a good result. The calculate the value $K_{Ic}^A(\overline{D}; \sigma_{YS}; E; \nu; \psi)$ gives a better result as it takes more information about the material.

The follow NDE are used:

$\overline{D} = \overline{D}(V_L; V_T HB)$ is NDE of $\overline{D}$, $(V_L; V_T HB)$ respectively by ASTM E 494:2015 and ASTM E 10:2018;

$\sigma_{YS} = \sigma_{YS}(V_L; V_T; \overline{D})$ - yield stress by Hall-Petch's relationship is NDE.

$(E; \nu) \Leftrightarrow (V_L; V_T)$ is NDE by ASTM E 494:2015;

$\psi = \psi(V_L)$ - regression, with coefficient of determination $R^2 = 99\%$.

$K_{Ic} = K_{Ic}^A(V_L; V_T; HB)$ is NDE of crack resistance. The errors of NDE for $(K_{Ic}^A / \sigma_{YS})^2$ is ~ 5 % and NDE for K_{Ic}^A is ~ 4 %.

Used norms

BGN EN 1706:2010, Aluminium and aluminium alloys - Castings - Chemical composition and mechanical properties (Bulgaria)

GOST (Russian GN) 25.506–85, Design, calculation and strength testing. Methods of mechanical testing of metals. Determination of fracture toughness characteristics under the static loading (Russia).

ASTM E 399:2017, Standard Test Method for Linear-Elastic Plane-Strain Fracture Toughness KIc of Metallic Materials.

ASTM B 645–10:2015 , Standard Practice for Linear-Elastic Plane–Strain Fracture Toughness Testing of Aluminum Alloys

ASTM E 494:2015. Standard Practice for Measuring Ultrasonic Velocity in Materials.

ASTM E 10:2018 . Standard Test Method for Brinell Hardness of Metallic Materials

ASTM E 2373:2014, Standard Practice for Use of the Ultrasonic Time of Flight Diffraction (TOFD) Technique.

9. References

1. Georgiev M., Ju. Simonov, Crack resistance in Fe-C alloys, BULVEST 2000, Sofia, 2011. /in Bulgarian/.

2.Kernshtein I.M., &, Fundamentals of experimental fracture mechanics, Moscow University, Moscow, 1989. /in Russian/.

3. Selivanov V.V, Fracture mechanics for solid bodies, Moscow, State Technical University "Bawman", 2006. /in Russian/ .

4. Hellan K., Introduction to Fracture Mechanics, Mc-Graw - Hall Book Company, New York, 1984.

5. Siratori M.,T.Meysi, H.Micusyta, Computational fracture mechanics, MIR,Moscow,1986./in Russian/

6. Malkin J., Tetelman A.S. Relation between KIC and microscopic strength for low alloy steels, Engng. Fract. Mech. – 1971.V. 3. № 2. ,p.151–167.

7. Andreykiv A.E., Spatial tasks in the theory of cracks, Naukova dumka, Kiev, 1982. /in Russian/ .

8.Armstrong R.W, Hall-Petch relationship use in characterizing Properties of Aluminum and Aluminum Alloys, In Encyclopedia of Aluminum and it Alloys; G.E. Totton and M. Tiryakioglu, editors; Taylor&Francis Group Publishers, U.K., 2016.

9. Trefilov V.I. In: Deformation strengthen and destruction of polycrystalline materials, Kiev, Naukova dumka, 1987. /Russian/ .

10. Markovitc, M.P, Non-samples methods for determining the mechanical properties of metals, MPEI, Moscow, 1983. /in Russian/ .

11. Forsythe G.E. &, Computer Methods for Mathematical Computations, Prentice-Hall Inc. New York , 1977.

12. G.R.Irwin. Crack-Extension Force for a Part-Through Crack in a Plate, Journal of Applied Mechanics, Vol. 29(4), 651 - 654, 1962. DOI: 10.1115/1.3640649.

13. J. C. Newman and I. S. Raju. An empirical stress-intensity factor equation for the surface crack.
Engineering Fracture Mechanics, 15(1):185–192, January 1981. doi: 10.1016/0013-7944(81)90116-8.

DETERMINATION OF GEYSER EVENTS IN A THERMOSYPHON WORKING WITH GRAPHENE OXIDE NANOFLUID

Kujawska A.[1], Zajaczkowski B.[1], Woluntarski M. [2], Buschmann M.H.[3]
Faculty of Mechanical and Power Engineering – Wroclaw University of Science and Technology, Poland [1]
Institute of Electronic Materials Technology, Warsaw, Poland [2]
Institut für Luft- und Kältetechnik, Dresden, Germany [3]

Agnieszka.Kujawska@pwr.edu.pl

Abstract: *Two-phase closed thermosyphons are efficient passive devices with potential for using in many heat transfer applications. One of the boiling regimes that may occur is the geyser boiling. It is a repetitive irregular process of pushing liquid without its previous evaporation in the direction of condenser. Although it does not affect time-averaged thermal performance of the device, it causes additional mechanical load and shortens the life-time of the device. Unfortunately, geysering is not well investigated, thus no precise definition exists. This paper focuses on the process of data reduction that leads to geyser boiling detection. It may be applied for various working fluids and operating conditions. Two parameters are crucial for recognizing geyser events from the background noise (pressure variations followed by the geyser): the minimum amplitude of pressure increase and waiting period between ensuing events. We compared two working fluids: water and graphene oxide nanofluid. In general, with increase of heat flux the frequency of geysers increases and their amplitude decreases.*

Keywords: THERMOSYPHON, GEYSER BOILING, NANOFLUID, GRAPHENE, HEAT PIPE, BOILING REGIME

1. Introduction

Two-phase closed thermosyphons show great potential for efficiency improvement in many applications covering energy transport. Operation principle is based on the evaporation-condensation closed cycle of working fluid. The energy from external source of heat is applied into the lowest part of the pipe - evaporator. Working fluid evaporates and the vapor goes up through the adiabatic section. It condenses in the upper part (condenser) as a result of contact with colder walls. Heat is released to the surrounding environment (cooling medium, e.g. water) and condensate returns to the evaporator relying on gravity. It imposes location of the evaporator below the condenser.

For some working conditions, the nucleate pool boiling in the evaporator may be turned into pseudo-stable boiling regime, called *geyser boiling*. It occurs mostly under low pressure conditions, for high filling ratios, and during start-ups. Figure 1 schematically showcases such a process.

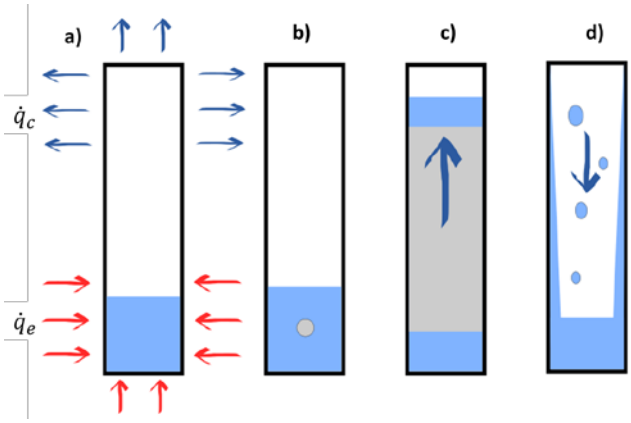

Fig. 1: *Scheme of geyser boiling phenomena. Phases a) to d) as follows: (a) the superheat between the evaporator wall and working fluid in the evaporator increases, (b) nucleation of the bubble and its quick growth to the size of pipe diameter, (c) bubble expansion and propulsion of the fluid trapped above the bubble, (d) and downfall return of the displaced liquid. Reprinted from* [1] *under the terms of the CC BY 4.0 (http://creativecommons.org/licenses/by/4.0/).*

During geyser event vapor bubble that grew to the size of pipe diameter pushes upwards the liquid accumulated above. The large difference between the vapor pressures inside the bubble and in the condenser section forces the high speed of the liquid. The propelled liquid returns to the evaporator due to gravity forces, and in most cases is separated from condensate film on the thermosyphon wall. Afterwards, the quiet period occurs again until the fluid pool temperature reaches the superheat enough to nucleate another bubble. The phenomenon is repetitious and rapid, but periods between successive events vary. Geysering detection requires continues and precise pressure measurements, still the amassed data needs to be meticulously analyzed in order to locate geyser boiling occurrences. Thus, the phenomenon often remains unrecognized and only few research on that topic are available in the literature. Although the time-averaged thermal resistance seems to be not affected by geysering, it may introduce disturbances to the continuity of heat transfer through the device. It causes additional mechanical load, and engender shock damage of the components. Thermosyphons are used in systems expected to operate for long periods of time, thus more and more effort is put to improve understanding of the phenomena.

As reported in our previous work [1], there is a lack of research concerning dependence of nanofluids (understood as suspension of particles with at least one size below 100 nm in a base fluid) on geysering, except one paper on gold nanofluid [2]. In this paper we check if proposed methodology for data reduction can be implemented regardless of the working fluid or operation conditions. The behavior of graphene oxide nanofluid and water is then analyzed and compared.

2. Test rig and materials

Experiments were conducted using copper thermosyphon with the dimensions shown in Fig. 2. Tested device is divided into three parts: evaporator heated by circulating water, adiabatic section and condenser cooled by another coil filled with water. The whole device was insulated with Armaflex shell. Inlet temperatures of heating medium controlled by thermostat varied between 40°C and 85°C in 5°C steps. The inlet temperature of cooling water was 25 ± 0.14°C for each test case presented here. Volume flow rates of both cycles were set on 12 l/h and measured with magneto-inductive flow meters. The inlet and outlet temperatures of heating and cooling water were determined by Pt100 – elements with the maximum uncertainty of ± 0.32°C. The pressure inside the device was characterized by three pressure transmitters with an accuracy of ± 0.25% located along the thermosyphon and two parallel gauges with different measurement range at the top of the device. For each combination of operation conditions, all parameters were recorded for an hour after reaching a steady-state condition. Detailed characterization of the device is described in [1].

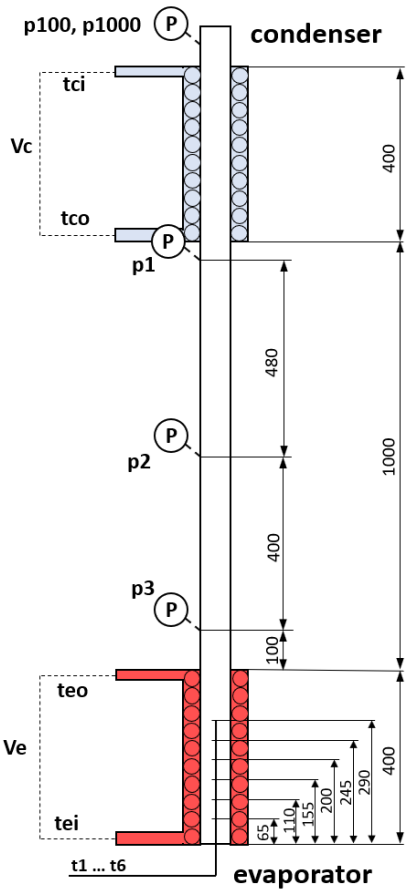

Fig 2. *Scheme of thermosyphon with dimensions and used nomenclature.*

Deionized water and graphene oxide nanofluid were used as working fluids. Graphene oxide flakes (GO) were prepared at Institute of Electronics Materials Technology in Warsaw, in Poland through modified Hummers method [1]. The concentration of flakes was 0.1 g/L and no additional stabilizer was added [1].

3. Results

Time-averaged data

One of the fundamental parameters showing the efficiency of heat transfer in the thermosyphon is its thermal resistance. It is defined as the ratio of average temperature difference between evaporator and condenser section and the amount of heat released in the condenser [1]. Figure 3 showcases the difference between the thermal resistance when device is filled with water and graphene oxide nanofluid. Arrows indicates the result obtained for the same operating condition (inlet temperature of cooling and heating water). For low temperatures of the evaporator and small differences between evaporator and condenser, nanofluid allows not only for lowering the thermal resistance but also transfers higher amount of energy in form of heat. It makes it interesting for application with specific requirements, such as heat recovery, geothermal or HVAC systems. Although for high heat fluxes (and high temperatures of the evaporator) the time-averaged data suggests that working fluid does not affect the thermal performance of the device, in this region different processes of boiling occurs, including geysering.

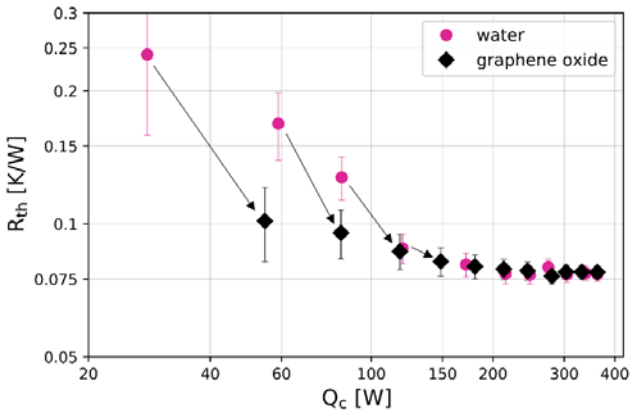

Fig 3. *Thermal resistance of the thermosyphon working with water and graphene oxide nanofluid. Arrows indicates the same operating conditions.*

Time-dependent data

Precisely characterized definition of geyser boiling does not exist in the literature. The phenomenon is rather understood as explosive and irregular boiling process. It leads to difficulties with data analysis to determine whether the pressure increase may be counted as geyser event. One of *typical* pressure patterns describing such a phenomenon is shown in Fig. 4. All the figures presented in this section are based on the pressure signal p3, pressure transmitter closest to the boiling pool. It was located in the adiabatic section, 500 mm from the bottom of the device and 100 mm above the evaporator section.

Geyser event is characterized by abrupt and prominent increase in pressure. The increment in pressure signal is detected by subsequent transmitters, starting from the lowest one (p3, see insert of Fig. 4). Depending on working fluid and operation conditions, the speed of pushed working fluid calculated from the time difference of peak detected by subsequent transmitters is about 3-10 m/s. After the return of expelled liquid to the evaporator, the period of nucleate boiling starts and long-lasting pressure drop occurs.

To automatize detection of geyser events, two parameters must be defined: the minimum amplitude of pressure increase and the minimum waiting period between following geysers. The first one – the lowest pressure difference between the current and time-averaged values - protects from counting the noise following from liquid eruption or intensive nucleate boiling. As various working fluids behave differently depending on operating conditions, it is impossible to set one threshold value for all cases. Thus, we propose to use the probability density. We assumed that all pressure values that describe geysering are likely to be outside the range of -2σ to 2σ (standard deviation) from the pressure averaged over the experiment time at given conditions. Then, every peak exceeding the threshold line given by 2σ value (see *mph* value in Fig. 6) with rising trend is further examined as potential geyser event.

The second crucial parameter is waiting period (*mpd*) determining the minimum time step between consecutive geyser events. It protects against calculating the noise following from violent abruption of liquid and its return due to gravity forces. The determination of minimum time step starts with an analysis of the waiting period effect on the final results. The example for water at high temperatures of evaporator is presented in Fig. 5. We choose the value on the constant line after bending the curve. The last step is to check if events marked by described script [3] overlaps the ones seen with the naked eye.

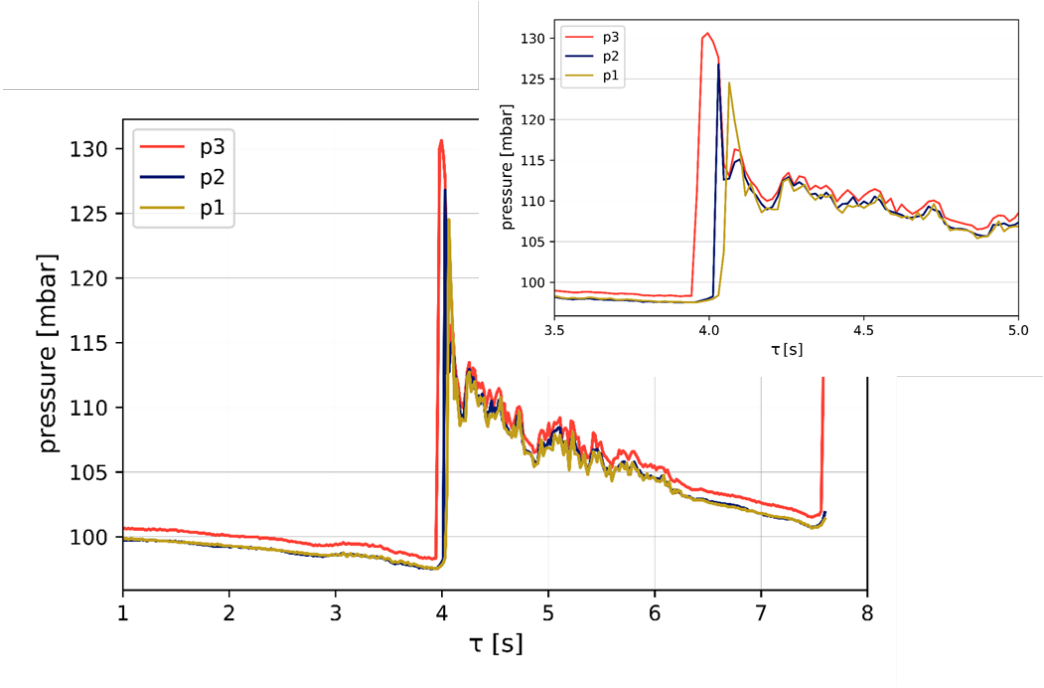

Fig 4. *Example of geyser pattern for water (inlet temperature of heating water: 75°C). The insert presents the same event but in different time-scale.*

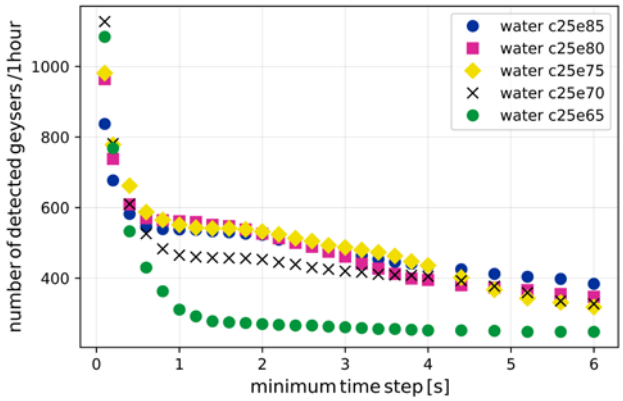

Fig 5. *Analysis of waiting period (minimum time step between two successive geyser events) depending on working conditions.* c25 *indicates the temperature of condenser (25°C),* e65-85 *indicates the inlet temperature of heating medium in the evaporator (65-85°C).*

The importance of properly chosen waiting period is presented in Fig 6 and 7. Two time steps are compared: 0.1s and 2s (*mpd* of 5 and 100, respectively). Figures covers the same operating conditions (inlet temperature of heating medium: 75°C, of cooling medium: 25°C). For both working fluids, noises following from geyser event are marked in the case of mpd 5. At waiting period of 2s some peaks are missed for water case, e.g. the small event before the highest peak in the upper plot of Fig. 6. According to analysis shown in Fig. 5, time step for water at given conditions should be between 1-1.5 sec. For GO nanofluid, this waiting period seems to be properly selected – all big peaks are included in calculations and increases coming from unsteady state following the real geysers are eliminated.

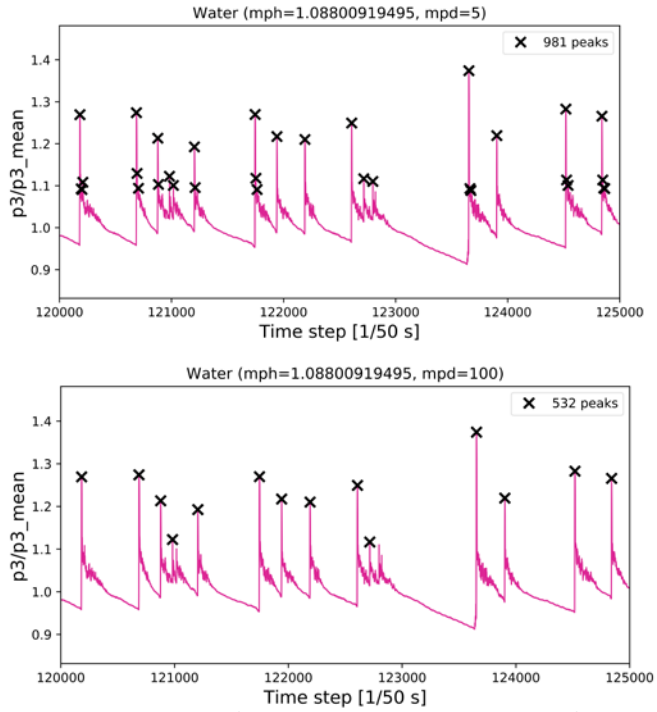

Fig 6. *Geyser events (peaks) for water at evaporator temperature of 75°C included in calculations for different waiting periods (mpd)*

The amplitude and waiting period differ significantly between individual events for water pattern (see Fig. 6). Weaker peaks following the main event may occur. In case of GO nanofluid (see Fig. 7), pressure peaks show almost constant value of 1.3-1.4. They occur less often and pretend to be more ordered. The nucleate boiling period following the liquid throw seems to be rather short and not intensive. Sporadically, additional weak event appears but opposed to water it is not preceded by a pressure drop.

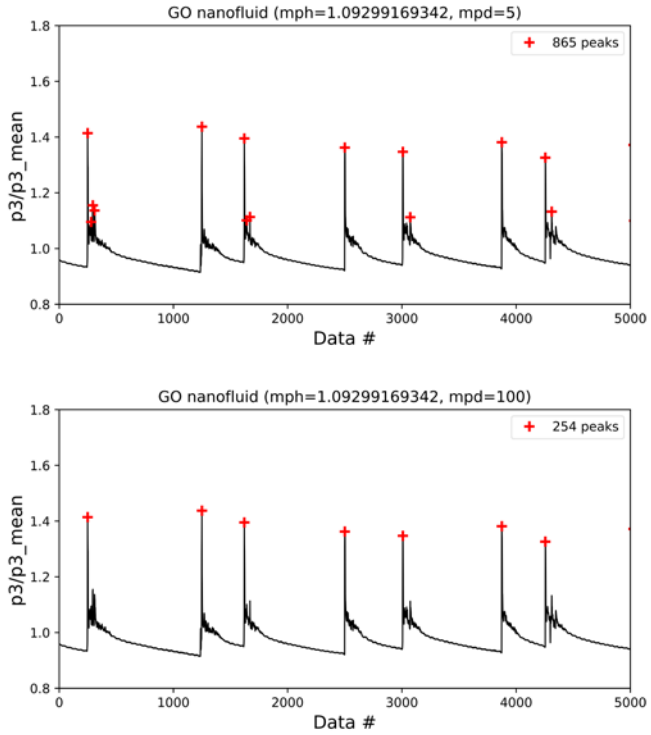

Fig 7. *Geyser events (peaks) for GO nanofluid at evaporator temperature of 75°C included in calculations for different waiting periods* (mpd)

The frequency and amplitude of detected geysers events differs depending on working fluid and operation conditions. In general, increase in the evaporator temperature leads to increase in the time-averaged frequency (see: Fig. 8). This trend follows previous conducted experimental research [4]–[7].

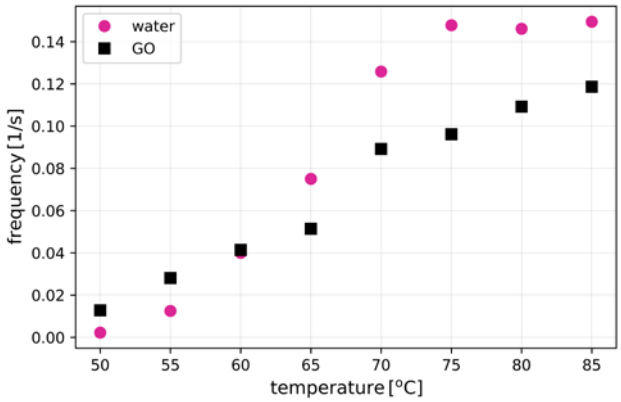

Fig 8. *Time-averaged frequency of geyser events*

At the same time, the mean amplitude of detected events (Fig. 9) decreases with evaporator temperature increment. It may be deduced that boiling becomes more violent but less impetuous with evaporator temperature increase. The effect of heat flux on the geysers amplitude was analyzed only in two papers, from which Khazaee et al. [6] showed the same trend as in this paper and Casarosa et al. [4] did not notice any difference.

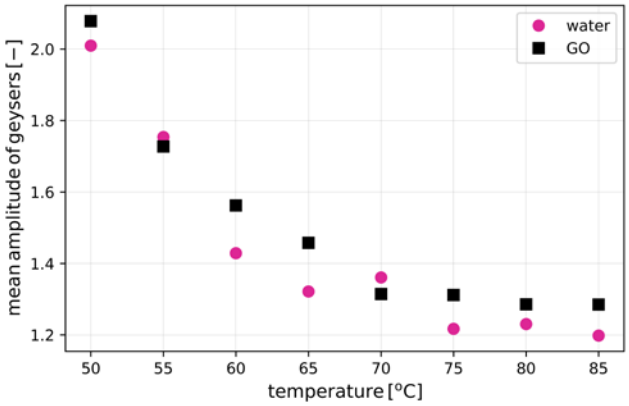

Fig 9. *Mean amplitude of detected geyser events*

4. Conclusions

The paper presents the analysis of time-averaged and time-dependent behavior of two working fluids: water and water-based graphene oxide nanofluid. To the best authors knowledge, no strict definition of geyser boiling exist in the literature. That is why the methodology of data reduction is proposed. As a result, the time-averaged frequency of geyser events occurrence and their amplitude are calculated and compared. In general, with the evaporator temperature increase, frequency of geysers increases but their amplitude decreases. It suggests that for higher heat fluxes the boiling process becomes more violent but less impetuous.

Acknowledgements

This work is a contribution to the Grant MF140079 and the NanoUptake COST Action (European Cooperation in Science and Technology) CA15119: Overcoming Barriers to Nanofluids Market Uptake. A.K. acknowledges the STSM funding supported by Nanouptake COST Action no. 35922, 37694, and 39240, and ITC grant no. 990.

References

[1] A. Wlazlak, B. Zajaczkowski, M. Woluntarski, and M. H. Buschmann, “Influence of graphene oxide nanofluids and surfactant on thermal behaviour of the thermosyphon,” *J. Therm. Anal. Calorim.*, 2018.

[2] U. Franzke and M. H. Buschmann, “Gold nanofluid prevents geyser effect in thermosyphon,” in *Turbulence, Heat and Mass Transfer 8*, 2015.

[3] M. Duarte, “DetectPeaks - iPython Notebook.” [Online]. Available: http://nbviewer.ipython.org/github/demotu/BMC/blob/master/notebooks/DetectPeaks.ipynb. [Accessed: 09-Jan-2019].

[4] C. Casarosa, E. Latrofa, and A. Shelginski, “The geyser effect in a two-phase thermosyphon,” *Int. J. Heat Fluid Flow*, vol. 26, no. 6, pp. 933–941, 1982.

[5] T. F. Lin, W. T. Lin, Y. L. Tsay, J. C. Wu, and R. J. Shyu, “Experimental investigation of geyser boiling in an annular two-phase closed thermosyphon,” *Int. J. Heat Mass Transf.*, vol. 38, no. 2, pp. 295–307, 1995.

[6] I. Khazaee, R. Hosseini, and S. H. Noie, “Experimental investigation of effective parameters and correlation of geyser boiling in a two-phase closed thermosyphon,” *Appl. Therm. Eng.*, vol. 30, no. 5, pp. 406–412, 2010.

[7] A. Kujawska, B. Zajaczkowski, L. M. Wilde, and M. H. Buschmann, “Geyser boiling in a thermosyphon with nanofluids and surfactant solution,” *Int. J. Therm. Sci.*, in press.

GRADIENT STRUCTURE AND METHODS FOR THEIR PREPARATION

G.I. Raab[1,2] – Dr.Sci, A.G. Raab[1,2] - Ph.D., A.P. Zhilyaev [2,3] – Dr.Sci
[1] Ufa State Aviation Technical University, IPAM, Ufa, Russia
[2] Nosov Magnitogorsk State Technical University, Magnitogorsk, Russia
[3] Institute for Metals Superplasticity Problems, RAS, Ufa, Russia

Abstract. *The development of new technological methods of SPD for the production of mass production with improved properties due to the deep grinding of the original structure is an important task. The purpose of this work was to study the active bending to grind the structure and create promising, for operational use, gradient structural states in long rods of copper grade M1. Active bending was performed using an extruder according to the "Conform" scheme. The results of the analysis stress-strain state is using computer simulation and structures using optical microscopy. It is established that the active bending method provides over four processing cycles high strain accumulation (e = 3-4) and formation subgrained- structure UFG type.*

KEYWORDS: *METAL PROCESSING BY PRESSURE, SEVERE PLASTIC DEFORMATION, FINITE ELEMENT METHOD.*

1.Introduction

In the modern world, the need for new materials is increasing, as well as for the improvement of their physical and mechanical properties. In this regard, there is an increasing need for the creation of promising industrial methods allowing to achieve improved properties in the material. The most effective methods are SPD [1,2]. However, their development is hampered by low manufacturability of the proposed technical solutions, especially for the production of mass products. In this regard, the paper considers the method of active bending, based on the use and advantages of the "Conform" scheme [3-5]. Its main advantage is the improvement of the tribological situation in the process of the formation of ultrafine-grained (UFG) gradient structures providing products with increased wear resistance and ductility at high strength indices [??]. The object of the study was a long rod of technically pure copper.

2.Concept of process

Principal diagram of active bending used in research is presented in Figure 1. The proposed development is based on the well-known ECAP- "Conform" scheme, while in the deformation process, the workpiece 3 is pushed into the stationary bending matrix consisting of two elements of the matrix 1,2 due to active friction forces of the drive roll with engraving 4. The method makes it possible to combine the high-performance "Conform" process with bending deformation, which leads to a considerable intensification of the hardening process of especially the near-surface layers of the deformable material due to the formation of the structure. Active friction forces ensure continuity of the process.

For the simulation, program Deform 3D was used, intended for the analysis of three-dimensional (3D) metal behavior in the processes of pressure treatment. This made it possible to obtain important information about the nature of the material flow in the forming tool, the stress-strain state and the temperature distribution in the deformation process.

When modeling the bend according to the "Conform" scheme at angle of 90 degrees, a square section blank of 10x10 mm in length and more than 150 mm in length was used for the first deformation cycle, the bending radius was 10 mm. For the subsequent cycles, a samples obtained by modeling on the previous cycle was used in order to obtain generalized data after passing through four samples processing cycles.

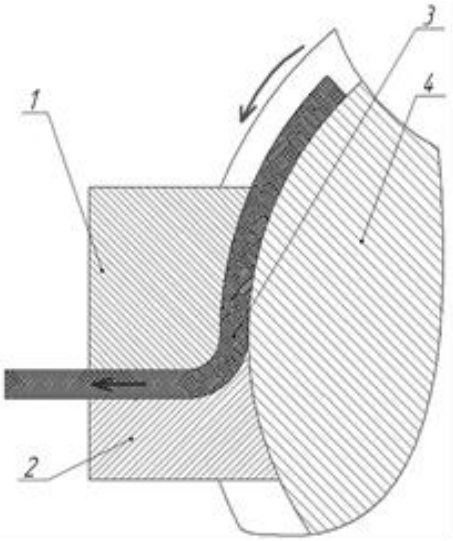

Figure. 1. *Principial schem of bending of samples due to active friction forces according to the "conform" scheme in a stationary bending matrix: 1, 2 - two matrix elements for bending; 3 - sample; 4 - drive roller with engraving.*

Process simulation parameters

- Initial sample plastic body, with a number of finite elements 70000 pcs.
- Tool - absolutely rigid body.
- Tool without a finite element mesh.
- The rotational speed of the drive roller is selected constant - 1 rad / sec.
- The temperature at the first treatment cycle was taken at room temperature and was 20 ° C.
- Simulation is performed taking into account the increase in the temperature of the workpiece from the heat effect during plastic deformation (deformation heating).
- The temperature of the rollers is constant, corresponds to - 20 ° C.
- Use Siebel coefficient of friction f = 0,2.
- The impermeability condition is set on the contact surfaces of the equipment.
- Number of modeling steps more than 1000 for all four cycles of the bending process.

3. Results and discussion

The conducted virtual experiment and its analysis showed that in the process of processing on the surface of the workpiece during bending at angle of 90 degrees, maximum values of the strain intensity are observed. So after one cycle in the upper part of the workpiece, the accumulated strain intensity reached e = 1.04, and in the lower e = 0.88 and increased proportionally with the number of sample passes through the deforming channel (see Fig. 4).

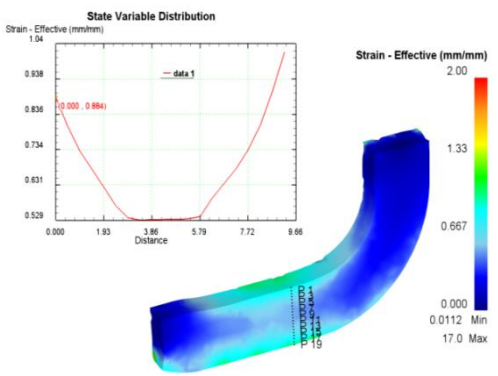

a

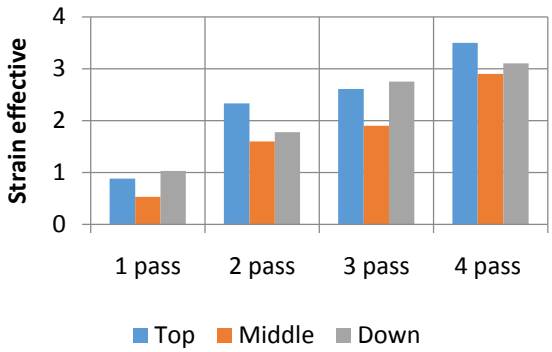

b

Fig. 3. *Picture of the deformed state of the sample after the first bending cycle at 90 ° (a) and the diagram of the strain intensity accumulated over the cross section of the workpiece after four passes (b)*

Plastic deformation by the proposed method leads to formulations that allow one to obtain a gradient of properties in a deformable material. So, with a subsequent analysis of the accumulated strain in the process of bending an angle of 90°, it can be seen that with an increase in the number of bends, the accumulated strain also increases. So after four cycles of deformation processing, the accumulated deformation is e = 2.8 ... 3.5 for an angle of 90 °, with the maximum value of accumulated deformation observed in the near-surface region of the deformable sample, and lower values in the middle area.

The results of laboratory studies for obtaining experimental samples and structural studies are presented in Figure 5. It has been established that a finer grain-subgrain-type structure is formed in the surface layers.

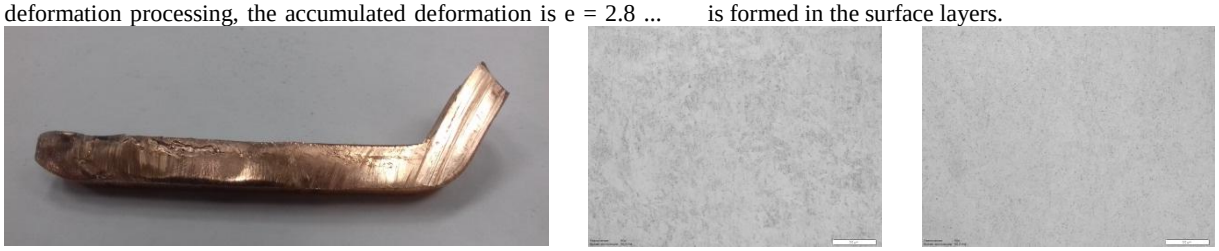

a b c

Figure 5. a *- general view of the sample in the process of active bending, b - the structure of the middle zone of the cross section of the sample (OM), c - the structure of the surface area of the cross section of the workpiece (OM)*

4. Conclusion

It is established that when using the method of active bending in a deformable copper sample, a gradient of a grain-subgrain structure of the UFG range is formed. Using virtual simulation, it is shown that the method of bending according to the “Conform” scheme provides, after 4 processing cycles, the level of accumulated deformation e = 2.8 in the middle region and e = 3.5 in the near-surface region of the cross section of the sample.

Acknowledgements: the authors acknowledge the financial support by the Ministry of Education and Science of Russian Federation under Grant agreement acknowledge the financial support from the Grant 14.Z50.31.0043

5. References

1. Valiev RZ, Zhilyaev AP, Langdon T. J. Bulk nanostructured materials: the fundamentals and applications. St. Petersburg, Eco-Vector. 2017. 480 p.
2. F.Z. Utyashev, G.I. Raab, V.G. Shibakov, M.M. Ganiev. Theory and practice of deformation methods for the formation of a nanocrystalline structure in metals and alloys / - Kazan: Kazan publishing house. University, 2016. 208 p.
3. Valiev R.Z., Aleksandrov I.V. Bulk nanostructured metallic materials: production, structure and properties. - M.: ICTs “Akademkniga”, 2007. - 398 p.
4. Raab G.I., Valiev R.Z. Equal-channel angular pressing of long blanks. Non-ferrous metallurgy-2000 -№ 5, p.50-53
5. Patent 2345861 Russian Federation, IPC B21J5 / 06, B21J13 / 00. Device for continuous angular pressing / G.I. Raab, R.Z. Valiev, V.M. Kapitonov, A.G. Raab; Applicant and patent holder of the "Ufa State Aviation Technical University". - No. 2006145916/02; declare 12/22/2006; publ. 27.06. 2008. - 3s

SURFACE HARDENING OF METALLIC MATERIALS BY USE OF COMBINED MAT-FORMING TREATMENT AND ELECTROSPARK DOPING

Prof. Bagliuk G., Dr. Sc.[1], Makovey V., PhD. Borodiy Yu., PhD.[2]
Institute for Problems of Materials Science, National Academy of Science of Ukraine [1],
National Technical University of Ukraine "Igor Sikorsky Kyiv Polytechnic Institute" [2],
Kyiv, Ukraine
E-mail: gbag@ukr.net

Abstract: Analysis of the structural state and phase composition of surface metal layers after combined treatment of steel which includes preliminary surface plastic deformation of the workpiece, electrospark doping with use of rotating disk electrode 2 mm thick, made of WC-Co hard alloy and subsequent surface ball smooth rolling, has been performed. It was shown that the use of combined treatment provides a gradient-layered structure with low surface roughness. Phase composition of the obtained layer consist of ferritic α-Fe phase and a number of carbide phases formed during the interaction of the electrode material with steel: F_3W_3C, WC and W_2C semi-carbide. Wear resistance of the material after treatment exceeds similar properties of the original carbon steel up to 4 times.

Keywords: ELECTROSPARK DOPING, SURFACE PLASTIC TREATMENT, MICROSTRUCTURE, HARDNESS, WEAR RESISTANCE.

1. Introduction

The improving and raise of competitiveness of engineering products require the use of new technological processes, allowing to increase the service life and reliability of equipment in the conditions of increasingly stringent requirements for the operational characteristics of products. A promising way for the improvement of the bearing capacity of structural materials is to strengthen their surface layers or to deposit strengthening coatings, that increase the surface strength and wear resistance and, as a consequence, the operational lifetime of the construction and tool materials.

Various methods have been developed to enhance wear resistance of parts of friction units. Each of the currently known methods has its merits and deficiencies limiting their scope. The most common ways to restore the worn surfaces of metal parts at the present time are various types of gas-thermal coating and welding deposition. However, during welding deposition, a large amount of heat is supplied to the part, which leads to skellering and the need for subsequent processing.

Recently electrospark doping (ESD) is becoming more common for obtaining the coatings with high wear resistance of the metallic materials

The spark discharge occurs only in local volume in microscopically small volumes during 100–400 microseconds, when in the local metal-coating contact zone the high-temperature plasma regions appear, which provides the necessary adhesion of the formed coating to the base material. Very high densities of energy flows are realized in this process without the noticeable heating of the specimen under treatment. The process is characterized by an essential inequilibrium, so it is possible to obtain fundamentally new materials in the surface layers of the coatings, which is impossible under the usual equilibrium conditions [1, 2].

The method of electrospark doping differs from other surface treatment methods in its simplicity, reliability, and cost-effectiveness. Depending on the anode material, an extended surface layer with high strength, tribological, and other properties is formed on the work piece [3, 4].

For the instantiation of the ESD processes the devices containing manual or mechanical end electrode vibrators and generators of electrical voltage pulses of a certain shape and duration that are applied to the spark gap (between the electrode and the surface of the workpiece) [5] have found the greatest distribution.

However the ESD methods have some disadvantages as follows: high surface roughness of the treated surface of a workpiece, the presence of cracks, discontinuities and micropores. Besides, such devices have low productivity - up to 3 cm^2/min.

To reduce the roughness introduced by the electrospark doping, the methods based on the mechanical impact on the modified surface are used (surface-plastic strain, running the ball, nonabrasive ultrasonic treatment, etc.), as well as treatment with concentrated energy flows (plasma flow, electron and ion beams, laser beams) [6-9].

Significantly higher performance and surface condition are provided by mechanized devices with a rotating disk electrode, which is pressed against the material of the workpiece with a small controlled force [10].

An effective type of surface treatment of metallic materials is also surface plastic deformation [6, 7]. As a result of its application, due to work hardening in the surface layers, the shape and size of crystal grains are modified, accompanied by changes in the substructure and microstructure of the metal of the surface layer. The hardness of materials increases and compressive stresses are formed, contributing to increased wear resistance and resistance to fatigue failure.

Therefore the **aim** of the present paper is to specify the effect of combined surface treatment on structure and properties of the surface layer of carbon steel subjected to mat-forming plastic processing and electrospark doping.

2. Experimental Procedure

For realization of complex processing of the axially symmetrical bodysurface, a device was developed and made (fig. 1) on the basis of turning-screw-cutting machine, allowing to combine preliminary surface plastic deformation of the workpiece and mechanized ESD process with rotating disk electrode 2 mm thick, made of WC-Co hard alloy installed in a special water-cooled unit, attached to the tool holder.

The design for the surface plastic deformation device (fig. 2) includes a main deformation tool fixed in the carriage - a ball 3 with ∅10 mm hardened to 62-65 HRC, which in the process of operation leans on the bearing 4. The force of pressing the ball 3 to the treated surface at processing is changed by changing the force of the spring 2 compression by the adjusting screw 1.

The surface treatment of the experimental samples was carried out according to the scheme: plastic surface treatment with a ball - electrospark doping - surface treatment of the applied coating.

The microstructure of the alloys was studied on the XJL-17 optical microscope. X-ray phase analysis of the samples was carried out on DRON-3 diffractometer in filtered Co-K_α radiation using step-by-step scanning in the angular range of 20÷130°. The microhardness distribution over the sample section was determined on a PMT-3 microhardness meter.

To assess the comparative wear resistance of the obtained coatings, friction tests were carried out according to the "shaft-insert body" scheme with contact force of 400 N using a M-22M friction machine while cooling a friction couple with water.

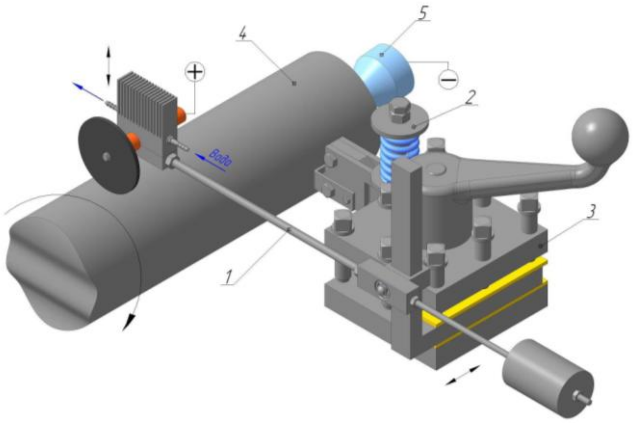

Fig. 1. *Three-dimensional scheme of the device for the formation of combined wear-resistant coating: 1 - device for ESD; 2 - unit for surface plastic deformation; 3 - carriage of the turning-screw-cutting machine; 4 - machined part; 5-center*

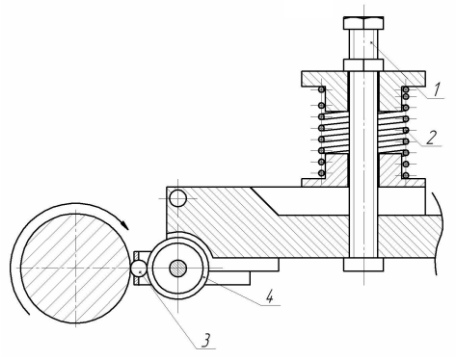

Fig. 2. *The scheme of the unit for surface plastic deformation: 1 - adjusting screw; 2 - spring;3 - ball; 4 - bearing*

3. *Experimental results and their discussion*

As our preliminary studies had shown [10], the optimum pressing force of the ball to the treated surface of ductile steels is 2.0÷3.5 kN. The increase in pressure leads to a violation of the integrity of the metal on the surface and the emergence of the peeling of the surface. At the same time, the hardness of the parts when rolling should not exceed 50 HRC.

The results of investigations of microhardness and material structure distribution over the depth of the sample (fig. 3, 4) showed that it can be conditionally divided into three zones. The base material I of У7 carbon steel, has a ferritic-pearlitic structure (fig. 4, a, c) with an initial hardness of HV 220÷240.

Intermediate transition layer II (fig. 4), that was formed during the primary surface plastic processing of the specimen, is located at a depth of 100÷250 μm from the surface. It differs in monotonically decreasing hardness from the surface over the layer thickness (from HV 650 to HV 250) (fig. 3) and is of distinctly more fine-grained structure compared to the base metal (fig. 4,c).

The upper layer III of maximum hardness (HV 650-1040) with a depth up to 100 μm (fig. 3, fig. 4, a, b) is formed as a result of the interaction of electrode material (BK8 hard alloy) with surface material of the sample being processed during the electrospark doping.

The layer resulting from the electrospark treatment is characterized by an extremely highly dispersed cellular substructure. According to the X-ray structure analysis and electron microscopy, cited in [1, 11, 12], the dimensional parameters that characterize the coating cellular substructure that was formed in the ESD process is of range within 20-200 nm, that provides entirely new physicomechanical properties of the materials. The separate micropores with size of up to 2 μm are observed in the coating structure too.

It is noteworthy that after the electrospark doping with the rotating electrode and the subsequent surface plastic processing of the coating obtained, the surface is characterized by sufficiently high continuity and low surface roughness, while the electrospark coatings obtained with use of devices with end electrode vibrators are usually characterized by high surface roughness of the treated surface [1, 5].

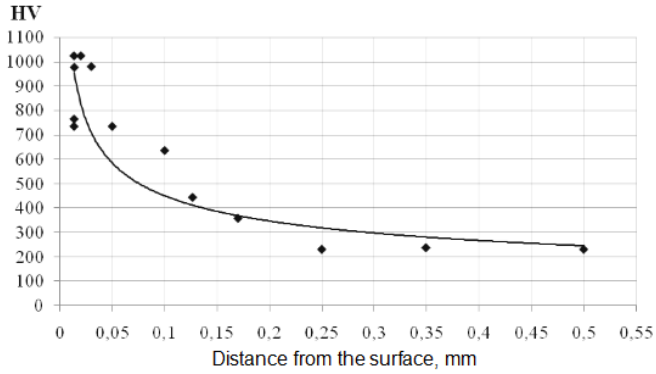

Fig. 3. *Distribution of microhardness throughout the depth of the coating*

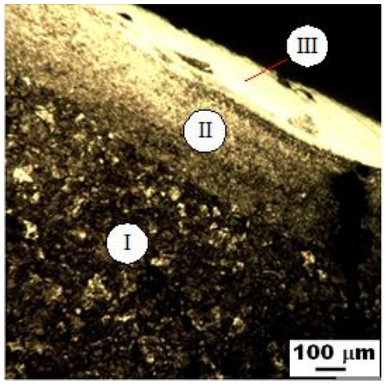

(a)

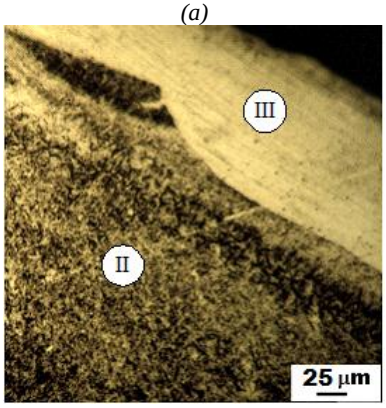

(b)

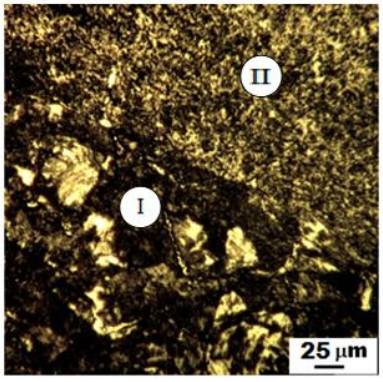

(c)

Fig. 4. *The microstructure of steel surface subjected to combined superficial plastic processing and electrospark doping: I – carbon steel base material; II - intermediate transition layer; III – the layer of electrospark coating*

The results of X-ray spectral analysis of the initial material and the layers subjected to various types of processing (surface plastic deformation, ESD) showed that, in the initial state, У7 steel contains α-Fe and cementite Fe_3C phases (fig. 5, a). The value of the bcc lattice parameter of α-Fe is a = 0.28664 nm. The diffraction lines of the matrix α-Fe phase are narrow, which indicates a low concentration of lattice defects (fig. 5a).

X-ray diffraction lines of α-phase from the intermediate layer, obtained after surface plastic deformation, are significantly diffused (fig. 5, b). In particular, the magnitude of the physical broadening of the α-Fe diffraction line increases to the level of $\beta_{220} \approx 21 \cdot 10^{-3}$ rad, whereas for steel in the initial state, the value of $\beta_{220} \approx 2{,}5 \cdot 10^{-3}$ rad. Such increase in the value of physical broadening is associated with an increase in the concentration of lattice defects (dislocations, vacancies, etc.) in the α phase in the process of intense surface plastic deformation. The fact that the ratio $\beta_{220}/\beta_{110} \approx tg\theta_{220}/tg\theta_{110}$ testifies in favor of this conclusion too.

Besides, the value of the crystal lattice parameter of α-Fe significantly increases after surface plastic processingin in comparison with non-deformed steel and reaches values of 0.28679 nm. The authors of [1, 11, 13] consider that such an increase in α–Fe crystal lattice parameter can be caused by deformation-induced dissolution of cementite particles Fe_3C in the process of steel intense plastic deformation when it is rolled.

The analysis of phase composition of the samples upper layer after electrospark doping showed, that in addition to ferritic α-Fe phase, it contains a number of phases formed during the interaction of the electrode material with steel. The predominant compound is F_3W_3C carbide with a cubic lattice, WC, W_2C semi-carbide and possibly high-temperature β-W_2C carbide are fixed (fig. 5, c). The lattice parameter of the α-Fe phase increased in the alloying process from 0.28654 nm of the initial steel to 0.28689 nm for the coating surface.

The broadening of the X-ray β_{220} line profile of the surface layer treated with ESD reaches $36{,}141621 \cdot 10^{-3}$ rad, which indicates the formation of a substructure in the alloyed steel surface. The ratio β_{220}/β_{110} is close to the ratio of the tangents of the angles ($tg\upsilon_{220}/tg\upsilon_{110}$), which is caused by a significant deformation of the α-Fe phase crystal lattice. Since the composition of electrodes for electrospark doping includes Co, that can form an unlimited solid solution with iron, and also taking into account the rather high solubility in tungsten iron (up to 30%) at liquidus temperatures, it can be assumed that the increase in α-Fe phase lattice parameter after ESA is conditioned by dissolution of the electrode components in Fe.

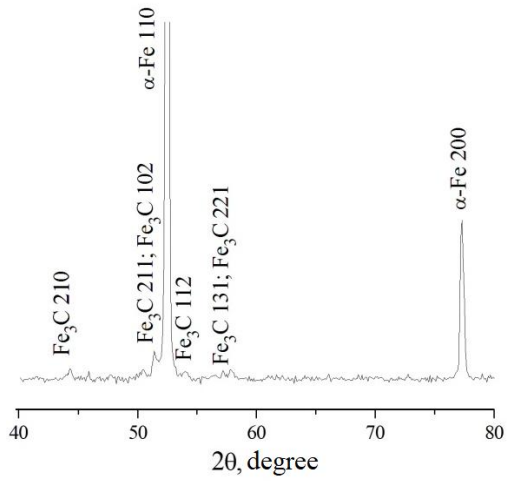

(a)

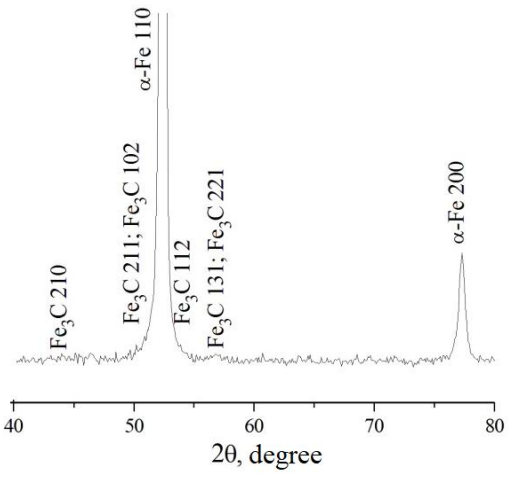

(b)

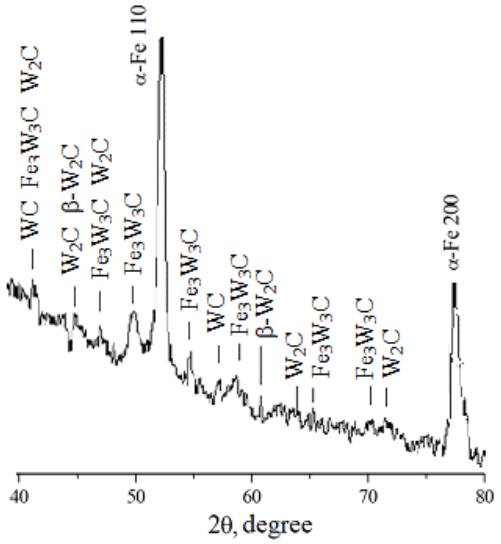

(c)

Fig. 5. *Fragments of X-ray diffractograms from the internal (a), intermediate (b) and surface (c) layers of the specimens*

Comparative assessment of the wear resistance of the original У7 steel and the material of the samples subjected to complex surface treatment including surface plastic deformation, ESD followed by rolling of the applied layer with a ball showed (fig. 6) that the wear of the original steel after the path of 25 km exceeds the wear of samples subjected to surface treatment for ~4 times, and the amount of wear obtained on the original steel after the path of 50 km (450 mg) is achieved on samples subjected to processing only after 200 km.

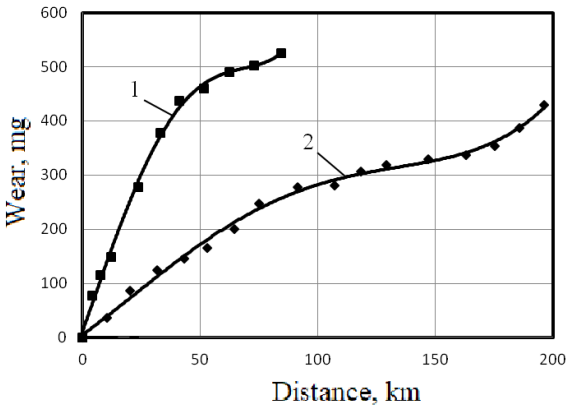

Fig. 6. Dependence of mass wear for the samples from У7 steel (HV 220 ... 240): 1 – samples without surface treatment; 2 – samples subjected to complex surface treatment

4. Conclusions

1. It is shown that the use of combined treatment of steel surface, including surface plastic deformation processing, electrospark doping and additional smooth rolling of the applied coating with a steel roller, provides a gradient-layered structure with entirely new physicomechanical properties and low surface roughness.

2. Based on the X-ray analysis of the surface obtained after the electrospark treatment, it has been established that the phase composition of the layer in addition to the ferritic α-Fe phase contains a number of carbide phases formed during the interaction of the electrode material with steel: F_3W_3C, WC and W_2C semi-carbide. The lattice parameter of the α-Fe phase increased during the doping process from 0.28654 nm for the initial steel to 0.28689 nm of the coating surface, which may be caused by electrode components dissolution in Fe.

3. The efficiency of complex surface treatment of steel is shown, which provides surface layers, the wear resistance of which exceeds similar properties of the original carbon steel up to 4 times.

5. References

1. Mikhailyuk A. I., Zhitaru R. P. Features of Plastic Deformation of Electrospark Coatings and Ways for Improvement of Their Strength Characteristics at Friction // Surface Engineering and Applied Electrochemistry. – 2008. – Vol. 44, No. 5. – P. 383–389.

2. Paustovskii A. V., Tkachenko Yu. G., Alfintseva R. A., Kirilenko S. N., Yurchenko D. Z. Development of Electrode Materials for Electrospark Hardening and Reconditioning of Worn Out Surfaces: The Structure and Properties of the Coatings // Surface Engineering and Applied Electrochemistry, 2011, Vol. 47, No. 2, pp. 126–131.

3. Верхотуров А.Д. Формирование поверхностного слоя металлов при электроискровом легировании. - Владивосток: Дальнаука, 1995. - 323 с.

4. Машков Ю. К., Коротаев Д. Н. Микроструктура и свойства поверхностного слоя при электроискровом легировании // Технология металлов, 2006, № 3, с. 10-13.

5. Белик В.Д., Литвин Р.В., Ковальченко М.С., Рогозинская А.А. Влияние длительности импульса и величины межэлектродного промежутка на процесс электроискрового напыления // Порошковая металлургия. – 2001. - №1/2. – С.115- 121.

6. Мазурский М.И. , Еникеев Ф.У. О некоторых принципах получения однородной сверхмелкозернистой структуры методами обработки металлов давлением // Кузнечно-штамповочное производство. – 2000. – №7. – С. 15-18.

7. Суслов А.Г., Блюменштейн В.Ю., Гуров Р.В. и др.Технология и инструменты отделочно-упрочняющей обработки деталей поверхностным пластическим деформированием: справочник. В 2-х томах. Т. 1. / Под общ. ред. А.Г. Суслова. — М.: Машиностроение, 2014. — 480 с.

8. Бабей Ю.И., Бутаков Б.И., Сысоев В.Г. Поверхностное упрочнение металлов. -К.: Наукова думка, 1995. - 256 с

9. Klopotov V. D., Denisova Yu. A., Teresov A. D. et al. Combined treatment of steel, including electrospark doping and subsequent irradiation with a high-intensity electron beam // IOP Conf. Series: Materials Science and Engineering, 124 (2016) 012125, doi: 10.1088/1757-899X/124/1/012125

10. Бородій Ю. П. Розробка технологій та устаткування для нанесення комбінованих зносостійких покриттів на деталі типу валу // Вісник НТУ «ХПІ». - 2014. - № 5 (1048). - С. 111-119.

INFLUENCE OF THE SYNTHESIS METHOD ON THE CRYSTALLINE STRUCTURE, PHASE COMPOSITION AND PROPERTIES OF TiCrFeNiCuC EQUIATOMIC ALLOYS

M.Sc. Marych M., Mamonova A., PhD., Prof. Bagliuk G., Dr. Sc.
Institute for Problems of Materials Science, National Academy of Science of Ukraine,
Kyiv, Ukraine

E-mail: gbag@ukr.net

Abstract: *Equiatomic alloys TiCrFeNiCuC were made by two methods of powder metallurgy – vacuum sintering and hot forging followed by annealing. In the process of sintering the TiCrFeNiCuC blanks, the influence of entropy of mixing resulted in the formation of solid substitution solutions mainly on the basis of the FCC lattice, and also formed titanium carbide ($TiC_{0.74}$). In samples obtained by hot forging and subsequent annealing, two carbides TiC and Cr_3C_2 were found, and titanium carbide being formed with lower carbon content ($TiC_{0.58}$). In addition, the forged samples showed significantly higher values of the defect of the crystalline structure, which leads to increase in their hardness.*

Keywords: *EQUIATOMIC ALLOYS,* MICROSTRUCTURE, PHASE COMPOSITION, HARDNESS, SINTERING, HOT FORGING.

1. Introduction

In the field of creating new classes of materials with increased physical, mechanical and operational properties, the approaches based on the development of high entropy alloys (HEAs) are the most promising.

A characteristic feature of such alloys is the content in their composition of not less than 5 basic elements, mainly in the equiatomic ratio. The presence of a large (not less than five) number of heterogeneous, but in an equal number of atoms, having different individual properties, imposes its specificity on the formation of a solid solution of high entropy alloys. The high entropy of mixing causes the minimization of the free Gibbs energy, which leads to the preferential formation of solid solutions with a BCC, FCC or FCC + BCC structure. The phases formed on the basis of solid solutions are more stable [1-3]. Alloys with such structures have high hardness, strength, wear resistance, oxidation resistance, etc. These properties of high entropy alloys are due to the slow diffusion of atoms in a multicomponent matrix, a significant distortion of the lattice, which arises in connection with the difference in the atomic dimensions of the constituent elements of the alloy, as well as the interaction between elements in phases based on a solid solution [4-9]. When giving carbon in the alloys, high entropy carbides will form.

To obtain HEAs the most widely used were various casting technologies [1-6]. However, in recent years, the methods of powder metallurgy are gaining increasing popularity in the development and production of these alloys [7-10].

The purpose of the work is to study the influence of the manufacturing method on the crystalline structure, phase composition and properties of the TiCrFeNiCuC equiatomic alloys.

2. Experimental Procedure

The initial Ti, Cr, Ni, Cu, Fe, and C powders with the purity of 99.5 - 99.9% were used as the starting elements for the preparation of the equiatomic alloys of the Ti-Cr-Fe-Ni-Cu-C system. Alloys were produced by two methods of powder metallurgy – vacuum sintering and hot forging with subsequent annealing.

The starting powders were dosed on an electronic scales. The charge of the equiatomic composition was prepared by mixing the powders in a drum mixer with a diagonal axis for 2 hours with the addition of alcohol. From the obtained mixture, cylindrical billets with a diameter of 20 and 40 mm at a pressure of 700 MPa were extruded in a steel matrix. Consolidation of powder blanks by hot forging was carried out on a dougostator press at a temperature of 1050 ° C in argon. Sintering of the samples and annealing of the forged samples were carried out in a vacuum induction furnace at 1200 °C for 2 hours.

X-ray diffraction studies were carried out on a DRON-3 X-ray diffractometer in filtered Co radiation by a step-scan method in the angular range 20÷130°. A quantitative micro-X-ray spectral analysis was performed on a CAMECA MS-46 X-ray microprobe at a probe mode of 20 kV, 12 nA and a probe diameter of 3 μm. The microstructure of the alloys was studied with an XJL-17 optical microscope and with a JEOL Superprobe 733 scanning electron microscope. The density and porosity of the alloys were determined by hydrostatic weighing. The microhardness was measured on a PMT-3 device. The hardness was measured on a TK-14-250 hardness tester. The theoretical density of the alloy, calculated from the additivity formula, is equal to 6.55 g/cm^3.

3. *Experimental results and their discussion*

X-ray diffraction studies of high entropy TiCrFeNiCuC alloys, obtained by different methods, revealed features both in the phase composition and in the defectiveness of their crystal unit cell. Regardless of the method of preparation, alloys had a heterogeneous structure. On the X-ray diffraction pattern of the alloy obtained after sintering at 1200 ° C for two hours, a number of lines characterizing the phase with a FCC lattice are fixed, as well as TiC carbide. On the lines with the indices of the atomic planes (311) and (222), we can assume the presence of two phases with FCC lattices with close values of the crystal lattice parameter (Fig. 1, a). The phase with the BCC structure is fixed weakly.

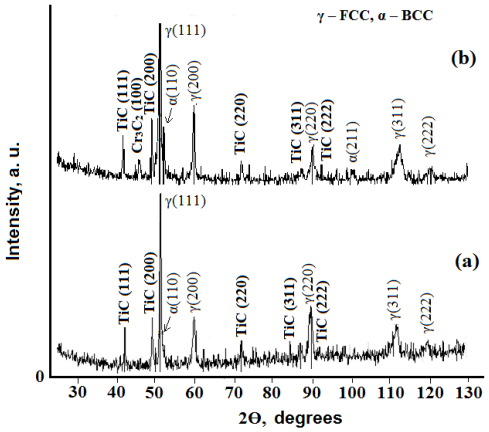

Fig. 1*. XRD patterns of TiCrFeNiCuC alloys, obtained by vacuum sintering (a) and hot forging with subsequent annealing (b)*

On the X-ray diffraction pattern of the sintered alloy, the diffraction maxima (111) and (222) were divided into two components (Fig. 2). The calculated crystal lattice parameters for both FCC phases are: a = 0.36098 nm and a = 0.35877 nm. It is known that nickel and copper are systems with unrestricted solubility based on the structural type of FCC. It should be assumed that one phase of FCC with a = 0.36098 nm is formed with a high copper content (a_{Cu} = 0.36176 nm), another phase a = 0.35877 nm – with a high nickel content (a_{Ni} = 0.35195 nm). An analysis of the structural state of phases with a FCC structure indicates that both

phases of the FCC have a number of imperfections in their crystal lattice and a difference in the quantitative ratio of their defectiveness, characterized by the values of the parameters of the fine structure elements. Thus, for FCC with a high copper content with a = 0.30988 nm, the defectiveness of the crystal structure is denoted by the following parameters: coherent scattering region (CSR) = 36.2 nm, microdistortion $\Delta a/a = 54.6 \times 10^{-3}$, dislocation density $\rho = 8.2 \times 10^{11}$ cm^{-2} . For a FCC structure with a high nickel content a = 0.35877 nm. Data on the imperfections of the FCC alloy structure is much higher in comparison with the analogous results for the phase with the predominant copper content and are denoted by the following parameters: CSR = 10.0 nm, $\Delta a/a = 77.2 \times 10^{-3}$, $\rho = 17.3 \times 10^{11}$ cm^{-2}. The FCC phase, which is formed with the predominant content of the more ductile element of copper, naturally has a less distorted crystal lattice in comparison with the FCC lattice with a harder nickel base. This conclusion is confirmed by microhardness measurements: a FCC structure with a crystal lattice parameter equal to a = 0.36098 nm has a microhardness of 4.9 GPa, a structure with a crystal lattice parameter equal to a = 0.35877 nm has a microhardness of 6.8 GPa.

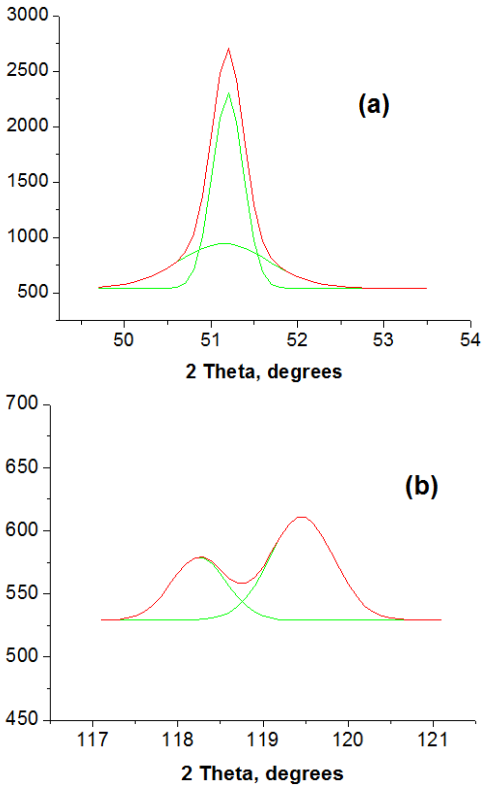

Fig. 2. *Fragments of the XRD pattern of the TiCrFeNiCuC alloy, obtained by sintering at 1200 ° C for 2 hours, in the peak region (a) (111); (b) (222)*

Along with solid solutions of the FCC type in the highly entropic TiCrFeNiCuC alloy obtained by sintering at 1200 °C for two hours, titanium carbide with a crystal lattice parameter of 0.43215 nm is formed. According to the dependence of the TiC cell parameter on the amount of carbon bound in it [12] in the sintered alloy, there is a TiC phase with an atomic ratio of carbon to titanium of 0.74 ($TiC_{0.74}$).

The formation of phases in highly entropic alloys, the appearance of two or three phases is associated with a certain electronic concentration in the alloy, with the difference in the atomic radii of the components that make up the alloy. Hot forging is a significant influence on the formation of the crystal structure of high entropy alloys. Hot forging of porous blanks can be considered one of the cycles of thermomechanical processing, during which a developed substructure is created. This developed substructure is the primary factor determining all other structural causes of thermomechanical hardening of steel. [11].

X-ray diffraction studies of the alloy TiCrFeNiCuC, obtained by hot forging and subsequent high-temperature annealing, indicate the formation of a heterophase structure of the alloy. The X-ray spectrum of the alloy is represented by phases of FCC, BCC, TiC and Cr_3C_2 carbides (Fig. 1 b).

Analysis of the X-ray spectrum of the alloy revealed the following features. Estimating the nature of the profiles of the X-ray lines of the FCC structure, several blurred profiles should be noted that describe the phase with the FCC grating, which is especially noticeable at large reflection angles. Thus, for a FCC lattice along lines with indices of atomic planes (311) and (222), it is possible to assume the presence of two phases with FCC lattices with close parameters. This is confirmed by calculations on the lines (222): a_1 = 0.36460 nm and a_2 = 0.35815. On the XRD pattern of the forging alloy, the diffraction maxima (111) and (222) were decomposed into two components (Fig. 3).

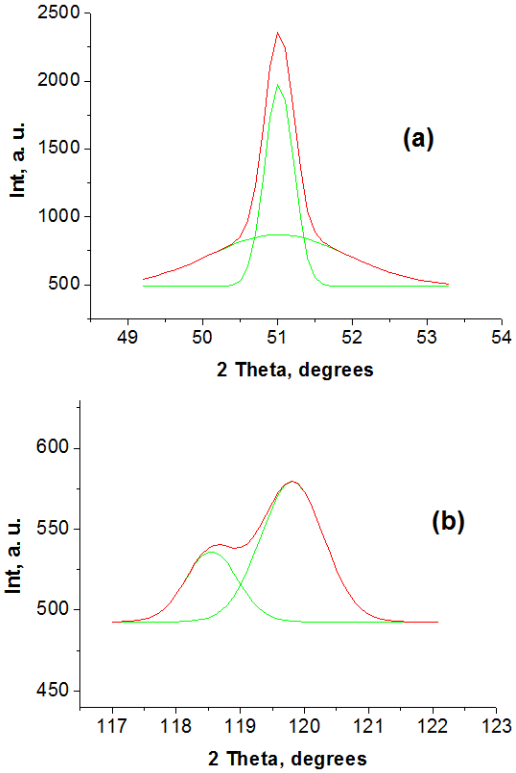

Fig. 3. *Fragments of the XRD pattern of the TiCrFeNiCuC alloy obtained by hot forging at 1050 ° C, followed by annealing at 1200 ° C for 2 hours, in the peak region: a) (111), b) (222)*

One of the phases with the parameter a_1 = 0.36046 nm a_2 = 0.35815 copper i.e. with a high copper content, another phase of FCC with a_2 = 0.35815 nm is closer to the nickel parameter, i.e. with a high content of nickel.

An analysis of the structural state of phases with a FCC structure indicates that both phases of the FCC have a number of imperfections in their crystal lattice and a difference in the quantitative ratio of their defectiveness, characterized by the values of the parameters of the fine structure elements. Thus, for the FCC lattice with a high copper content a = 0.36098 nm, the defectiveness of the crystal structure is denoted by the following parameters: CSR = 5.2 nm, microdistortion $\Delta a/a = 90.4 \times 10^{-3}$, dislocation density $\rho = 22.6 \times 10^{11}$ cm^{-2} For a FCC structure with a high nickel content a = 0.35815 nm. Data on distortion of the lattice of the FCC structure of the alloy is much higher in comparison with the analogous results for the phase with the predominant content of copper and are denoted by the following parameters: $\Delta a/a = 119.8 \times 10^{-3}$, $\rho = 42.0 \times 10^{11}$ cm^{-2}. There is no grain fragmentation in the coherent scattering region (CSR = 112.3 nm, i.e, commensurate with the grain size), the structural defect is due to the distortion of the crystal lattice. The FCC phase, which is formed with the predominant

content of the more ductile element of copper, naturally has a less distorted crystal lattice in comparison with the FCC lattice with a harder nickel base. This conclusion is confirmed by microhardness measurements: a FCC structure with a crystal lattice parameter a = 0.36098 nm has a microhardness of 5.5 GPa, a structure with a lattice parameter a = 0.35877 nm has a microhardness of 7.3 GPa.

The most intense line (110) of the structure with a BCC lattice on the x-ray spectrum of the sample is indicated by a line of weak intensity, which indicates a small amount in the sample alloy. In addition to line (110), we can consider the line (211) belonging to the BCC structure as a weak diffuse reflex. Line (220) is almost overlapped with the background. The diffuse character of the BCC reflections is due to the distortion of the crystal lattice, which is confirmed by the quantitative characteristics of the fine structure elements. So the value of the regions of coherent scattering is 50.0 nm (probably somewhat overestimated as a result of overlapping of the part of the profile from the side of the small angle by the line of the FCC lattice (110)), microdistortions equal to 175.87×10^{-3}, the dislocation density is $\rho = 62.0 \times 10^{11}$ cm^{-2}. The results on the distortion of the crystal lattice of the BCC phase are the largest for all the emerging highly entropic phases. The phase with the BCC structure is formed upon mutual dissolution of iron and chromium, has the parameter a_{bcc} = 0.2858 nm, has so small a grain that it was impossible to measure the microhardness.

It was pointed out that on the XRD pattern of the alloy, in addition to a series of phase lines of FCC and BCC structures, a number of reflections belonging to TiC and Cr_3C_2 carbides. The TiC lattice parameter is 0.4311 nm, hence, the TiC phase is present in the alloy with an atomic carbon to titanium ratio of 0.58 ($TiC_{0.58}$). In the sintered alloy, the atomic ratio of carbon to titanium is 0.74.

The microstructure of the sintered and forged alloys consists mainly of two structural regions. According to micro-X-ray spectral analysis, the light phase has an increased content of Cu, Fe, and Cr. The darker phase is the result of the maximum interdiffusion of all elements of the alloy and has an increased concentration of Ni, Ti and C. Consequently, the dark phase contains TiC. In the forged alloy, a much greater dispersion of the structural elements is observed compared to the sintered alloy, as well as the presence of two carbides – TiC and Cr_3C_2, which is explained by the influence of hot forging.

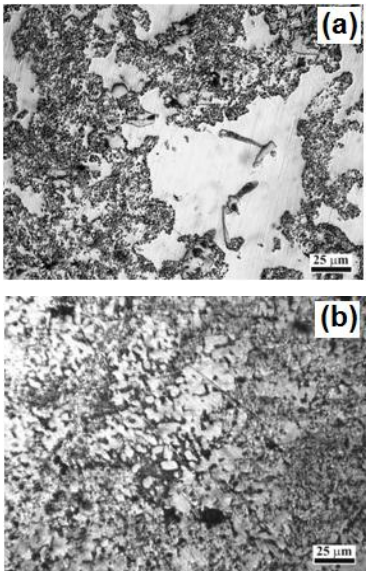

Fig. 4. *Microstructures of sintered (a) and forged (b) equiatomic TiCrFeNiCuC alloys*

Analysis of the processes of structure formation of high entropy phases formed in alloys of TiCrFeNiCuC composition, inclusions of various compounds showed a significant increase in the defectiveness of crystal structures and, accordingly, an increase in the microhardness of both individual structural components and hardness of the alloy as a whole, using preliminary hot forging of porous blanks. In the sintered alloy, the hardness is 30 HRC, in the alloy with the preliminary hot forging, the hardness increased to 42 HRC (Table 1).

Table 1. *Characteristics of TiCrFeNiCuC alloys obtained*

№	Production method	Density, g/cm^3	Porosity, %	Hardness, HRC
1	Sintering	6,28	4,0	30
2	Hot forging and annealing	6,40	2,2	42

3. Conclusions

Thus, preliminary hot forging during the formation of a high entropy alloy intensifies the processes of structure formation, causes redistribution of carbon (with the formation of chromium carbide Cr_3C_2, titanium carbide TiC is formed with a smaller carbon content in TiC to 0.58), and also provides processes that lead to significant distortion of the crystalline lattice of the forming phases, which contributes to the strength of the alloys.

References

1. *Wang Y.P. et al.*, "Microstructure and compressive properties of AlCrFeCoNi high entropy alloy," Mat. Sci. and Eng. A 491, pp. 154—158, 2008.

2. *Wang F.J., Zhang Y.* Effect of Co Addition on Crystal Structure and Mechanical Properties of Ti0.5CrFeNiAlCo High entropy alloy // J. Mater. Sci. Eng. A 496, pp. 214 — 216, 2008.

3. *Zhang Ch. et al.*, Computational Thermodynamics Aided High-Entropy Alloy Design // JOM, vol. 64, No. 7, pp. 839—845, 2012.

4. *Yeh J.W.* Recent progress in high-entropy alloys // Ann. Chim. Sci. Mat., vol. 31, pp. 633—648, 2006.

5. *Tang W.-Y. et al.* Microstructure and Mechanical Performance of Brand-New Al0.3CrFe1.5MnNi0.5 High-Entropy Alloys // Advanced Engineering Materials, vol. 11, No. 10, pp.788—794, 2009.

6. Firstov S.A., Gorban V.F., Krapivka N.A. Mechanical properties of cast multicomponent alloys at high temperatures // Current problems of physics material science. - 2008. - Issue. 17. - P. 126-139.

7. *Fan Y. H, Zhang Y. P, Guan H. G, Suo H. M, He L.* AlNiCrFe*x*$Mo_{0.2}$CoCu High Entropy Alloys Prepared by Powder Metallurgy // Rare Metal Materials and Engineering. – 2013. Vol. 42, No.6. – P. 1127–1129.

8. *Qiu X. W.* Microstructure and properties of AlCrFeNiCoCu high entropy alloy prepared by powder metallurgy // Journal of Alloys and Compounds. – 2013. – Vol. 555. – P. 246–249.

9. Yurkova A.I., Chernyavsky V.V., Gorban V.F. Structure and mechanical properties of high entropy AlCuNiFeTi and AlCuNiFeCr alloys, obtained by mechanical alloying with subsequent sintering under pressure // Powder Metallurgy. - 2016. - No. 3/4. - P. 37-52.

10. Bagliuk G.A., Marych M.V., Mamonova A.A., Gripachevsky A.N. Features of the structure formation in the sintering of compacts from a multicomponent charge of the TiCrFeNiCu system // Powder Metallurgy. - 2015. - No. 9/10. - P. 46-52.

11. Bernstein M.L. Structure of deformed metals. - Moscow: Metallurgy, 1977. - 432 p.

12. Kyparisov S. S., Levinsky Yu. V., Petrov A. I. Titanium carbide: production, properties, application. - Moscow: Metallurgy. 1987. - 216 p.

FATIGUE ANALYSIS APPROACHES FOR VEHICLE COMPONENTS MADE OF RUBBER

M.Sc. Tomposne Szüle V.[1],
Department of Applied Mechanics – University of Széchenyi István, Győr, Hungary
szule.veronika@sze.hu

Abstract: Generally, the most frequently used structural materials are metals which have high strength and stiffness. However, there are many cases, when other important properties come to the fore as well as high deformation by elastic behavior, high viscosity namely good damping effect. Vehicle components made of rubber usually exhibit large deformations. One of the most important properties of rubber is the ability to withstand large strains without permanent fractures. This feature makes it ideal for many engineering applications. On the other hand, the task becomes more complicated because of some features of rubber parts. The temperature of rubber increases significantly after deformations. Material properties of rubber change after these above mentioned temperature changes. Thus it is necessary to understand the mechanics underlying the failure process. This paper summarizes the applied equations and the basic physical laws which are responsible for the theoretical background of the strain and temperature changes and the analysis approaches that are available for predicting fatigue life in rubber, especially in vehicle components made of rubber.

Keywords: RUBBER, HIGH DEFORMATIONS, THERMODYNAMICS, FATIGUE ANALYSIS

1. Introduction

Rubber can be classified as a so-called hyperelastic polymer which has a typical geometrical and material nonlinear behavior. It means that the relationship between displacements and internal forces can be described by functions whose order is higher than linear. The geometrical nonlinearity is easy to handle mathematically, however the material nonlinearity is only described approximately [1], [2]. Independently of the experimental investigations which deal with the material behavior of rubber, a number of theoretical works treated rubber as an ideally nonlinear elastic, in particular hyperelastic material. One of the properties of the constitutive equations of hyper-elastic material is that stresses are derived from stored elastic energy function. Hyper-elasticity can be described by particularly convenient constitutive equation given its simplicity and it constitutes the basis for more complex material models such as elastoplasticity, viscoplasticity, and viscoelasticity [3,4,5,6].

Furthermore, the task becomes more complicated because of some features of rubber parts. The temperature of rubber increases significantly. Therefore, the temperature- and displacement fields are coupled, and it means that special solving algorithms are required [7]. So the equations of mechanics and thermodynamics are coupled. As described above, the goals of this paper are the following:

It is necessary to summarize the applied equations and the basic physical laws which are responsible for the theoretical background [8,9]. Clarification of these relationships is essential because the material laws of rubber cannot violate those basic physical laws. It is necessary to extend these relationships like balance of linear momentum and balance of angular momentum, the first and second law of thermodynamics to high deformation of rubber and rubberlike polymers. An algorythm will be presented which allows to calculate strain changes and temperature changes of the rubber part of a vehicle component under certain conditions. The present numerical algorithm is the basis of the further fatigue and lifetime-calculations. After this, it will follow the literature survey which is responsible for predicting fatigue life.

2. Governing equations

2.1 Equilibrium of linear momentum

The differential formulation of the equilibrium of linear momentum in the current configuration is

$$\rho\dot{\vec{v}} = \underline{\underline{\sigma}} \cdot \nabla + \vec{f} \tag{1}$$

where ρ is the mass density, $\vec{v}$ is the velocity, $\underline{\underline{\sigma}}$ is the Cauchy stress, $\vec{f}$ is the volume force.

2.2 Equilibrium of angular momentum

The next equality shows the differential form of the balance of the moments.

$$\underline{\underline{\sigma}} = \underline{\underline{\sigma}}^{T} \tag{2}$$

2.3 First law of thermodynamics

When deformations repeatedly occur, significant increase in temperature can be observed. The differential form of the first law of thermodynamics is in the current configuration

$$\dot{e}\rho = \left[-\nabla \cdot \vec{q} + h\right] + \underline{\underline{\sigma}} \cdot \cdot \underline{l} \tag{3}$$

where e is the internal energy per unit mass, $\vec{q}$ is the heat flux, h is the heat source, $\underline{l}$ is the velocity gradient, $\underline{l} = \underline{\underline{F}} \cdot \underline{\underline{F}}^{-1}$, $\underline{l} = \vec{v} \circ \nabla$.

2.4 Second law of thermodynamics

The behaviour of viscoelastic materials is described by the second law of thermodynamics. The second law of thermodynamics in the current configuration can be written as

$$\dot{\eta}T\rho \geq -\nabla \cdot \vec{q} + \frac{\vec{q} \cdot \nabla T}{T} + h \tag{4}$$

where η is the entropy per unit mass and T is the absolute temperature. It will be practical to change the variable from entropy per unit mass to temperature by applying the Legendre-transformation and by using the Helmholtz-free energy

$$\psi = e - \eta T \tag{5}$$

Substitute the Eqn. (5) into to the Eqn. (3) and subtract Eqn. (3) from Eqn. (4) the following expression will be generated

$$-\left(\dot{\psi} + \eta\dot{T}\right)\rho + \underline{\underline{\sigma}} \cdot \cdot \underline{l} - \frac{\vec{q} \cdot \nabla T}{T} - \mathrm{D} \geq 0 \tag{6}$$

which is known as Clausius-Duhem inequality [2].

2.4 Constitutive model

The property of an elastic element is that the total mechanical energy is reversible. The free energy of the body is the function of the strain and temperature. Dissipation comes only from heat conduction.

In order to make the further calculations easier it is necessary to split the Eq. (5) to temperature-dependent and temperature-independent parts. Based on known functions $\tilde{\psi}_0\left(\underline{\underline{C}}\right)$ and $e_0\left(\underline{\underline{C}}\right)$ for the free energy and the internal energy at a given reference temperature and the given heat capacity at a reference temperature, one obtains the following general structure for the thermoelastic free energy from the Eq. (5):

$$\psi\left(\underline{\underline{C}},T\right)=\tilde{\psi}\left(\underline{\underline{C}},\tilde{T}\right)=\frac{T}{T_0}\psi_0\left(\underline{\underline{C}}\right)+(1-\frac{T}{T_0})e_0\left(J\right)+\int_{T_0}^{T}\hat{c}\left(\underline{\underline{C}},\tilde{T}\right)\left(1-\frac{T}{\tilde{T}}\right)d\tilde{T} \quad (7)$$

where $\underline{\underline{C}}$ is the right Cauchy-Green strain tensor [2]. In the following section we are going to investigate the isotrop materials and we are going to apply the Neo-Hookean material law. It means that which is used in free energy depends on the scalar invariant of the right Cauchy-Green strain tensor. The internal energy is zero applying the entropic theory and the heat capacity is constant with good approximation.

2.5 Equation of heat conduction

Starting from the first law of thermodynamics and introducing the internal energy and changing the variable from entropy to temperature, the equation will have the next form:

$$\rho_0 c\dot{T}=\left(\underline{\underline{S}}-\rho_0\frac{\partial\psi}{\partial\underline{\underline{C}}}\right)\cdot\cdot\frac{1}{2}\dot{\underline{\underline{C}}}+\rho_0\frac{\partial^2\psi}{\partial T\partial\underline{\underline{C}}}\cdot\cdot\dot{\underline{\underline{C}}}T-q_0\nabla_0+h_0 \quad (8)$$

where $\left(\underline{\underline{S}}-\rho_0\frac{\partial\psi}{\partial\underline{\underline{C}}}\right)\cdot\cdot\frac{1}{2}\dot{\underline{\underline{C}}}$ is the non-recoverable part of the mechanical power, which is zero in the case of a pure elastic element [1], [2]. In this case the reological model is regarded to be a pure elastic element. So the free energy of the body is characterized by the deformation and temperature. Furthermore, we are assuming that there are not heat sources in the rubber and the temperature field shows homogeneous distribution. Thus, the equation of the heat conduction is the following:

$$c\dot{T}=T\frac{\partial^2\psi}{\partial T\partial\underline{\underline{C}}}\cdot\cdot\dot{\underline{\underline{C}}} \quad (9)$$

2.6 Example

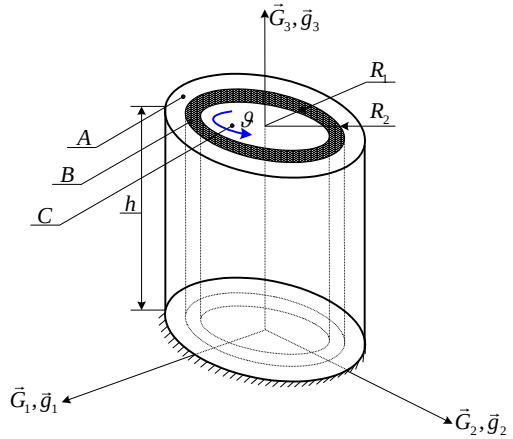

Fig. 1. Mechanical model of a silent block

Let us consider the mechanical model of a silent block, thus the A, B, C axisymmetric bodies (see Fig.2). The A and C bodies are rigid bodies, and B is a deformable one. Regarding the structure of the silent block it consists of two metal elements whose are connected by the rubber which is vulcanized between them. The inside rubber part provides a non-linear elastic connection between the two metal elements in the following way: it transfers loads however filters out the harmful vibrations, i.e. it has damping effect. All three bodies are axysymmetric and their symmetry axes are the same.

The external body (A) is fixed and the internal one is imposed by a given rotation.

Further assumptions:

Planes perpendicular to the symmetric axis will be planes after the deformation. The magnitude of the displacement is linear function of the measured distance from the axes of symmetry. Furthermore, we are assuming that there aren't heat sources in the rubber and the temperature field shows homogeneous distribution, $h_0=0, q_0=0$. Fig.2 presents the temperature change by the effect of vibration frequency 1 Hertz.

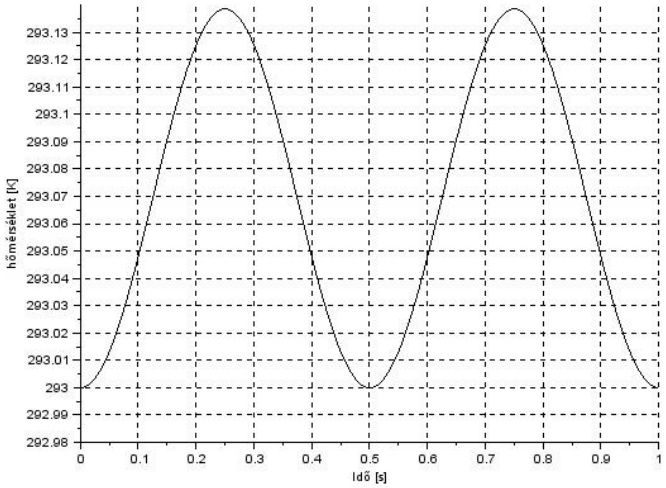

Fig. 2. Temperature change as the function of time

The calculation of temperature changes which is caused by the effect of vibration frequency 1 Hertz is obtained by the using of Eq.(9), i.e. $c\dot{T}=T\frac{\partial^2\psi}{\partial T\partial\underline{\underline{C}}}\cdot\cdot\dot{\underline{\underline{C}}}$. Substitution of the next relation to the Eq.(9), $\varphi=\vartheta\sin\left(\omega t\right)\frac{R_2-R}{R_2-R_1}$ the temperature changes can be calculated. Generation of calculations and the representation of the temperature changes as the function of time were determined by the SCILAB program. This calculation will be the basis of the further fatigue and lifetime calculations. In the next a brief literature survey on fatigue analysis approaches will be presented.

3. Literature survey: types of fatigue analysis approaches of rubber

The facility of rubber is the resistance finite strains without permanent deformation makes it ideal for engineering applications e.g. vehicle components made of rubber, as can be seen in the first figure. These loading cases impose large static and time-varying strains over a long period. The fatigue failure analysis have two distinct sections. The first section is a time during which cracks nucleate in regions. The second section is a time during nucleated cracks grow to the point of failure. Two further models for predicting fatigue life in rubber have to be considered. One theory occupies with the predicting crack nucleation life, given the history of quantities like stress and strain in the current configuration. The other theory derives from fracture mechanics, focuses on prediction of the growth of each cracks. Some of the information described in this paper has been reviewed previously [10-15]. Another paper summarizes factors that influence the fatigue life of rubber [16]. These factors are the effects of the mechanical loading history, environmental effects, rubber formulation, and effects due to dissipative aspects of the constitutive response of rubber.

3.1 Models for predicting crack nucleation life

Let us consider fatigue crack nucleation life which is defined as the number of cycles required to cause the appearance of a crack or cracks. The first study of this was Wöhler's work in the 1860's [17]. The maximum principal strain and the strain energy density

are the two widely used fatigue life parameters for crack nucleation approach in rubber. Strain can be directly determined from displacements, which can be measured in rubber. The strain energy density can be estimated from a hyperelastic strain energy density function, which can be defined in terms of strains. The alternating and mean values of maximal principal strain predict nucleation life. The earliest fatigue studies in rubber occupied with the developing of the description of the number of cycles to failure as a function of starin. Cadwell et al. [18] considered unfilled rubber and investigated minimum engineering strains and strain amplitudes in determined range. They stated that, for constant strain amplitude, the fatigue life of rubber improves with extending minimum strain, up to a high strain level, and the additional minimum strain decreased the life. Generally, in the case of strain crystallized rubbers, by increasing the minimum strain of the strain cycle can significantly elongate the fatigue life.

The strain energy density is the second most important parameter which can be used for prediction of fatigue crack initiation. The energy release rate is proportional to the product of strain energy density in certain conditions and the crack size [19, 20]. Several paper can be mentioned in which researchers investigated strain energy density as a fatigue life parameter in rubber. According to the research of Roberts and Benzies [21], and Roach [22], the equibiaxial tension fatigue life of natural rubber is longer than simple tension fatigue life, in the case of using equal strain energy density. Furthermore, Roach gave the best correlation between simple and equibiaxial tension fatigue data, i.e. Roach proposed –in the case simple tension-that all of the strain energy density is available for flaw growth.

3.2 Models by using crack growth approach

The pre-existing cracks or flaws are in the focus of the crack growth approaches. The two main bases of this type of approach are the works which were publicated by Inglis and later Griffith [23]. Griffith offered a fracture criterion based on energy balance including both the mechanical energy of a cracked body, and the energy associated with the crack surfaces. This approach was further developed by for the case of rubber by Thomas, Lake, Mullins, Lindley and Rivlin. The original application of this approach in the case of rubber was predict to static strength, and later Thomas extended it to the analysis of the growth of the cracks under cyclic loadings in natural rubber. Thomas discovered a square-law context between energy release rate and crack growth rate in the case of unfilled natural rubber. According to Griffith's hypothesis the crack growth is due to the conversion of the stored potential energy to surface energy is in connection with new crack surfaces. He presented that the surface energy associated with the crack faces of a broken glass cane was equal to the elastic energy caused by the fracture. The potential energy (in rubber) released from surrounding material is spent on both reversible and irreversible changes to create the new surfaces. The energy release rate is simply the change in the stored mechanical energy ∂u , per unit change in crack surface area ∂A. This quantity is often called tearing energy T in rubber literature.

$$T = \frac{\partial u}{\partial A}$$

The energy release rate was first applied to the analysis of rubber specimens under static loading, and the above mentioned concept also applied to crack growth under cyclic loading. The experience was that the maximum energy release rate achieved during a cycle determined the crack growth rate, for R=0 cycles [24].

4. Summary

An algorythm was presented which allows to calculate strain changes and temperature changes of the rubber part of a vehicle component under certain conditions. In the future I would like to develop a solving computer program in order to apply it as a thermodynamically consistent description. The present numerical algorithm is the basis of the further fatigue and lifetime-calculations. The literature survey will be used to create the connection with the calculations.

5. Acknowledgement

Supported BY the ÚNKP-18-3 New National Excellence Program of the Ministry of Human Capacities.

References

[1] Bonet, J., Wood, R. D.: Nonlinear Continuum Mechanics for Finite Element Analysis, Camebridge University Press (1997).
[2] Holzapfel, G. A.: Nonlinear Solid Mechanics, John Wiley&Sons, Chichester, (2000).
[3] Ogden, R. W., Large deformation isotropic elasticity: on the correlation of theory and experiment for incompressible rubberlike solids, Proc. Royal Society of London, Series A 326, pp. 565-584. (1972)
[4] Ogden, R. W., Elastic deformations of rubberlike materials, H.G.Hopkins and M.J. Sewell, eds., Mechanics of Solids, the Rodney Hill 60th Anniversary Volume, (Pergamon Press, Oxford), pp. 499-537, (1982).
[5] Reese S., Wriggers P.: A material model for rubber-like polymers exhibiting plastic deformation: computational aspects and a comparison with experimental results, Computer methods in applied mechanics and engineering, Vol 148, pp. 279-298, (1997).
[6] Böl, M., Reese, S.: Finite element modelling of rubber-like polymers based on chain statistics, International Journal of Solids and Structures, Vol 43, pp. 2-26, (2006).
[7] Pere, B.: Solution of Coupled Thermomechanical Problems Using p-FEM, 8th European Solid Mechanics Conference (ESMC2012), (CD-ROM, 2 pages), Graz, Austria, 9-13 July (2012).
[8] Holzapfel, G. A., Simo J., C.: Entropy elasticity of isotropic rubber-like solids at finite strains, Computer methods in applied mechanics and engineering, Vol 132, pp. 17-44. (1996).
[9] Égert J., Pere B.: Finite Element Analysis, Universitas Győr Nonprofit Kft., Hungary, Győr (2011).
[10] Lake GJ. Fatigue and fracture of elastomers. Rubber Chemistry and Technology 1995;68:435–60.
[11] Thomas AG. The development of fracture mechanics for elastomers. Rubber Chemistry and Technology 1994;67:G50–G60.
[12] Ellul MD. Mechanical fatigue. In: Gent A, editor. Engineering with rubber, How to design rubber components. Munich: Carl Hanser Verlag; 1992. [chapter 6].
[13] Lake GJ, Thomas AG. Strength. In: Gent A, editor. Engineering with rubber, How to design rubber components. Munich: Carl Hanser Verlag; 1992. [chapter 5].
[14] Lake GJ. Aspects of fatigue and fracture of rubber. Progress of Rubber Technology 1983;45:89–143.

[15] Gent AN. Strength of elastomers. In: Eirich FR, editor. Science and technology of rubber. New York: Academic Press; 1978. p. 419–54.
[16] Mars WV, Fatemi A. Factors that affect the fatigue life of rubber: a literature survey. Rubber Chemistry and Technology; in press.
[17] Wöhler A. Wöhler's experiments on the strength of metals. Engineering 1867;2:160.
[18] Cadwell SM, Merrill RA, Sloman CM, Yost FL. Dynamic fatigue life of rubber. Industrial and Engineering Chemistry, Analytical Edition 1940;12:19–23.
[19] Gent AN, Lindley PB, Thomas AG. Cut growth and fatigue of rubbers. I. The relationship between cut growth and fatigue. Journal of Applied Polymer Science 1964;8:455–66.
[20] Lee MP, Moet A. Analysis of fatigue crack propagation in NR/BR rubber blend. Rubber Chemistry and Technology 1993;66:304–16.
[21] Roberts BJ, Benzies JB. The relationship between uniaxial and equibiaxial fatigue in gum and carbon black filled vulcanizates. In: Proceedings of Rubbercon '77, vol. 2.1. 1977. pp. 2.1–2.13.
[22] Roach JF. Crack growth in elastomers under biaxial stresses. Ph.D. Dissertation. USA: University of Akron; May 1982.
[23] Griffith AA. The phenomena of rupture and flow in solids. Philosophical Transactions of the Royal Society of London, Series A 1920;221:163–98.
[24] Mars WV, Fatemi A.A literature survey on fatigue analysis approaches for rubber. In: International Journal of Fatigue, Vol, pp. 949-961. 24., 2002.

RECYCLED TIRE RUBBER MODIFIED BITUMENS FOR IMPROVING THE QUALITY OF THE ROAD CONSTRUCTIONS IN ALBANIA

Dhoska K. PhD., Markja I. PhD.
Faculty of Mechanical Engineering – Polytechnic University of Tirana, Albania

kdhoska@upt.al

Abstract: *Nowadays, only a small percentage of waste tires are being landfilled in Albania. The large environmental impact has made the government to support some companies for building up the recycling industry of the waste tire in Albania. The Recycled Tire Rubber have been used in many fields such as agricultural uses, sport applications, civil engineering, rubber modified asphalt applications etc. Therefore, different parts of the world have used rubber modified asphalts where the benefits were being more widely experienced and recognized. Based on it, our paper will be focused on the asphalt mixtures produced with Recycled Tire Rubber Modified Bitumen's (RTR-MBs). Our proposal can reduce environmental impact from the waste tires and improving the quality of the road constructions in Albania.*

Keywords: RTR-MBs, ROAD CONSTRUCTIONS, ASPHALT APPLICATION, WASTE TIRES, ENVIRONMENTAL IMPACT.

1. Introduction

In recent decades, the worldwide growth of the automobile industry and the increasing use of vehicles as the main means of transport have tremendously boosted tire production [1]. This has generated massive stockpiles of used tires [1, 2]. Extensive research works were carried out on how to use used tires in different applications [2]. Furthermore, some of the fields are linked with agricultural uses, sport applications, civil engineering, rubber modified asphalt applications which have used Recycled Tire Rubber.

The increasing use of vehicles and traffic intensity on the roads has pushed Albanian government to speed up the quality policies on the road constructions and to reduce the environmental impact caused from the waste tires. The quality of the road constructions and the large environmental impact has made also the government to support some companies for improving the paving industry and building up the recycling industry through the waste tires. The use of rubber is of interest to the paving industry because of the additional elasticity imparted to the binder and enhanced safety related to improved roadway skid resistance [3].

Tire recycling is one of the most important processes in the industry [4-6]. The Fig. 1 depicts the technologies of the possible waste tire treatment routes.

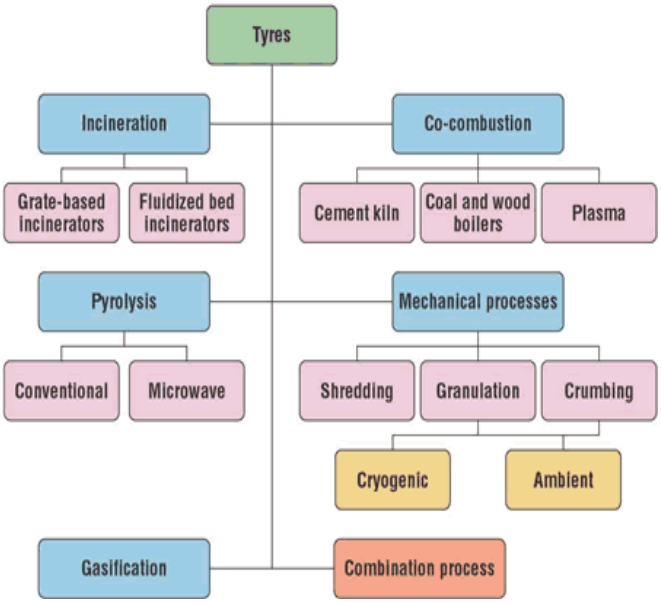

Fig. 1 *Technologies for managing scrap tires [7]*

Due to economic reason the recycling technology in ambient temperature has been used in this research work. This is also the widespread method used in most of the countries for recycling technology. The importance of the usage of Recycled Tire Rubber Modified Bitumen's for improving the quality of properties of this material will briefly described in this paper.

2. Materials and Methods

Tire recycling is one of the most important processes in the industry [1-11]. Table 1 depicts the materials characterization of the waste tire that is used in recycling process.

Table 1. *Materials characterization of the waste tire.*

Ingredients	Percentage (%)
Elastomers	47
Carbons	21.5
Metals	16.5
Textile fibers	5.5
Zn-oxide	1
Sulfur	1
Additive	7.5

Through tire recycling process we can eliminate metal materials and fibrous with textile nature from inside the rubbers. Afterward, particle size of the rubbers would influence in the performance of the rubber modified asphalt. Non-regular sizes of the rubbers having a specific area of greater than regular size were more likely to react with bitumen at high temperature through wet process asphalt forming. In our research work, the wet process asphalt forming has been used to produce rubber modified asphalts, see Fig. 2.

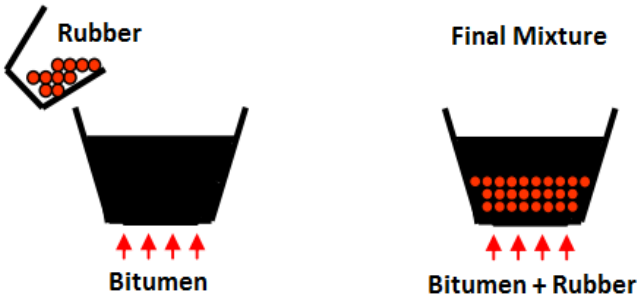

Fig. 2 *Rubber modified asphalts.*

The quantity of the Recycled Tire Rubber (RTR) in the mixture of the asphalt was 10%. Particles size of the rubbers varied from 0.85 mm to 2.36 mm and 1 mm to 4 mm. The modification of this material is carried out to reinforce the bitumen properties through the physical-chemical coupling between bitumen and rubber at high temperatures.

3. Summary Results

Addition of elastomeric rubber to the asphaltic bond, regardless of the method used for obtaining the final product, makes it possible to reinforce the properties of the asphalts which are as follows. The Fig. 3 depicts the comparisons of the crack levels during the years.

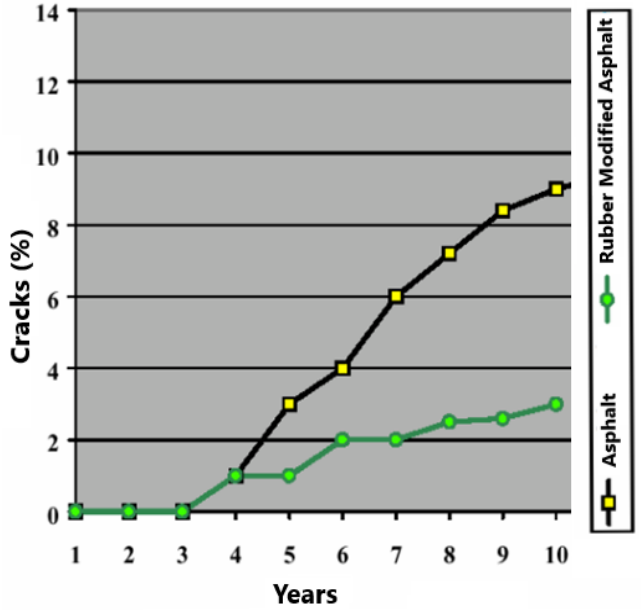

Fig. 3 *Comparisons of the cracks level during the years.*

The results have shown that the cracks level during the years were more lower in rubber modified asphalt than conventional asphalt. Another important analysis is focused on the comparisons of the penetration values between rubber modified asphalt and conventional asphalt, see Fig. 4.

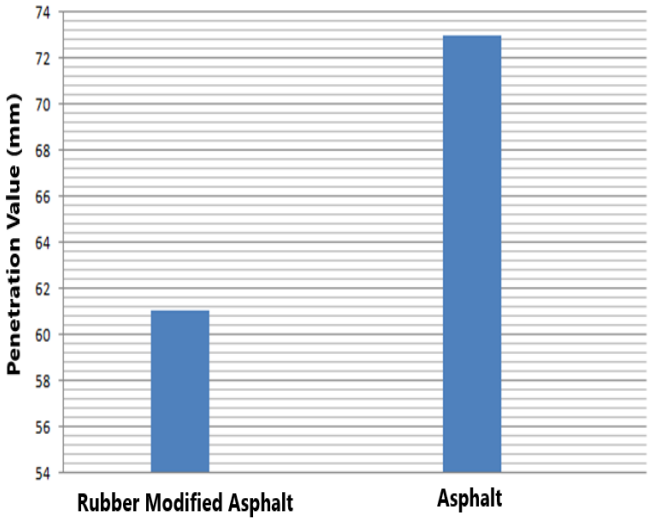

Fig. 4 *Penetration value for rubber modified asphalt and conventional asphalt*

The results have shown that penetration value is lower for rubber modified asphalt in comparisons of the conventional asphalt.

4. Conclusions

The importance of the usage of Recycled Tire Rubber Modified Bitumens for improving the quality of properties of this material has been briefly described. This proposal have shown that rubber modified asphalts will reduce environmental impact by using recycling process and improve the quality of the road constructions in Albania. Further studies should be done to investigate long term performance of field test sections under various traffic conditions.

5. Acknowledgment

The authors gratefully acknowledge ELBA ltd. Laboratory and the Polytechnic University of Tirana for partial funding of this research work.

6. References

[1] M. Bekhiti, H. Trouzine, A. Asroun.: Mechanical Properties of Waste Tire Rubber Powder, Engineering, *Technology & Applied Science Research*, vol. 4, No. 4, pp. 669-672, 2014.

[2] E. Ganjian, M. Khorami, A. A. Maghsoudi, "Scrap–tyre–rubber replacement for aggregate and filler in concrete", *Construction and Building Materials*, vol. 23, No. 5, pp. 1828-1836, 2009

[3] M. B. Takallou, H. B. Takallou. "Benefits of Recycling Waste Tires Rubber Asphalt Paving" *Transportation Research Record*, vol. 1310, pp. 87-92, 2015.

[4] D. K. Appiah, V. N. Berko-Boateng, T. A. Tagbor, "Use of waste plastic materials for road construction in Ghana," *Case Studies in Construction Materials*, vol. 6, pp. 1-7, 2016

[5] D. Le Presti, "Recycled Tyre Rubber Modified Bitumens for road asphalt mixtures: A literature review," *Construction and Building Materials*, vol. 49, pp. 863-881, 2013.

[6] G. N. King, H. W. King, "Polymer modified asphalt, an overview," *American Society of Civil Engineering*, vol. 1, pp. 240-254, 1986.

[7] E. Muzenda, "A Discussion of Waste Tyre Utilization Options," *2nd International Conference on Research in Science, Engineering and Technology*, March 21-22, pp. 198-202, 2014 Dubai (UAE).

[8] B. Adhikari, and S. Maiti, "Reclamation and recycling of waste rubber". *Progress in Polymer Science*, vol. 25, pp 909–948, 2000.

[9] S. Pechpoothong and M. Kopystecki, Analysis of Rubber Waste utilization at Pandora Production Company Limited, *World Academy of Science, Engineering and Technology*, Vol. 77, pp. 733-737, 2013.

[10] H. Trouzine, A. Asroun, N. Asroun, F. Belabdelouhab, N.T. Long, "Problem of waste tires in Algeria", *Nature & Technologies*, Vol. 5, pp. 28-35, 2011

[11] R.K. Dhir, M.C. Limbachiya, K.A. Paine, Recycling and reuse of used tyres, *Thomas Telford Publishing–Thomas Telford Ltd*, London, 2001

SURFACE TREATMENTS AND COATINGS APPLICATION ON THE ALUMINUM PRODUCTS

PhD. Markja I[1], PhD. Dhoska K.[2], Prof. As. Elezi D.[3]
Faculty of Mechanical Engineering - Polytechnic University of Tirana, Albania
Mother Teresa No.4, 1001 Tirana, Albania,
imarkja@fim.edu.al , irida.markja@gmail.com

Abstract: *The aim of this work is to present the influence of anodic surface treatment parameters on thickness and structure of an anodic layer formed on aluminum products.*

The materials used in this study are the aluminum products from Alumil Company in Albania. The analyses of samples were performed using Optical Microscopy (Leica DMI 5000 M) for characterization of macrostructure of anodizing layer and Vickers micro-hardness (HMV-2 tester) of non-anodized aluminum products and anodized aluminum products. Aluminum product of the series A6060 are taken in Alumil Company in Albania. Comparing the results in this research (analyses) we have concluded the characteristics of anodizing layer in the aluminum product, which have improved and increase their surface and product performance.

Keywords: ALUMINUM ALLOY, MICRO-HV, OM, ANODAZING, MICROSTRUCTURE

1. Introduction

Surface treatments and coatings are applied to aluminum products to enhance their performance. In order to improve surface properties of final products, such as wear resistance, corrosion resistance - different types of surface treatments are applied. [1,2]

Anodizing is one the best technique for protective and decorative purposes is the most common method of superficial oxidation processes and is carried out through anodic oxidation.

The usability of aluminum after anodizing depends mainly on the properties of oxide layers occurred during this process. [1,2]

Table one presents the chemical composition of A6060 [4]:

Table 1: *Chemical composition of the A6060 aluminum alloy*

	Alloy elements							
Alloy	Si	Fe	Cu	Mn	Mg	Cr	Zn	Ti
A6060	0.44	0.33	0.029	0.039	0.43	0.0095	0.053	0.016

Evaluation of the thickness of the oxide layer was carried out in the transverse section of the anodized profile, after polishing. Observations for thickness estimation of the oxide layer were performed on the 500x and 1000x metallographic microscope as well as the micro-hardness (Vickers) 400x magnification. [1,2,5]
The metallographic preparation of the samples and measurement are performed in Materials Science and Technology Laboratory, in Mechanical Engineering Faculty in Tirana-Albania. [1,2]

We focused the experimental part of our work on estimating the thickness of the anodized layer and its hardness. Performing Optical Microscopy using Leica DMI 5000 M software for characterization of macrostructure of anodizing layer and performing micro-hardness Vickers (HMV-2 tester) on aluminum products with anodizing treatment on the surface and also aluminum products without treatment. [1,2]

2. Discussion and Conclusions

- The A6060 products were coating with a layer anodizing and the level of strengthening was followed up and measured by micro-hardness test with 10gf, force applied for 10 sec in one indenter;
- The thickness of the anodized layer depends on the maintaining time in the anodizing bath;
- The A6060 products were coating with a layer anodizing and the level of strengthening was followed up and measured by micro-hardness test with 10gf, force applied for 10 sec in one indenter;
- In figure 1 it is shown the microstructure of sample from an aluminum profile products, taken from metallographic microscopy;

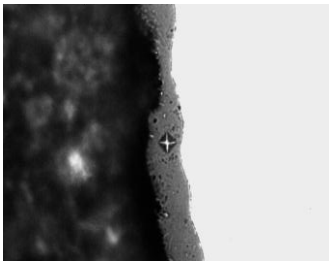

Fig.1. *Micro-hardness (HV) indenter with magnification 500x*

- The anodizing surface of aluminum products Based on the micro-hardness measurement results have higher hardness compared with the simple aluminum products without treatments in the surface;
- The micro - hardness of layer anodizing it is in the range between 420 – 560 HV comparing with the results of aluminum samples without treatments in the range between 55 – 70 HV.

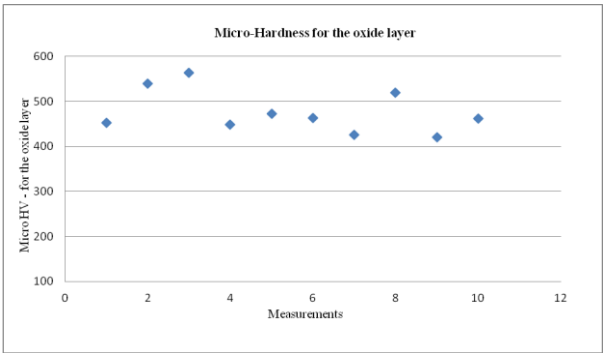

Graph. 1. The results of micro-HV comparing the homogeneity of surface treatments

- Evaluation of micro-hardness of the oxide layer with thickness ~11microns determined with metallographic microscope by Leica Soft – provides the anodizing efficiency by increasing the hardness 8 times more versus aluminum products without treatments or coating on their surface.

REFERENCES

[1] E. Lamani, I.Markja, 'Aspects of the surface treatments/coatings application on the aluminum products' – Sympozium, Faculty of Mechanical Engineering.

[2] M.Ardelean1, S.Lascău2, E.Ardelean1 and A.Josan1 'Surface treatments for aluminium alloys' International Conference

on Applied Sciences (ICAS2017) IOP Conf. Series: Materials Science and Engineering 294 (2017)

[3] J.Konieczny*, K.Labisz*, M.Polok-Rubiniec*, A.Włodarczyk-Fligier* "Influence of aluminium alloy anodizing and casting methods on structure and functional properties" Arch. Metall. Mater., Vol. 61 (2016), No 3, p. 1337–1342

[4] www.pfonline.com/articles/aluminum-anodizing

[5] Paul J.D. Whiteside, Jeffrey A. Chininis and Heather K. Hunt 'Techniques and Challenges for Characterizing Metal Thin Films with Applications in Photonics' Department of Bioengineering, University of Missouri, Columbia, MO 65211, USA;paulwhiteside@mail.missouri.edu (P.J.D.W.); jacrf5@mail.missouri.edu (J.A.C.)

ИДЕНТИФИКАЦИЯ ПОЛИМЕРНОГО МАТЕРИАЛА TEKRONE

IDENTIFICATION OF TEKRONE POLYMER MATERIAL

д. н. гос. упр., к.т.н., проф. Кобец А.[1], к.т.н. доц. Деркач А.[1], к.т.н., доц. Кабат О.[1], асп. Муранов Е.[1], инж. Шаповал А.[2]
[1] Инженерно-технологический факультет – Днепровский государственный аграрно-экономический университет, Украина
e-mail: derkach_dsau@i.ua
[2] Общество с ограниченной ответственностью, «Научно-производственное предприятие «Союз-Композит», Украина

Abstract: *Authentication of polymeric material of TEKRONE, that is used for making of dumps of ploughs, is conducted. Analogues are certain - superhigh molecular полиэтилены PE- 500 and PE- 1000. Experimental standards are made. Their capacity is well-proven.*
KEYWORDS*: COMPOSITE MATERIALS, .*

1. Вступление

В соответствии с принципами, разработанными Европейской комиссией по ключевым технологиям (European Commission Key Enabling Technologies) создание новых материалов являются приоритетными задачами.

Сельскохозяйственное машиностроение сегодня интенсивно внедряет инновационные решения. Машины и механизмы, которые используются для обработки почв, оснащаются деталями и узлами из полимеров и полимерно-композитных материалов (ПКМ) на их основе, что позволяет существенно повысить надежность и долговечность машин, а затраты на сервис снизить в разы. Одними из таких деталей является отвалы лемешных плугов.

Наиболее перспективными являются полимеры или ПКМ на их основе [1 -3]. Благодаря своим уникальным свойствам они нашли широкое применение практически во всех сферах деятельности человека и является "материалами будущего", из которых получают широкую номенклатуру изделий. Логично, что данное направление будет и дальше интенсивно развиваться.

2. Постановка проблемы

Несколько лет назад в Украине появились отвалы плугов из ПКМ марки "TEKRONE" (рис.1). Такие изделия являются надежными и долговечными деталями, которые при соответствующей эксплуатации могут работать и в полном объеме выполнять свои функции в течение длительного периода [4, 5]. Однако, этот материал производится в Европе и его формула не раскрывается для отечественных машиностроителей.

Цель работы – идентификация материала марки "TEKRONE", исследование некоторых свойств, а также выявить аналоги данного материала.

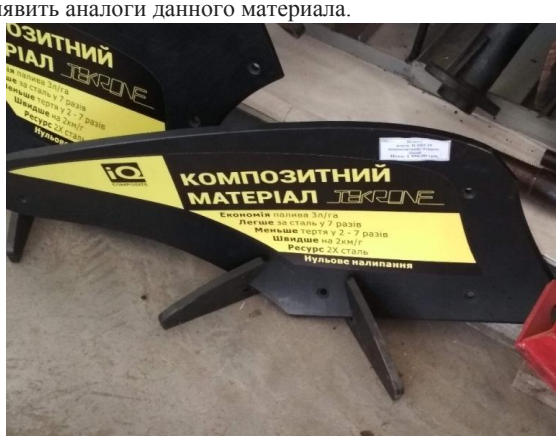

Рисунок 1 – Отвал лемешного плуга, изготовленный из полимера “TEKRONE”

Согласно информации, предоставленной производителем [5], использование отвалов с "TEKRONE" способно обеспечить следующие преимущества:

- повышение производительности работы пахотного агрегата на 9 %;
- экономию топлива до 3 литров в расчете на 1 га;
- высокие антиадгезионные свойства "TEKRONE" обеспечивают практически полное отсутствие налипания при возделывании влажной почвы, что в свою очередь повышает производительность работ, а также экономит время, затрачиваемое на регулярную чистку плуга от грязи, способствует снижению тягового сопротивления.

Стоимость одного отвала "TEKRONE" плуга ПЛН-3-35 составляет на начало 2019 - около 52 € [5].

3. Методы исследований

Для первичной идентификации достаточно исследовать физико-механические свойства и сравнить их с ближайшими по свойствам материалами. Поэтому, определяли следующие параметры: плотность; ударную вязкость по Шарпи; прочностные свойства.

Плотность образцов определяли методом гидростатического взвешивания в водной среде согласно ГОСТ 15139-69. Ударную вязкость определяли с помощью копра КМ-0,4 по методу Шарпи согласно ГОСТ 4647-80. Исследования прочностных свойств осуществляли на испытательной машине FP-100 согласно ГОСТ 4651-82.

4. Решение рассматриваемой задачи

Результаты исследований показали, что ПКМ марки "TEKRONE" - это материал на основе термопластичного полимера с содержанием черного пигмента 0,5 ... 0,7 % масс. Кроме того, установленные свойства этого материала (табл. 1) близки к свойствам сверхвысокомолекулярных полиэтиленов PE-500 и PE-1000.

Таблица 1 *– Некоторые свойства исследуемых полимеров*

Из данных, приведенных в табл. 1 можна сделать вывод о том, что материалы на основе PE-500 и PE-1000 по своим свойствам соответствуют ПКМ марки “TEKRONE”. Также установлено, что толщина отвалов составляет 12 мм, а это соответсвует толщине листов PE, поставляемых в Украину из стран Европейского Союза.

Марка полимера	Параметр			
	Плотность, кг/м^3	Предел текучести при сжатии, МПа	Теплостойкость по Вика, ^{o}C	Ударная вязкость, кДж/м^2
TEKRONE	954	17,9	95	44
PE 500	960	24	80	50
PE 1000	930	19	80	80

Проводя анализ рынка по продаже данных материалов можно сделать вывод, что материалы РЕ 500 и РЕ 1000 до 2 раз дешевле, чем ПКМ марки "TEKRONE", поэтому изделия из них тоже могут быть либо дешевле, либо рентабельность производства выше. Следует отметить, что материал РЕ 500 на 20% дешевле, чем РЕ 1000 (90 евро против 119 за 1 лист). Таким образом, было принято решение изготовить опытную партию отвалов плугов лемешных.

Для изготовления экспериментальных отвалов были закуплены полимерные материалы РЕ-500 и РЕ-1000 в виде листового профиля, выпускающихся промышленностью Бельгии. Геометрические размеры 3000 × 1500 × 12 мм.

Стоимость листа РЕ-500 - 90 €; РЕ-1000 - 119 €.

Рационально разместив проекции отвалов плугов, укомплектованных обычными культурными отвалами, получили 16 отвалов и 12 полевых досок (рис.2). При этом наименьшее расстояние между заготовками составило 5 мм.

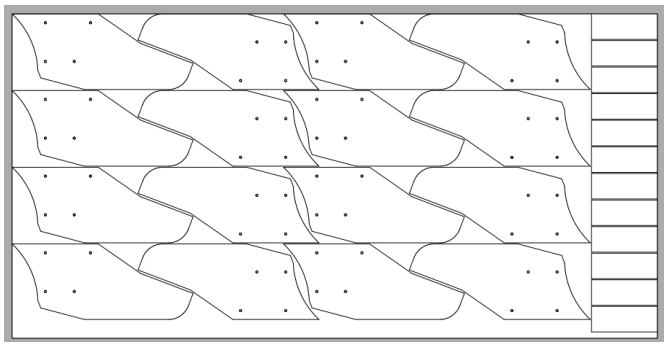

Рисунок 2 *– Схема размещения заготовок отвалов.*

Лист разрезали на отдельные заготовки. В дальнейшем их нагревали до температуры 120 °С и изгибали. Охлаждали до температуры окружающей среды.

Полученные таким образом опытные отвалы были предоставлены на полевые испытания из материалов: РЕ-500 - 2 единицы, РЕ-1000 - 1 единица. Они были установлены на плуг ПЛН-3-35, производства ООО «Велес Агро» (г. Одесса).

а) *б)*

Рисунок 3 *– Плуг, укомплектованный экспериментальными отвалами: а) конструкция позволяет регулировать угол наклона отвала; б) визуализация размещения отвалов по маркам.*

Обычный агрофон - стерня ранних зерновых колосовых, глубина обработки - 25 ... 27 см. Экстремальный агрофон - стерня подсолнечника - глубина обработки - до 30 см.

При эксплуатационно-технологической оценке определяли:

- производительность за час сменного времени;
- удельный расход топлива;
- количество обслуживающего персонала;
- качество обработки.

Эксплуатация агрегата проходила в штатном режиме, рабочая скорость - 8 ... 9 км / ч. В качестве эксперимента на отдельных участках выполнялась вспашка на повышенных скоростях - до 10 ... 11 км / ч.

Экспериментальным агрегатом была выполнена вспашка на площади 63,8 га, на таких агрофонах:

- стерня ранних зерновых колосовых - 42,4 га, глубина обработки - 25 ... 27 см;

- стерня подсолнечника после дискования - 21,4 га - глубина обработки - 27 ... 30 см.

Кратковременно, периодически выполнялась экстремальная вспашка на глубину 31 ... 32 см (общая площадь такой пахоты - не более 0,03 га).

Грунты - черноземы обычные среднемощные, класс - 3. Относительная влажность на период первых испытаний составила 26%, что является оптимальным показателем.

Результаты. В течение всего периода испытаний отказов, отклонений от агротехники, других осложнений, вызванных экспериментальными изделиями, не было. После первых проходов было отмечено инертную реакцию композитных отвалов в почву - налипание или минимальное, или отсутствует. В процессе дальнейших испытаний исчезла необходимость очистки отвалов от налипания почвы и растительных остатков. Как следствие - оперативное время агрегата в работе возросло.

При этом качество вспашки улучшалось.

5. Заключение

1. После выполнения наработки 63,8 га визуальный осмотр и диагностика технического состояния отвалов плугов показали отсутствие видимых признаков их износа, все параметры находятся в номинальных пределах, экспериментальные отвалы пригодны к дальнейшей эксплуатации.

2. Уменьшено расход горючего не менее, чем на 2 л / га с одновременным увеличением производительности агрегата МТЗ-82.1 + ПЛН-3-35РЕ на 36 %.

3. Комплекс проведенных научных исследований и полученных результатов свидетельствует о целесообразности использования разработанного продукта для изготовления отвалов лемешных плугов.

6. Литература

Ashby M.F., Jones D.R.H. Engineering materials 1. An introduction to their properties and applications. Butterworth-Heinemann, Oxford, 2002. 306 p.

2. Kabat O., Sytar V., Sukhyy K. Antifrictional polymer composites based on aromatic polyamide and carbon black. Chemistry & Chemical Technology. 2018; 12 (in press).

3. Klymenko A., Sytar V., Kolesnyk Ie. Adhesion of poly (m-, p-phenylene isophtalamide) coatings to metal substrates. Progress in Organic Coatings, 2014, vol. 77, 11, pp. 1597-1602. https://doi.org/10.1016/j.porgcoat.2014.04.028;].

4. Філія АТ «Промарматура» «Агротехсервіс». [Електронный ресурс]. Режим доступа от 03.01.2019: http://www.agroservice.dp.ua/

5. http://www.iqcomposite.com/products/otval-pluga-pln/